UNIVERSITA' DEGLI STUDI DI PADOVA

SCUOLA DI INGEGNERIA

DIPARTIMENTO DI INGEGNERIA INDUSTRIALE
CORSO DI LAUREA MAGISTRALE IN INGEGNERIA DEI MATERIALI

Tesi di Laurea Magistrale in Ingegneria dei Materiali

OTTIMIZZAZIONE DEL TRATTAMENTO TERMICO DI UNA GHISA MULTILEGATA CON GRAFITE LIBERA

STUDY ABOUT THERMAL TREATMENTS ON A MULTI-ALLOYED IRON WITH FREE GRAPHITE

ÉTUDE DU TRAITMENT THERMIQUE D'UNE FONTE MULTI ALLIÉE AVEC GRAPHITE LIBRE

Relatore: Prof. Irene Calliari

Correlatori : Prof. Jacqueline Lecompte-Beckers
Ing. Jérôme Tchoufang Tchuindjang
Ing. Hakan Paydas
Ing. Olivier Dedry

Laureando: TOMMASO MAURIZI ENRICI

ANNO ACCADEMICO 2015/2016

1. Abstract

English version:

The research about the High Speed Steel (HSS) for Hot Strip Mill is moving to the opportunity of safe money decreasing the roll change with anti-sticking and lubricant properties; in the last year a composition was characterized to investigate the simultaneous presence of graphite, in particular spheroidal graphite, and a hard microstructure. The aim is to combine the hard martensite matrix, hard carbides coming from particular carbide-forming elements as vanadium and niobium, and spheroidal graphite nodules in the shell of a duplex material roll. The Marichal Ketin Industries with the University of Liège collaborate to arrive on this combination; a considerable amount of vanadium, silicon, molybdenum and niobium were granted for both the aim. In this work two compositions, coming from the evolution of a first trial, are investigated to evaluate the carbides presence to ensure a hard microstructure, verify the graphite shape evolution and the increase of the graphite amount to have the possibility of anti-sticking properties, investigate on the solidification steps to understand the causes of the structure formation and evaluate the effects of different thermal treatments on the HSS with free graphite. Thermocalc simulations, DTA tests and microscope surveys were carry out to analyze the microstructure; moreover Dilatometer tests, Magnegage analyses and Hardness tests were performed to investigate the behavior of the HSS in the different depths and to evaluate the influence of thermal treatments on the microstructure. The graphite was observed and evaluated into the microstructure together with all the carbides to understand especially the solidification steps and the possible behavior during the use of the HSS with free graphite.

French version:

Les aciers de coupe rapide de type HSS (High Speed Steels) ainsi que les fontes fortement alliées représentent une famille d’alliages couramment utilisés comme cylindres de laminoir dans les trains à bandes à chaud, et particulièrement les bandes finisseuses, où les propriétés recherchées sont la tenue à l’usure et à l’oxydation à chaud, ainsi qu’une bonne résistance à la friction. Tous les étages des trains à bandes finisseuses ont connu des développements avec l’élaboration de nouvelles nuances de cylindres de type HSS, à l’exception des dernières cages où on trouve toujours des fontes de type ICDP, qui contienne du graphite libre qui est essentiel pour assurer une bonne lubrification. C’est ce qui justifie les derniers développements en cours pour l’élaboration d’un alliage de type HSS avec du graphite libre, pour les dernières cages finisseuses. Un tel alliage comportant à la fois une matrice dure martensitique, des carbures de solidification résistants à l’usure et formés par des éléments carburigènes tels que V, Mo, Nb, et du graphite libre, devrait permettre d’améliorer le rendement des campagnes de laminage à chaud des tôles fortes. L’entreprise Marichal Ketin collabore avec l’Université de Liège pour caractériser une telle nuance. C’est ainsi que la présente étude porte sur des matériaux ayant des compositions chimiques proches, de type HSS graphitique, qui ont été élaborés par MK avant d’être caractérisés au MMS. Trois compositions chimiques sont étudiées, et elles sont obtenues en faisant notamment varier de manière plus ou moins significative des éléments tels que C, Ni, Nb, Cr, pour voir l’influence de telles variations sur la structure de solidification, la nature des carbures, la forme et la quantité de graphite, etc. En outre on réalise des traitements thermiques et on étudie leur influence sur le graphite libre, et sur la teneur en austénite résiduelle. Différents outils et méthodes d’investigation sont utilisés dans cette étude, tels que les simulations thermodynamiques avec ThermoCalc, les analyses par ATD et dilatométrie, les caractérisations de la microstructure en optique et en microscopie électronique à balayage, les essais de duretés, les analyses avec jauge magnétique. Les résultats des différentes investigations sont discutés et des corrélations sont établies. La caractérisation du graphite dans la microstructure permet de comprendre les étapes de la solidification et du dégager les perspectives pour l’utilisation du HSS graphitique dans le cadre de l’application visée.

Italian version (large version):

La ricerca riguardo gli acciai rapidi (HSS o High Speed Steel) per laminazioni a caldo si sta muovendo verso l'opportunità di risparmio di denaro, diminuendo il cambio di rulli da laminazione con proprietà di anti-attacco e di lubrificazione; nell'ultimo anno una composizione è stata caratterizzata per investigare sulla simultanea presenza di grafite, in particolare grafite sferoidale, e una microstruttura dura. Lo scopo è il combinare una matrice dura di martensite, carburi duri provenienti da particolari elementi formatori come vanadio e niobio, e noduli di grafite sferoidale nella parte esterna di un materiale duplex per rulli. L'industria Marichal Ketin con l'Università di Liegi collaborano per arrivare a questa combinazione; una considerabile quantità di vanadio, silicio, molibdeno e niobio sono utilizzati a questo scopo. Marichal Ketin grazie alla continua innovazione ha avuto nell'ultimo secolo una posizione chiave nella produzione di rulli per laminazione di qualità, sia per le avanzate tecniche di produzione, sia per l'elevato controllo tanto da creare specifiche classi di materiali per le laminazioni a caldo (Hot Strip Mills o HSM). Attualmente la produzione è portata avanti con il processo di colata centrifuga (Centrifugal casting), capace di produrre un ampio range di ICDP (Indefinite Chill Double Poured Cast Iron), Enhanced ICDP, HiCr Iron (High Chrome Iron), HiCr Steel (High Chrome Steel), SHSS e HSS come materiali esterni in rulli duplex da laminazione. Questo processo insieme a specifiche procedure di produzione per regolare l'evoluzione della solidificazione, ottiene grande precisione sulla struttura del materiale, possibilità di produrre rulli duplex e assicurare una finitura superficiale ottima. Le forze centrifughe e uno studio della solidificazione consentono un legame metallurgico tra il materiale esterno ("shell material") e il materiale interno o centrale ("core material"), necessario per assicurare un'elevata qualità nel successivo utilizzo del rullo. Il materiale centrale deve essere tenace e di solito è ghisa grigia o sferoidale, mentre il materiale esterno duro con un'alta resistenza ad usura. Negli anni si è tentato sempre di migliorare le proprietà dello strato esterno per migliorare le prestazioni generali del rullo; l'uso di costosi elementi formatori di carburi ha portato alla presenza di carburi più duri come i carburi MC, quindi tentando solo di incrementare la durezza superficiale del rullo da laminazione. Le elevate forze e le ampie superfici di contatto presenti nelle passate finali di laminazione però hanno sempre portato a fenomeni di attacco delle superfici e di conseguenza molti incidenti durante l'utilizzo dei rulli. Questo attacco tra le superfici porta a prodotti di laminazione con una finitura superficiale scarsa e possibilità di cricche per gli stress residui. La classe HSS, rispetto a tutte le altre tipologie, ha mostrato le migliori prestazioni come proprietà di anti-criccatura e anti-attacco, ma gli incidenti sono frequenti e continue interruzioni dovute al cambio dei rulli non sono desiderate dalle industrie per avere un'alta produttività. Come già detto in precedenza al momento la ricerca si sta muovendo per dotare il materiale esterno di rulli duplex di proprietà lubrificanti intrinseche e di anti-attacco; la presenza della grafite all'interno della microstruttura e le sue proprietà correlate sono già conosciute. Le possibili nuove proprietà del metallo date dalla presenza di essa sono state verificate accompagnate a durezza superficiale e resistenza ad usura. Durante lo scorso anno una prima composizione è stata caratterizzata, essa presentava una microstruttura dura e grafite sferoidale; per arrivare a questa combinazione è stato utilizzata una considerevole quantità di vanadio, silicio, molibdeno e niobio per ottenere entrambi. Alcune analisi vennero effettuate su questo primo tentativo a tre distanze differenti dalla superficie (10, 25 e 40mm) per valutarne le caratteristiche; analisi Thermocalc, analisi DTA e rilevazioni al microscopio sono state effettuate per valutarne la microstruttura. La presenza della grafite è stata verificata ed accompagnata da alcuni carburi: carburi primari MC, carburi euttetici M_7C_3, carburi eutettici M_2C e carburi secondari M_xC_y. In questo studio due composizioni, provenienti dall'evoluzione di un primo tentativo, sono considerate per valutare la presenza di carburi per assicurare una microstruttura dura, verificare l'evoluzione della forma e l'incremento del quantitativo di grafite per assicurare la possibilità di proprietà di anti-attacco, studiare le fasi di solidificazione per capire le cause della formazione di una particolare struttura e valutare gli effetti di diversi trattamenti termici sul HSS con grafite dispersa. Il primo test effettuato è la simulazione Thermocalc in condizioni di equilibrio e pseudo-equilibrio per avere un'indicazione delle possibili fasi formatesi partendo unicamente dalla composizione; questo test in particolare sarà utile per avere un'indicazione sulla temperatura notevole di

Liquidus e quindi sulla temperatura massima da impostare all'analisi DTA per avere la completa fusione dell'HSS. Per studiare la variazione di forma della grafite sferoidale all'allontanarsi dalla superficie con diversi trattamenti termici si è utilizzato un microscopio ottico su vari campioni trattati con diversi trattamenti termici: campione (prima composizione) trattato termicamente con doppia tempra a 530°C in 24h (campione X), campione X trattato successivamente con una reaustenitizzazione a 1025°C/1h (campione R1), un campione (seconda composizione) non trattato termicamente (N0) e due campioni trattati termicamente con due diverse doppie tempre partendo da N0. Oltre alle immagini che mostrano l'evoluzione della grafite sia per quanto riguarda la quantità sia per la forma, si è utilizzato il software Stream Analysis per valutare esattamente questa evoluzione nella lunghezza totale del campione per ogni millimetro. Per valutare esattamente e per confrontare la microstruttura rispetto al primo tentativo di composizione si è utilizzato insieme analisi DTA con due diverse temperature massime e osservazioni con il Scanning Electron Microscope. Si è utilizzato prima come temperatura massima 1300°C dopo l'indicazione del test Thermocalc e successivamente 1450°C (temperatura massima durante il casting del materiale) per determinare possibili differenze tra i due test; le osservazioni con il SEM sono state effettuate prevalentemente alle stesse distanze delle prove DTA per abbinare ad ogni picco dello spettro una fase della microstruttura. Ulteriori osservazioni al SEM sono state svolte sul campione X e sul campione N0 per valutare le possibili modifiche delle fasi dopo i test DTA e Dilatometro. Infatti test al Dilatometro con temperatura massima 1025°C, evitando la fusione del campione e quindi stando al di sotto della temperatura Solidus, sono stati effettuati per valutare i fenomeni legati al riscaldamento della struttura e in particolare i fenomeni legati alla grafite. Infine sui campioni X, R1 e N sono state effettuati i test di durezza (Vickers HV 30) e valutazione della austenite residua con il Magne Gage per valutare la variazione di queste caratteristiche per le due differenti composizioni, a più distanze dalla superficie e con diversi trattamenti termici. Dalle analisi precedenti si è potuto valutare la composizione e la morfologia dei carburi già presenti nel precedente studio; il vanadio e niobio in particolare sono stati rilevati nei carburi MC. I carburi M_7C_3 sono stati osservati in due diverse morfologie in accordo con la microstruttura circostante e con la stessa composizione chimica; i carburi M_2C invece si presentano solo nella morfologia regolare complessa ed è importante sottolineare l'alto valore di silicio e molibdeno in essi. Attraverso le analisi DTA, le osservazioni al SEM e i test al Dilatometro (in particolare per l'effetto Budding, legato alla destabilizzazione dei carburi euttetici) è stato possibile ricostruire la sequenza di solidificazione e capire la correlazione tra la formazione della grafite e la formazione dei carburi M_2C, che si formano dallo stesso liquido dopo la formazione dei carburi M_7C_3. Si è rilevato, rispetto al primo tentativo, un incremento della grafite in superficie passando dal 0.7% al 2-3%. La sua forma tende ad essere sferoidale nei primi 35-40mm dalla superficie e mostra un aumento delle ramificazioni tra i grani all'aumentare della distanza dovuto al maggior grado di raffreddamento e da una microstruttura differente, infatti l'HSS mostra dopo i 40mm la "zona con la strana forma" dove la grafite mostra una morfologia vermiculare o a scaglie dovuto al fenomeno del riscaldamento dopo la gettata del "materiale core" all'interno dello stampo durante la gettata del rullo. Si è riscontrato infatti la presenza di quattro distinte zone con quattro diverse microstrutture dove la solidificazione avviene con condizioni leggermente diverse, lasciando diverso quantitativo di liquido o uno spazio differente alla nucleazione e accrescimento della grafite e del carburo M_2C. Le zone, e quindi le microstrutture, vicino alla superficie tendono a lasciare più spazio tra i grani e liquido favorendo una crescita igroscopica dei noduli di grafite. Osservando questa evoluzione della grafite si è quindi provveduto a simulare i possibili trattamenti termici attraverso un particolare test DTA a tre step di riscaldamento e i test con il Dilatometro per verificare che effetti poteva avere la matrice supersatura in carbonio sulla grafite e viceversa e i possibili fenomeni del materiale. Si è riscontrato un continuo possibile movimento del carbonio dalla matrice ad altre fasi, tra cui probabilmente la grafite, e in particolare la formazione della "grafite secondaria" dalla destabilizzazione dei carburi M_2C, insieme con la formazione di carburi secondari M_6C. Le conseguenze dei diversi trattamenti termici quindi sono stati valutati sulle fasi e sulla struttura, notando che essi portano ad un ritardo delle trasformazioni di fase, in particolare la decomposizione della martensite che può indurre alla precipitazione dei carburi secondari M_xC_y più stabili. Infine è stata valutata la quantità di austenite residua e la durezza dopo i diversi trattamenti termici negli stessi punti ed è stata ideata una funzione di prestazione per valutarle insieme; come risultato il miglior trattamento termico è la doppia tempra a 525-530°C, il campione dove si ha il minor quantitativo di austenite residua, caratteristica predominante.

Summary

2. Acknowledgments

This work has been possible thanks to the Marichal Ketin foundries and the University of Liège. My deep acknowledgments go to Mr. Mario Sinnaeve and Pr. Jacqueline Lecomte-Beckers, respectively the charge of Marichal Ketin research and my tutor professor during my Erasmus period. Thanks for the really interesting project and for opportunity to have collaborated and worked with you. Thanks also to Pr. Irene Calliari for the support in this project.

My respectful greetings go to my thesis master, Jérôme Tchoufang Tchuindjang, whom passion for the subject and kindness where much helpful during the whole research here in Liège. He is an example of professionalism and conduct. I would thank the entire Metallic Material Science unit that welcomed me with much enthusiasm, in particular Neda Hashemi, Hakan Paydas and Olivier Dedry for the friendship and the support that they gave me in this period. Merci a tout!

I would thank all the people that I met in these seven months in Belgium, all of you made me grow as person. In particular I have to thank the people that lived very close to me in the PRISON CAMP of Sart-Tilman, we became as a family and I will remember with joy all the special moments with all of you. Devo menzionare per forza le tre mie sorelle acquisite : Elena La Mamma, Roberta Il Disagio e Gloria Voglio Morire. Thanks to Anett being blondie. Grazie a Edo e Luciano per l'amicizia e per le risate insieme. Grazie per avermi sostenuto e per aver vissuto grandi momenti insieme.

Vorrei ringraziare i miei amici italiani più stretti per esserci sempre stati in un modo o nell'altro, non faccio nomi solo perché ci tengono alla privacy. In particolare devo ringraziare gli altri tre TOP PLAYERS per gli anni trascorsi insieme e per le risate insieme, sperando di continuare cosi.

Ringrazio la mia migliore amica da tanti anni ~~Beatrice Pezzutto~~… ops… Bibi per esserci sempre quando ne ho davvero bisogno.

Un ringraziamento devo per forza darlo per l'appoggio nel mio periodo Erasmus e precedente ai membri polisportiva Lupino e in particolare a quelli nel gruppo toooooom 1337...*…

Ultima ma perché più importante ringrazio la mia famiglia per aver creduto in me anche quando non me lo meritavo, grazie per tutti i bei momenti passati insieme.

Dedicato ai miei genitori e a mio fratello Mattia

3. Introduction

3.1. Marichal Ketin Industries and the research

This project takes its roots within the walls of Marichal Ketin Industries (MK) located at Liège. Since 1911, this company is one of the leaders in rolling mill manufacturing and Marichal Ketin casted the first European compound static roll in the 1951; still there is always a particular attention on the on-going innovation. The continuous research and developments had maintained this industry as one of the highest roll producers (as quality); the results of the most advanced technologies in casting, control and machining to roll manufacturing create specific roll grades for the Hot Strip Mills (HSM). Nowadays, the roll casting is done with the Centrifugal casting or rotocasting process; it is capable to produce full range of ICDP, Enhanced ICDP, HiCr Iron, HiCr Steel, SHSS and HSS roll shell materials. This process combined with specific procedure to regulate the solidification evolution obtains a high precision of the material, possibility to cast rolls with duplex material and ensure optimum roll barrel surface quality. The centrifugal forces and specific procedures ensures a metallurgical bonding between the “core” material and the “shell” material, that it is necessary for an elevated quality in the successive manufacturing. The core material must be tough and usually is cast iron, meanwhile the shell material must be hard, with a high wear resistance. During years the layer part properties were improved and developed to achieve performances of the rolls; the use of expensive carbide-forming elements gave the opportunity to form harder carbides such as MC carbides. Since the 90’s HSS and semi-HSS are superior to the older grades for their smooth roll surface during rolling, especially in the middle-late stands.

3.2. New possible properties

The research until this moment went only to the direction to improve the carbide amount, thus only to increase the hardness; but the high forces and the high contact surfaces present especially in the middle-late stands of the manufacturing processes provide as consequence many incidents and problems bonded with the sticking of the surface. That sticking can give a non-smoothed surface product and the possibilities of crack extending by the compressive residual stress. The HSS shows better performance of anti-cracking and anti-sticking properties but the incidents are common and frequent interruptions due to the roll changing are not desirable to reach a high rolling productivity; farther the grinding is an outstanding cost for an industry. Nowadays the research is moving to diminish the roll changing in those stands maintaining the same hardness level and results level. The aim is to combine the hard martensite matrix, hard carbides coming from particular carbide-forming elements as vanadium and/or niobium and spheroidal graphite particles in the shell of the duplex material. The graphite presence inside a metallic matrix is already known and the properties bonded to it are also known. The high anti-sticking and lubricant properties of the metal coming from that presence were verified but accompanied with weak performance as hardness and wear resistance.

3.3. First trial

The Marichal Ketin foundries invest and bet on this opportunities of safe money decreasing the roll changing and in the last year a composition was characterized to investigate the simultaneous presence of graphite, in particular spheroidal graphite, and a hard microstructure. To arrive on this combination a considerable amount of vanadium, silicon, molybdenum and niobium were granted for both the aim. Analyses were done to a first composition at three different depths (10, 25 and 40mm) to investigate the characteristics; Thermocalc analysis, DTA tests and microscope surveys were taken to analyze the microstructure. The graphite presence was found together with several carbides in a martensitic matrix: primary MC carbides, eutectic M_7C_3 carbides, eutectic M_2C carbides and secondary M_xC_y carbides.

3.4. Current trials

The current study is about the next compositions to evaluate again the carbides presence to ensure a hard microstructure, verify the graphite shape evolution and the increase of the graphite amount to have the possibility of anti-sticking properties, investigate on the solidification steps to understand the causes of the structure formation and evaluate the effects of different thermal treatments on the HSS with free graphite. Again Thermocalc Simulations, DTA tests and microscope surveys were taken to analyze the microstructure; moreover Dilatometer tests, Magnegage analyses and Hardness tests were taken to investigate the different behavior of the HSS in the different depths and to evaluate which consequence the thermal treatments can have on the phases. Two different compositions (Composition 1 and Composition 2) were available from Marichal Ketin plus the results from the first composition studied (Composition 0). The graphite was observed and evaluated into the microstructure together with all the carbides to understand especially the solidification steps and the possible behavior during the utilization of the HSS for the application in the Hot Strip Mills.

4. Bibliography

4.1. Rolls for hot strip mills

Since the industrial era the laminated steel or laminated metals are one of the most used and formed products, thus the lamination process has become even more important. The increasing technology knowledge has enhanced the types of process with more safety and control, but the rolls are the direct responsible for a high final product quality and then their progress is mandatory.

4.1.1. History and evolution of rolls

Before the early 80's the most diffused materials for lamination rolls were the ICDP (Indefinite Chill Double Poured Cast Iron), the High Chrome Steel (HiCr Steel) and the High Chrome Iron (HiCr Iron). European rollmakers developed those roll grades that are considered as first modern materials for lamination rolls; they have been introduced since then in most of the existing roughing stands of Hot Strip Mills (HSM) as well as into the early finishing stands of compact strip mills. Nowadays these roll types are still the standard grades in many HSMs in the world, but even increasing roughing mills in terms of cost/performance ratio, including higher throughput and product quality, have stimulated the rollmakers to develop new different materials. In the early 90's High speed steel rolls (HSS) or semi-High speed steel rolls (semi-HSS) were introduced for the use in hot strip mills and gradually started to replace all the older grades for their superior wear resistance and the smooth roll surface during rolling. The ICDP was enhanced with the adding of MC carbides to have an improvement, but in comparison with the conventional ICDP it had only a wear resistance increase of the 1.2 to 1.5 times. The HSS rolls had much higher wear resistance (4 or 5 times) but they keep exhibiting manufacturing problems especially in the final stands. Today special HSS are studied to resolve these problems. [4, 7]

Figure 1 : A roll after heat treatment in Marichal Ketin Industry. [25]

4.1.2. Applications

The roll grade of ICDP and all the other roll types are used in many different layouts as Hot strip mills, Steckel mills (used for the stainless steel production), Plate mills, in Cold mills as work roll and Back up roll in Skin pass mills. In the same manufacturing can exist also many various example as full continuous hot strip mill with 5 to 7 roughing stands, three-quarter continuous hot strip mill (includes at least a reversing roughing stand and one or several one-way roughing stands), semi-continuous hot strip mill that combines one reversing roughing mill with a vertical edger and twin-tandem reversing roughing mill. All these applications need a high control of the performances and a smooth surface especially in the latest stands where the applied forces are higher. [5]

4.1.3. Commercial names

There are produced a few grades in the Marichal Ketin Indutries (MK) and their names depends on composition and on the kind of material used. The HiCr Iron is called COMET and it is stood out in based on the amount of carbon and chromium; the HiCr Steel is called GALAXY or GALILEO in based on their carbides amount and the possible applications. The HSS finally is called SIRIUS, KOSMOS or AURORA for their alloying elements amount and for the carbides presences in the matrix. All are used as work rolls and the main their characteristics are in the Table 1 (is placed also the normal produced ICDP to make a comparison with the other grades). [26]

	Tensile strength (MPa)	**Hardness (Vickers HV)**	**Best characteristics**	**Applications**	**Carbide amount (%)**
ICDP	350/450	500/730	SO, Sl	HSM, Steckel Mills and Heavy Plate Mills	35/45
COMET 90	700/800	500/800	WR, FC	Front finishing stands of HSM, Backup and work rolls for Hot Skin-pass Mills	25/30
COMET 70	600/800	390/680	WR, FC	Heavy Plate Mills and Hot Mill roughing stands (Steel & Aluminum)	20/25
GALAXY	700/800	500/730	WR, FC	Continuous and reversing roughing stands of HSM	8/10
GALILEO	700/800	500/730	WR, FC	Continuous and reversing stands of HSM and for Plate mills	/
SIRIUS	800/1000	580/690	WR, SO	continuous and reversing roughing stands of HSM and for Steckel Mill roughing stands	/
KOSMOS	900/1000	600/730	WR, SO	Early stands of HSM, Steckel Mills and Direct Strip Casting Mills	
AURORA	800/1000	600/730	WR, SO, FC	Early finishing stands of HSM (conventional and Minimill) and work rolls for Steckel Mills	/
		Legend :		• WR= Wear resistance • SO=Sticking-roll oxidation • FC=Fire cracks • Sl= Slippage	

Table 1 : List of the principal MK compositions with the main characteristics [26]

The grades are placed in order to the Tensile Strength, the characteristics and the applications are similar for type of grade according to the hardness and the carbides amount (not all data are available).

4.1.4. Manufacturing by casting

There are many casting processes and their choice depends especially on the roll type and the materials use; they can be divided in static casting, spin casting and continuous pouring casting based on the characteristics. The continuous introduction of new casting and processing technologies from the 1970’s integrated with pickling and continuous annealing lines gave a constant increase of the performances; the productivity and the product yield increased, tail-out roll defeats decreased and rolled steel quality was improved with the introduction of continuous processing lines. When defects like roll marks or heat streaks occur, the resultant damage increases at an emergency stop or strip breakage. Thus it is required to keep continuous lines operating in a steady and stable state. The rolled tonnage became dependent on roll surface roughening texture or roll surface roughness loss and until the 1980’s, technology developments centered on the manufacture of rolls of a thicker hardened depth by adding alloy elements that improve hardenability. As a result, the effective use of rolls diameter raised and many manufacturing rolls type were developed in that direction. [7, 10, 11]

4.1.4.1. Static casting

The static cast is the simplest possible casting system and it is a low cost manufacturing method. It is used for mono-structure rolls as Back-up and Structural rolls without special treatment or movement; the mould is prepared and the melt metal is injected in a specific procedure to control of the level, to regulate the solidification evolution and to ensure the optimum roll barrel surface quality. Each mould design incorporates massive barrel and bottom neck chills, resin bonded sand top necks and insulated feeder heads together with an integral bottom pour runner and ingate system. These designs ensure rapid solidification rates in the roll barrel while maintaining the best possible liquid metal feed during roll solidification. The pouring system incorporates a tangential ingate to provide smooth clean metal flow with minimum turbulence during mould fill. [27]

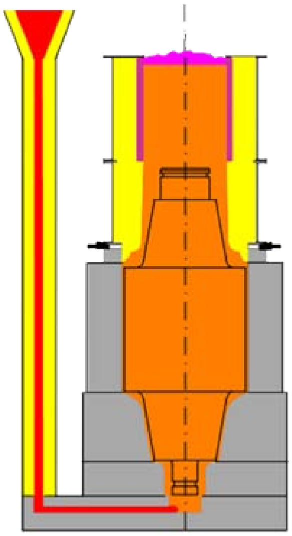

Figure 2: Structure of the static casting. [27]

4.1.4.2. Horizontal static cast

The horizontal static casting is composed by a spin casting of the external shell and a static casting of the core; this type of cast is used for mono and complex structure rolls with materials higher alloyed than the static cast ones. In the first the chill mould is placed horizontally in a centrifugal casting machine and the horizontal axis of the mould is putted on rotation, then the melted shell metal is poured inside of it and the rotation is maintained until the stability of the shell. The mould is moved and it is brought in the vertical position with inside the solidified shell but still at elevated temperature (rotated through 90°C). The perpendicular axis chill section is placed onto a bottom refractory lined neck box as a part of the mould assembly procedure and then the top refractory neck box is placed into the upper position ready for the introduction of the core metal. In the final step the liquid (tough core) metal is poured under control from the bottom part of the composed mould; the core metal has to fill in the central part of the roll (where there is also the shell) and the two peripheral parts (necks). [29]

4.1.4.3. Centrifugal casting

The centrifugal casting or rotocasting is one of the newest castings and MK use that process for their alloyed rolls with duplex material; it is possible to produce a full range of ICDP, Enhanced ICDP, HiCr Iron, HiCr Steel, SHSS and HSS roll shell materials with this casting. Computerized technology combined with rigidly defined specifications and procedures ensures that the highest level of process control is applied to every cast. The use of a vertical spin casting process combined with a single piece chill containing the roll barrel and necks allows for the entire roll to be cast in a single, continuous operation with minimal delays between steps, thereby ensuring the highest degree of control and consistency. The shell is usually made up with a hard material, both wear and thermal resistant, while the core and the necks are made up with a ductile and toughness material. The process can be divided in shell (called also mill's barrel) casting and core casting; due to the shell casting the pouring nozzle is not straight but is placed with an angle among vertical axis. When the melt metal is poured the spout puts it directly in the mould shell space; the results are the perfect filling of the shell space and a little excess of shell metal in the lower part of the mould shell space due to the centrifugal force field and due to the shape of the nozzle as shown in Figure 3. [28]

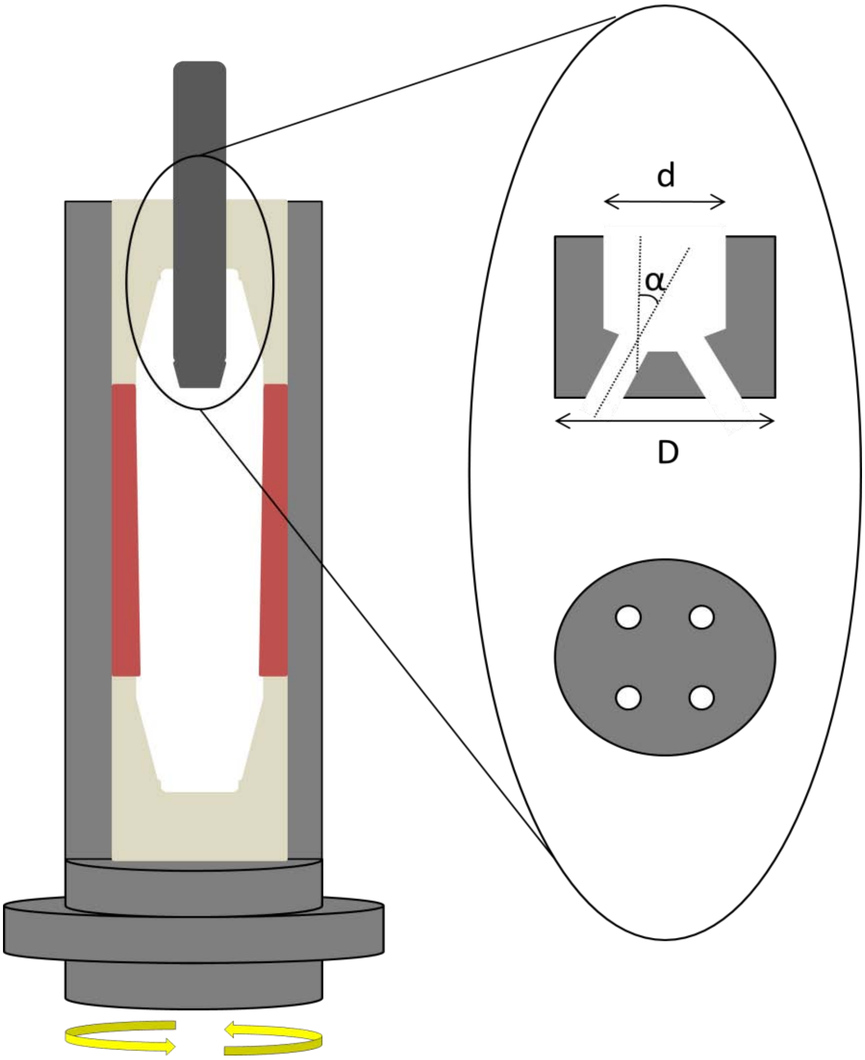

Figure 3: The centrifugal casting structure, with a focus of the casting nozzle on the side view and the bottom view.

When the shell metal is stable (usually it needs four minutes and still at elevated temperatures) the melt core metal can be injected to fill in it; in this same step the necks (called also journals) are also casted. The rotation applied by the spincaster is higher in the shell step (600 rpm) and during the filling is wound down gradually. The spincaster can rotate from 300 to 3000 rpm. The mould contains sand pieces whose job is providing their shape to the journals and is closed by two plates. Exceptional care is taken during the spin casting process to ensure that the integrity of the interface between the shell and core material will withstand the varying forces generated during the roll service lifetime. After all the steps the mould with the roll inside is taken out of the spincaster and puts at rest for cooling; it needs one week to reach a temperature below 100°C as we can see in the Figure 4. The casting is usually a fine-grained casting with a very fine-grained outer diameter, owing to chilling against the mould surface. Impurities and inclusions are thrown to the surface of the inside diameter, which can be machined away. [24]

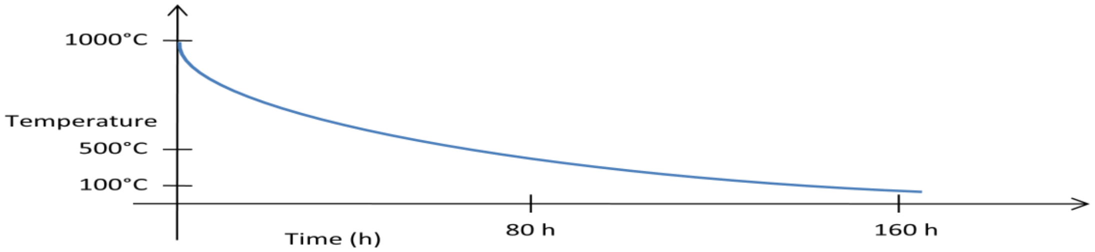

Figure 4 : Time scale of the cooling process. [24]

Centrifugal casting was the invention of Alfred Krupp, who used it to manufacture cast steel tyres for railway wheels in 1852.

4.1.4.3.1. Homogeneity of metallographic structure

In the centrifugal casting strong centrifugal forces are applied and segregation during solidification is likely to occur with this process due to their. Whether visible clear segregation can be found on roll surface, its pattern may be transferred to the rolled strips when the rolls are used in the last stand, which may lead to severe quality problems. Two of the typical segregation patterns observed on the roll surface of centrifugal cast rolls are called “cat mark segregation” and “shadow segregation”. The first one corresponds to a few millimeter-sized round spots appeared all over the roll surface, which correspond to matrix distribution worn preferentially, consequently recognized as craters or pits. The second one observes the cross section view at the corresponding part of the roll, laminated segregations composed with different microstructure size layers are found. From the roll surface, boundaries of the laminated layers appear as segregation. These types of segregation are formed by a combination of manufacturing and material conditions such as cooling rate, pouring speed, pouring temperature, density of molten metal and molten metal movement in a centrifugal force field. These conditions need to be critically controlled for each roll material in order to achieve homogeneous metallographic structure. [4]

4.1.4.4. Continuous Pouring process for Cladding (CPC)

The CPC process is a centrifugal casting concurrent for the manufacturing of new composite rolls. Alloy additions are not limited substantially in the casting of HSS materials, the solidification and cooling rates are high, a fine cast structure is obtained with solidification progressing from the surface toward the center or in the radial direction of the roll. The casting is vertical as the spin casting but the core is cast before the shell. The molten shell metal is poured into a gap between the vertical core and the water-cooled mould arranged concentrically with the core.

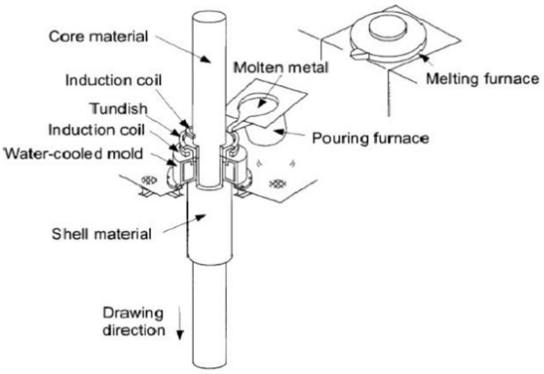

Figure 5 : Schematic drawing of a CPC process. [11]

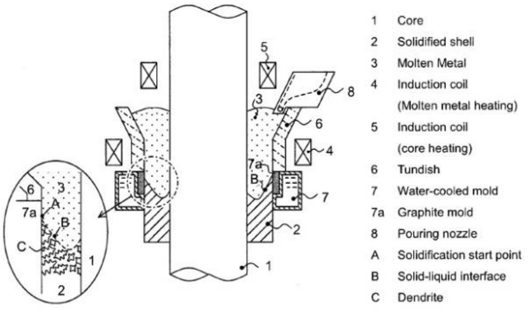

Figure 6 : Continuous pouring process for cladding (CPC). [11]

The shell is progressively solidified to be tightly bonded with the core and is intermittently downward to form roll. During the shell solidification the front basically moves in the radial direction of the roll or in the horizontal direction. To ensure the connection between the two materials two different induction coil are present to heat the connection zone of both parts, but to give a high connection in many rolls another intermediate layer of different composition is obligatory and thus more steps or a more complicate casting are necessary unlike the centrifugal casting. [10, 11]

4.1.5. Properties required for the rolling mill rolls

The rolls for roughing stands must have some specific properties to be considered adapt for the mill demands:

- ✓ **High shell resistance against wear, thermal fatigue and oxidation/corrosion; a homogeneous wear resistance allowing longer rolling campaigns and reduced downtime**
- ✓ **High fire crack and heat resistance**
- ✓ **High roll bite based on high friction coefficient is maybe the most important characteristic because it allow high reductions per pass without chattering or slippage, thus high throughput with reduced heat loss of the product**
- ✓ **Perfect roll surface quality over long runs; that is related to no peeling, no banding and no microspalling**
- ✓ **High safety against roll failures**

The ways to improve the characteristics usually are having lower carbide content but harder and no network of carbides, with those the shearing resistance and the absence of micro-spalling is enhanced. [7]

4.1.6. Problems in the manufacturing

During the manufacturing the later stands have the highest applied forced on the metal piece at the enhancing of the applied deformation and the highest manufacturing velocity due to the process. The deformation in a hot condition (hot lamination) is not the best way to consider the real process conditions, the deformation velocity $\acute{\varepsilon}$ is better in comparison with the normal deformation ε because considers also the rolls velocity V_r:

$$\varepsilon = \frac{\Delta h}{h_0} \tag{1}$$

Equation 1: Deformation definition with $\Delta\mathbf{h} = \mathbf{h_f} - \mathbf{h_0}$ [22]

$$\acute{\varepsilon} = \frac{V_r}{L} \ln\left(\frac{h_0}{h_f}\right) \tag{2}$$

Equation 2 : Deformation velocity definition; where the final value of the interested dimension (thickness in our case) is$\boldsymbol{h_f}$, the initial value of the dimension is $\boldsymbol{h_0}$, the difference of values is$\Delta\boldsymbol{h}$ and L is a parameter of work [22]

The applied pressure and the force can be correlated directly with the desired deformation velocity:

$$P_{av} = \frac{2\,C}{\sqrt{3}\,(m+1)} \cdot \acute{\varepsilon}_f^{m} \cdot \left(1 + \frac{\mu\,L}{2\,h_{av}}\right) \tag{3}$$

$$F = L\,W P_{av} \tag{4}$$

Equation 3: Average pressure where C and m are referred to the mechanical properties of metal piece, the applied deformation velocity is $\boldsymbol{\acute{\varepsilon}_f^m}$, the friction coefficient is $\boldsymbol{\mu}$ and the average value of the difference of the desired depth is$\boldsymbol{h_{av}}$. [22]

Equation 4: Relative force in a lamination process where W is the width of the worked piece. [22]

The deformation velocity in the Equation 3 has the higher contribution to the pressure and force (as shown in the Equation 4) varying and at the decreasing of the h_0 (later stands in a manufacturing work) the deformation increases, as the Equation 2 explains. The velocity of the rolls has an important contribution in the Equation 2 and thus for the industry habit that wants high production and high velocity means higher values of deformation on the material. The applied pressure and the force in later stands have to be higher to arrive at high reduction and then the rolls have to support it. For these reasons rolling incidents tend to occur more frequently in HSM later stands; the typical roll incidents are the wear of the surface due to the high pressure or the cobble incident due to sticking. The first one is a normal consequence of rolls use due to the contact between two metals of different hardness and the second one is the worst possible accident because it compromises suddenly the manufacturing quality instead of the previous. [4, 22]

4.1.6.1. Cobble incident

The cobble incidents are due to the concentrated contact stress between the backup roll and the work roll at the adhered strip, in this area strip steel may stick to the roll surface. That aspect can give in the same time non-smoothed surface products and the possibilities of crack extending by the high compressive residual stress (when the crack forms some angle between the perpendicular line of the roll surface). The HSS in later stands shows inferior anti-crack and anti-sticking behavior in comparison with the old or enhanced ICDP and thus the latest is the widely used material in the later stands of the finishing train. The HSS has the advantage to have a higher wear resistance and then less need of grinding. Usually, there are 7 stands in which the earlier are with HSS and the latest ICDP in a standard HSM; the HSS can arrive to achieve over 5000 to 10000 tons of rolling without grinding, instead of the ICDP can achieve from 1500 to 2000 tons per each roll grinding (values without incidents). Frequent interruption of the rolling operation due to the roll change is not desirable in an effort to achieve the highest rolling productivity, farther the grinding is a high and relevant cost. [4, 5]

4.2. Materials for rolls

The materials used for the casting of the duplex material rolls can be very various; the hard shell part can be made up by materials considered steel, iron or cast iron and the tough core material can be various types of cast iron. In the first part the amount of the elements depending on the material can vary a lot, the carbon (C) can vary from 1% to 3%, chromium (Cr) from 1.5% to 11% and nickel (Ni) from 1% to 6%. For the iron materials those three main elements with the carbides formers give all the wear and hardness properties that the shell needs. The core materials usually are cast iron with different types of graphite (lamellar or nodular) with higher carbon amount (3-3.5%) and a completely different microstructure in comparison with the shell one.

4.2.1. Structure and microstructure

In the roll material for hot rolling, the alloys which dispense a large amount of carbide in the matrix are widely used because they are superior in abrasion resistance. High-alloy white cast irons, in which amount of carbides disperses in the hardenable matrix, are widely used for abrasion resistant parts. Steel strip mills are also one of their important application fields, through the durability of high-alloy cast iron rolls is superior to conventional low-alloy ones. The structure of the shell materials usually is made up to a hard martensitic matrix with a little amount of bainitic phase and dispersed carbides inside; the variety of it depends on the composition (total and local), the cooling rate and other phenomena during the casting. The core material is made up to cast iron with a matrix that can be pearlitic, ferritic or mixed and with a low percentage of cementite (<5%) to have a high toughness. [6, 8]

4.2.2. Carbides

The carbides role in the high alloyed metals is complex and variable. In general in the Fe-alloy the carbides have the tendency to precipitate in the intra-grain spaces and also are less present along the grain boundaries. Some carbides morphology has harmful consequences for the ductility for their fragility; nevertheless the carbides can give high enhancing of the break resistance, wear and abrasion resistance for their elevated hardness. The carbides are phases composed by carbon and various groups of ferrite stabilizer elements or iron; in low-alloyed steels the principal and in general simplest carbide is the cementite (M_3C) where the M is almost completely iron. Usually, this phase is present as ledeburite in the cast iron, a structure made up to perlite and that carbide. The cementite has lower hardness (800-1000 HV) in comparison with all the carbides and can give also fragility whether the amount is too high; the positive aspects of its presence are those which produce a uniform wear and a possible protective oxide layer whether the relatively low difference in hardness with the matrix is not too high. In high-alloyed steel to arrive to an enhancing of the properties, the intention is the variation of the ferrite stabilizer elements that can give harder eutectic carbides and with different morphologies in a martensitic matrix. The carbides that come from ferrite stabilizer elements can be divided in primary carbides that appears at high temperature with a possible precipitation from the liquid, eutectic carbides that appear at the eutectic temperature and secondary carbides that appear at lower temperatures with the possible precipitation through the solid phase. The primary and secondary carbides usually are placed inside the grain (intra-grain carbides) and the eutectic carbides in the grain boundaries (inter-grain carbides). An important general aspect of the carbides structure is that carbides must be well distributed and do not have to be with excessive dimensions; a continuous carbide network and then too much bonds between carbides must be avoided because it will be a help to the crack increasing and extending. Whether all those aspects are observed, the high-alloyed steels can have increased proprieties with a lower amount of carbides. [3, 6, 31]

4.2.3. Morphology

The carbides morphology is a huge and complex argument because a lot of variables like composition, cooling rate, carbides position and transformations can condition it.

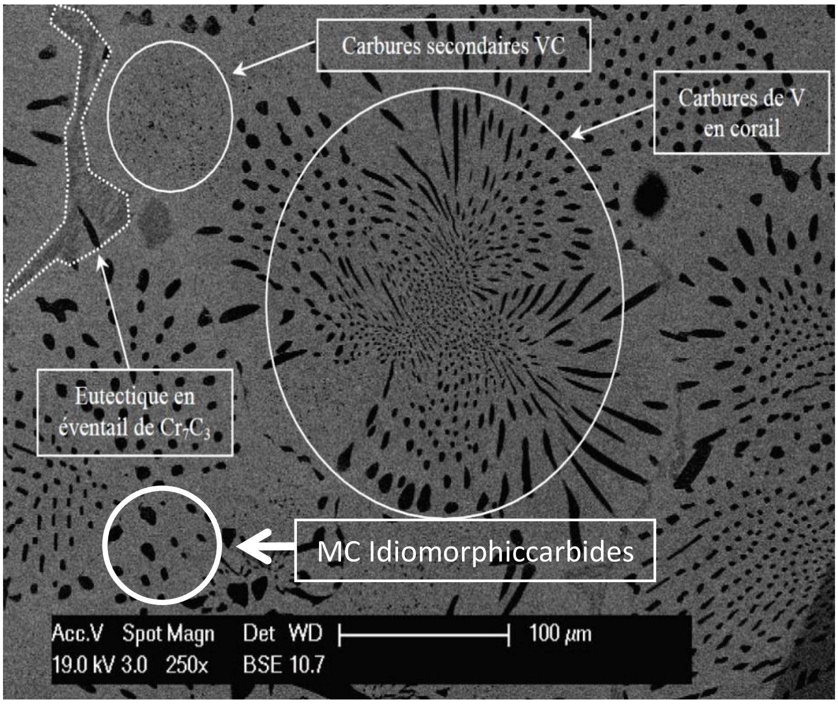

Idiomorphic

Figure 7 : SEM figure of a general microstructure view of a low carbon steel (St37); idiomorphic MC primary carbides are present in the low left part, petallike MC carbide in the centre(called encorail in the figure), idiomorphic MC secondary carbides in the high left part and also a eutectic M_7C_3 carbide. [16]

The idiomorphic is like isolated massive carbide and usually is typical of the primary carbides.

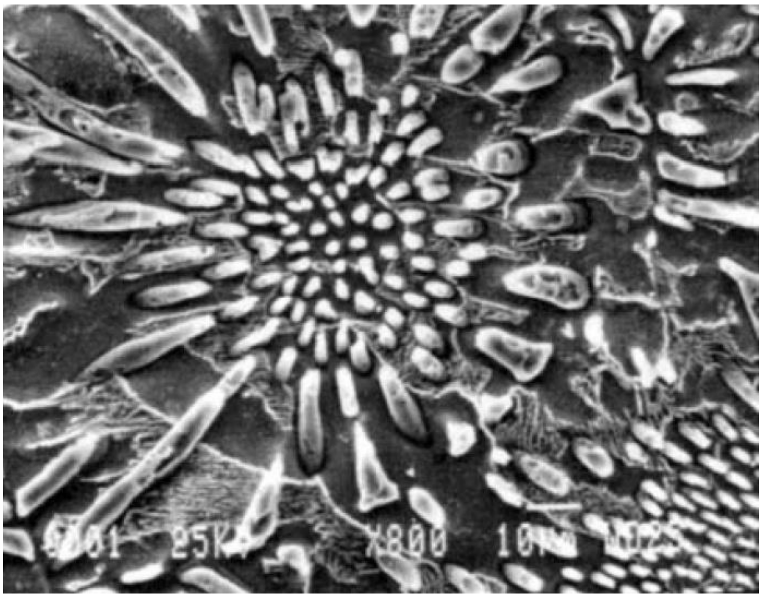

Petallike or
Fibrous

Figure 8 : SEM figure etched to expose the eutectic phases; Fe-V-C system. [3]

In the Figure 8 the petallike or fibrous VC particles radiate outwards from the center of the cellular colony. Petallike morphology is with a central heart and a few little ramifications with a big diameter.

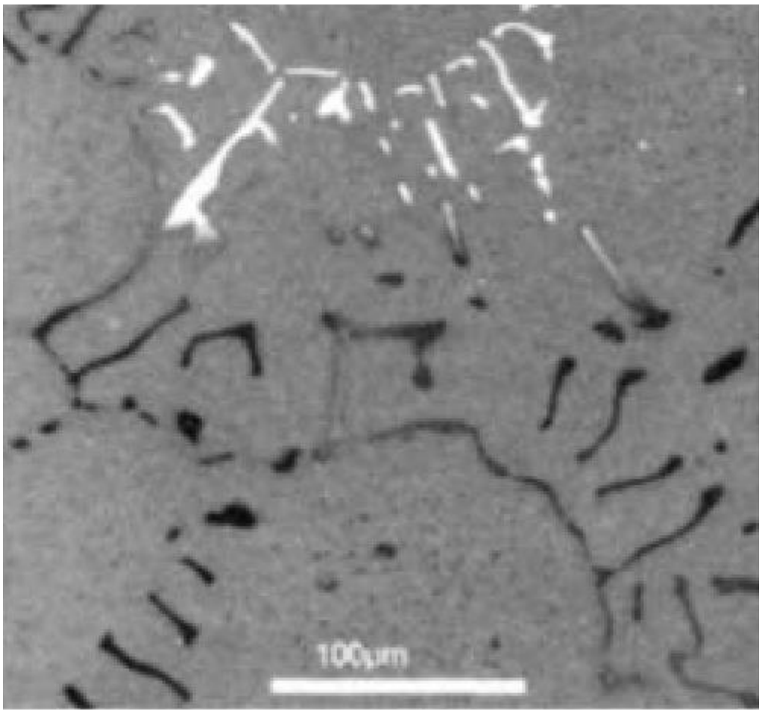

Branched petallike

Figure 9 : SEM figure of an Fe-V-Ta-C alloy slowly cooled from the liquid at 5°C/min. [3]

In the Figure 9 Austenite dendrites are surrounded by a (V,Ta)C eutectic. The dark carbides are rich in vanadium and the light carbides are rich in tantalum. Branched petallike is a connected structure of long branches usually situated in the inter-grain zones.

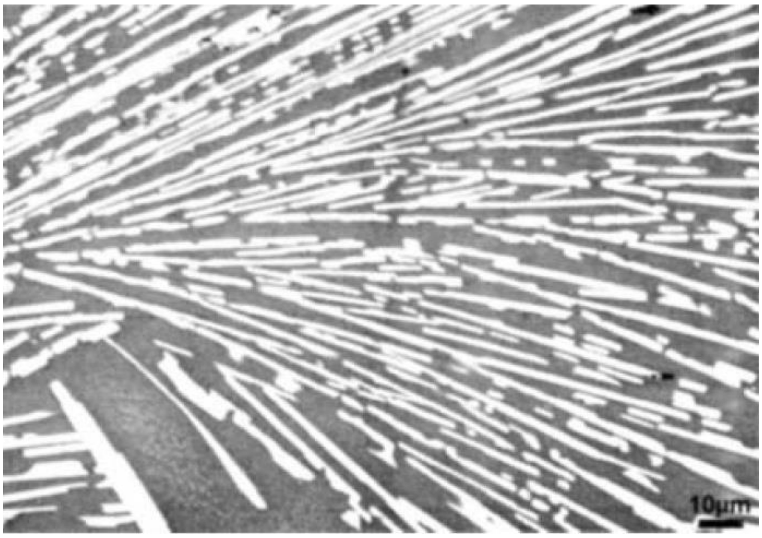

Irregular

Figure 10 : SEM figure of a Fe-C-Mo alloy; the carbides present is a eutectic Mo_2C. [3]

The irregular is characterized by radiating clusters that does not clearly outline the interface between matrix and eutectic pool.

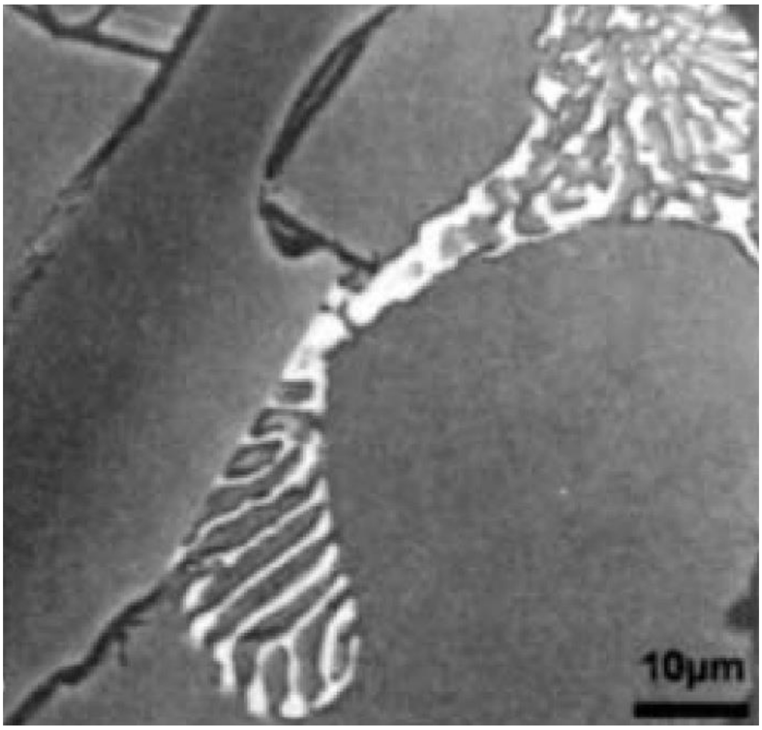

Complex
regular

Figure 11 : SEM figure of as-solidified alloys that is Fe-3.3C-16Cr-3Mo-1Mn-0.5Si alloy (back-scattered electron Figure). [3]

In the Figure 11 Mo_2C complex irregular appears white, while M_7C_3 carbide has a dual grey contrast, corresponding to two different Mo concentrations, respectively 1.3 and 5 at %. The complex regular forms a clear outline and it forms cells with macrofacets. Here the M_7C_3 carbide shows morphology defined Massive Globular.

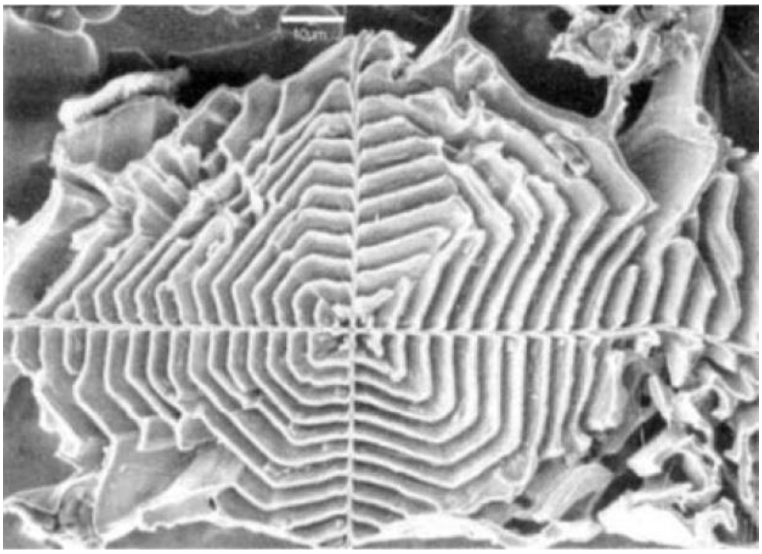

Lamella-like

Figure 12 : SEM figure of a Fe-Mo-C system. The M_6C particles are lamellar and some have branches at 120°. In the polished section, the carbides show a fishbone morphology. [3]

The lamella-like or “fish-bone” morphology is characterized by the presence of a central carbide platelet from which arises secondary platelets separated from each other by the matrix phase. [12]

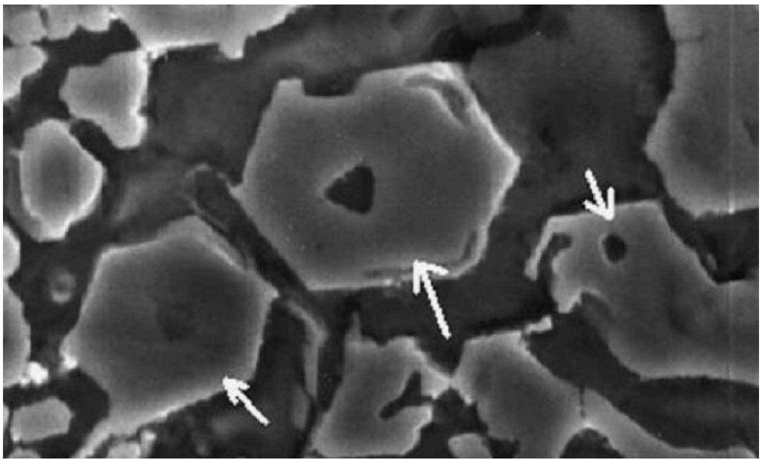

Pencil-like

Figure 13 : SEM figure showing typical pencil morphology of M_7C_3 carbide (arrow) in Low Cr white iron. [15]

The pencil-like morphology can be founded in a couple of carbide types and its grain shape depends on the carbide structure; the M_7C_3 carbide in this case has a hexagonal-shape structure and during the solidification it growths around austenite. [13]

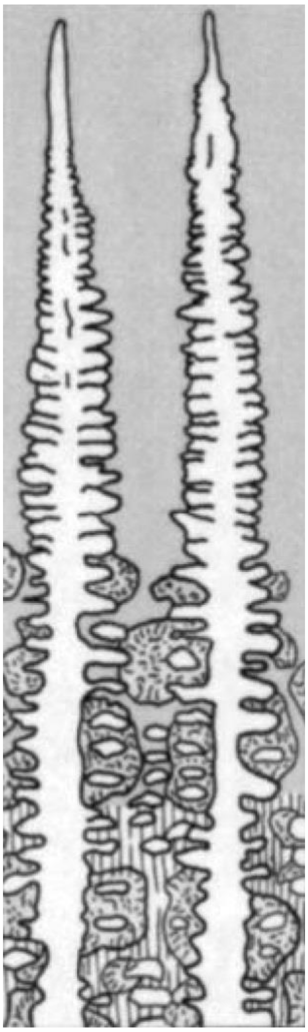

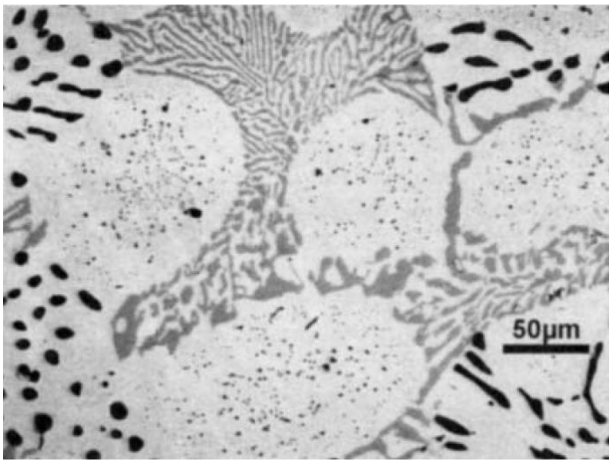

Lanceolate

Figure 14 (Upper figure): SEM figure of a Fe-2.4C-5.4Cr-6V alloy cooled from the liquid at 5°C/min. [3]

Figure 15 (Figure on the left): Schematic representation of the corresponding microstructure observed by quenched-interrupted unidirectional solidification. [3]

The lanceolate is a typical M_7C_3 morphology of the vanadium-containing alloy cast iron as it is possible to see in the Figure 14. The formation of this carbide is bonded with the formation of the VC eutectic that is formed first and after the M_7C_3 carbide is formed at lower temperatures. The second figure shows the structure of the forming carbides: the VC carbides solidify first and form globular cells with Idiomorphic morphology, while the M_7C_3 carbides have an oriented lanceolate morphology.

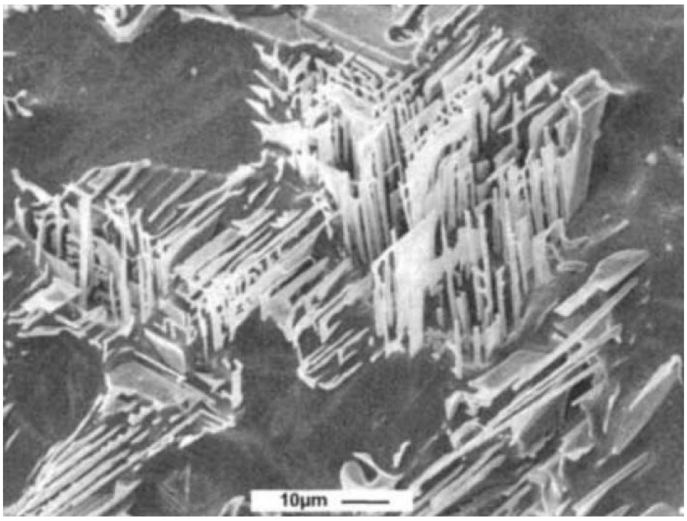

Chinese script

Figure 16 : SEM figure of a Fe-Nb-C system. The NbC particles are in the form of orthogonally branched lamellae. Martensite needles are faintly visible in the matrix. [3]

In a polished section, the NbC particles have a so-called Chinese script morphology. This morphology is particular for the MC carbide and it is present for high cooling rate. This morphology name is also used for a particular graphite shape.

The composition conditions the morphology because its change can give a formation shift and give as in the case of the MC idiomorphic primary carbides instead branched petallike intra-grain carbides. The cooling rate can also condition the morphology because a slow rate can give the time for having a structure order as in the case of the M_2C carbide, even whether with a high-alloyed composition, the rate takes less importance. The carbides positions in the nucleation moment is an important aspect, but it is a consequence of the composition, in fact the carbide can be growth-free as in the case of the primary carbides or it can be in a inter-grain position with a preferential direction of growth; the composition is the key of the position because it conditions the carbide nucleation starting point. There are some particular reactions like the perictetic and metatetic reactions that can give unusual morphologies due to the local remelting like string of carbides or concentric rings of precipitates formed along the regression interface. [3, 9, 15, 16]

4.2.4. Formation mechanisms

The formation or carbides nucleation is strongly bonded with the liquid composition during the solidification steps. The Fe-C-X ternary systems (X is a ferritic-stabilizer) include various eutectics. In the phase diagrams, numerous pseudo-perictetic transformations often occur along the monovariant eutectic line. In the case of the MC carbides a percentage higher than 2% in weight of vanadium is enough to give nucleation of primary carbides that can precipitate directly from the liquid, preceding all other solidification reactions. The presence of austenite can give other phenomena because its formation concentrates elements in front of the line formation and thus a local high amount of ferrite stabilizers; whether δ-primary ferrite is present this local change can cause the local remelting and usually concentric carbides lines suggest this. The austenite growth in general creates in the inter-grain zones particular and local concentration where temperatures and compositions conditions are ideal for the various carbides formation. The same reasoning can be applied between different carbides that do not use some elements and they create favorable conditions for other carbides. [3, 9]

4.2.5. MC carbide

These carbides usually are formed at high temperature near the Liquidus temperature like distinct particle heterogeneously distributed in inter-grain, trans-grain or intra-grain position. The MC carbide has a face centered cubic structure (FCC) and is the simple combination between carbon (C) and reactive refractory metals as niobium (Nb), vanadium (V), tantalum (Ta) or titanium (Ti). The stability can be reduced by the presence of Mo or W that have the ability to weaken the bond forces between the MC atoms and sometimes form more stable carbides as $M_{23}C_6$ or M_6C with particular heat treatment or on work. This phenomenon occurs for temperature above 815°C but the Nb and Ta adding contrast this effect. Like this the MC carbides can be stable until 1200-1260°C; in fact the MC carbide presence directly from the bulk liquid phase (primary carbides) is promoted at the increasing of the Nb, V and C amount in the HSS; usually they have a spheroid shape like and their dimensions depend to the austenite formation. In the steel MC carbides can arrive at a hardness of 2000-3000 HV and are preferred (especially V) little for a better distribution. Three types of MC eutectic carbides can be distinguished: divorced or idiomorphic (MC carbide occurs as isolated massive crystals as shown in the Figure 7, irregular (poorly coupled eutectic in which the MC carbide has a petallike morphology as shown in the Figure 8) and complex-regular (coupled eutectic in which MC carbide has a branched petallike morphology as shown in the Figure 9). The latter is also called regular or lamellar. In the divorced MC eutectic carbide, it is likely that the dendrites of peritectic austenite play the role of heterogeneous nuclei for the formation of the eutectic austenite, making it impossible to distinguish it. In the irregular carbide seems that austenite and carbide begin to grow with a certain level of cooperation through the carbide is somewhat ahead, and some point the austenite is able to overgrow the carbide and close the halo around it. The formation of the lamellar can be understood in the same way of the latter, but without the formation of the austenite halo because with the increase in the volume fraction of the MC carbide in the eutectic, the austenite is no longer able to overgrow it. The MC secondary carbides are placed inside the grains and they have little size in comparison with the primary carbides because they are formed at lower temperatures. The vanadium and niobium presence can determinate the presence of secondary carbides for their effect on the matrix solubility.

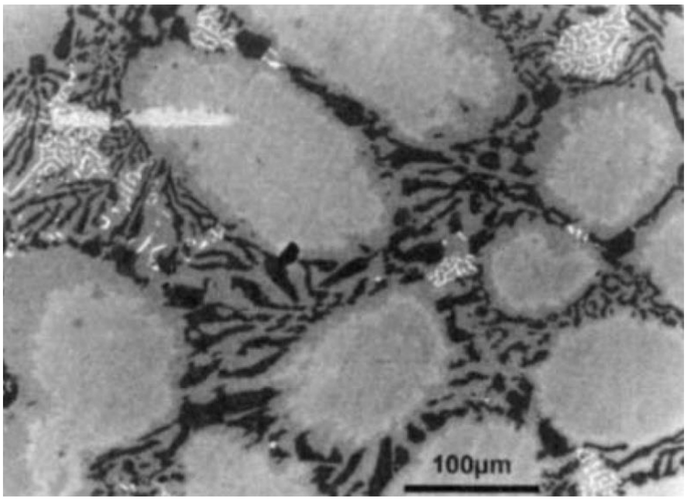

Figure 17 : SEM figure of an Fe-2.1C-14.7Cr-1Nb alloy cooled from the liquid at 2.5°C/min. [3]

The Figure 17 shows an alloy cast iron containing niobium, slowly cooled during a DTA test. The centre of the primary austenite dendrites have transformed to martensite (light contrast). The coarse M_7C_3 eutectic carbides are in black and the finer NbC eutectic carbides are white. The solidification steps are: primary austenite dendrites, M_7C_3 eutectic formation and finally NbC eutectic formation. The comparison with this structure and the structure in the Figure 14 reveals the difference in the property of the two alloys to form martensite and to give or not precipitation of secondary carbides. In niobium presence, the amount of carbon in solution in the austenite remains small at all temperatures during solidification; consequently, the austenite transforms readily to martensite. When vanadium is present instead, the carbon solubility is significantly higher during solidification, but decrease on further cooling causing the precipitation of secondary vanadium carbides as it is possible to see in the grain of the vanadium-rich structure. Nevertheless, the residual carbon and vanadium contents in solution are too high to allow martensite transformation; to occur it is necessary to heat the alloy at about 900°C in order to increase the carbide precipitation and so decrease the elements amount in the austenite. [3, 9, 17, 21]

4.2.6. M_2C carbide

The M_2C carbide presents a hexagonal crystalline structure and is principally composed by molybdenum (Mo) and vanadium with a hardness that can vary with the composition between 1400 to 2000 HV. The structure of this carbide is influenced by many aspects as the chemical composition, the cooling rate and minor additions of certain elements such as aluminum and nitrogen. The morphology of M_2C eutectic carbides can be irregular characterized by a ragged boundary that does not clearly outline the interface between the matrix and the eutectic pool as it is possible to see in the Figure 10, instead the complex regular one that shows smooth boundary as shown in the Figure 11. In the first eutectic the carbide has a platelike morphology and a tendency to assemble as radiating clusters showing also an extensive branching, which is responsible for avoiding overgrowth by austenite. The second eutectic shows a regular distribution of M_2C eutectic carbide over small areas, forming cells with macrofacets. Irregular M_2C eutectic is chiefly promoted by low cooling rate or high vanadium content and the complex-regular by the contrary. As the cooling rate increases, the difference between the growth rates of M_2C carbide (faceted phase) and austenite (non-faceted phase) also increases and the eutectic morphology becomes strictly controlled by the characteristics of the M_2C carbide growth (hexagonal hopper crystal), ensuring the formation of a complex-regular structure. The M_2C carbide, whether being metastable, decomposes into MC and M_6C carbides when reheated to between 900 and 1150°C, and it has been shown that kinetics of this breakdown and the distribution of the carbide products is influenced by the morphology of M_2C carbide. [3, 9]

4.2.7. M_7C_3 carbide

The M_7C_3 carbides have many different possible forms; they can be eutectic that tend to appear for low cooling rate in the grain boundary, primary from the liquid or may precipitate as secondary carbides from austenite. M_7C_3 eutectic carbides tend to be massive and in a lamellar shape as aggregate, instead the M_2C carbide that usually are thinner. The M_7C_3 hardness has a medium value of 1200-1700 HV and the composition can vary a lot in the same aggregate as shown in Figure 11. This type carbide often show a phenomenon calls discontinuous change in composition; it can concerns carbides like M_7C_3 and M_3C that contain more than one metallic element, such as $(Fe,Cr,Mo)_7C_3$ or $(Fe,Cr,Mo)_3C$. These carbides are heterogeneous in as-solidified alloys. The phenomenon is clearly visible in the scanning electron microscope for heavy substitution elements, such as molybdenum and tungsten. The concentration of the substitution element does not vary continuously within the carbide as would be the case with an ordinary segregation process, but appears to change in distinct steps. The transition zone can be studied by transmission electron microscopy, and no change in crystal structure is apparent. Recent studies have reported results that are not agree with the discontinuous change founding constant composition in those carbides. The possible elements presences are also here confirmed because in the M_7C_3 carbide was detected no detectable amounts of Ti, Ta, Nb and Zr. The formation of the different types of M_7C_3 carbides is depending on the carbon and chromium local concentrations and to the carbon general concentration; for example in the hyper-eutectic alloy first solidifies $L \rightarrow M_7C_3$, forming a nucleation sites for the growth during the eutectic reaction, instead in a near-eutectic alloy first solidifies as $L \rightarrow \gamma$-austenite with the subsequent eutectic reaction. As such, faceted hexagonal-shaped carbides are allowed to grow among the austenite rosette-type clusters formed by eutectic reaction $L \rightarrow M_7C_3 + \gamma$-austenite as in Figure 13. As consequence in the first case we have mainly hexagonal-shaped carbides and the second a mixed morphology of hexagonal- shaped with also coarse facets of the quasi-rectangular and blade-like carbides. [3, 9, 13, 15]

4.2.8. M_6C carbide

That eutectic carbide type is formed at high temperatures from 800 to 1000°C with tungsten and molybdenum presences (amount between 6-8%); those replace the chromium in the FCC carbide structure. Usually has a hardness of 1500 HV. There are three different morphology of that eutectic, characterized by the presence of a central platelet of M_6C carbide, from which arises secondary platelets of M_6C separated from each other by austenite. These secondary platelets are usually thicker at the end, interrupting the continuity of the austenite and forming a “wall” of carbide around the eutectic colony. The optical microscopy reveals that the cross-sections of the platelets are lamella-like (or “fish-bone” morphology) as shown in Figure 12. The morphology of the M_6C eutectic is not influenced by chemical composition nor cooling rate (considering values as high as 10^6 K s^{-1}), except that at faster cooling rates the distance between platelets is decreased. [3, 9, 12]

4.3. Cast Iron

“The term cast irons covers a wide range of iron-base materials, whose principal common feature is relatively low melting point compared to steels.” [cit. 3]

Cast iron is carbon-rich iron-base alloys with a composition close to the cementite or graphite eutectic in the corresponding Fe-C or multi-component phase diagram. Usually they are used as casted as their name implies, because they are too brittle to be hot worked; sometimes although heat treatment it is possible to optimize the microstructure. Depending on the composition, the solidification and the degree of the undercooling attained the carbon-rich eutectic can be a carbide or graphite; the corresponding materials are white or grey cast irons. The differences between two in solidification steps and temperatures are due to the different composition and to the minor phase presences that can act as nucleants. [3]

- White cast irons have as carbon-rich eutectic constituent either cementite or alloy carbide, usually a chromium carbide.
- Grey cast irons have the carbon present in the form of graphite, in flake or nodular (spheroidal) morphology.
- Some cast irons have mixed (mottled) structures, with both main phases.

Typical compositions of three types of cast iron are noted in the Table 2:

Type	C	Si	Cu	Ni	Mn	Mo	Cr	Ce	Mg	S
White	1	1		0.2-1	0.5-1	1.5	5-12			
Grey	3.2-3.5	1.8-2.3	0.15-0.4	0.05-0.2	0.6-0.9	0.05-0.1	0.05-0.2	0.05-0.2	0.03-0.05	0.02
SG	3.5-3.9	2.2-3	0-0.5	1	0.3-1	0-0.05	0.1	0.05-0.2	0.03-0.05	0.02

Table 2: Typical composition of three types of cast iron. [3]

4.3.1. White cast iron

The typical morphology in low alloy white cast irons is known as ledeburite, a eutectic composed by γ-Fe and cementite. The cementite gives relatively high hardness, excellent erosion and abrasion resistance; it forms a carbide network, within the austenite is not continuous and as a consequence the toughness is subsequently low. Most of the common cast irons are hypo-eutectic in order to compensate the cementite stiffness by a larger volume fraction of austenite. A rapid cooling rates lead to greater undercooling and as a consequence carbide eutectic formation is promoted.

4.3.1.1. Ni-hard cast iron

A particular group of medium alloy white cast iron has a higher nickel presence in the composition and this leads to a martensitic matrix. Inside this group the first family contains 3-5% of nickel to retard the pearlite transformation and 1-4% of chromium; this combination ensures the formation of carbides by countering the graphite-promoting effects of nickel and silicon. The second family contains 5-7% of nickel and 7-11% of chromium. Here the cementite is replaced by the M_7C_3 carbide as eutectic carbide. The M_7C_3 carbide lanceolate morphology tends to impair toughness and the carbide volume fraction in the eutectic is lower. [3, 7]

4.3.1.2. Cr cast iron

Cr cast iron as can suggest the name contains a higher chromium amount, from 11% to 23% with up to 3.5% molybdenum. The matrix can be austenitic or martensitic depending on the heat treatment and the high chromium amount ensures good corrosion and temperature oxidation resistance. Molybdenum and other alloying elements (W, V and Nb) participate in the formation eutectic carbides and also specific carbides as Mo_2C or VC (Figure 14). Large casting has coarse dendritic structures, with marked segregations; those are difficult to remove by heat treatment and they keep being heterogeneous. [3, 7]

4.3.2. Grey cast iron

The grey cast iron contains 2-3% of silicon and it forms eutectic graphite on slow cooling, as twisted flakes. The composition and the cooling rate determine the matrix that can be austenite, ferrite or a mixture of ferrite and perlite. The main problem of this material is the lack of toughness associated with the brittleness and the morphology of the graphite flakes, which promote the initiation and propagation of microcracks. To modify the graphite shape some liquid inoculants are used to pass to a vermicular graphite shape as in the Figure 18 , finer in comparison of the flakes. In order to conserve a high fluidity for the casting, it is preferable not to approach the eutectic composition (4.2% C).

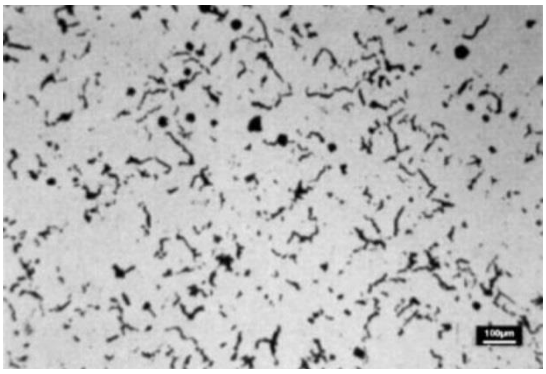

Figure 18 : Optical figure of a hypo-eutectoid grey cast iron showing a vermicular graphite morphology. [3]

4.3.3. Spheroidal graphite (SG) cast iron

“Ductile spheroidal graphite (SG) cast iron was discovered in the 1950s. However, «lf coke (which is high in sulfur) had not he en used for melting iron and whether high purity ores had been used, then ductile iron would have been accepted as the normal form of iron, with flake graphite iron only being discovered much later as an accident of adding S and O. This seems to have been close to the situation in China where spheroidal graphite irons were produced over 2000 years ago.” [cit. 3]

The SG cast irons have a composition very similar to the flake graphite grades. The graphite morphology is obtained by means of a special liquid metal treatment and it is in the form of roughly spherical nodules. The ductility is significantly improved with the graphite shape change and for this reason it is called also ductile cast iron. The introduction of SG grades has considerably extended the range of application of grey cast irons. To explain the growth of the graphite nodules several two main mechanisms are proposed, according to different observed morphologies. The first consist of a compact bundle of cones radiating outwards from a common nucleus and each cone is built up by helical growth around a dislocation.

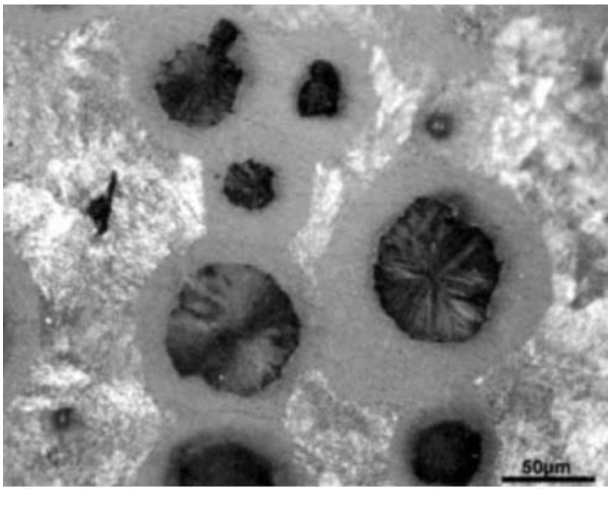

Figure 19 : SG cast iron in which the matrix has partially transformed to ferrite around the nodules. [3]

The second mechanism forms a cabbage-like structure and involves more layered lateral growth.

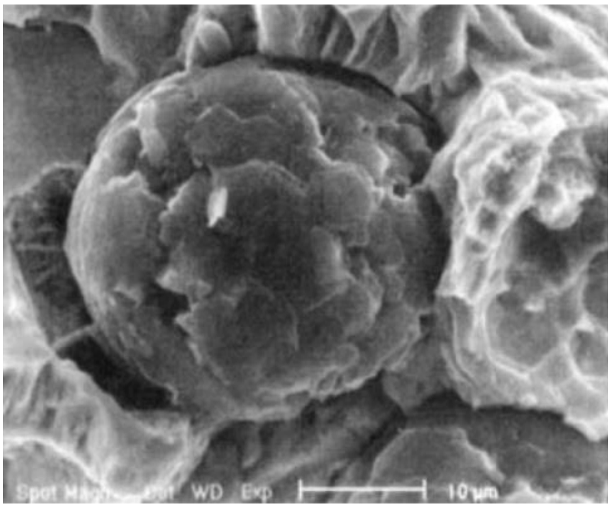

Figure 20 : Graphite nodule observed on the fracture surface of ferritic SG cast iron. [3]

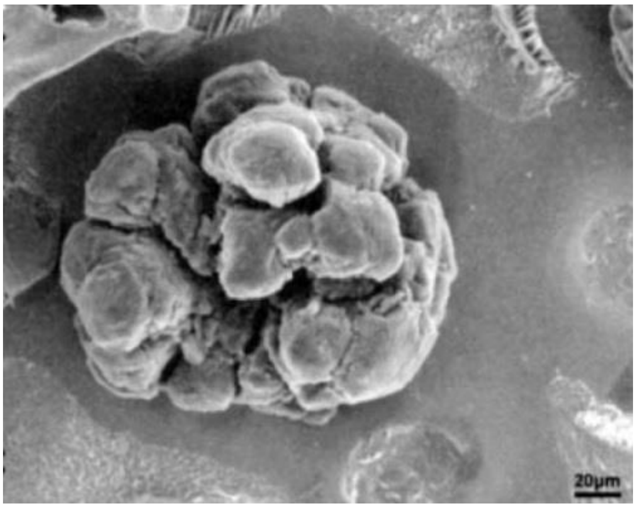

Figure 21 : Degenerate graphite nodule exposed by deep etching in an alloy cast iron. [3]

The nodular morphology here can degenerate in the presence of excessive quantities of strong carbide-forming elements, or when the graphite-stabilizing elements are exhausted. The spheres then can also develop branches that can sometimes evolve into tangled filaments, similar to vermicular morphology. [3, 19]

4.3.3.1. Graphite-stabilizing elements

Two key graphite-stabilizing elements are silicon and magnesium with two different aspect combined together. Spheroidal graphite cast irons are produced directly by the solidification of a melt containing sufficient silicon to have graphite formation, after the removal of sulphur and oxygen; the magnesium additions to the bath can tie up sulphur and oxygen. The probability of the formation of the stable eutectic phase (in this case graphite) is greater whether it is larger the difference in equilibrium temperature with respect to that for the metastable eutectic; silicon increase rapidly the difference between two eutectic temperatures and the graphite becomes much less dependent on the solidification conditions. Magnesium is also important for the graphite growth morphology changing, it reacts with oxygen to form MgO, which floats to the surface and it can be skimmed off. The oxygen content decreases from typical levels of 90-135 ppm to 15-35 ppm. Magnesium can also react with sulphur and it can be eliminated as the oxygen but with more difficulties. Usually in the grey cast iron solidification oxygen and sulphur tend to be adsorbed preferentially on the hexagonal planes of the forming graphite, inhibiting parallel growth to z axis and leading to a lamellar morphology. The removal of sulphur and oxygen by the inoculants such as the Mg allows a more isotropic growth. This is the explanation of the spheroidising effect of the magnesium and with a careful choice of alloying additions is used to adjust the deoxidation, graphitizing and nucleation effects and steps. [3]

4.3.3.2. Formation of ferrite halos around graphite nodules

The SG structure formation can be divided in three main stages: solidification (governed by the nucleation process), graphite growth (together with the growth of their austenite envelopes) and ferrite formation halo around the graphite nodules when the temperatures falls below that of the eutectoid transformation. Below the eutectic temperature new metastable equilibria tend to be established at the interfaces. The graphite nodules tend to drain the carbon from the surrounding matrix until it arrives to the equilibrium composition as in the figure (the first).

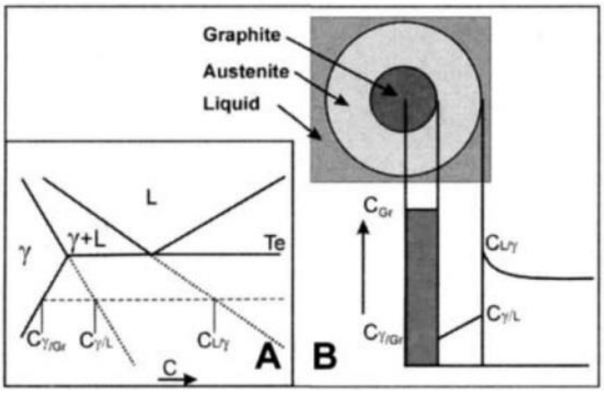

Figure 22 : Schematic mechanism of graphite nodule formation [3]

A. On the left a schematic phase diagram for a given degree of supercooling. The interface concentrations are read from the metastable extensions of the phase boundaries (dotted)

B. Carbon concentration profile at a nodule

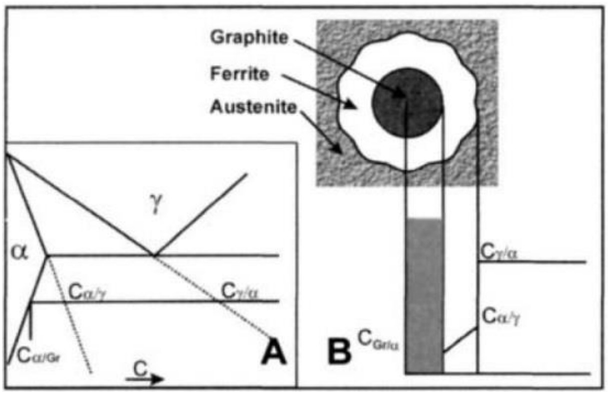

Figure 23 : Formation of ferrite halos around graphite nodules [3]

A. On the left a schematic phase diagram for a given degree of temperature. The interface concentrations are read from the metastable extensions of the phase boundaries (dotted)

B. Carbon concentration profile at a nodule in the next formation step respect of the previous figure.

With a high silicon amount, around 4%, that is necessary for the graphite formation the consequence is the ferrite formation around the graphite nodules, forming a halo. The diffusion exchanges become more complex with the temperature decreasing and with the carbon excess increasing into the austenite that must diffuse through the ferrite to the graphite. The diffusivity of carbon in ferrite is several orders of magnitude faster than in the austenite. The ferrite halo grows depending on the cooling rate. When the cooling is slow, the whole of the matrix transforms to ferrite and the austenite disappears at low temperature (around 800°C depending on the composition) where the stable phases are graphite and ferrite. Whether instead the cooling is rapid, the matrix remains carbon supersaturated and retained metastable austenite remains between the two phases, and then transforms to pearlite. [3, 19]

4.4. Graphite

In the 1961 the International Connection of Pure and Applied Chemistry (IUPAC) took on the isotope ^{12}C as the basis for atomic weights. Carbon has four electrons in its valence shell (the outer shell) and the electron configuration is $1s^2 2s^2 2p^2$. Each carbon atom can share electrons with up to four different atoms, since its shell can hold eight electrons; this configuration gives a unique set of properties. Carbon is found free in nature in three allotropic forms: amorphous carbon, graphite, diamond and buckminster-fullerene C_{60}. Carbon alone can form the familiar substances graphite and diamond; graphite is soft and slippery, on the contrary diamond is one of the hardest materials known to man. [14]

4.4.1. Structure

The difference is in the way the carbon atoms form bonds with each other. [14, 30] In the following figures the structures are showed:

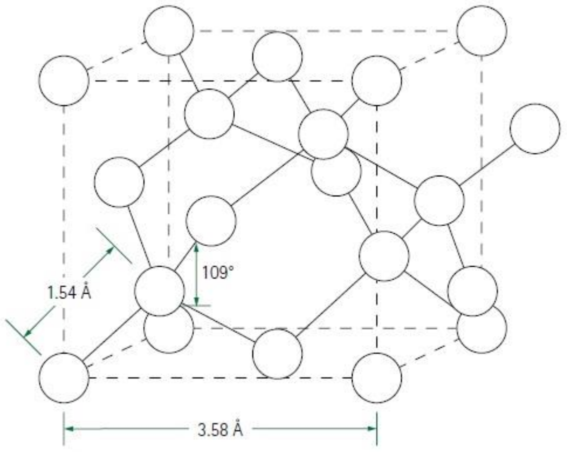

Figure 24 : Crystal structure of diamond. [14]

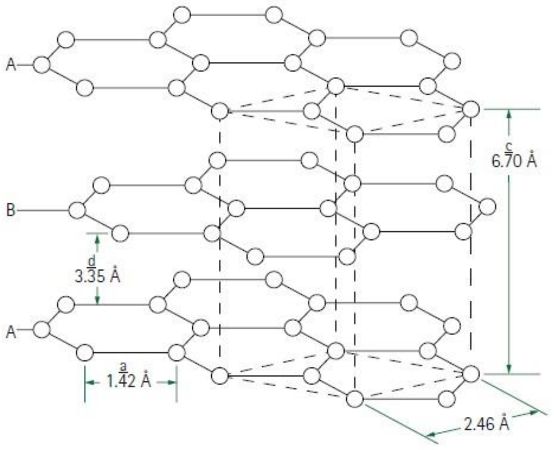

Figure 25 : Crystal structure of graphite. [14]

The forces within and between crystallites determine the extreme differences between the two forms. The diamond has a crystal structure in face-centered cubic and the interatomic distance is 1.54 Å, with each atom covalently bonded forming a tetrahedron; the graphite on the contrary has only 1.42 Å carbon-carbon distance. The three-dimensional isotropic structure gives the extreme hardness to diamond, unlike the graphite that has a structure with a succession of parallel layers to the basal plane of hexagonally linked carbon atoms. The interlayer distance is 3.35 Å and as a consequence the density is 2.226 g/cm^3, meanwhile 3.53 g/ cm^3 as the diamond. Graphite has sp^2 hybridization and thus only four valence electrons form regular covalent bonds (σ-bond) with adjacent atoms; the fourth electron (π-bond) resonates between the valence bond structures. The difference between the two bonds is huge since the energy between the planes (1.3-1.4 kcal/[gram atom]) is only two percent of the planes; the weaker bonds can be explained as a result of the orbital π. As in the Figure 25 the three-dimensional graphite network is composed by an ABAB layers sequence and this gives the high mobility (electronic) of graphite. The weak forces between the layers consequently account for:

- Tendency of graphitic materials to fracture along planes
- Interstitial compound formations
- Lubricating, compressive and many other properties of graphite

4.4.2. Classification

Graphite in general can be classified in synthetic and natural simply based on the provenience and the formation of it. The world production of natural graphite According to the United States Geological Survey (USGS) in 2012 was 1,100,000 tons. The major exporters are: China (750 kt), India (150 kt), Brazil (75 kt), North Korea (30 kt) and Canada (26 kt). Graphite is not mined in the United States, but U.S. production of synthetic graphite in 2010 was 134 kt valued at $1.07 billion. [30]

4.4.2.1. Synthetic graphite

The synthetic graphite can be produced from pitch and coke; it tends to be higher purity in comparison with the natural graphite wellbeing less crystalline. This graphite type consists mainly in graphitic carbon that has been obtained by heat treatment of non-graphitic carbon, graphitization or chemical deposition from hydrocarbons at temperature above 1825°C. There are two main synthetic graphite types: electro-graphite that is pure carbon produced from calcined petroleum coke and coal tar pitch in an electric furnace and synthetic graphite produced by heating calcined petroleum pitch to 2800°C. Synthetic graphite has a higher amount of porosity in comparison with the natural one and this increased porosity makes it unsuitable for refractory applications. [14, 30]

4.4.2.2. Natural graphite

The natural graphite is a mineral composed to natural graphitic carbon and it has a high crystallinity variation. Usually it has a high impurities presence because the most commercial graphites are mined and contain other minerals, subsequently to mining the graphite often it requires a considerable amount of mineral processing of depuration. [30] Natural graphite can be subdivided into three types:

- Amorphous
- Flake
- High Crystalline

4.4.2.2.1. Amorphous natural graphite

This graphite type is the least graphitic between the natural graphites and the term “amorphous” is not completely correct since the material is still crystalline; the graphite content ranges from 25 to 85 % dependent on the geological conditions. It is found as minute particles in beds of mesomorphic rocks such as coal, slate and shale deposits; it is mined primarily in Mexico, North Korea, South Korea and Austria.

4.4.2.2.2. Flake natural graphite

In metamorphic rocks Flake graphite is found distributed through the body of the ore or in concentrated lens shaped pockets; the carbon amount is from 5 to 40%. This graphite occurs as scaly or lamella form in limestone, gneiss and schists. After a froth flotation process the graphite contains the 80-90% of graphite and with chemical beneficiation processes it is possible arrive to an amount >98%. Flake graphite is present in most parts of the world.

4.4.2.2.3. High Crystalline natural graphite

This particular graphite is supposed to originate from crude oil deposits that through time have converted in graphite, with the correct temperature and pressure. The fissures are typically between 1 cm and 1 m thick, and are typically >90% pure. This form is found in all over the world, but it is only commercially mined in Sri Lanka.

4.4.3. Properties

In general graphite and especially the natural graphite is an excellent conductor, it is stable over a wide range of temperatures and is a highly refractory material (high melting point of 3650°C).Its structural strength at high temperature, thermal shock resistance, high thermal conductivity, low thermal expansion and good chemical resistance are of paramount importance in many applications. [14]

In the following Table 3 there are some key properties:

Property	Commercial graphite
Bulk Density (g/cm^3)	1.3-1.95
Porosity (%)	0.7-53
Modulus of Elasticity (GPa)	8-15
Compressive strength (MPa)	20-200
Flexural strength (MPa)	6.9-100
Coefficient of Thermal Expansion (x10^{-6} °C)	1.2-8.2
Thermal conductivity (W/m.K)	25-470
Specific heat capacity (J/kg.K)	710-830
Electrical resistivity (Ω.m)	5x10^{-6}-30x10^{-6}

Table 3: Commercial graphite key properties. [14]

4.5. Graphite presence in rolls for hot strip mills

The graphite presence in shell materials for hot strip rolls is not anything new; the ICDP and enhanced ICDP for example are present since the 1990’s. In the ICDP materials were present soft free graphite particles, a network of hard and wear resistant carbides and a tough martensitic/bainitic matrix. The real problem was the hardness drop with the increasing of the graphite amount. It was showed with hardness measurement on “VIS” Carbide Enhanced ICDP that the key to not have this hardness drop was the shape and the size of the graphite unite with the utilizing of high hardness carbides. This difference between the flake graphite of the normal ICDP and the spheroidal graphite in the new development is the same that is present between grey cast iron and spheroidal cast iron, due to the isotropy properties of the particles. [5]

4.5.1. Graphite actions and anti-sticking properties

High graphite content does not offer a high performance because of poor wear resistance. On the other side too low graphite content does not give a good performance either because rolls will be more prone to cracking, thus the graphite particles have anti-cracking properties. For the rolls requirement it is important to analyze the anti-sticking properties to have a homogeneous manufacturing during the time. Anti-sticking properties of roll materials were investigated in the case of a cobble or strip sticking happens. These incidents were evaluated in condition of pressing strip against roll surface with high rolling load very quickly by friction thermal shock test as shown in the Figure 26 (FTS test).

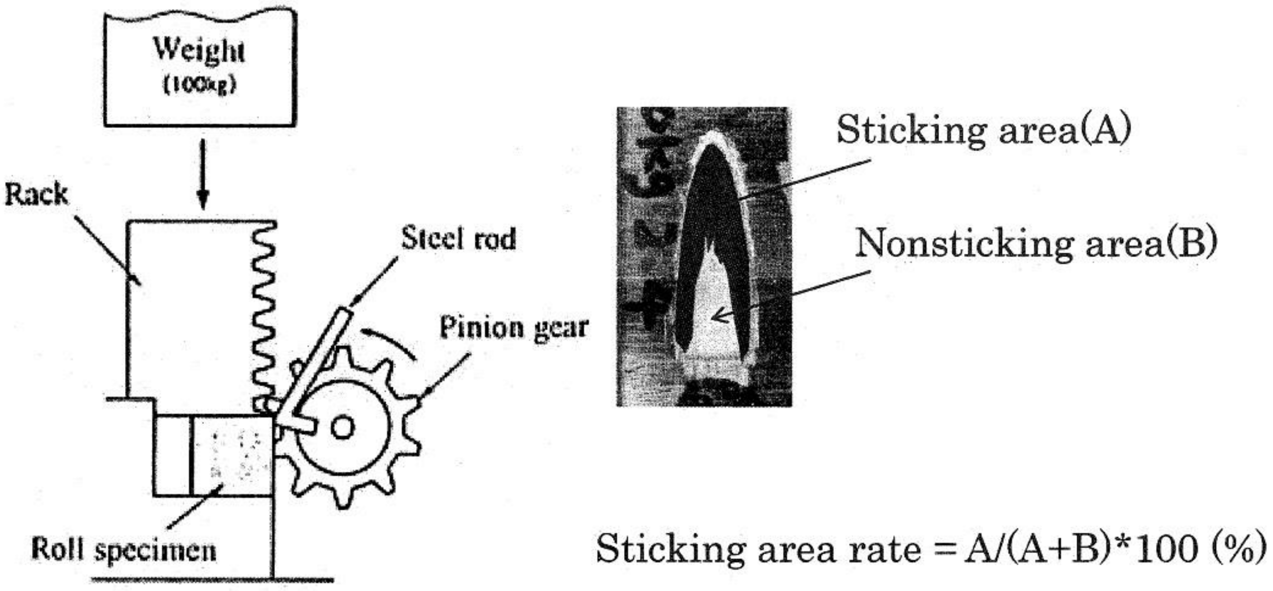

Figure 26 : Schematic representation of FTS test on the left and on the right a sample after FTS test with.

That test simulates the roll bite with the observation of the impression and the sticking. The test results underline the high anti-sticking properties of the spheroidal graphite presence and the necessary equilibrium between carbide presence and graphite presence. The cross-sectional microstructure was observed at the interface between specimen and stuck steel rod after FTS test as in the Figure 27 and it was evident that the graphite was deformed and stretched between the steel and the specimen. This deformation at the surface may prevent direct contact and sticking of both materials as lubricant. As it is possible see in the chips removal the shavings and the tool chest can give together a microwelding especially whether they are similar metals, here it is the same concept. Whether one of the metals contains graphite and it is present into the boundary of the metals acting as lubricant and thereby preventing sticking; especially whether graphite has a nodular shape. [4, 5]

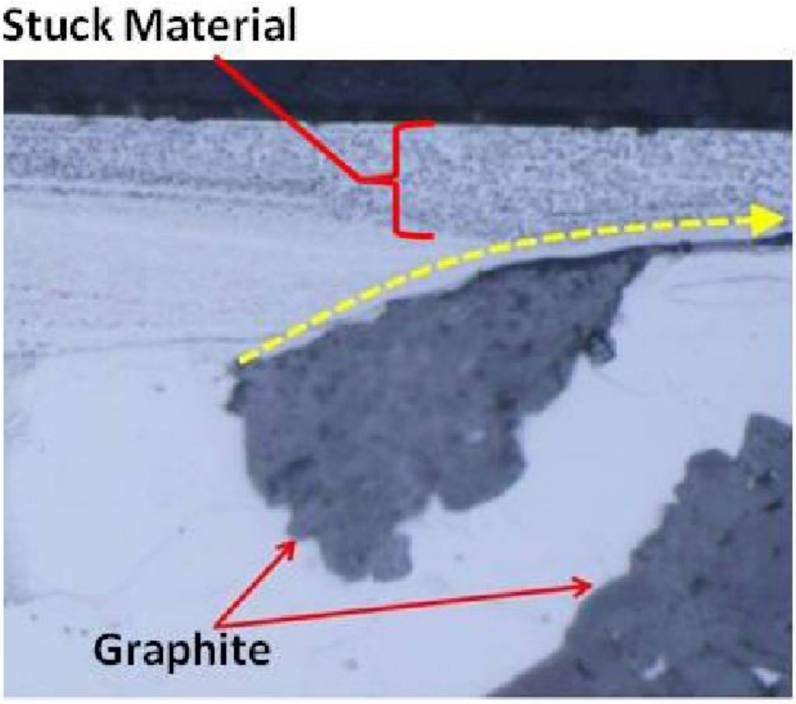

Figure 27 : Cross section microstructure around a graphite particle of a sample after FTS test [4]

4.5.2. Reduce roll changes in middle and late stands

Manufacturing and rolling results of the developed materials were also investigated with the utilizing of a roll composed by an outer shell of the material and a spheroidal cast iron as core, casted by centrifugal casting. Compressive residual stresses were comparable to the conventional and enhanced ICDP, which is about the half of conventional HSS value. The residual stresses present are influenced by the thermal stresses and the transformation induced stress developed during roll manufacturing; as consequence the residual stresses and the fracture toughness (K_{ic}) values have influence to anti-crack resistance. The compressive residual stress is also influenced by Young's modulus difference between the two materials rolls, thus mean that the materials cannot be so different. The studied material contained graphite (spheroidal); therefore its elastic coefficient is lower than the normal HSS, which reduces the compressive residual stress to a lower level. These evaluations indicate that the studied material had comparable anti-crack resistance with ICDPs, which were used in the later stands.

	Alloy content mass %	**Graphite ratio %**	**Carbide ratio %**	**Sticking surface ratio %**
Enhanced ICDP	< 1	2-3	28-38	16-36
HSS	10.2-12.28	0	15-25	61-85
Spheroidal Graphite	< 1	6-7	< 1	4-9
Development material	7-7.8	2-3	22-32	18-33

Table 4 : List of FTS test sample with the detail and results. [4]

The developed material had a higher amount of alloy content mass % as it is possible see in the Table 4, but lower than the HSS. The wear amount comparison after a middle-late stand was done between the new roll and an enhanced ICDP roll; the data has shown that the wear amount of the new roll is about one third of the enhanced ICDP as is shown in the Figure 28.

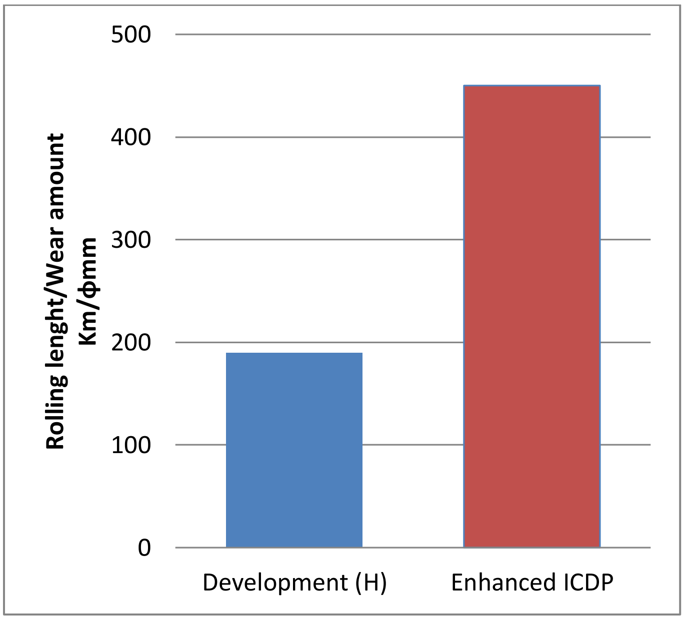

Figure 28 : Performance example in a middle-late stand (rolling length per wear amount. [4]

The developed rolls were used in twice length campaigns without grinding compared to ICDP in most of the cases. The final results were that the ton/mm in this mill increased to 3 times the performance of enhanced ICDP and the average rolling amount in tons/grinding was found to be 1.8 times as are shown in the following two graphs.

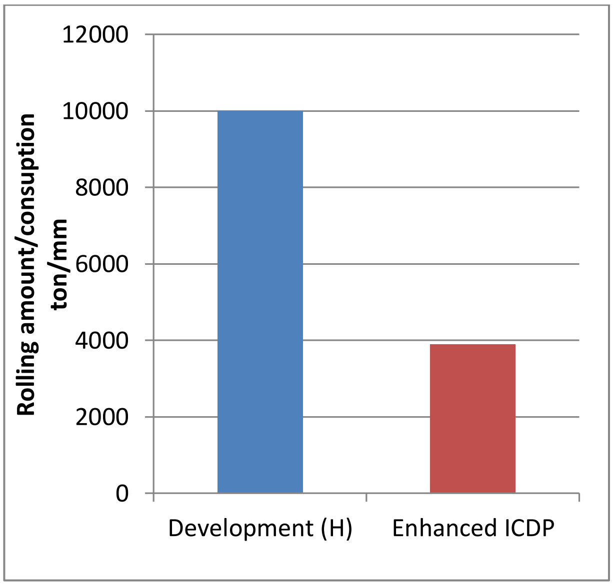

Figure 29 : Performance example in a middle-late stand for rolling/consumption. [4]

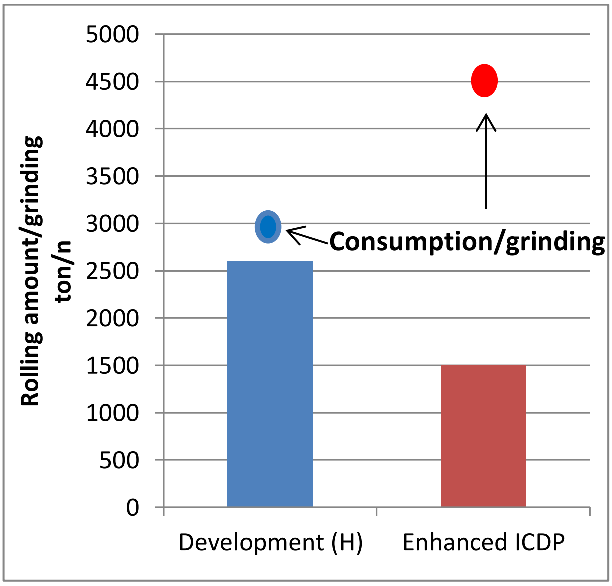

Figure 30 : Performance example in a middle-late stand for rolling/grinding and consumption/grinding. [4]

Cobble incidents in these mills happened several times without issues proving the anti-crack resistance of the new material that is similar to ICDP materials. [4, 5, 6]

4.6. Previous trial on multi-alloyed iron with free graphite: Composition 0

A precedent composition respect on the actual compositions was characterized to investigate his phases and his microstructure. The old composition is similar to the new ones that are studied; from it the new compositions were taken to give better properties or higher amount of a phase. DTA test, optical microscope analysis and Thermocalc analysis were taken to analyze the phase presences. [1]

The Composition 0 was analyzed taking three samples in different depths to the surface: 10,25 and 40 mm.
the conclusions taken after the analyses are:

- The Thermocalc analysis was taken in equilibrium conditions and pseudo-equilibrium conditions to simulate the solidifications steps and to know the probable main temperatures like the Liquidus temperature. The Liquidus temperature was almost 1250°C and the graphite presence was predicted.
- The DTA test was taken with a rate of 5°C/min from room temperature to 1300°C for the heating and after same conditions for the cooling (equilibrium conditions). The test determined the phase transformations and the solidification steps. The main temperatures were identified (for example the Liquidus temperature is 1240°C) and some phases were identified: primary MC carbide, austenite, eutectic M_7C_3 carbide, eutectic M_2C carbide and secondary carbides M_XC_Y.
- In the optical microscope analysis before the DTA test, the sample structure was analyzed in the polished state and with two different attacks: Groesbeck and Nital. All the carbides identified in the DTA test were present and graphite presence was pointed out. The matrix is martensitic.

5. Materials and methods

5.1. Sample positions and characteristics

The Marichal Ketin foundries invest to find an ideal composition for a HSS with free graphite, a first trial (Composition 0) was characterized to investigate the simultaneous presence of graphite, in particular spheroidal graphite, and a hard microstructure. To arrive on this combination a relevant amount of vanadium, silicon, molybdenum and niobium were granted for both the aim. For this study, three alloys having their chemical compositions close one to another were used. The exact chemical compositions are kept confidential at the request of MK. Therefore, only an average of the chemical composition is given in the table below for the three alloys. The three alloys were named Composition 0, Composition 1 and Composition 2, with the enhancement of the relative elements amount.

	Si	C	Ni	Cr	Mo	V	Nb	Mn	Fe
Composition 0	2.0-3.0	2.5 -3.0	4.0-6.0	2.0-3.5	3.5-4.5	1.5-2.5	0.2-1.2	0.5-1.5	Balance
Composition 1									
Composition 2									

Table 5 : The three different average compositions evaluated (mass %).

The differences within the chemical composition of the three alloys consist in small variations within C, Ni, Cr, V and Nb contents, the remaining alloying elements being present in similar amount. The variations within the aforementioned elements had been set as higher, medium and lower, depending on their relative amount. Such variations are intended to allow assessing their influence on the subsequent microstructure.

The first two massive pieces provided by Marichal Ketin was about the Composition 1, it was thermal treated with a double tempering of 530°C for 24 h after the casting followed by calm air cooling in the oven. During the study several samples were used and they were obtained from the massive pieces, it is important to know their positions to understand the differences. X1, X2 and X3 samples were obtained from the Composition 1 first massive piece with a cutting operation; X1 sample is from the surface to 19.6 mm depth in the shell; X2 sample is between 19.6 mm and 40 mm depth; X3 sample is an additional sample located close to the bonding zone of the X2 sample with a length of 21 mm. All the samples have a width of 15 mm.

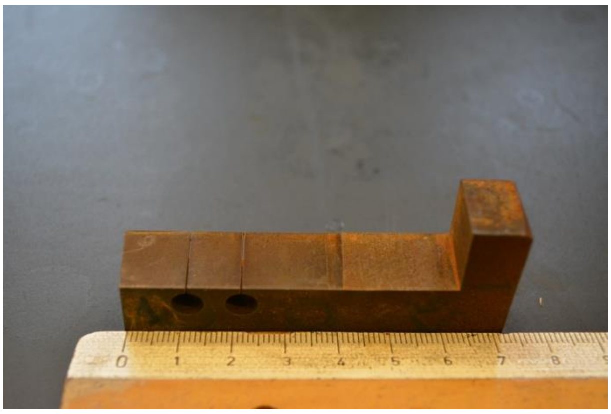

Figure 31 : Composition 1 first massive piece.

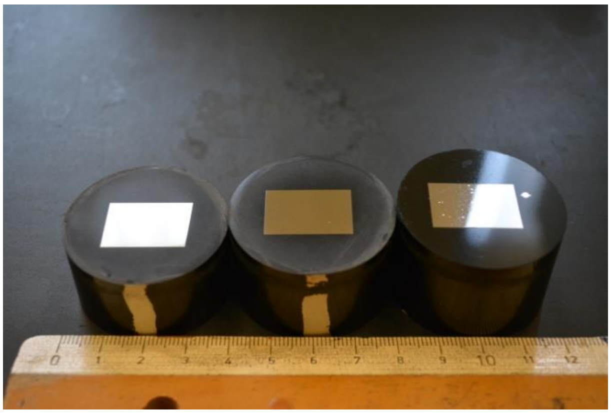

Figure 32 : X1, X2 and X3 samples obtained from Composition 1 first massive piece.

In the Figure 31 it is possible to see the first massive piece cut with also the holes of the DTA samples obtained from it. The DTA samples are in two different depths from the surface, the first at 12 mm (considerate X1) and the second at 22 mm (considerate X2). The weights of the DTA samples are in the Table 6. In the Figure 32 it is possible to see three different samples obtained; X1 sample is the left one that is closer to the surface and X3 sample is the one on the right, in the latter there is a reference of the core position and there are also some hardness indentations on it. From the second massive piece provided by MK all the dilatometer samples and four DTA samples were obtained. Three different carrots were cut as is shown in the Figure 33:

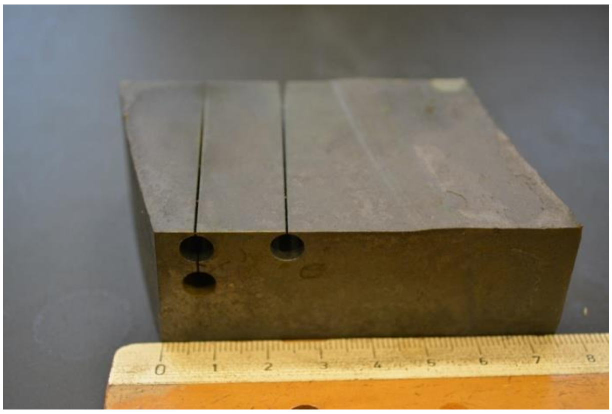

Figure 33 : Composition 1 second massive piece.

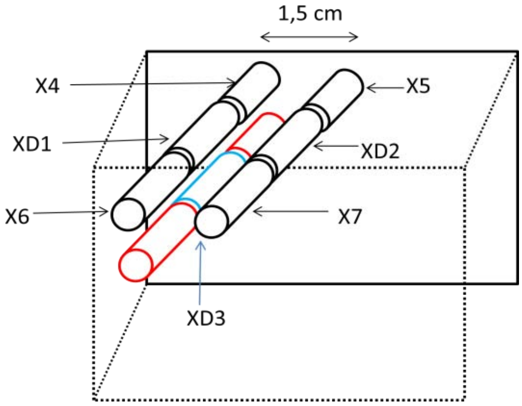

Figure 34 : Schematic drawing of the sample positions in the Composition 1 second massive piece; all the DTA samples and dilatometer test are pointed at with a black arrow, XD3 sample is in blue and the pieces in red were not used.

In the Figure 34 the positions of all the samples are shown and it is possible to see that there is a variation of depth from the surface inside the dilatometer test because the carrots are not parallel with the surface. XD1 and XD3 have a depth that goes from 10mm to 15mm; instead XD2 has a depth from 25 mm to 30 mm because it is closer to the core (1.5 cm of distance from the other carrot). The length of the dilatometer test is 23.9 mm for the XD1, 19.38 mm for the XD2 and 23.76 mm for the XD3. The distances from the surface of the DTA samples are shown in the Figure 35. The samples in the upper part of the picture are from the first massive piece and in the lower part they are from the second massive piece.

	X1	X2	X4	X5	X6	X7
Weight (mg)	972.1 1529.6	971.3	925.7	931.8	969.2	1031.6

Table 6: Weight of all the DTA samples

In the Table 6 the weight of the DTA samples are reported, the second weight of the X1 is referred to a particular DTA test done with the same piece extracted from the Composition 1 massive piece.

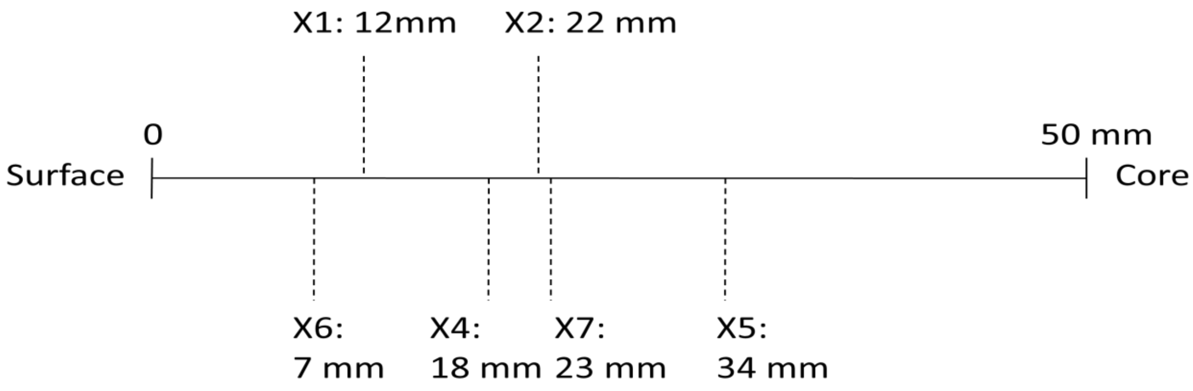

Figure 35 : Schematic drawing of the DTA sample positions with the relative distances from the surface.

In the cutting operation a little part of material can be lost and the difference of the distance between the sample (for example X6 and X7) can be different with the ideal distance that is shown in the Figure 34.

A bar of the Composition 1 was thermal treated with a reaustenitization treatment (treated at 1025°C during 1h after casting the normal double treatment followed by calm air cooling) in the lab (R1) and after it was polished by Marichal Ketin; it was used for the optical microscopy, its dimensions are 60 mm as length and 25 mm as width. It is shown in the following picture:

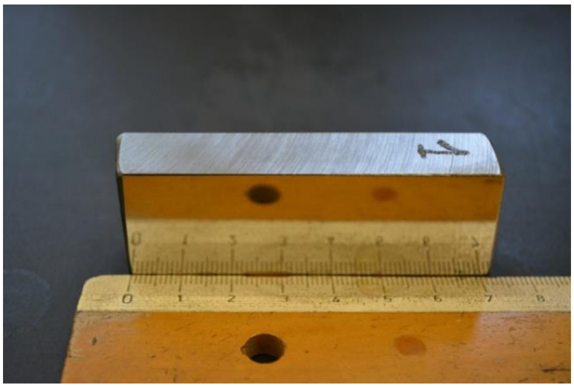

Figure 36 : Reaustenitizated sample (R1)

In the study two compositions were used, they are very similar and samples from the Composition 2 were used for several tests. Seven different as-casted bars were available from Marichal Ketin, one was analyzed as-casted (Industrial as-cast conditions or N0) and the other six samples were treated with six different thermal treatment (double tempering of 5 h each, followed by calm air cooling within MMS lab furnaces performed on bars in the as-cast conditions) in the laboratory and after polished by MK.

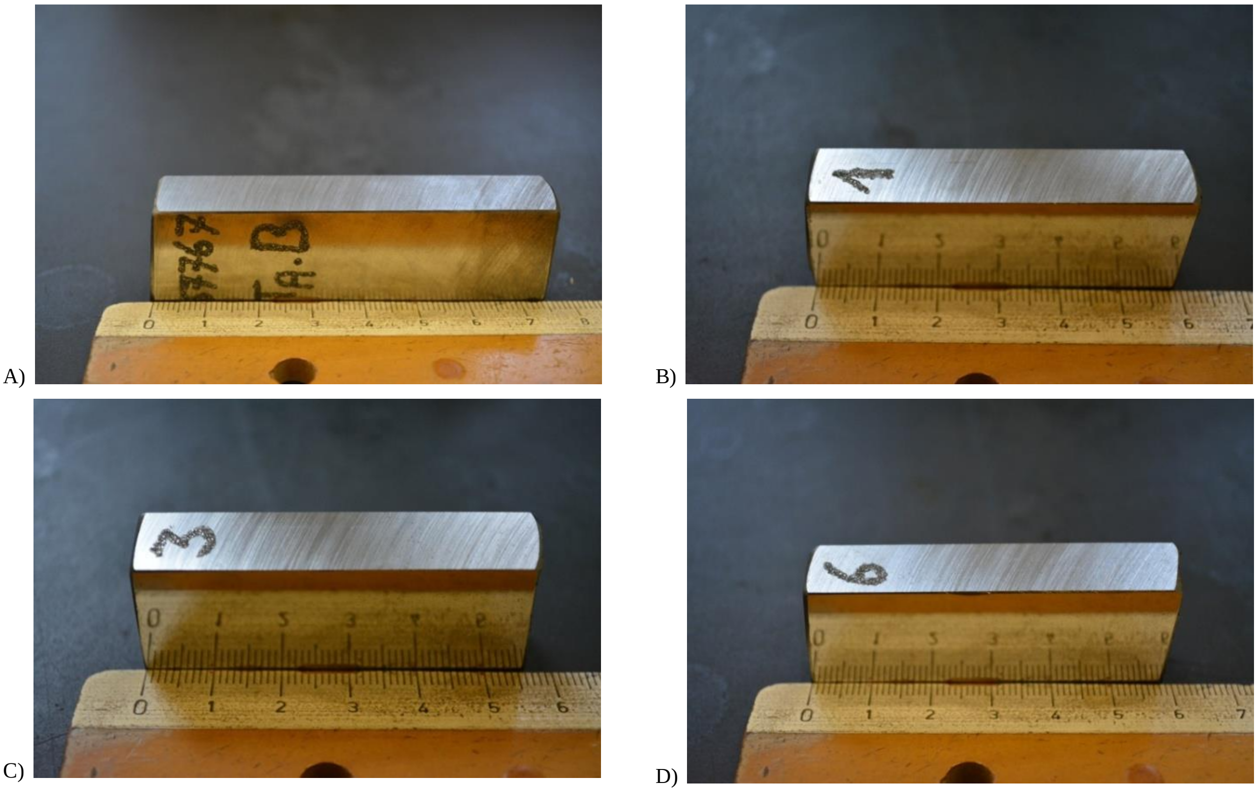

A)
B)
C)
D)

Figure 37 : A) N0 sample in as casted conditions; B) N1 sample heat treated with double tempering at 425°C; C) N3 sample heat treated with double tempering at 475°C; N6 sample heat treated with double tempering at 550°C.

The six tempering temperatures range was between 425°C and 550°C, with step of 25°C. They were called in order to the thermal treatment temperature from smaller to higher value, for instance N6 sample is the one with double tempering at 550°C. In those pictures there are shown four of the seven samples. The Industrial as-cast conditions sample has dimensions of 75 mm as length and 25 mm as width, meanwhile the other samples have dimensions that can vary from 53 to 60 mm as length and 25 mm as width.

A sample from a composition precedent at this study was analyzed with the optical microscope; it is divided in three circles that correspond to three different depths from the surface: 10, 25 and 40 mm.

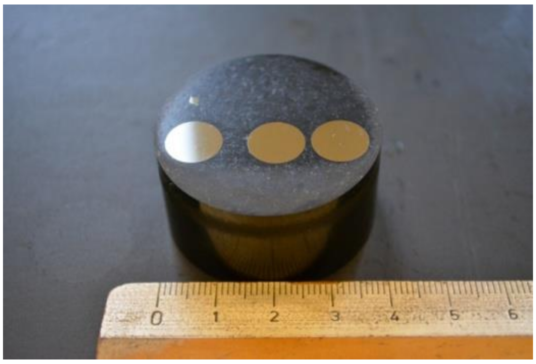

Figure 38 : Sample from the composition of a previous study.

Several DTA samples and two dilatometer samples after the tests were prepared to be observed with the Optical microscope and SEM, they were incorporated in the resin as the other samples and worn of the half of the diameter to observe the center axis. In the following pictures they are showed:

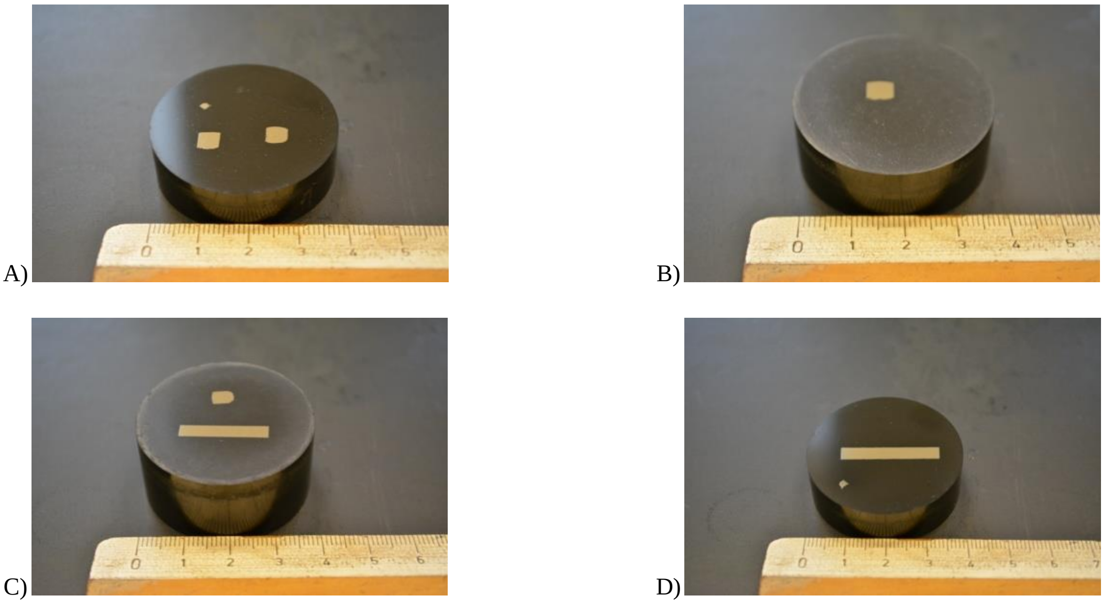

Figure 39 : A) DTX1 and DTX2 samples after DTA test; B) DTX4 sample after DTA test; C) DTX7sample and XD2 after the respective tests; D) XD1 sample after Dilatometer test.

Two explicative tables now are reported; the Table 7 explains all the tests done on the sample coming from Marichal Ketin for the three different compositions, meanwhile the Table 8 is a table that reassume all the samples analyzed with the thermal treatment and the test done for every sample. For the microscope observations the DTA samples after the test are recalled adding DT in the start of the sample name to do not confound it (for evidence X1 after the DTA test is called DTX1).

Analysis	**Materials**											
	Composition 1: treated with double tempering (2*530°C/24h)				Composition 2: 1 Brut + 6 samples treated with six different temperature of double tempering (5h each)							Composition 0
	X1	X2	X3	R1	N0	N1	N2	N3	N4	N5	N6	(previous studies)
Thermocalc analysis	√	√	√									√
DTA analysis	√	√										√
Optical microscope	√	√	√	√	√	√					√	√
Stream analysis	√	√	√	√	√	√					√	
SEM	√	√			√							
Dilatometer test (maximum 1025°C)	√	√		√								
Amount of residual austenite by Magne Gage	√		√	√	√	√	√	√	√	√	√	
Macro hardness analysis (Vickers HV 30)	√		√	√	√	√	√	√	√	√	√	

Table 7 : Explication of all the tests done on the samples of the three different compositions. In the Table 8 are reported the explanation for all the samples.

Sample	**Thermal treatment sequence +Analysis**
X1, X2,X3,X4,X5,X6 and X7	As-cast + Double Tempering conditions (2*530°C/24h) [see Figure 35]
R1	As-cast+ Reaustenitization at 1025°C during 1h
DTX1, DTX2, DTX4 and DTX5	As-cast + Double Tempering conditions+ DTA test (reheated and remelted up to 1300°C)
DTX6 and DTX7	As-cast + Double Tempering conditions+ DTA test (reheated and remelted up to 1450°C)
XD1	As-cast + Double Tempering conditions + Dilatometer test (up to 1050°C with a heating rate of 5°/min) [see Figure 34]
XD2	As-cast + Double Tempering conditions + Dilatometer test (up to 1050°C with a heating rate of 5°/min) [see Figure 34]
XD3	As-cast + Double Tempering conditions+ Austenitized (1025°C during 1h) + Dilatometer test (up to 1050°C with a heating rate of 5°/min) [see Figure 34]
Industrial as-cast conditions or N0	Industrial as-cast conditions
N1	As-cast + Double Tempering conditions up to 425°C (double tempering of 5 h each, followed by calm air cooling within MMS lab furnaces)
N2	As-cast + Double Tempering conditions up to 450°C (double tempering of 5 h each, followed by calm air cooling within MMS lab furnaces)
N3	As-cast + Double Tempering conditions up to 475°C (double tempering of 5 h each, followed by calm air cooling within MMS lab furnaces)
N4	As-cast + Double Tempering conditions up to 500°C (double tempering of 5 h each, followed by calm air cooling within MMS lab furnaces)
N5	As-cast + Double Tempering conditions up to 525°C (double tempering of 5 h each, followed by calm air cooling within MMS lab furnaces)
N6	As-cast + Double Tempering conditions up to 550°C (double tempering of 5 h each, followed by calm air cooling within MMS lab furnaces)

Table 8 : Legend of all the samples analyzed

5.2. Thermo-calc Equilibrium Software

Thermo-calc Equilibrium Software is computer software used for thermodynamic simulation or database generation; it is a CALPHAD product and possesses a high quality of the predictions due to the quality of the databases. Starting from a composition it is possible to arrive to the equilibrium diagram or to the solidification steps simulation. Thermo-calc simulation can be divided in two types: equilibrium and pseudo-equilibrium conditions. They give different compatible simulation and some more precise information in one than in the other. The equilibrium conditions is more precise to predict the temperature ranges and the maximum possible amount of a phase, meanwhile the pseudo-equilibrium conditions is more accurate as kinetic phenomenon and it can predict exactly the phase presences above the Liquidus temperature. [32]

5.3. DTA test

The NETZCH STA 449C Jupiter was utilized for the DTA tests, it is a NETZSCH product and it can refer to the simultaneous application of Thermogravimetry (TGA) and Differential Scanning Calorimetry (DSC). In the Figure 40 the internal structure of the STA 449C is showed:

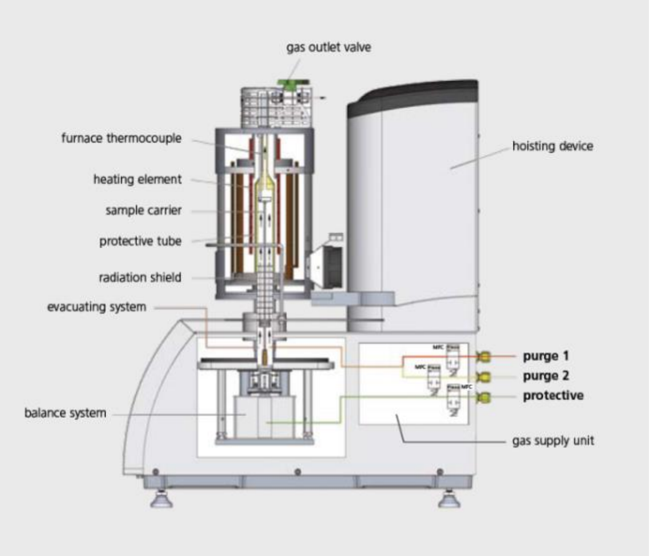

Figure 40 : Internal structure of the NETZCH STA 449C Jupiter. [33]

The first one has as possibilities the mass changes, temperature stability, oxidation/reduction behavior, decomposition and corrosion studies; while the second one has melting/crystallization behavior, solid-solid transitions, polymorphism, degree of crystallinity, glass transitions, cross-linking reactions, oxidative stability, purity determination, specific heat and thermokinetics. It can arrive to a high vacuum level or to a protective atmosphere and its sensor can be with various types based on the application. In the following Table 9 the main data are reported. [33]

Temperature range	**-150°C to 2400°C**
Furnace	Tungsten furnace (RT to 2400°C) or High-speed furnace(RT to 1250°C)
Heating and cooling rates	0.001 K/min to 50 K/min (dependent on furnace)
Weighing range	5000 mg
TGA resolution	0.025 µg
DSC resolution	< 1 µW (dependent on sensor)
Atmospheres	Inert, oxidizing, reducing, static, dynamic and vacuum
Gas flow device	Integrated mass flow controller for 2 purge gases and 1 protective gas
Vacuum-tight	Up to 10^{-4} mbar (10^{-2} Pa)

Table 9 : Main data of the NETZCH STA 449C Jupiter. [33]

5.4. Optical microscope and Stream Analysis Software

The Olympus BX60 Microscope was utilized for the optical microscope analyses and in the Figure 41 it is shown. It is endowed of 6-position objective turret with DIC/Analyzer slide slot and 4 position FL cube turret. The illumination can be Transmitted with 100 Watt Quartz Halogen Illuminator, Transmitted condenser (Aplanat Achromatic 1.4), Reflected/Epi-Fluorescence (100 Watt Mercury Illuminator) and Reflected/Epi-Fluorescence Power Supply (100 Watt with hour meter).

Figure 41 : Olympus BX60 Microscope. [34]

In the study it was utilized the 2.5x, 5x and 10x of magnitude between all the possible. In the Table 10 the main specifications about the microscope frame are reported. The microscope is gifted also of an automatic support for the sample movements.

Optical system	UIS optical system
Focus	Vertical stage movement: 25mm stroke with coarse adjustment limit stopper Torque adjustment for coarse adjustment knobs Stage mounting position variable High sensibility fine focusing knob (minimum adjustment gradations: 1 µm)

Table 10 : Main specifications about the microscope frame of the Olympus BX60 Microscope. [34]

The Stream Analysis Software was utilized to analyze the pictures obtained from the Olympus BX60 Microscope; Stream is advanced micro-imaging software that allows seamlessly acquiring, process, and measuring images, to create valuable data and reports. The software can easily be customized and provides sophisticated results with simple flexible operation. In the study it was utilized for the quantification of the graphite nodules and for the evolution analysis during the depth of the graphite shape. [34]

5.5. Scanning Electron Microscope

The Phillips XL30 FEG-ESEM was utilized in the SEM analyses and it is showed in the Figure 42. It employs Schottky based gun design using a point-source cathode of tungsten, which has a surface layer of zirconia (ZrO_2). The instrument has the performance of a conventional SEM but has the advantage that it is equipped also with a EDAX (energy dispersive x-ray detector with an ultra thin window). The EDAX software allows analysis from Boron onwards; automated point analysis, linescans and spectral mapping are available. The EDX-system allows acquiring analytical information in high vacuum and ESEM mode, because of a solid-state backscattered electron detector (BSE) and gaseous analytical detector (GAD) with cone as well as standard and high-pressure secondary detectors (ESD) for ESEM mode. In the study composition surveys were taken with those modality and normal images with the secondary electrons and in the common modality. The use of that microscope needs a sample preparation with a silver painting to bond the real sample with the bottom of it (resin part). In the Table 11 the main technical details are reported.

Figure 42 : Phillips XL30 FEG-ESEM. [36]

Resolution	**2.0 nm at 30kV**
High tension	Continuosly variable from 0.2 till 30 kV
Specimen stage	X & Y : 50mm Z : 50mm total Rotation : n x 360° Tilt : at FWD 10mm, -15° to +75° Max. free space (min. WD): 3mm in high vacuum
Multiple differential vacuum system	Specimen chamber, ODP and two pre-vacuum RP: 1x 10^{-4} Pa (1mbar) In high vacuum mode and 10 to 1330 Pa with H2 vapour or auxiliary gas Intermediate vacuum, IGP: 1x 10-5 Pa (1x10-7 mbar) Gun vacuum, IGP: 5x 10-7 Pa (1x 10-9 mbar)
Image storage	Standard image (702x484 pixels – 341 KB) High definition image (1404x968 pixels – 1.31 MB)
Backscattered electron detector	Better than 0.1 Z at Z=30

Table 11 : Main technical details of the Phillips XL30 FEG-ESEM. [36]

5.6. Dilatometry

The dilatometer tests were taken on a NETZSCH DIL 402C and it is showed in the Figure 43. The DIL 402C measurement device consists on a Dilatometer(measuring unit), power unit and computer system with also screen. The sample is placed in the homogeneous temperature zone of the furnace; the latter is heated according to a preselected temperature program (the temperature is controlled by a thermocouple).

Figure 43 : NETZSCH DIL 402C. [35]

Sample carrier and pushrod are also submitted to a change in length during the test. Thus there is measured and registered the sum of the change in length of the sample. The pushrod transmits this change in length mechanically to the displacement transducer (LVDT) and causes a displacement of the core of the latter. The resulting change in voltage is transformed by a carrier frequency measuring amplifier to a d.c. voltage which is proportional to the displacement; finally the signal is registered by the computer. It is possible to create a required sample atmosphere with a various gases; in the study the Argon (Ar) was utilized. In the Table 12 the technical data of the device are reported. [35]

Measurement path	**± 2.5mm**
Resolution of data acquisition	16 Bit
Measuring ranges	5000/500 µm
Contact pressure	15-45 cN
Sample holder (type and material)	Tube sample holder/rod sample holder Fused silica (RT… 1100°C) or Al_2O_3 (RT.. 1600°C)
Sample dimensions (length and diameter)	0-25mm (25-50mm possible) 3-12mm
Atmosphere in the sample chamber	Dynamic gas flow (inert gas only)
Temperature range	20..1600°C (depends on the furnace)
Heating rate	Recommended for dilatometer measurements <5 K/min

Table 12 : Technical data of the NETZSCH DIL 402C. [35]

5.7. Magnegage

A standard Magnegage Model 5-660 was utilized to investigate the retained austenite amount; this model is adapt for all general flat and curved surface work with which the gauge head can be lowered directly onto the point of measurement. The bases of the test are the magnetic properties of the different phase presences in the microstructure; the test consists to put the sample in contact with a magnet that it is bonded with a spiral, the latter applies a force on the magnet to separate it from the sample. The final value is the union between the first position of the castor when the magnet is in contact with the sample and the final one, until the tester (the magnet) is in contact. A low value means a high amount of retained austenite, meanwhile a high value means the contrary; the test is not considered accurate because the value considered "high" is relative. [37]

5.8. Hardness test

The EMCO M1C 010 was utilized to make some hardness indentation on the samples during the study; it is considered a digital low-load hardness testing machine. It is possible to utilize Vickers, Brinell, Knoop and Rockewell testing with various weights; it was utilized DIN EN ISO, ASTM E-92 HV 30 during the study. It is gifted of automatic exchange of lens and indenter, fully automatic test cycle, automatic lens focusing, leading-edge high resolution CCD camera, fully automatic image evaluation and manual cross slide.

Figure 44 : EMCO M1C 010. [38]

As it is shown in Figure 44 after the test, that it was done manually during the study, after the indentation it is possible to calculate the hardness value measuring the distances between the rhombus edges with appropriate software (ecos 010/Image) for the image analysis. [38]

5.9. Other instruments

The sample preparations can be divided in two steps, the cutting step and the polishing step. The cutting step was done with a Precision Cut-Off Machine or a Spark Erosion Machine depending to the sample type. The first one is used to the normal cutting of metal; meanwhile the second one is used to the cutting of massive pieces to obtain cylinder samples for the DTA tests and Dilatometer tests. An example of the latter cutting is shown in Figure 33 on the Composition 1 massive piece. In the polishing step a STRUERS Citopress-1 was used as mounting press for the sample incorporation with Bakelite and the STRUERS Tegramin-30 was utilized to polish the surface of the sample after the incorporation to arrive to a plan surface. The plan surface is necessary for the microscope analyses. Two different types of Bakelite were utilized, one harder on the cylinder surface where it is present the sample; the different resin are chosen based on the hardness of the material to polish. The Tegramin-30 has that name because has a disc sizes of 300mm; it is possible to level the surface with circular movements on wear papers with different grain size together with the utilizing of lubricant liquid correlate with the different grain sizes. Examples of the final results after polishing are shown in Figure 38 and Figure 39. [39]

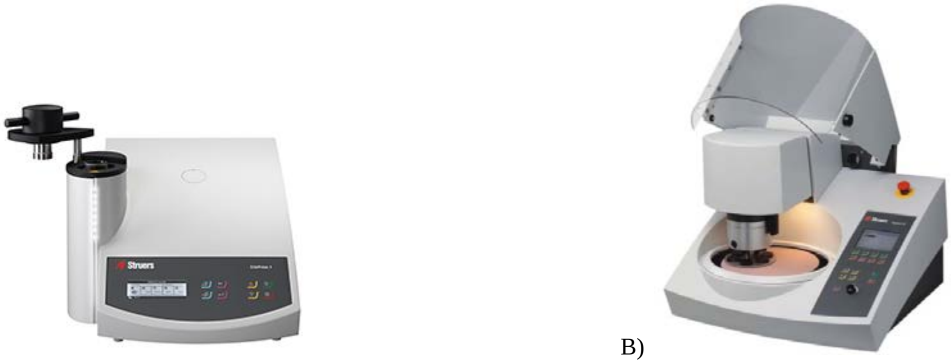

A) B)

Figure 45 : A) STRUERS Citopress-1 and B) STRUERS Tegramin-30. [39]

6. Results

6.1. Thermo-calc analyses

In this composition it is important to eliminate from the probable phase formation list the phase cementite (M_3C) and in the pseudo-equilibrium also the M_6C because there are not in the final samples; they disturb the simulation and the real results, not giving a right trend.

The software calls some phase with other names, in the following table the most interesting phases are explained:

FCC_A1#1	FCC_A1#2	FCC_A1#3
Austenite	MC (V)	MC (Nb)
BCC_A2	HCP_A3#2	MC_ETA
Ferrite	M_2C	MC (Mo, V)

Table 13: List of the possible phases with acronym names.

6.1.1. Equilibrium conditions

Thermo-calc simulation in equilibrium conditions was done with the consideration of M_6C presence using the mass percentage of the main elements present in the composition 1. In the Figure 46 is reported the output graph and in the Table 14 the main information are reported.

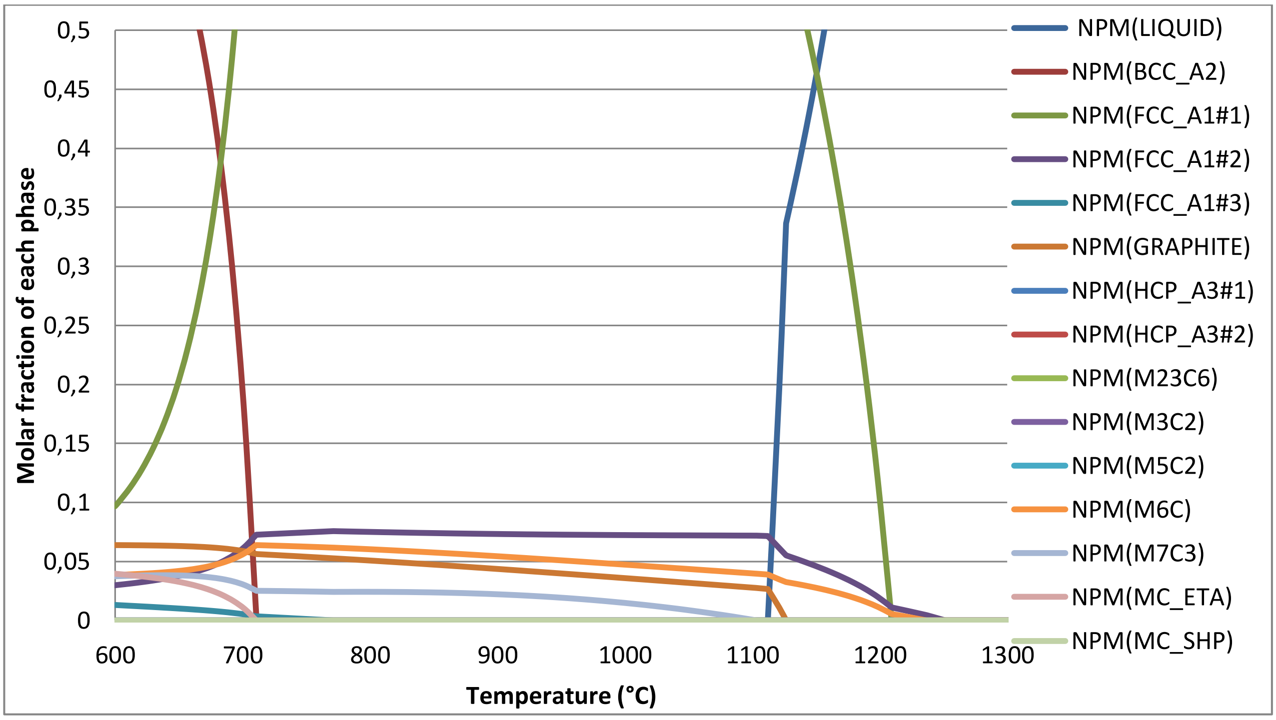

Figure 46: Thermo-calc graph in equilibrium conditions for the composition 1.

The graph reports the evolution of phase quantity in molar fraction percentage during the solidification from the liquid (1300°C) to the ending part of it (600°C).

	New composition
Liquidus(°C)	1251
Solidus (°C)	1115
Graphite (mass %)	2,6
MC (mass %)	7,15
M_7C_3 (mass %)	/
M_6C (mass %)	3,8

Table 14: Main temperatures and mass % of the most important phases taken at 1100°C predicted by Thermo-calc simulation.

Thermo-calc simulation with the same conditions of the previous one was done but without the consideration of M_6C presence and almost the same percentage was found with and without considering the M_6C. The austenitization range is slightly bigger than the previous composition. There is an increase of the graphite amount and other values are unchanged, except for the M_7C_3 carbide that it is not present at high temperature; it is formed and it started to precipitate below the austenitization range, with a maximum of 2.5 % at 600°C.

6.1.2. Pseudo-equilibrium conditions

Thermo-calc simulation with pseudo-equilibrium conditions was done to simulate more into the depth the solidification steps at high temperature because it is possible to simulate the retrodiffusion of the reference interstitial element (Carbon in this case), it is limited to the solidification sequence (ScheilGuliver Model).

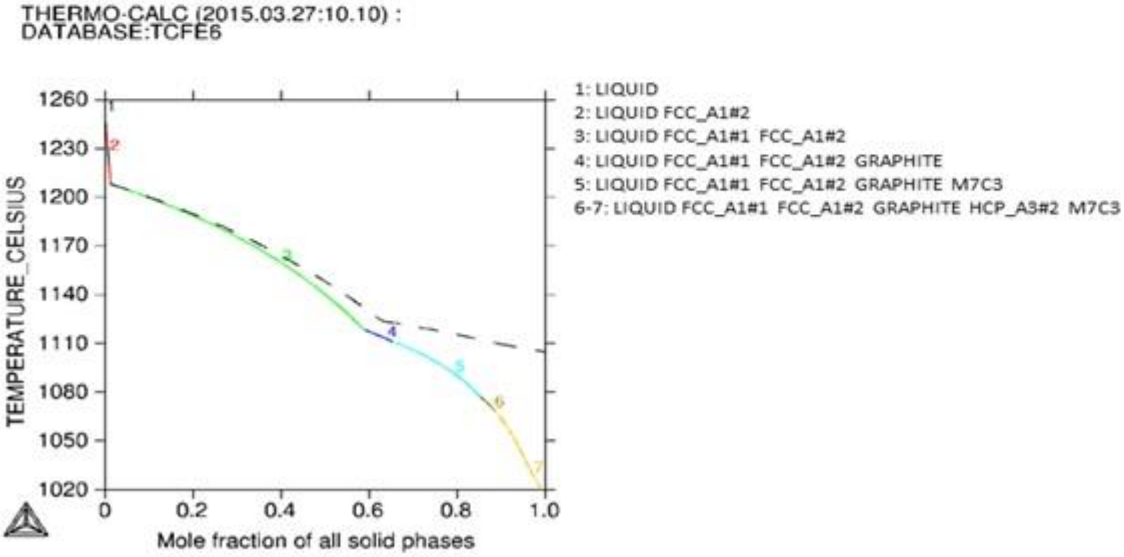

Figure 47 : Thermo-calc graph in pseudo-equilibrium conditions for the composition 1.

The names legend is in the Table 13; the Figure 47 is modified because the software considers disappeared the MC(V) carbide in the stage 6 that is not possible, thus the stage 6 and 7 are reported together. The old and the new composition curves are very similar except for the formation of graphite before the M_7C_3 carbide. The M_2C phase is formed at 1080°C, it cannot be formed in equilibrium condition because it needs the carbon diffusion. The Liquidus temperature is confirmed at 1250°C as seen in the equilibrium condition and the solidus temperature is positioned at 100°C less than the equilibrium prediction.

6.2. Optical microscope analyses

Optical microscope analyses were taken on the Composition 0 sample, on the Composition 1 samples, on the Composition 2 samples and on the DTA samples to study the graphite shape evolution into the depth and the changes due to the treatments.

6.2.1. Composition 0

The Composition 0 sample was analyzed to check the amount of the graphite, in the Figure 38 it is possible to see the sample and the figure from the optical microscope is in the Figure 48.

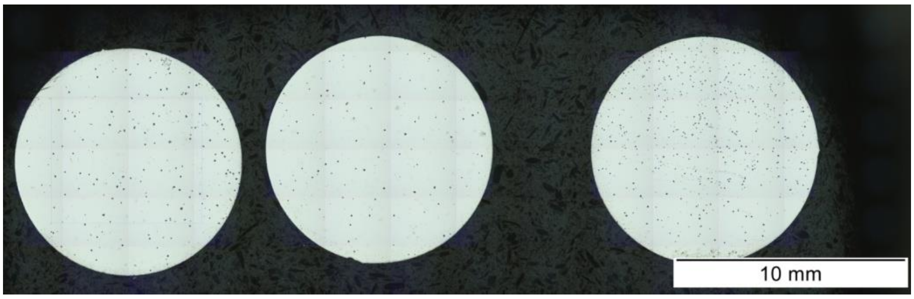

Figure 48 : Optical microscope figure with enlargement of 5x.

6.2.2. Composition 1

The Composition 1 samples were analyzed with the optical microscope to investigate the evolution of the graphite shape and the carbide amount in two different depths for the EDL method. For all the “X” samples a general figure, a quantification image and a figure every 5 mm of distance from the surface are reported, instead for the R1 three parts of the samples are reported.

6.2.2.1. Sample X1

In the Figure 32 it is possible to see the X1 sample on the left and in the Figure 49 there is a general view of the sample. The figure used for the graphite quantification and five zooms at different depths from the surface on the graphite particles are reported.

Figure 49 : Optical microscope figure at 2.5x of the general view of the X1 sample.

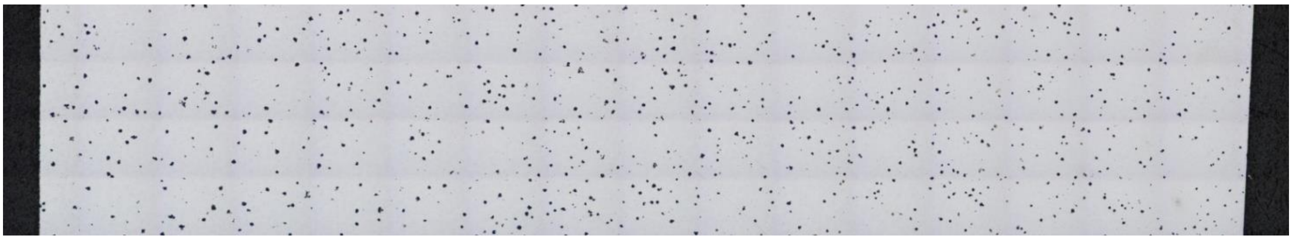

Figure 50 : Optical microscope figure at 5x of the general view of the X1 sample used for the graphite quantification.

Graphite particles are reported at 5mm, 10mm, 15mm and 20mm from the surface to show the changes with the depth. All the figures are taken at 5 mm from the upper part of the sample.

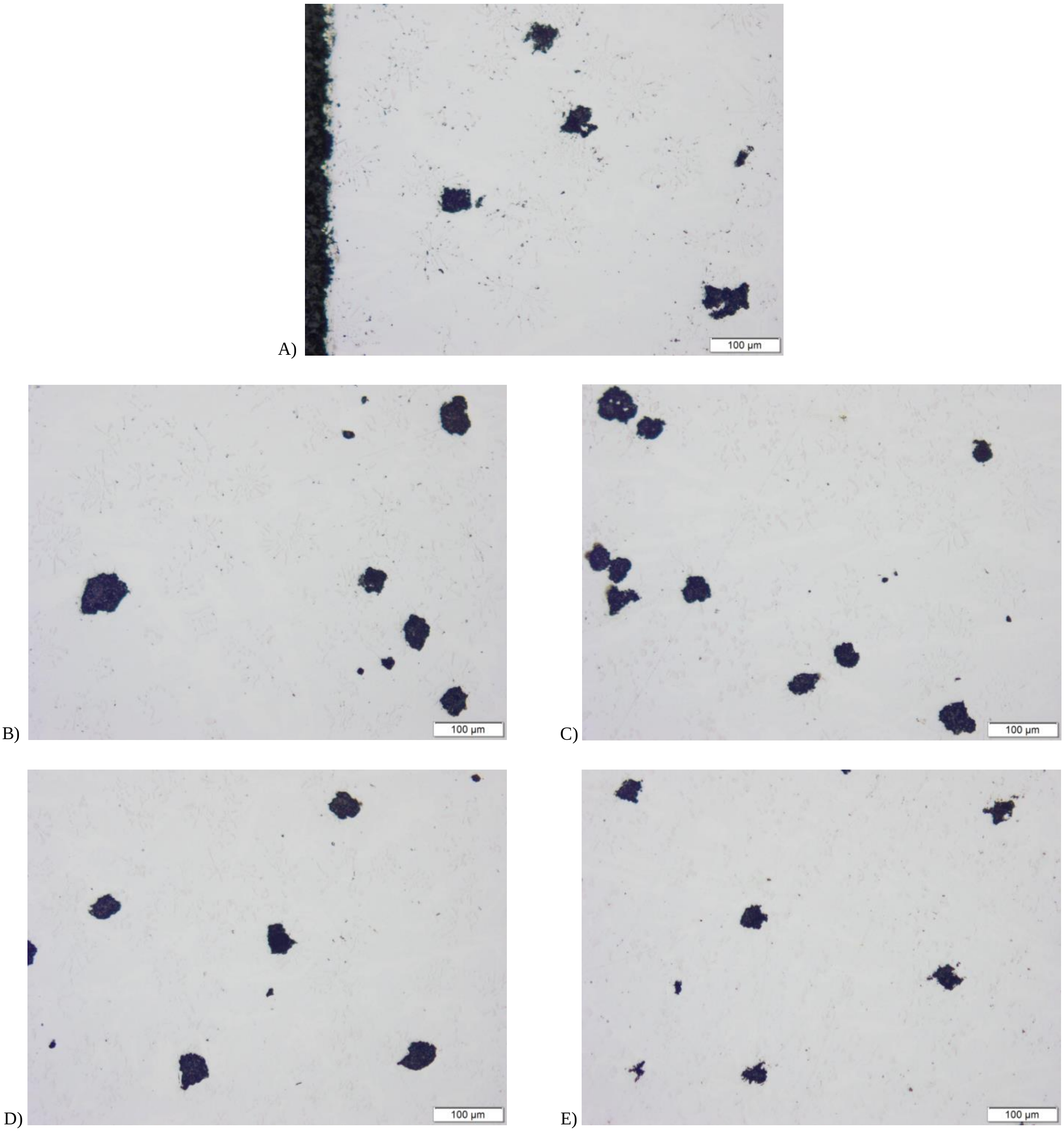

Figure 51 : Optical microscope figure of the X1 sample at 10x of graphite particles at the surface (A), at 5mm (B), 10mm (C),15 mm (D)and 20mm (E) from the surface.

6.2.2.2. Sample X2

In the Figure 32 it is possible to see the X2 sample on the centre and in the following Figure 52 there is a general view of the sample. The figure used for the graphite quantification and five zoom at different depths from the surface on the graphite particles are reported.

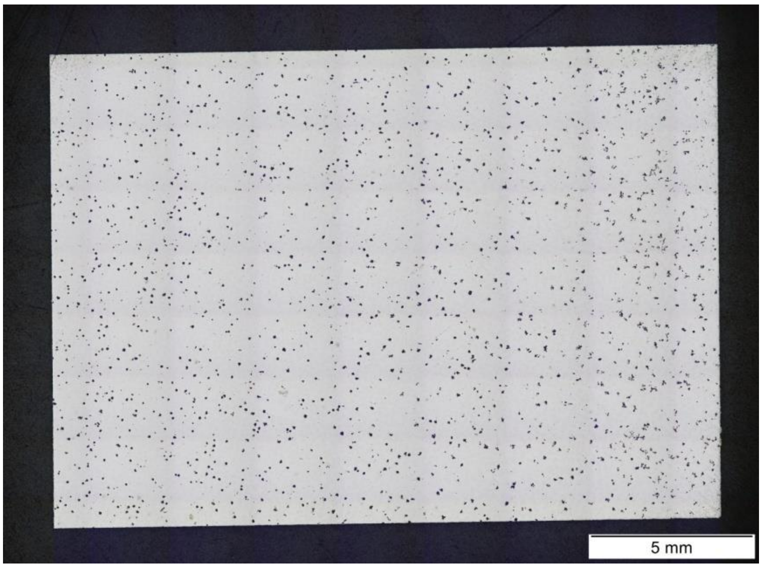

Figure 52 : Optical microscope figure at 2.5x of the general view of the X2 sample.

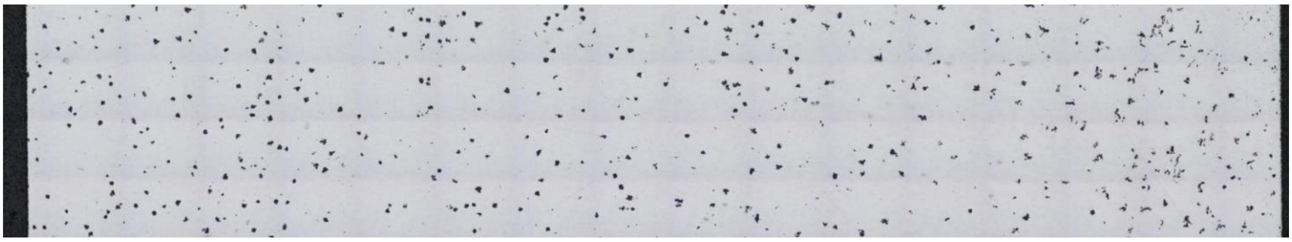

Figure 53 : Optical microscope figure at 5x of the general view of the X2 sample used for the graphite quantification.

Graphite particles are reported at 5mm, 10mm, 15mm and 20mm from the surface to show the changes with the depth. All the Figures are taken at 5 mm from the upper part of the sample.

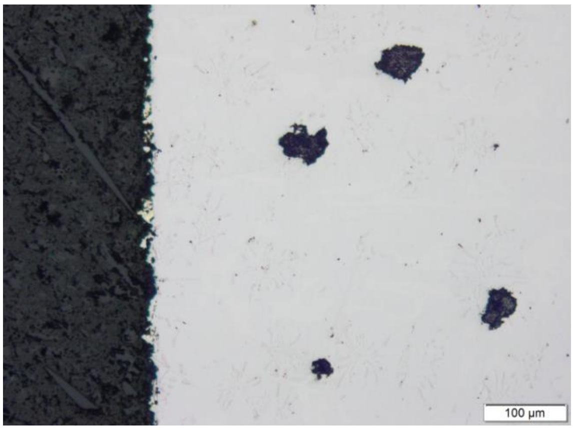

A)

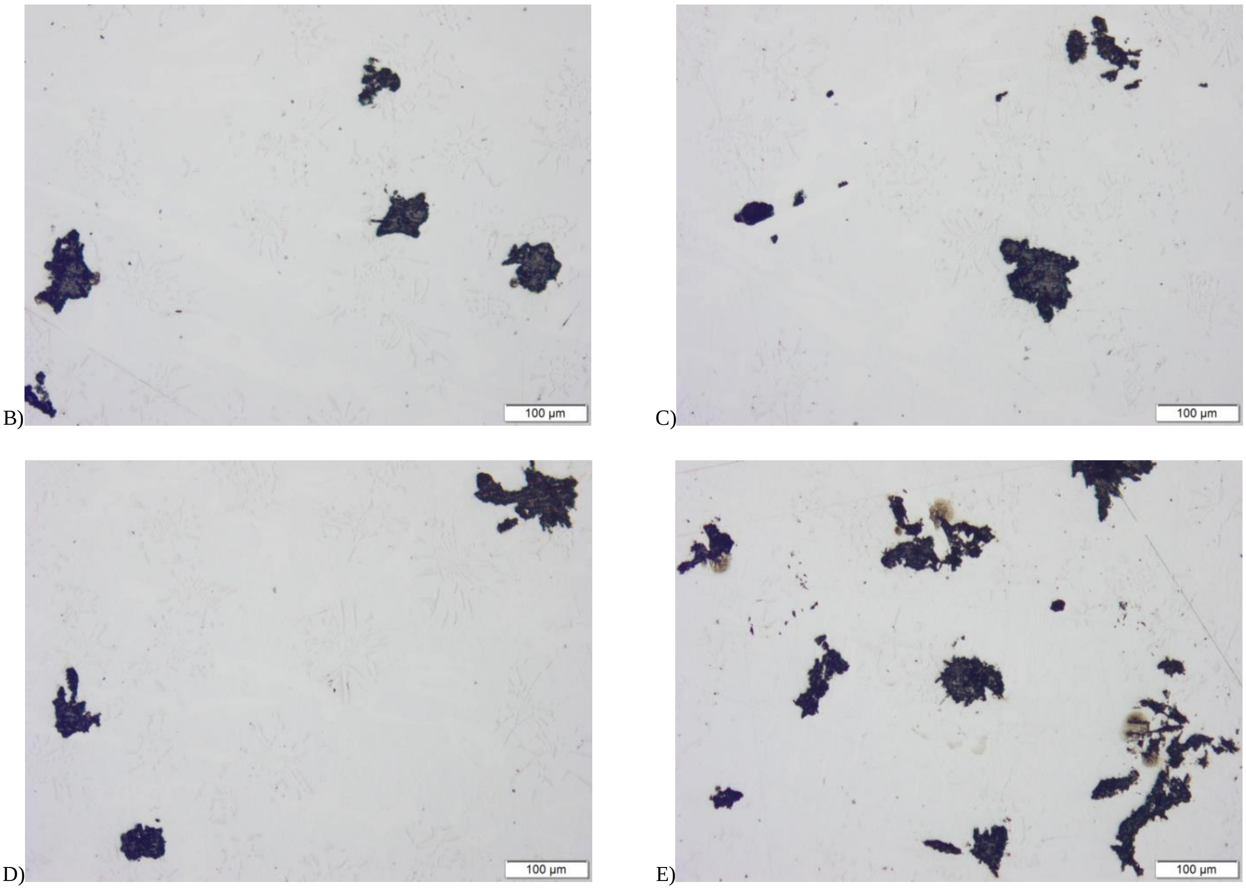

Figure 54 : Optical microscope figure of the X2 sample at 10x of graphite particles at the surface (A), at 5mm (B), 10mm (C),15 mm (D)and 20mm (E) from the surface of the sample.

6.2.2.3. Sample X3

In the Figure 32 it is possible to see the X3 sample on the right and in the following Figure 55 there is a general view of the sample with also the reference of the core presence on the right of the figure. The figure used for the graphite quantification and five zoom at different depths from the surface on the graphite particles are reported.

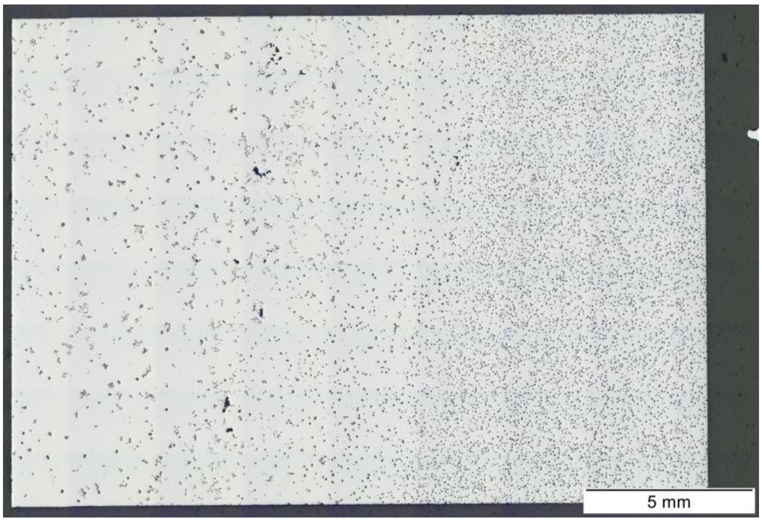

Figure 55 : Optical microscope figure at 2.5x of the general view of the X3 sample.

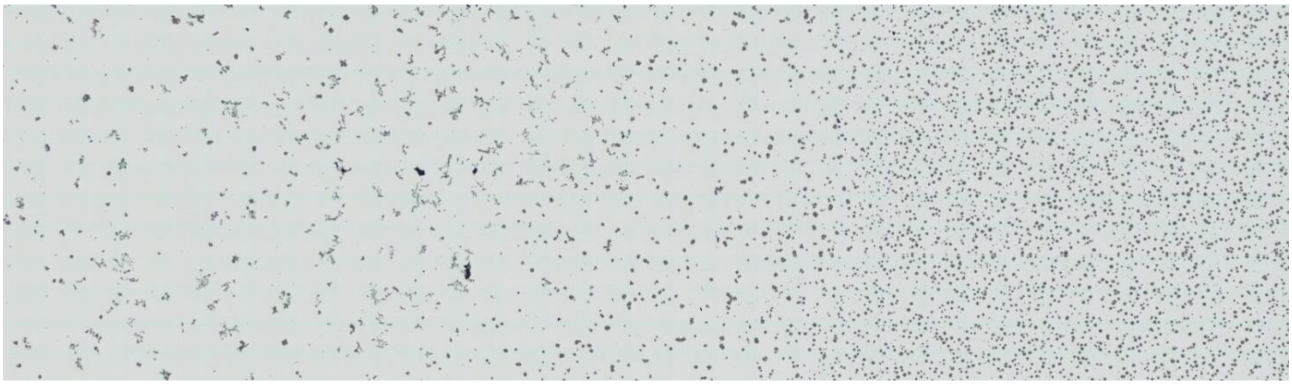

Figure 56 : Optical microscope figure at 5x of the general view of the X3 sample used for the graphite quantification.

Graphite particles are reported at 5mm, 10mm, 15mm and 20mm from the surface to show the changes with the depth. All the figures are taken at 5-6 mm from the upper part of the sample.

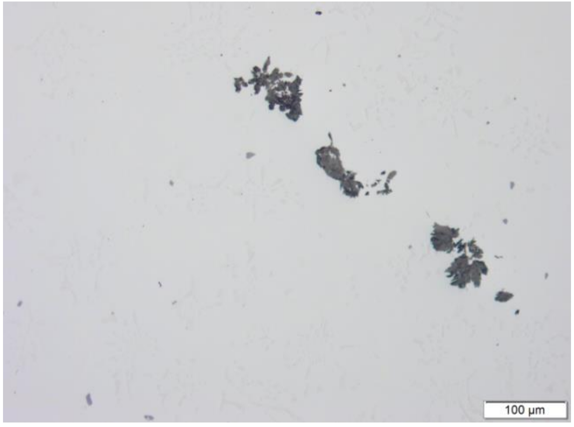

A)

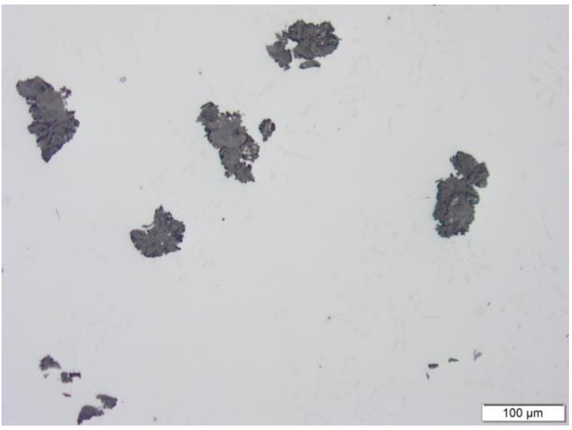

B)

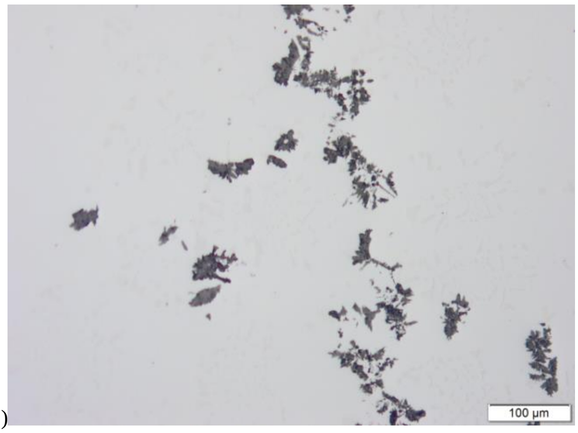

C)

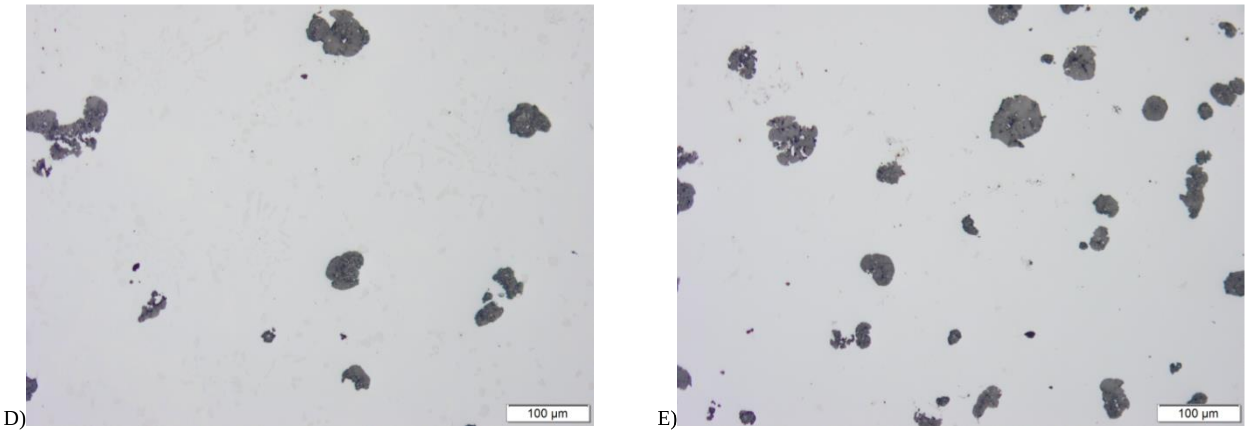

Figure 57 : Optical microscope figure of the X3 sample at 10x of graphite particles at the surface (A), at 5mm (B), 10mm (C),15 mm (D)and 20mm (E) from the surface of the sample.

6.2.2.4. Sample R1

The sample R1 (Figure 36) was divided in three different figures to analyze the evolution of the graphite shape after the reaustenitization treatment. The three figures have 2-3 mm in common to avoid losing of information; in the first part 26 mm, in the second part 22 mm and in the third part (26 mm were considered in the analysis.

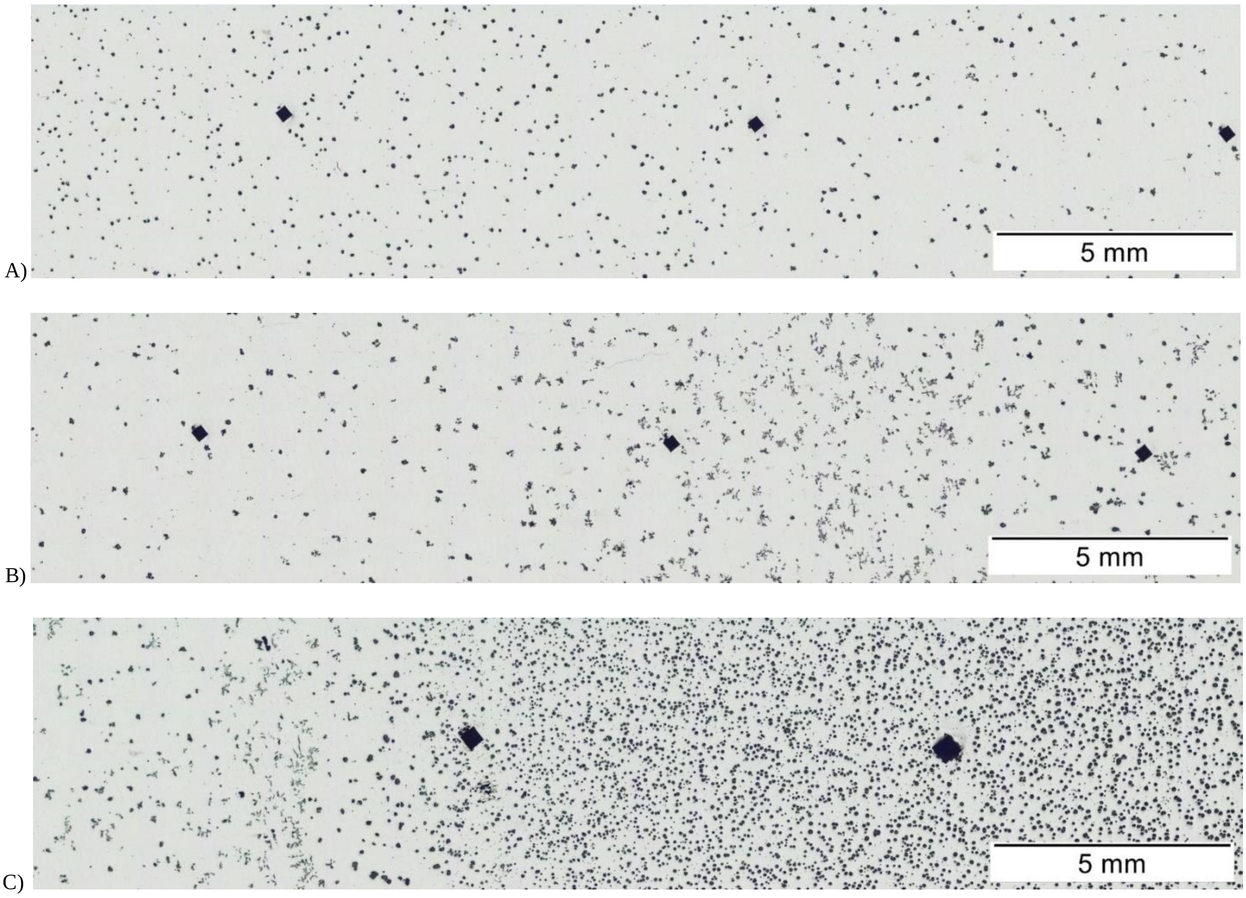

Figure 58 : Optical microscope figure at 5x of the R1 first (A), second (B) and third part (C).

6.2.3. Composition 2

The Composition 2 samples were analyzed with the optical microscope to investigate the evolution of the graphite. For all the “N” samples a general figure, a quantification image and a figure for every graphite shape change are reported.

6.2.3.1. Industrial as-cast conditions Sample (N0)

In the Figure 37 (A) it is possible to see the Industrial as-cast conditions sample and in the Figure 59 there is a general view of the sample. The figure used for the graphite quantification and seven zooms at different depths from the surface on the graphite particles are reported. Since the Industrial as-cast conditions sample has a high importance in the study because it is the as-casted sample and can be the base to understand all the other samples, a zoom was taken in every position where the graphite shape changes: 9mm, 34mm, 37mm, 41mm, 49mm, 56mm and 58mm.

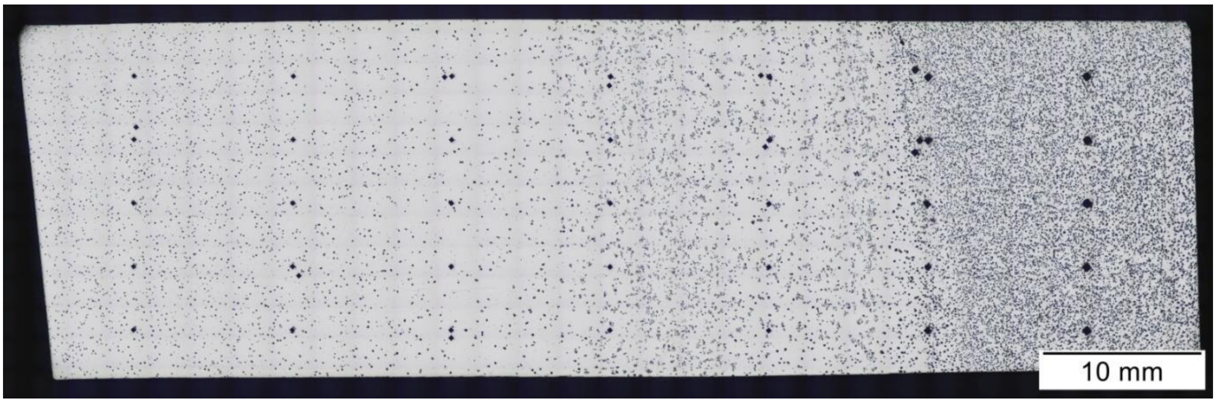

Figure 59 : Optical microscope figure at 2.5x of the general view of the Industrial as-cast conditions sample.

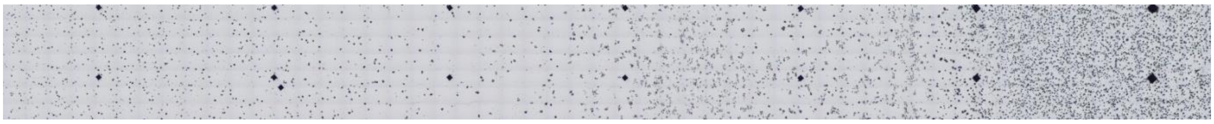

Figure 60 : Optical microscope figure at 5x of the general view of the X3 sample used for the graphite quantification.

All the following figures are taken at 5-6 mm from the upper part of the sample.

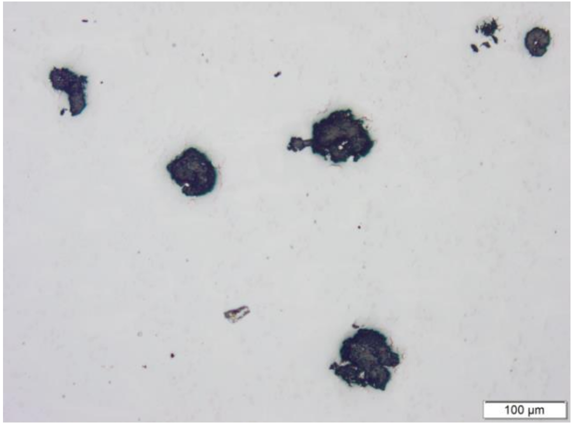

A)

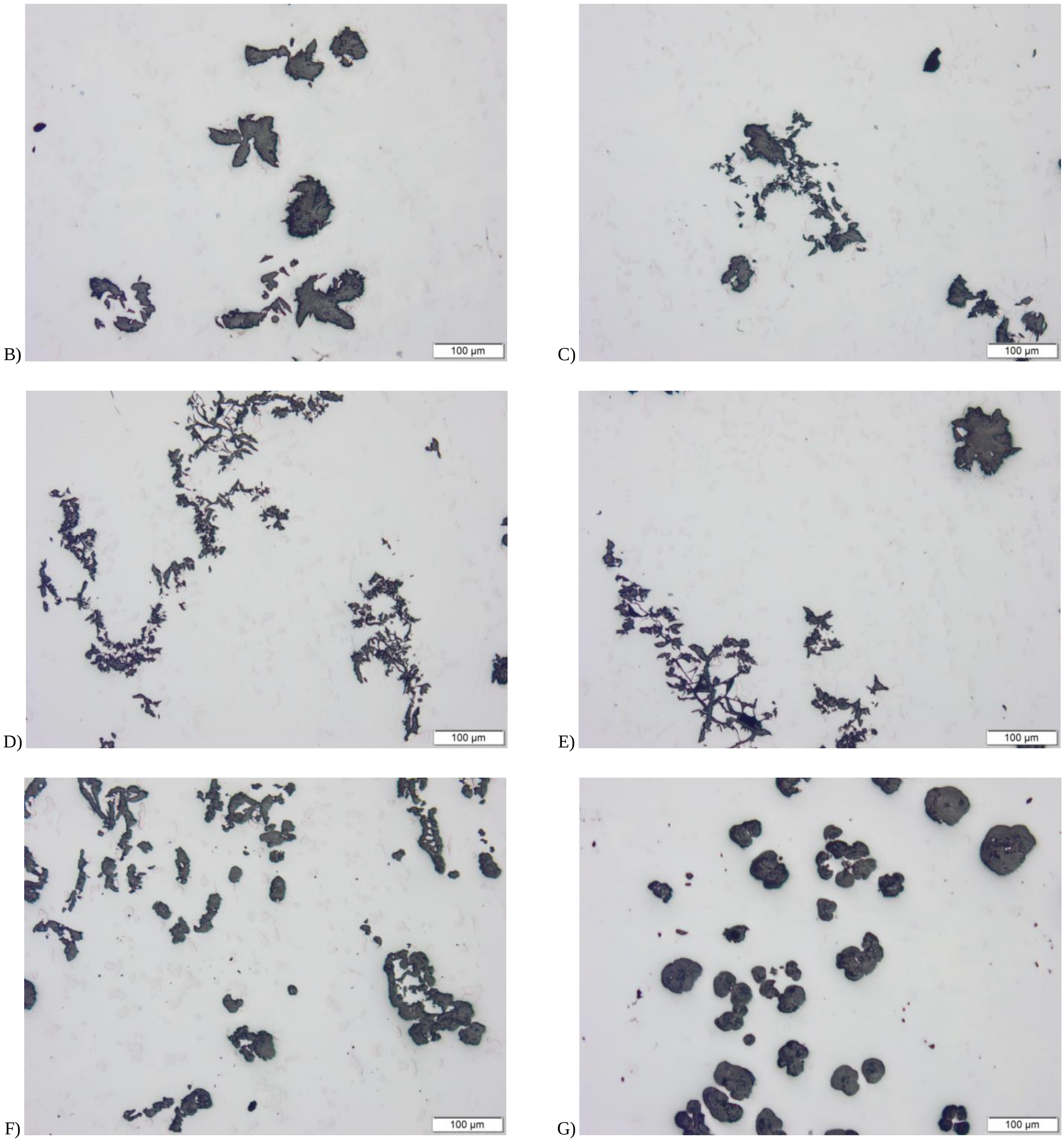

Figure 61 : Optical microscope figure at 10x of the NO at 9mm (A), 34mm (B), 37mm (C), 41mm (D), 49mm(E),56mm (F) and 58 mm (G) from the surface.

6.2.3.2. *Sample thermal treated at 425°C (N1)*

In the Figure 37 (B) it is possible to see the sample N1 and in the Figure 62 the image used for the quantification is reported. Seven zooms at the same depths of the N0 sample are reported to do a comparison. All the images of Figure 63 are taken at 5-6 mm from the upper part of the sample.

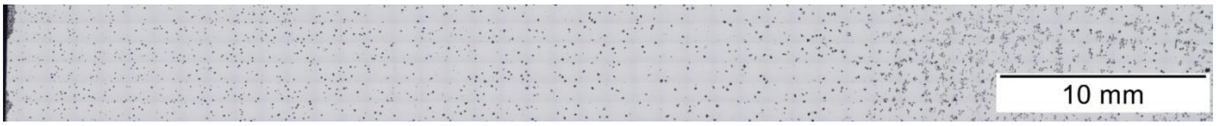

Figure 62 : Optical microscope figure at 5x of the general view of the N1 sample.

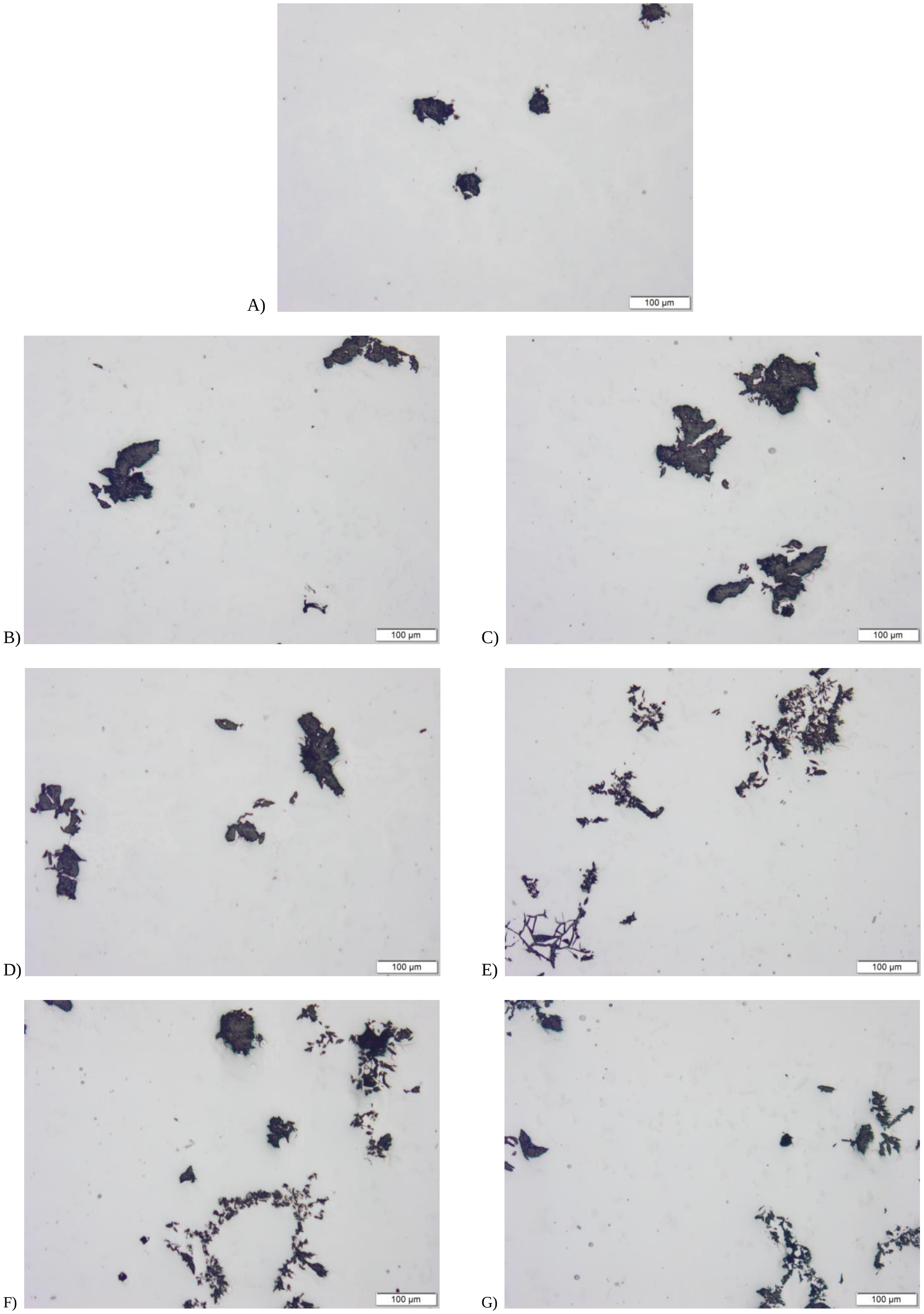

Figure 63 : Optical microscope figure at 10x of the N1 at 9mm (A), 34mm (B), 37mm (C), 41mm (D), 49mm(E),56mm (F) and 58 mm (G) from the surface.

6.2.3.3. Sample thermal treated at 550°C (N6)

In the Figure 37 (D) it is possible to see the sample N6, meanwhile in the Figure 64 the image used for the quantification is reported. Seven zooms at the same depths of the N0 sample are reported to do a comparison.

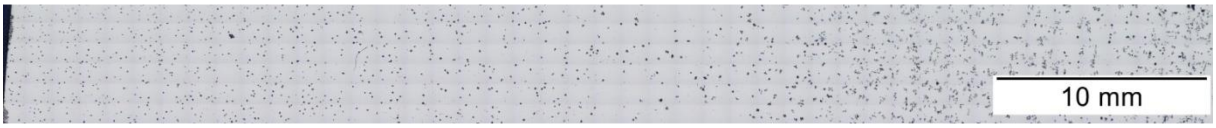

Figure 64 : Optical microscope figure at 5x of the general view of the N6 sample.

All the following figures are taken at 5-6 mm from the upper part of the sample.

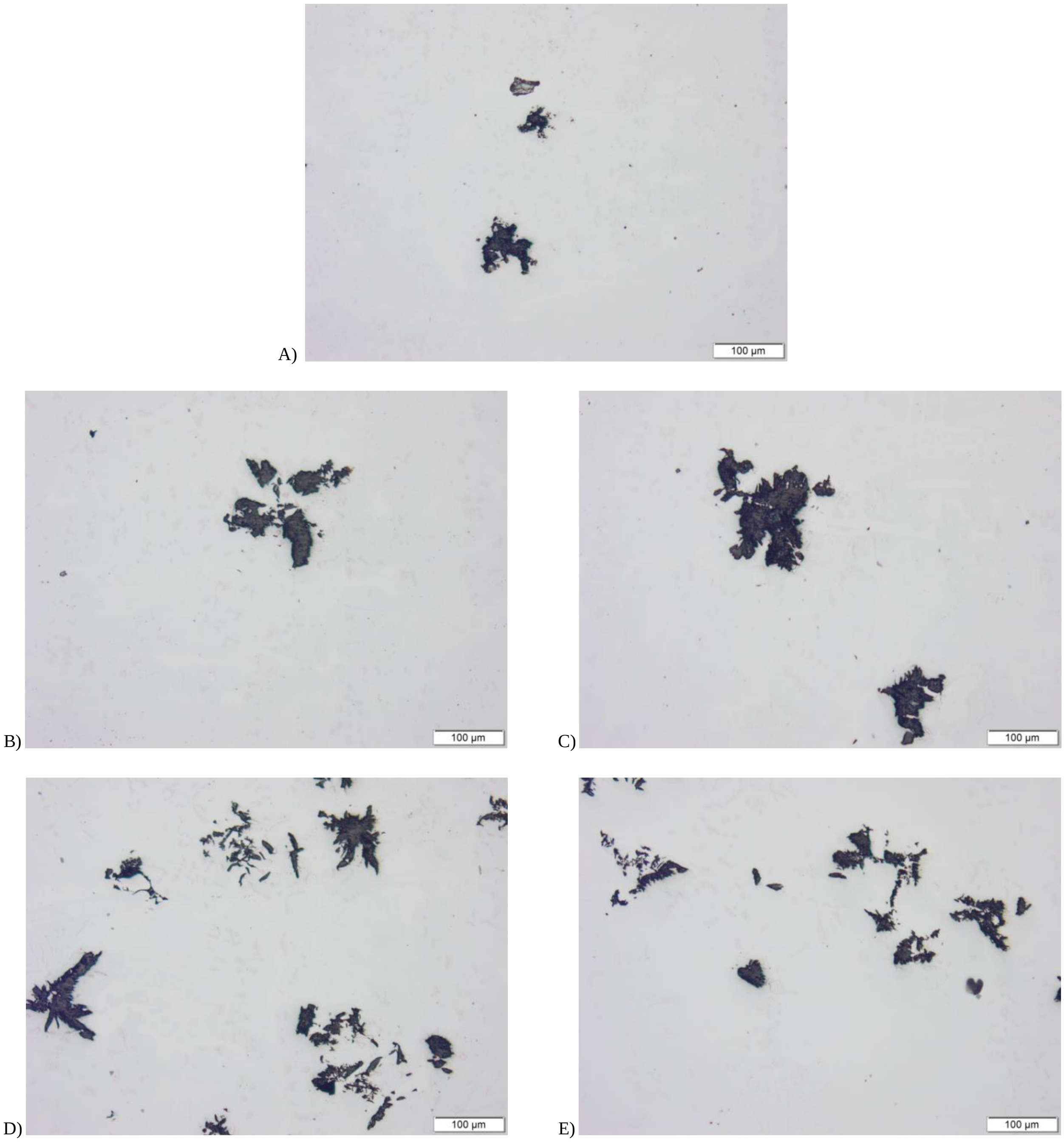

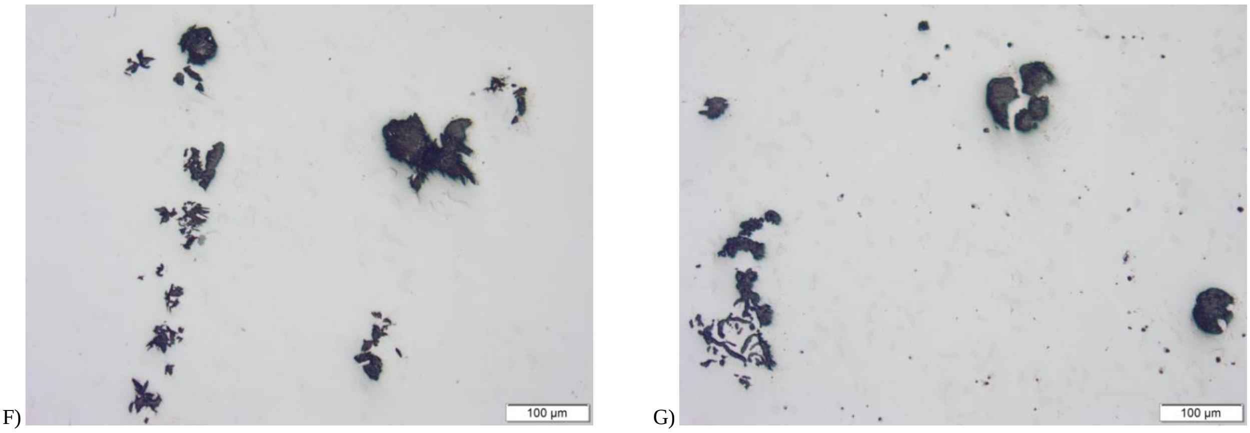

Figure 65 : Optical microscope figure at 10x of the N6 at 9mm (A), 34mm (B), 37mm (C), 41mm (D), 49mm(E),56mm (F) and 58 mm (G) from the surface.

6.2.4. DTA samples and Dilatometer samples

Several DTA samples and two dilatometer samples were analyzed with the optical microscope after the respective tests to check the phase formation or transformations and to have a better idea of the possible phenomena present during the tests. In the Figure 39 it is possible to see the samples in a normal picture and the following pictures show a general view of the samples in different magnitude.

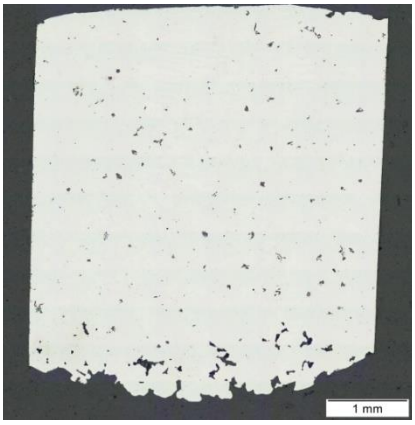

Figure 66 : Optical microscope figure at 10x of the general view of the DTX1 sample.

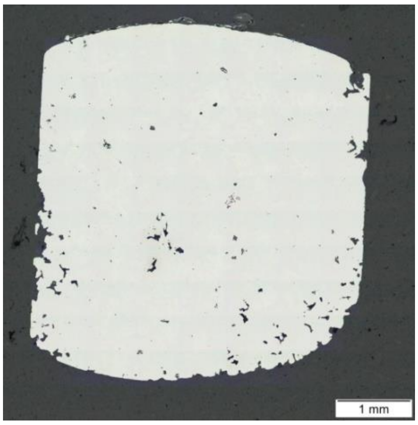

Figure 67 : Optical microscope figure at 10x of the general view of the DTX2 sample.

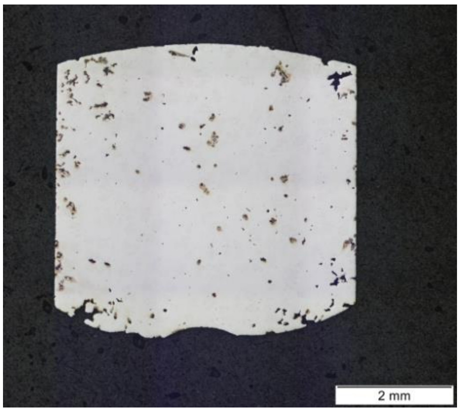

Figure 68 : Optical microscope figure at 2.5x of the general view of the DTX4 sample.

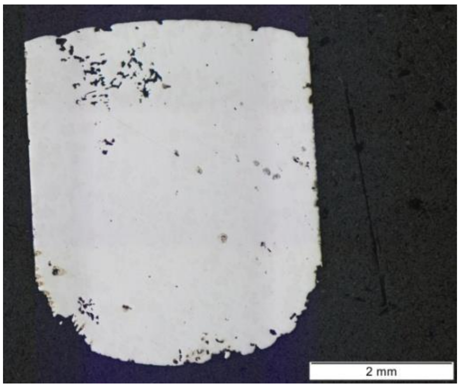

Figure 69 : Optical microscope figure at 2.5x of the general view of the DTX7 sample.

Figure 70 : Optical microscope figure at 5x of the general view of the XD1 dilatometer sample.

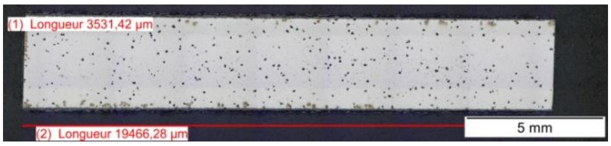

Figure 71 : Optical microscope figure at 2.5x of the general view of the XD2 dilatometer sample.

6.2.5. Optical microscope analyses observation

In the optical microscope analyses it is possible to note that the evolution of the graphite shape is palpable; in all the samples the first 40mm have a continuous shape change but the nodules look like almost spheroidal, in the as-cast conditions sample it is less marked because its thermal history is shorter thus it is better make arguments on it. As it is possible to see in the Figure 61 the image (B) has at 34mm keep to be almost spheroidal but with evident branches and in the image (C) the difference with a normal spheroidal nodule increase; in the images (D) and (E) the graphite looks none spheroidal and looks like more vermicular but keep to stay in a local zone until the 55mm from the surface (image F) where the graphite appears with various shapes due to the contact between shell material and core material.

As it is possible to note in the X sample (Figure 55) and in the N (Figure 59) the connection line between core and shell is inclined because the sample is not taken parallel to the surface, thus the distance of the graphite shape changes are relative and to make a comparison it is necessary to observe in a range of almost 4mm. In fact in the Figure 63 and the Figure 65 for the same distance to the surface the shape is not the same, due to the different thermal history and to this reason; in all the samples it is present almost 10mm of strange graphite shape zone near the core anyway. The graphite shape is analyzed more in the depth in the chapter 6.3 with the Stream Motion Analyses.

In the Figure 58 about the reaustenitizated sample it is possible to see the same evolution of all the samples but it is more evident a connection zone of 1-2mm between the graphite strange shape zone and the core.

For the DTA samples it is relevant to observe the presence of some black spots in different positions of the samples, for evidence in the Figure 68 about the DTX4 sample the spots are in the bottom part of the sample, meanwhile in the Figure 69 about the DTX7 are in the upper part of the sample. Those are investigated more into the depth in the subchapter 6.5.1.2 about the SEM analyses. After the DTA tests the graphite presence was observed, unlike the Composition 0 but in the latter case the sample was observed in the plane xy and in this study on the xz; thus probably the graphite was present also in the previous study since in the upper part of the DTX7 sample the graphite is not present.

In the Figure 70 and the Figure 71 the Dilatometer samples are shown but the optical microscope analyses do not observe relevant changes in the microstructure except for a possible layer of oxide that it is shown in the Figure 131. The microscope analyses of those samples are showed with the SEM in the subchapter 6.5.1.3.

6.3. Quantification and Stream Motion analyses

The Stream Motion software was used to quantify the graphite amount and analyze the optical microscope figures. The graphite amount was quantified in general in all samples and a more complex study was done on the evolution of the graphite shape and quantity during the increasing of the depth. In the Table 15 the amount of graphite in the old sample is reported:

%	10	25	40
Graphite	0,63	0,39	1,05
Graphite average		0,69	

Table 15 : Graphite amount of the old sample in the three different depths with the average value.

The quantification is referred to the sample in the Figure 38 and the maximum possible peak in Thermo-calc results was at 5 % (600°C). The Composition 1 pieces are divided in three samples to be analyzed; whereas the Composition 2 samples are analyzed entirely.

The graphite amount of all the other samples was analyzed with an intensity of 120 and with a particle surface minimum value of 1.5 µm²; the results are reported in the Table 16 and Table 17 for the two different compositions:

%	X1	X2	X3
Graphite amount	1,59	1,77	4,6
Graphite average amount		2,65	
	R1.1	R1.2	R1.3
Graphite amount	1,83	2,68	10,02
Graphite average amount		4,84	

Table 16: Graphite amount and graphite average amount from the quantification in the Composition 1 samples.

The complete R1 sample is longer than the complete X of 10mm so this quantification can be only an indication of the amount. The maximum possible peak for the Composition 1 in Thermo-calc results was at 6 % (600°C) that is higher than the previous and correctly the real quantification is lower than this value.

%	N0	N1	N6
Graphite amount	4,28	2,17	2,07

Table 17: Quantification value of the graphite amount in the Composition 2 samples.

Also here the Industrial as-cast conditions sample is longer that the other samples of almost 10mm and can be considered only an indication. To analyze the real amount into the depth the Stream Motion software was used to analyze and count every single graphite particles; they were numbered and organized based on their position. For every millimeters of the depth mean value of the graphite amount and mean value of the graphite sfericity were done; the results are shown in the following graphs. For the sfericity amount the deviation standard is reported because is high but not enough to disturb the observation on the graphs, instead for the surface amount it is not reported because it is not simple to understand the evolution. A high deviation standard is normal in a similar case because the graphite particles can have a huge dimension differences also in the same area. To have a lower deviation standard it is necessary to use a higher magnitude.

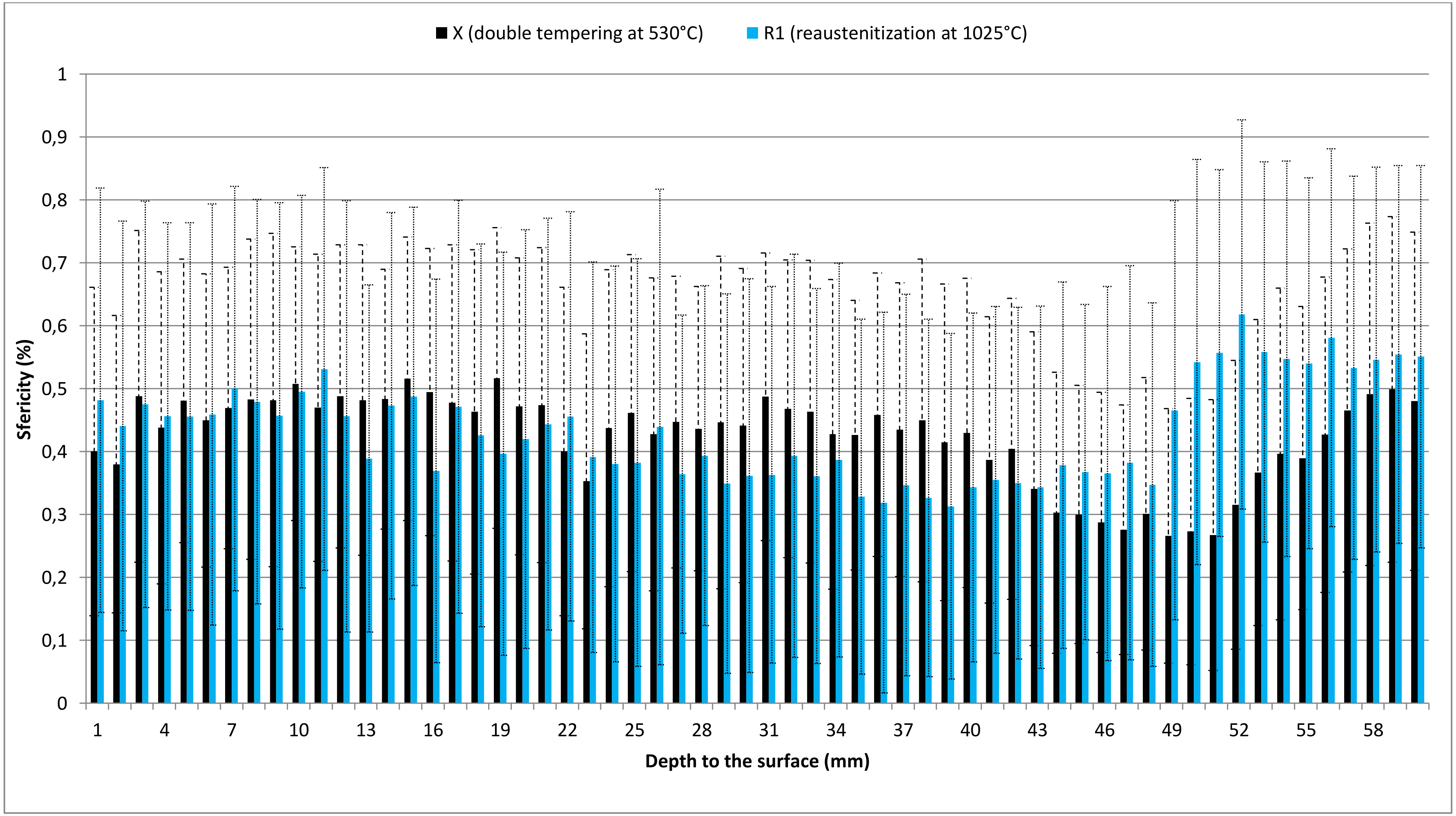

Figure 72 : Graphite sfericity evolution during the depth of the Composition 1 samples.

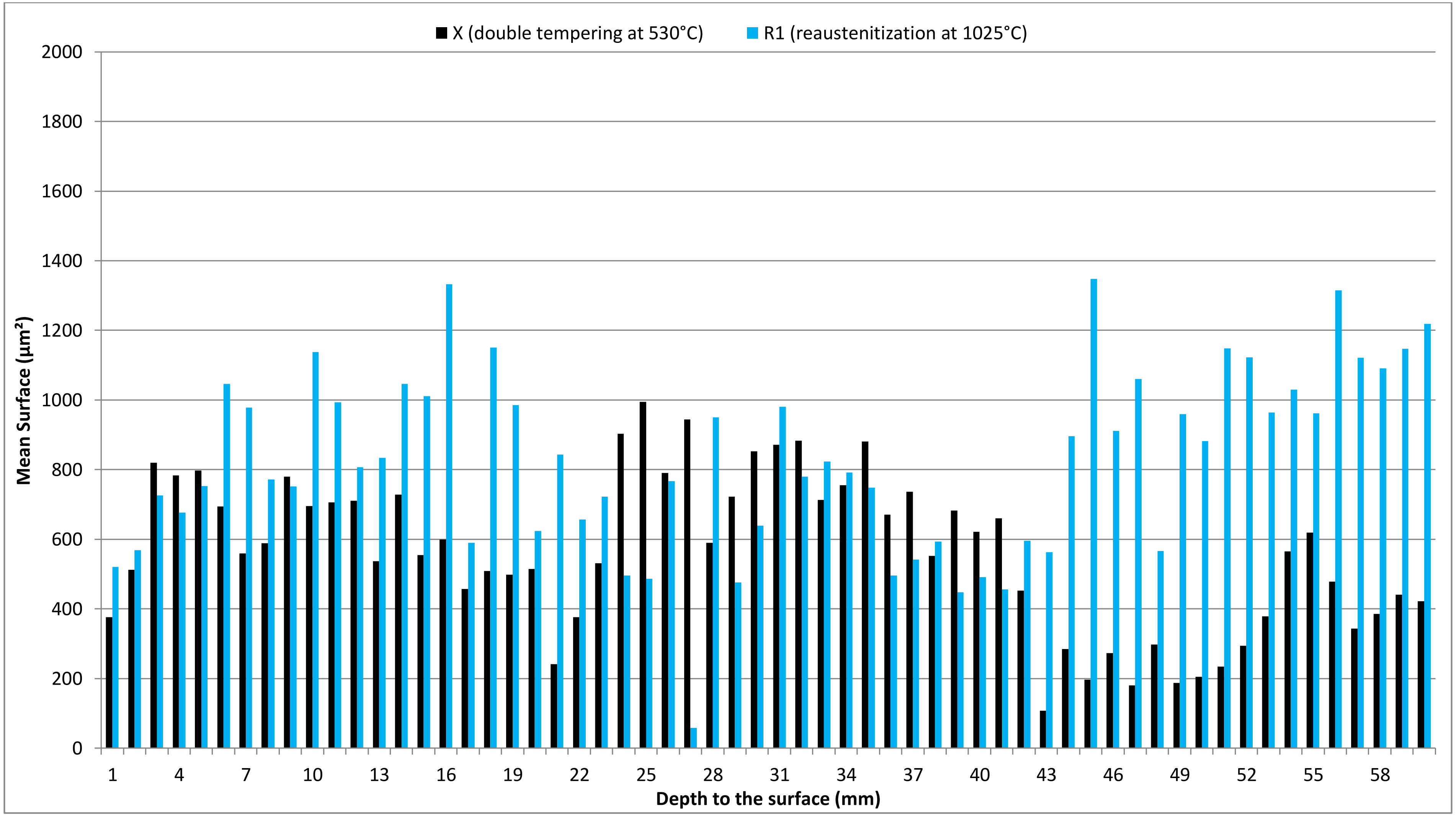

Figure 73 : Graphite amount evolution during the depth of the Composition 1 samples.

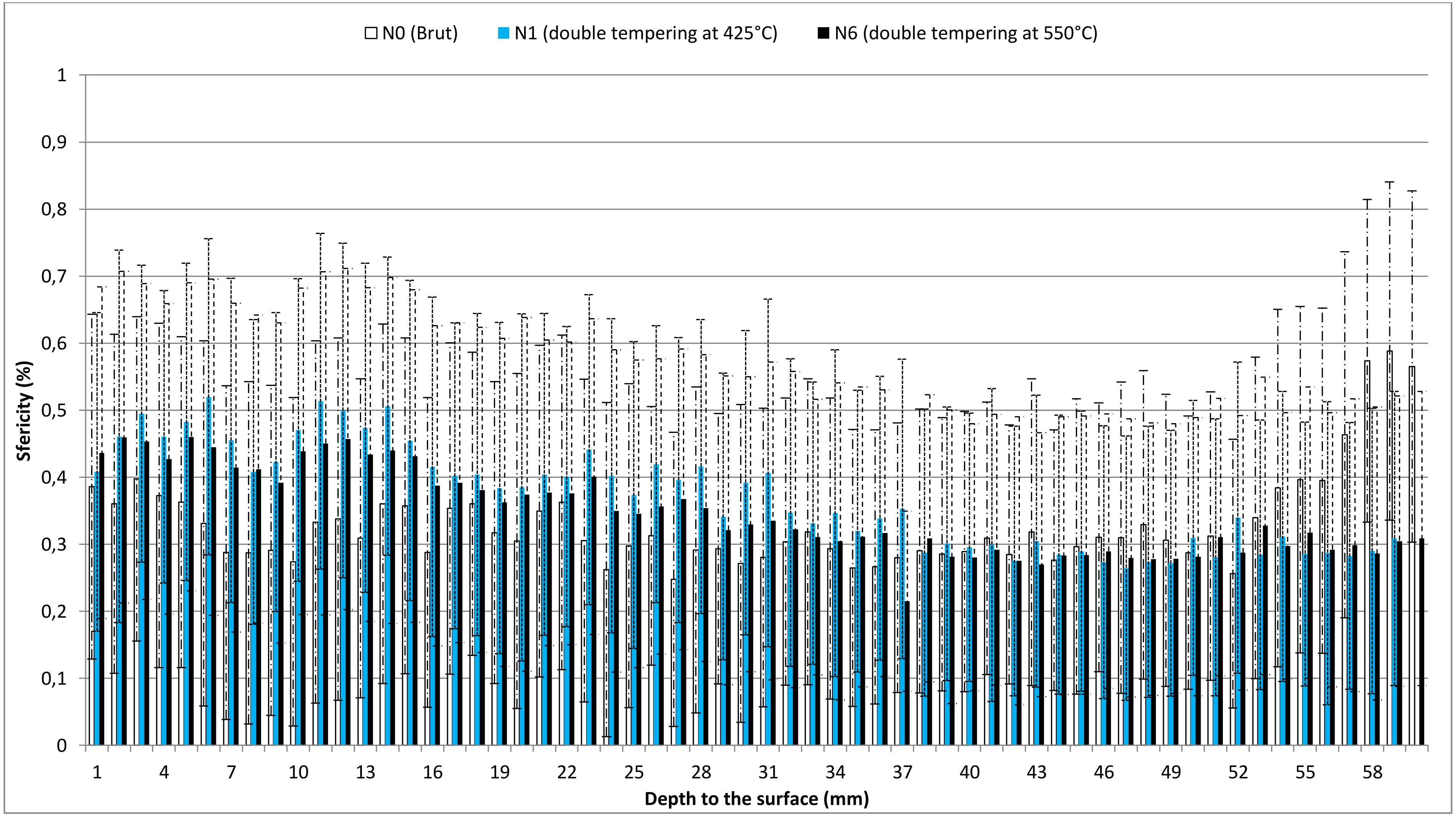

Figure 74 : Graphite sfericity evolution during the depth of the Composition 2 samples.

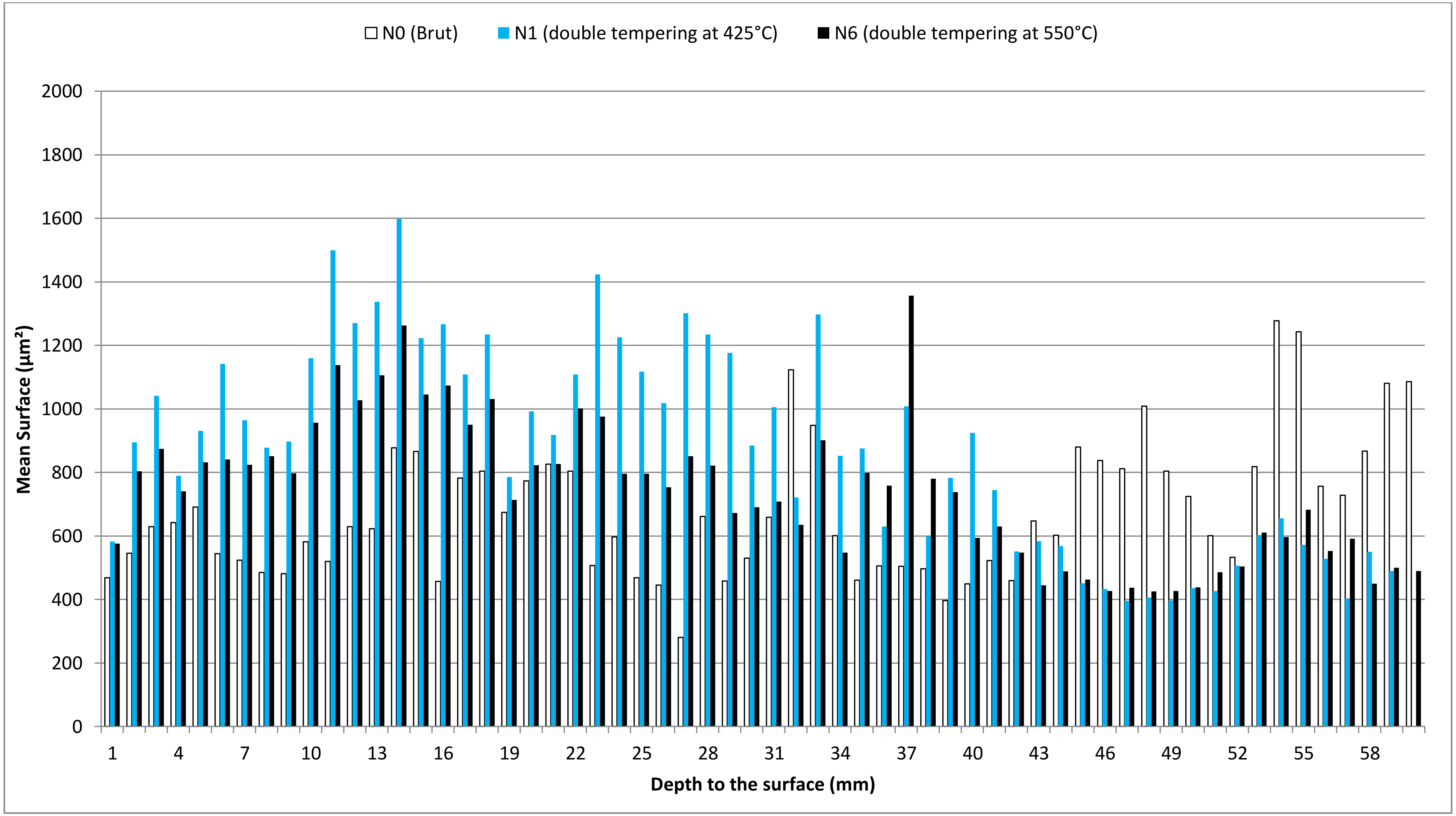

Figure 75 : Graphite amount evolution during the depth of the Composition 2 samples.

6.3.1. Stream Motion analyses observations

In both samples it is possible to see that the value dispersion is very high due to the high size difference between the graphite particles and due to the magnitude used; the first problem exists especially for the surface amount because the sfericity is not influenced by it, whereas the magnitude conditions both the surveys. The magnitude 5x was chosen because it is enough precise to give good results and explain the tendency of the samples without the use of very heavy figures. The magnitude 10x was tried but it was unmanageable to study and examine. Having a local idea of the shape and amount of the graphite in a material like that is relatively useful because in every depth many variables can give different results, thus it is better to understand it have a general idea as shown in the graphs. The single sample can give the general idea of its evolution in the depth and with similar samples (like the three N samples) it is possible to check the consequences of the various thermal treatments on the graphite, but it is important to underline that all the samples are different because the material is not homogeneous in the depth, for the casting process.

In the X samples case it is possible to see the effect of the reaustenitization at 1025°C for 1h on the R1 sample; the graphite sfericity in the first 22mm from the surface does not change with the treatment after the double tempering, whilst in the range 22-40mm the X sample has a higher value and in the end part (40-60mm) the R1 sample has the higher value. The graphite amount is everywhere higher in the R1 except for the center part (22-43mm) where the value is at least the same in both samples. In the Figure 72 it is shown that the starting of the core is at least in the point 50mm from the surface. In the N samples it is possible to see the effects of the two different double tempering on the as casted sample (N0); in the first 34mm the graphite sfericity is higher for both the tempering in comparison with the Industrial as-cast conditions, the center zone is not influenced by the treatment and in the part considered the start of the core (52-60) the N0 sample has higher value. The N1 and N6 samples have the same behavior, but the first one has in almost every position higher value. In the surface amount the N0 has lower amount in every depth except for the range 44-60mm; here the N1 has higher value from the surface to 35mm and at higher depth the N6 has superior surface amount.

6.4. DTA tests

Seven DTA tests were taken to study the phase presences and transformations. DTA tests were taken on the X1 sample, X2 sample, X4 sample and X5 starting from room temperature to 1300°C with a heating rate of 5°C/min, and then they were cooled with the same rate; in the case of X6 sample and X7 starting DTA tests were taken from room temperature to 1450°C with a heating rate of 5°C/min, and then they were cooled with the same rate. An additional DTA test was also taken on X1 to study its heating curve in the range of temperature 900-1100°C because there are two peaks about the possible destabilization of the eutectic carbides. The final temperature choice was a consequence of the Thermo-calc analysis (Table 14) because the simulated Liquidus temperature is at 1251 °C and thus it was taken 1300°C as the maximum temperature to have the complete melting. It was taken 1450°C as the maximum temperature for the next tests to evaluate the real casting conditions. In the heating spectra all the main peaks are endothermic and they can be a destabilization, decomposition and fusion; whereas in the cooling spectra all the peaks can be a precipitation, transformation or euctetic reaction.

6.4.1. Sample reheated and remelted up to 1300°C

6.4.1.1. Heating curves

In the heating curves it is possible to see the real presence of the phases in the material because with the remelting due to the DTA test there are some diffusion phenomena and transformations that give usually a lower number of peaks. The heating curve advantage is unfortunately also the problem because in general some peaks are not clear to see and with more peaks the understanding is more difficult. The peaks are difficult to see because often some of they are very close also. In the Figure 76 the DTA heating curves of all the samples are reported in the same graph and in the Table 18 the temperature ranges are reported with a possible peaks explanation. [17, 18]

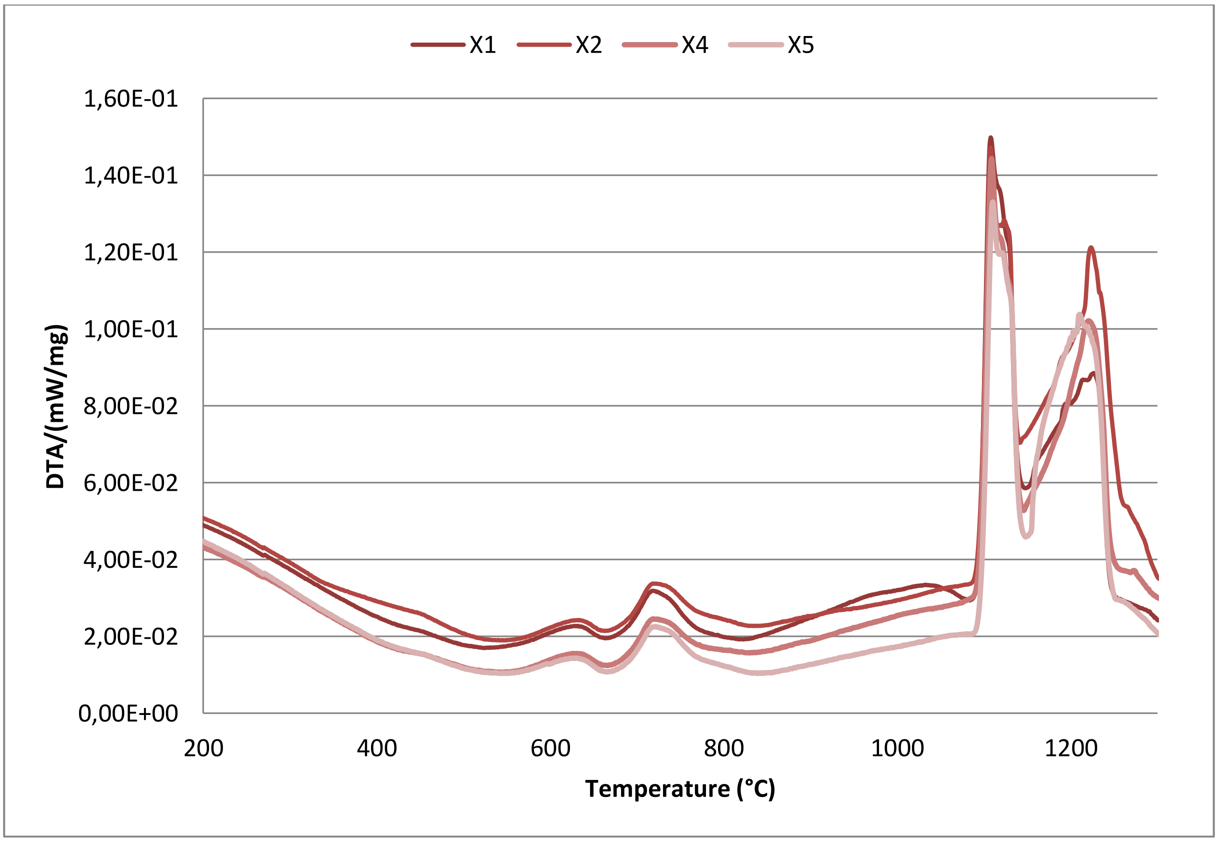

Figure 76 : DTA heating curves about the X1, X2, X4 and X5 samples in the range of temperature 200-1300°C

	Range of temperature				
Peaks	X1	X2	X4	X5	Reaction or transformation of phase
H1	410-460	?-451	429-456	429-456	Destabilization of the residual austenite
H2	550-630	568-635	562-635	562-635	Martensite decomposition
H3	688-721	672-721	678-723	678-723	Ac_1 ; allotropic transformation of the austenite
H4	?-733	?-737	?-738	?-737	Ac_3 ; end of the austenite transformation
H4’	?-794	?-805	?-805	?-804	Dissolution of carbides from martensite decomposition or matrix supersaturation
H5	850-973	?-933	865-893	?-977	Destabilization of the first eutectic M_2C carbide
H5’	?-1034	?-1052	?-1036	?-1067	Destabilization of the second eutectic M_7C_3 carbide
H6	1090-1108	1091-1108	1096-1108	1098-1110	SOLIDUS; direct fusion of the M_2C carbide (first eutectic)
H7	?-1118	1117-1119	?-1119	1118-1120	Graphite
H8	?-1129	?-1130	?-1130	?-1130	direct fusion of the M_7C_3 carbide (second eutectic)
H9	1154-1162	1142-1144	?-1150	?	direct fusion of the MC primary carbide (NbC)
H10	1189-1193	1186-1192	?-1208 Slope change	?	direct fusion of the MC eutectic carbide (third eutectic)
H11	?-1213	1217-1223	1213-1218	?-1218	Direct fusion of austenite
H12	1221-1226	1233-1234	?-1228	?-1226	LIQUIDUS ; Direct fusion of MC primary carbide

Table 18 : Temperature ranges relative to the heating peaks and the possible explanations

6.4.1.2. Cooling curves

The cooling curves are the considered the most accurate about the phase presences and the number of peaks is lower. In the Figure 77 DTA heating curves of all the samples are reported in the same graph and in the Table 19 the temperature ranges are reported with a possible peaks explanation. [17, 18]

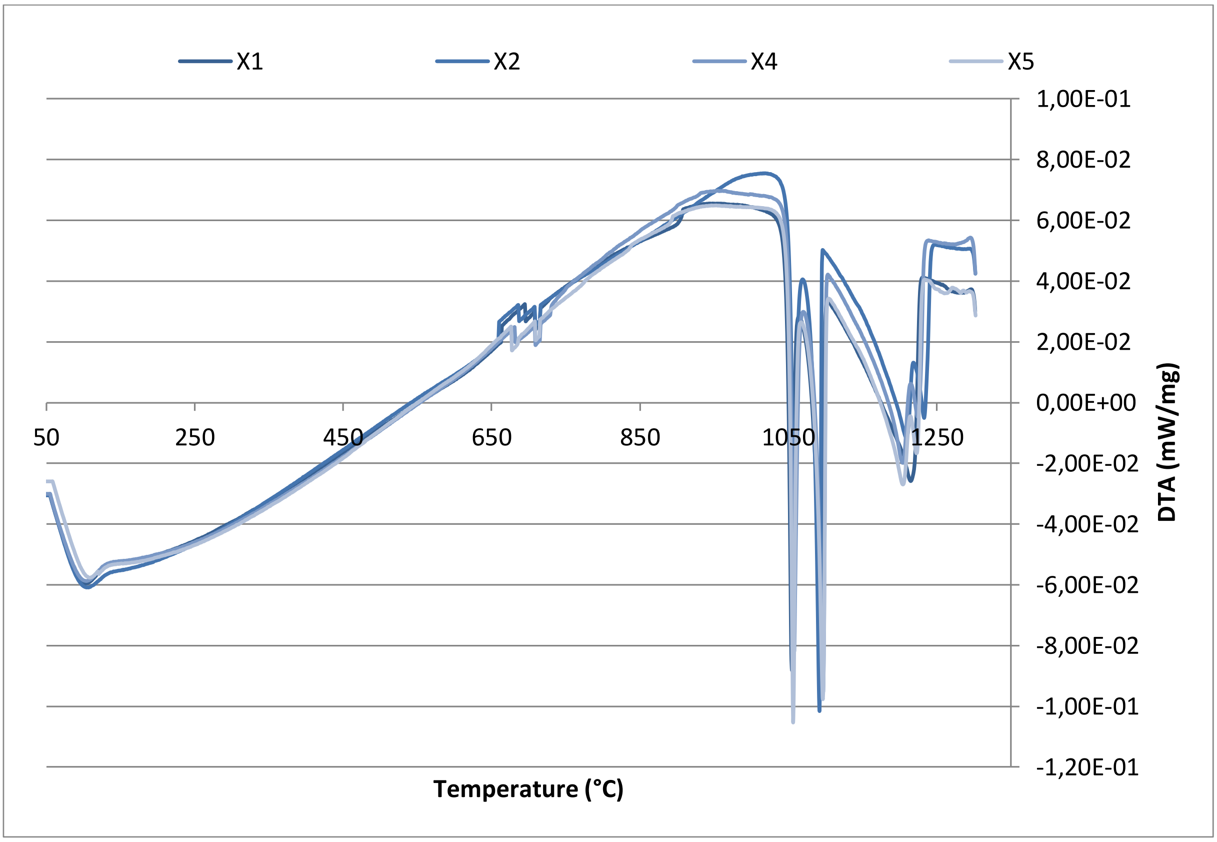

Figure 77 : DTA cooling curves about the X1, X2, X4 and X5 samples in the range of temperature 50-1300°C

	Range of temperature				
Peaks	X1	X2	X4	X5	Reaction or transformation of phase
C1	1298-1280	1296-1283	1295-1276	1296-1261 Complex!	LIQUIDUS ; direct precipitation of MC primary carbide (first type)
C2	1227-1218	1242-1233	1234-1224	1230-1223	Formation austenite γ
C3	?-1214 (complex peak) 1207-1202	?-1209 1201-1198	?-1204 1198-1196	?-1205 1197-1194	Eutectic reaction with formation of MC eutectic carbides (second type)
C4	1105-1094	1097-1092	1101-1096	1101-1096	Eutectic reaction with the formation of M_7C_3
C5	?-1054	?-1058	?-1058	?-1056	SOLIDUS; Eutectic reaction with the formation of M_2C + Graphite formation
C6	909?	/	/	895-?	Continuous changing of the composition with precipitation inside the grains by the carbides M_xC_y, probably $M_{23}C_7$
C6’	726 710 696	/ 710 687	749 710 682	776 710 678	Artifacts due to gas under the sample
C7	131-105	137-109	126-104	?-108 + Disturb	Martensitic transformation

Table 19 : Temperature ranges relative to the cooling peaks and the possible explanations

6.4.2. Sample submitted to a three steps reheating cycle

To check better the presence of the secondary carbides and the possible eutectic carbides destabilization, a DTA test with three steps was performed (all the steps are with a heating rate of 5°C/min):

- heating up to 920°C (under the first peak) and cooling to 25°C
- heating up to 1000°C (in the middle between the two peaks) and cooling to 25°C
- heating up to 1060°C (between the melting temperature and the second peak) and cooling to 25°C

6.4.2.1. Heating curves

In the Figure 78 the heating curves about three steps reheating cycle test are reported and in the Table **20** there are possible explanations for the peaks in the range of temperature [2]:

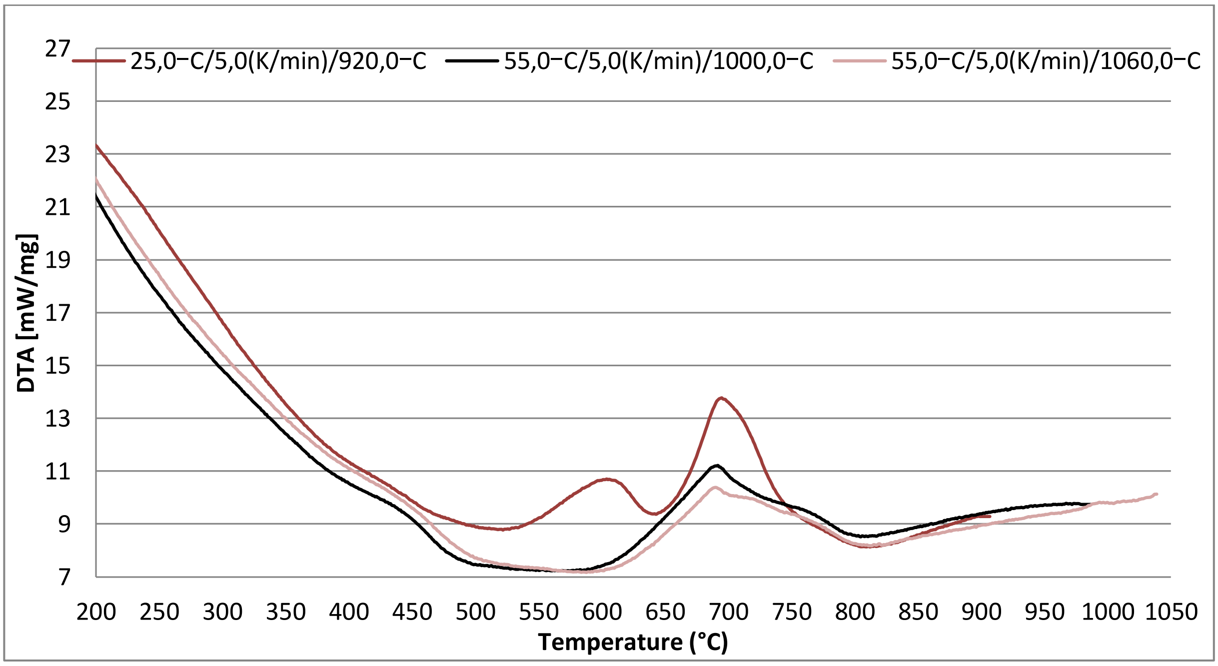

Figure 78 : Heating curves relative to the sample submitted to a three steps reheating cycle in the range of temperature 200-1050°C

	Range of temperature			
Peaks	Step 1	Step 2	Step 3	Reaction or transformation of phase
H1	?-445	392-436	?-438	Destabilization of the residual austenite
H2	540-606			Martensite decomposition
H3	651-696	619-693	619-692	Ac_1 ; allotropic transformation of the austenite
H4	?-710	/	?-726	Ac_3 ; end of the austenite transformation
H4'		?-762	?-766	Dissolution of carbides from martensite decomposition or matrix supersaturation
H5			?-996	Destabilization of the first eutectic M_2C carbide

Table 20 : Temperature ranges relative to the heating peaks and the possible explanations

6.4.2.2. Cooling curves

In the Figure 79 cooling curves about the three heating steps test are reported and in the Table 21 possible explanation are reported in the range of temperature:

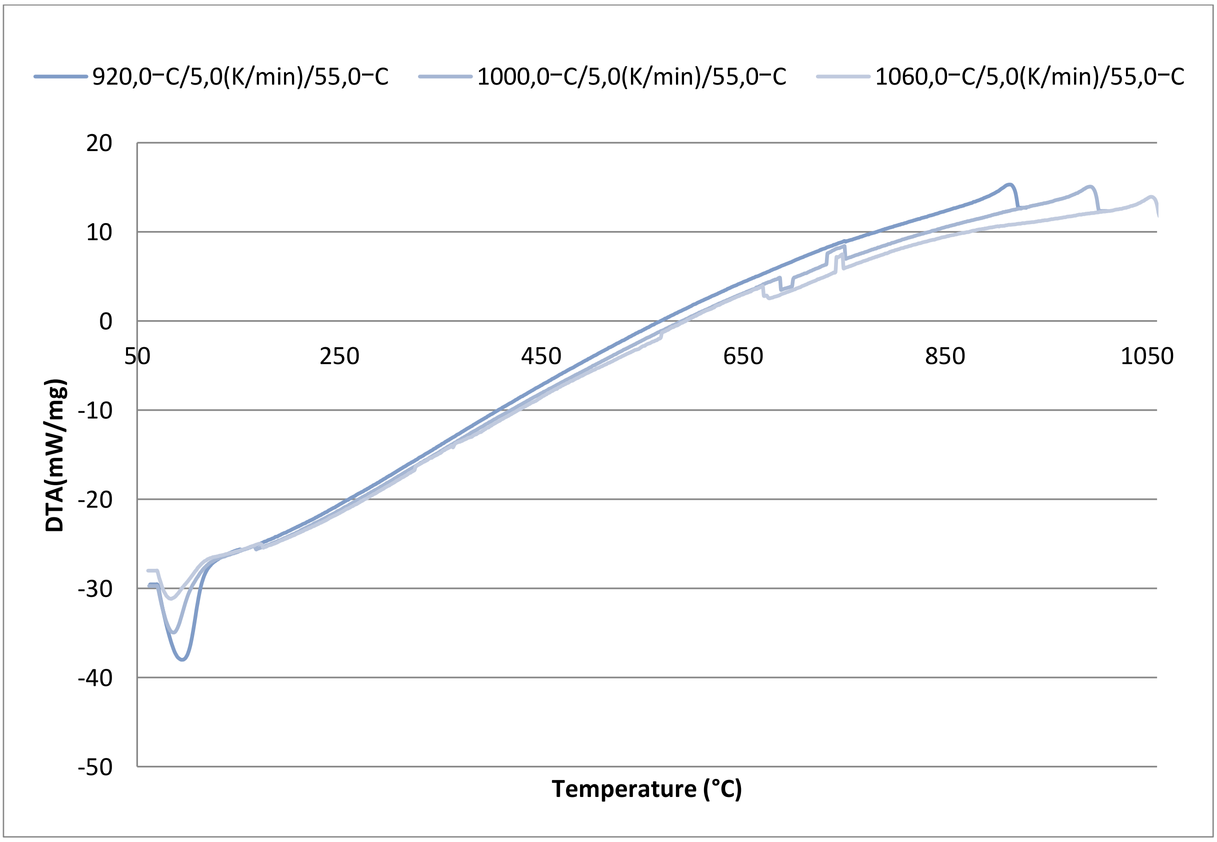

Figure 79 : Cooling curves relative to the Sample submitted to a three steps reheating cycle in the range of temperature 50-1060°C

	Range of temperature			
Peaks	Step 1	Step 2	Step 3	Reaction or transformation of phase
C6	/	/	/	Continuous changing of the composition with precipitation inside the grains by the carbides M_xC_y, probably $M_{23}C_7$
C6'	/	725 660 144	725 644 548 151	Artifacts due to gas under the sample
C7	98-75	95-66	94-65	Martensitic transformation

Table 21 : Temperature ranges relative to the cooling peaks and the possible explanations

6.4.3. Sample reheated and remelted up to 1450°C

To evaluate the real casting conditions, 1450°C was taken as a maximum temperature for the next tests. [17, 18]

6.4.3.1. Heating curves

In the Figure 80 heating curves about X6 and X7 samples are reported and in Table 22 there are possible explanations:

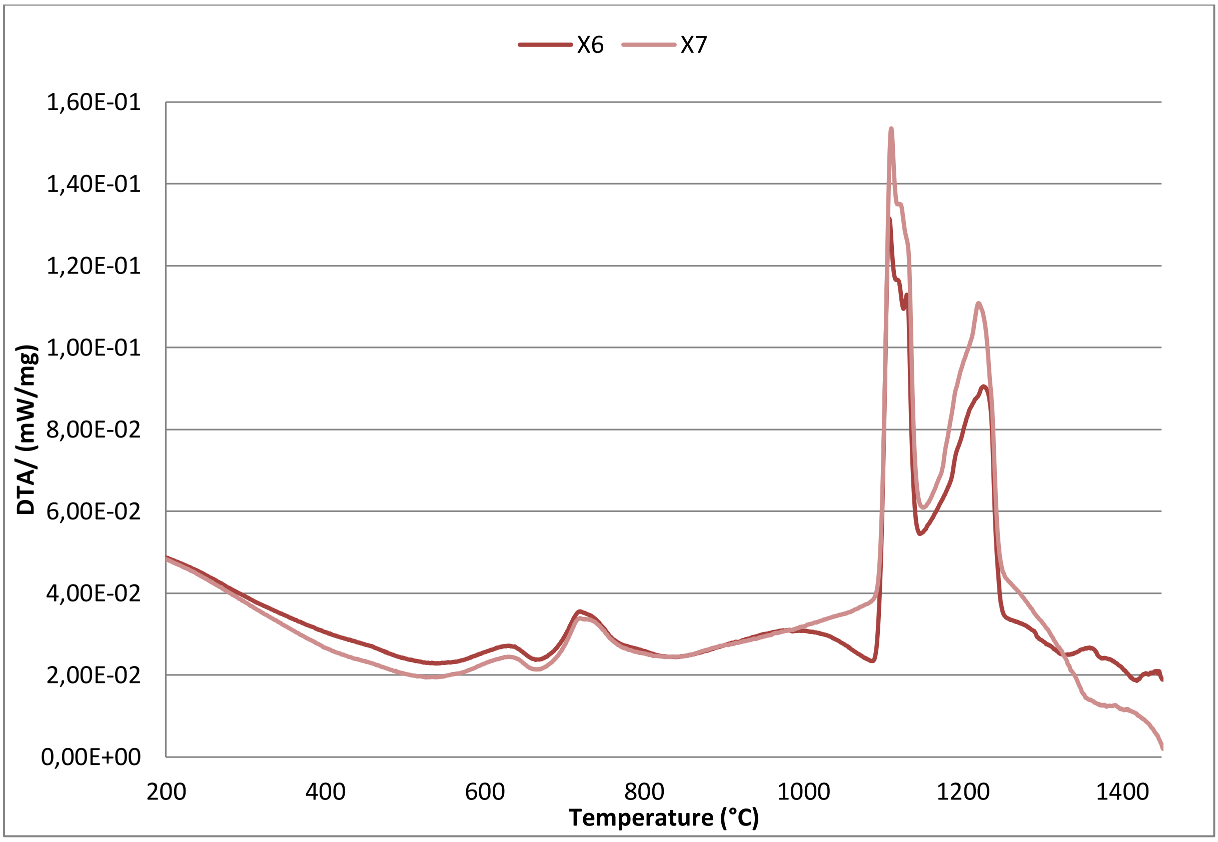

Figure 80 : DTA heating curves about the X6 and X7 samples in the range of temperature 200-1450°C

	Range of temperature		
Peaks	X6	X7	Reaction or transformation of phase
H1	?-460	?-453	Destabilization of the residual austenite
H2	550-636	558-634	Martensite decomposition
H3	681-722	678-722	Ac_1 ; allotropic transformation of the austenite
H4	?-734	?-733	Ac_3 ; end of the austenite transformation
H4’	?-791	?-801	Dissolution of carbides from martensite decomposition or matrix supersaturation
H5	?-981		Destabilization of the first eutectic M_2C carbide
H5’			Destabilization of the first eutectic M_7C_3 carbide
H6	1095-1109	1096-1110	SOLIDUS; direct fusion of the M_2C carbide (first eutectic)
H7	?-1120	?-1122	Graphite
H8	1128-1131	?-1131	direct fusion of the M_7C_3 carbide (second eutectic)
H9	?-1156	?-1156	direct fusion of the MC primary carbide (NbC)
H10	1188-1191	?-1192	direct fusion of the MC eutectic carbide (third eutectic)
H11	1221-1223	1213-1219	Direct fusion of austenite
H12	?-1229	?-1224	LIQUIDUS ; Direct fusion of MC primary carbide

Table 22 : Temperature ranges relative to the heating peaks and the possible explanations

6.4.3.2. *Cooling curves*

In the Figure 81 cooling curves about X6 and X7 samples are reported and in the Table 23 possible explanations are reported:

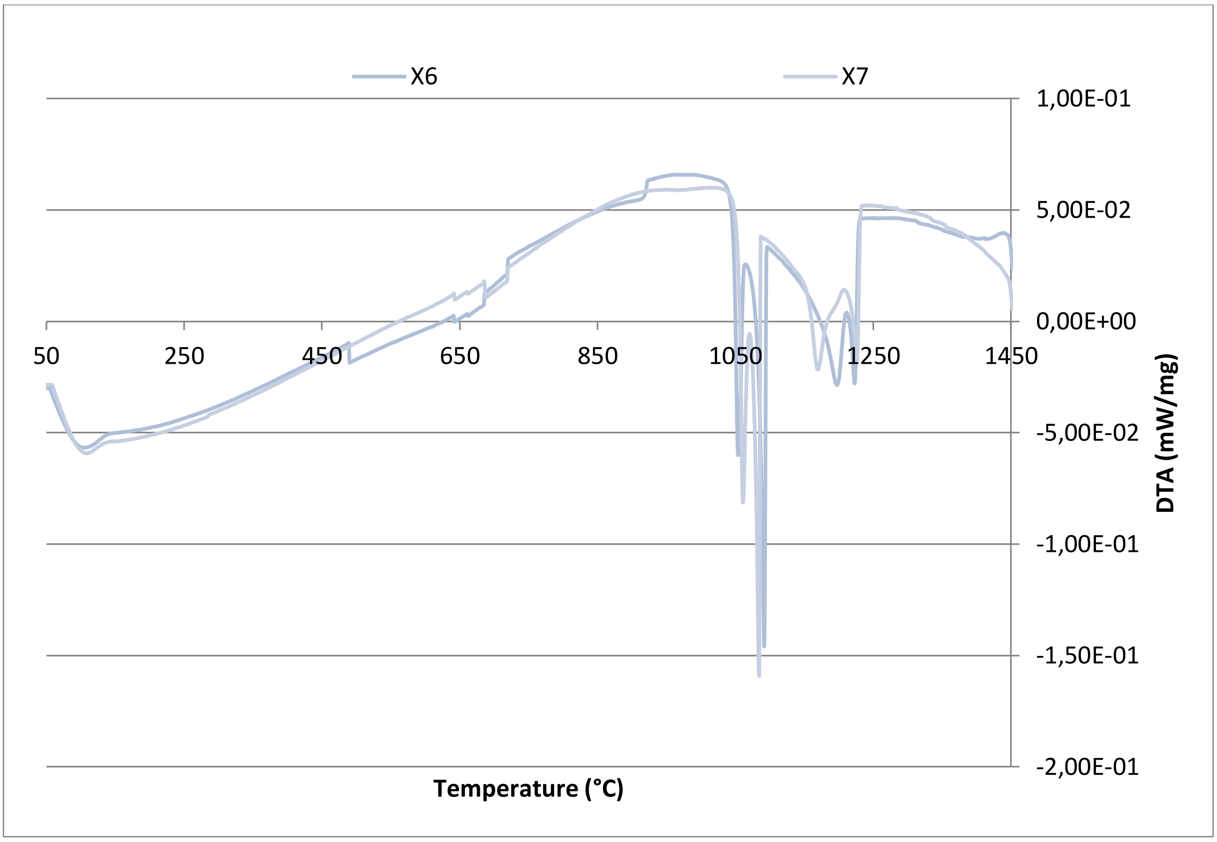

Figure 81 : DTA cooling curves about the X6 and X7 samples in the range of temperature 50-1450°C

			Range of temperature
Peaks	X6	X7	Reaction or transformation of phase
C1	1441-1415	/	LIQUIDUS ; direct precipitation of MC primary carbide (first type)
C2	1231-1223	1222-1214	Formation austenite γ
C3	1212-1198 1178	?-1158 1193-1182	Eutectic reaction with formation of MC eutectic carbides (second type)
C4	1096-1092	1075-1072	Eutectic reaction with the formation of M_7C_3
C5	?-1054	?-1049	SOLIDUS; Eutectic reaction with the formation of M_2C + Graphite formation
C6	923	/	Continuous changing of the composition with precipitation inside the grains by the carbides M_xC_y, probably $M_{23}C_7$
C6’	711 695	719 692	Artifacts due to gas under the sample
C7	146-109	128-100	Martensitic transformation

Table 23 : Temperature ranges relative to the cooling peaks and the possible explanations

6.5. SEM analyses

SEM analyses were done to Composition 1 samples and to Composition 2 sample (the Industrial as-cast conditions) to investigate about the microstructure and to search explanations of the other test results since the optical microscope is not able to recognize the different carbide and their compositions.

6.5.1. Composition 1

SEM Figures were taken on different types of sample of the Composition1: two normal samples that are shown in the Figure 32 (X1 and X2), four DTA samples (DTX1, DTX2, DTX4 and DTX7) and two Dilatometer samples (XD1 and XD2). The DTA samples and the Dilatometer samples are shown in the Figure 39.

6.5.1.1. Sample X1and X2

SEM analyses were done on X1 and X2 to check phase composition, morphology, solidification steps and the phase's amount. The analyses were done with the following outline:

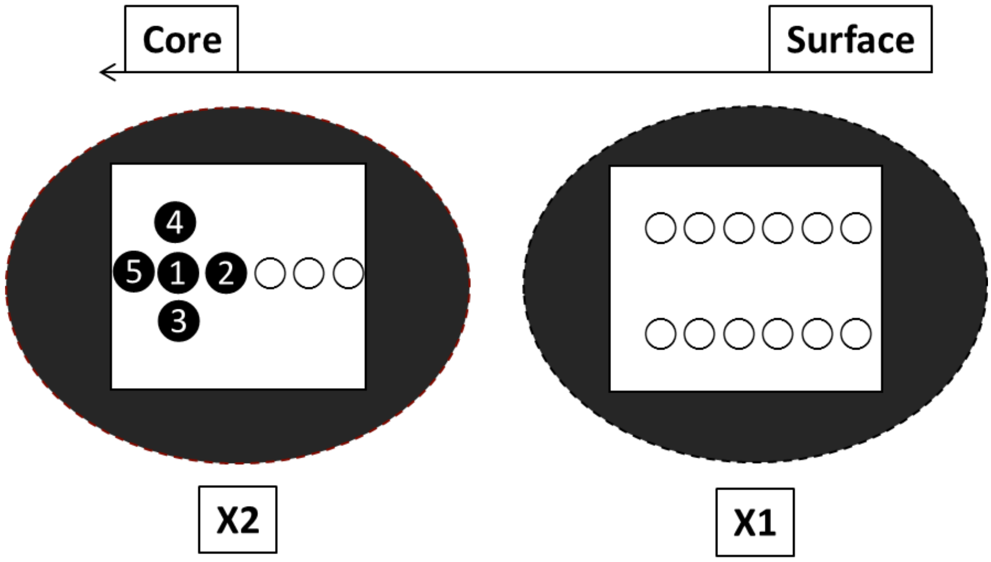

Figure 82: Explanation of the surveys, the sample on the left is the X2 sample (more near the core) and on the right there is the X1 sample (more near the surface). The position (0,0) is positioned in the center of the X1 sample and in the X2 sample is moved of 1mm on the left during the analyses.

In the X1 sample two lines of surveys were taken to have a more complete idea of the characteristics and in the X2 sample only one but with some grille surveys in the "strange shape graphite zone" to understand better the graphite morphology as shown in the Figure 116. The white circles are different zones examined and the numbered black circles are four grille surveys taken on the X2 sample. Every survey was taken 4mm far to another in length; the two normal surveys lines in the X1 sample are at 7mm one to the other in width as the grille surveys 4 and 3 in the X2 sample. The survey line in the X2 sample is in the middle of it and at 3.5 mm to the grille surveys 4 and 3. In the Figure 83 it is shown that in the entire X1 sample there is not an evident change of microstructure. It is possible to see in black the graphite particles, in different dark grey shade there are various carbides and matrix and in light grey M_2C carbides; the graphite is not totally spheroidal but with some branches.

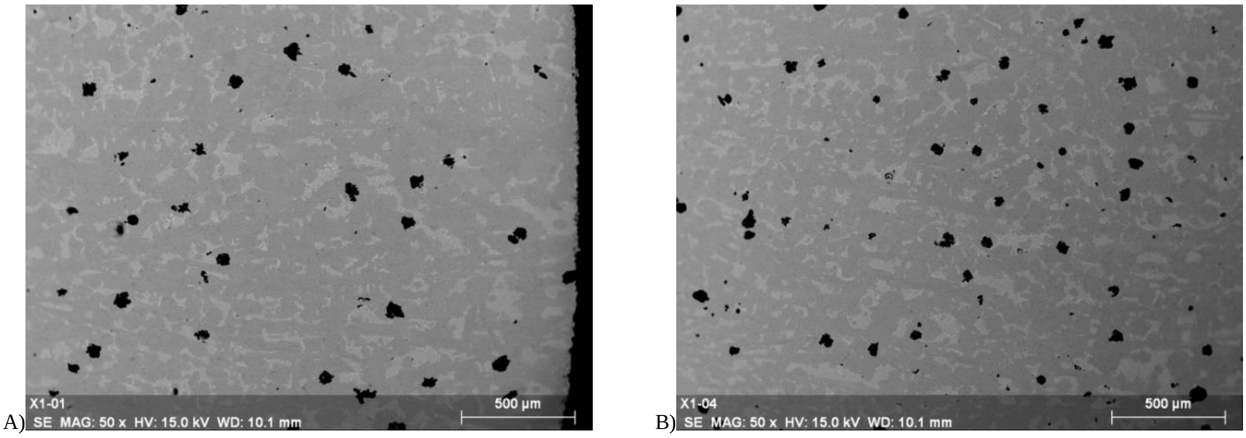

Figure 83 : A) SEM figure at 50x about the X1 sample in the position (10mm, 3.5mm) close to the surface; B) SEM figure at 50x about the X1 sample in the position (-2mm, 3.5mm).

6.5.1.1.1. Graphite observation

Three graphite particles are present in the following zoom; their shape is not spheroidal but looks like with a spheroidal shape base and some branches that go around the closest carbides.

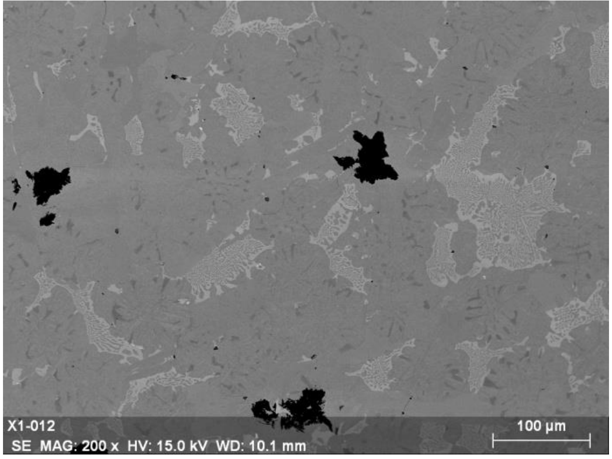

Figure 84: Zoom at 200x about the first analysis zone. There are three yellow circles to show where the graphite particles envelop the closest carbides

The graphite can be modified in the thermal history of the material, thus the double tempering at 530°C of the X sample may be able to modify the graphite morphology. In the Figure 85 X2 sample it was also analyzed the graphite shape evolution and using the grille surveys it was analyzed the influence of the silicon to the shape of the graphite as shown in the figure.

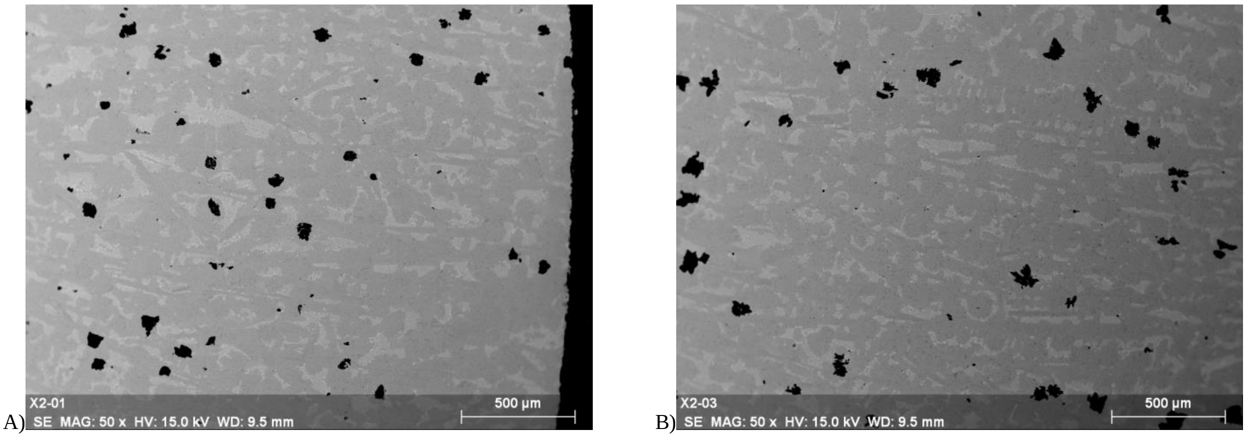

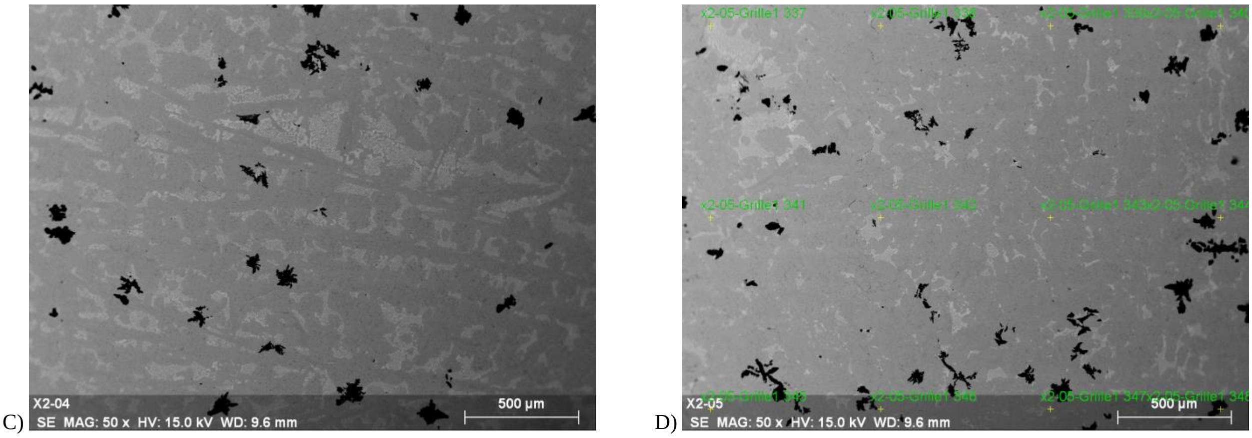

Figure 85 : A) SEM figure at 50x about the X2 sample in the position (8mm, 0mm) close to the surface; B) SEM figure at 50x about the X2 sample in the position (0mm, 0mm); C) SEM figure at 50x about the X2 sample in the position (-4mm, 0mm); D) SEM figure at 50x about the X2 sample in the position (-8mm, 0mm) with also the grille composition surveys.

It is important to note that from the figure (B) the graphite starts to have more and more different shape. Qualitatively it was observed that the graphite is usually near to a M_2C carbide (rich of silicon) and where there is a big M_2C carbide there is not a graphite presence (and the contrary). Probably they are formed together and from the same liquid; the factor that choose the formation of graphite or carbide is the ferritic-stabilizer elements local amount. Although the grille surveys were done some composition maps to understand better the graphite morphology in the “strange shape graphite zone”. In the Figure 86 it is possible to see the distribution of the silicon in the microstructure; the silicon presence is homogeneous in the entire matrix and in the M_2C carbides. This data was confirmed also with the grille analysis as shown in the Figure 87.

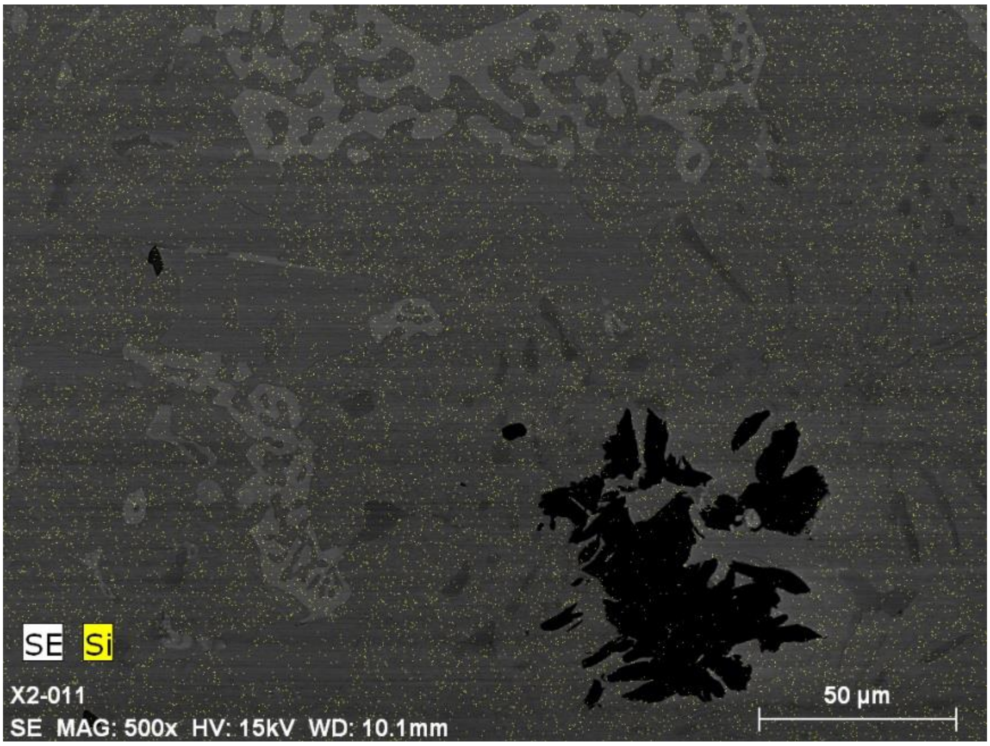

Figure 86: Composition map about the silicon presence zoom at 500x about the X2 sample; the yellow points are silicon.

The concentration of silicon is homogeneous and the elements with a little changing in the matrix composition are carbon and chromium. This analysis can say that the graphite shape is not influenced by some different local amount of silicon.

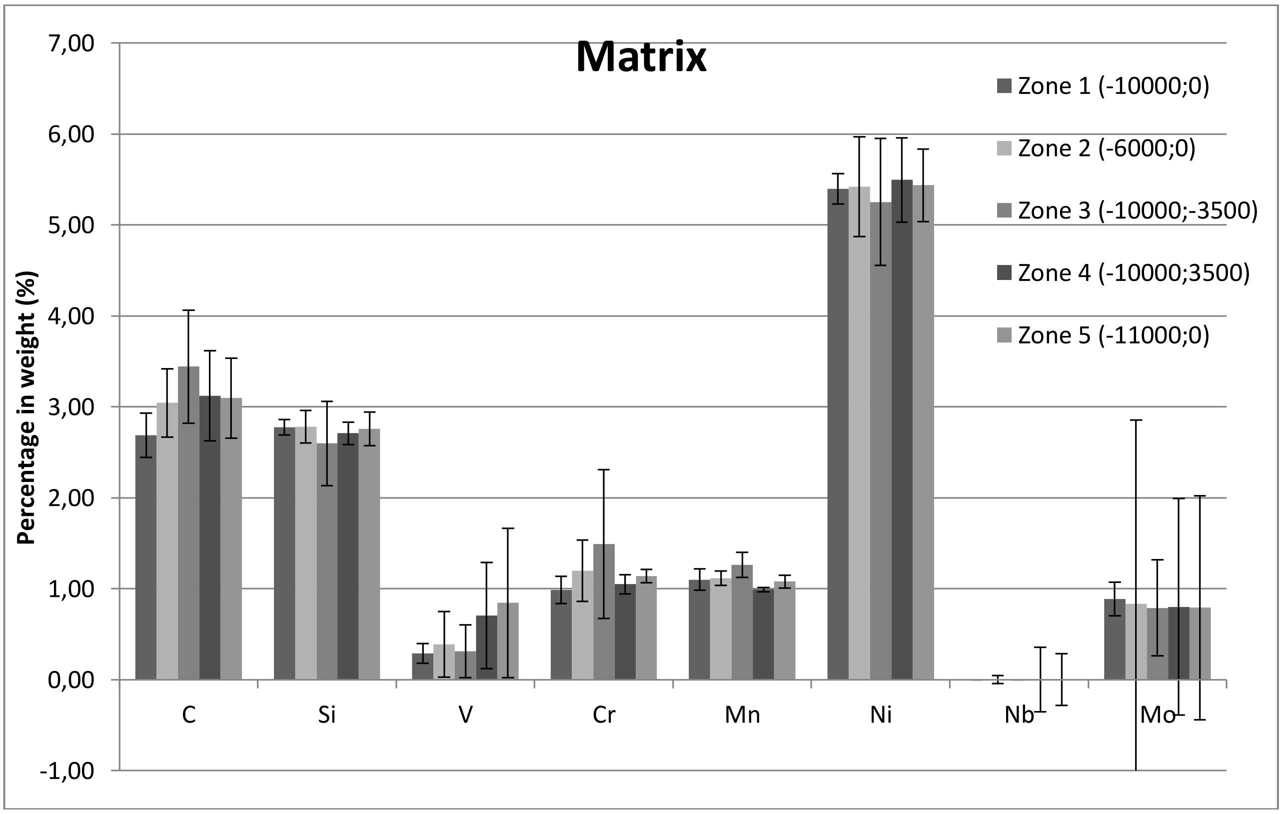

Figure 87 : Evolution of the percentage of the elements inside the matrix in five different zones of the X2 sample

It is important to note the high Nickel value because this can mean a high residual austenite amount, the aspect is considered with the Magnegage analyses.

6.5.1.1.2. Carbides observation: MC

The "X" sample structure was characterized analyzing all the carbides; they were divided in the different types, morphology and composition. The main categories are MC carbides, M_2C carbides and M_7C_3 carbides. The MC carbides in the microstructure are present in high amount with a lot of varieties and morphologies. In the Figure 88 all the different MC carbides are shown and in the Table 24 and all the compositions of the respective carbides are shown. The first MC carbides in the Table 24 are branched petallike MC carbides as shown in the Figure 8, in the second group are idiomorphic MC primary carbides as shown in the Figure 7 and the last two are MC primary carbides with morphology similar to a "raisin tige" characterized to a little percentage of titanium. The latter morphology was already observed in previous studies about a microstructure characterization on an ICDP; the composition was different in fact the niobium was the element more present and thus they were considered niobium MC carbides. Here they are considered VC carbides but there is a low amount of titanium that probably means the presence of slight titanium carbide (TiC) as in the previous observations. Those carbides are formed at high temperature and act as nuclei for the formation of other carbides, thus probably the MC "raisin tige" carbides or globular, as called in the previous study, are considered primary MC carbides. All the figures are taken in the X1 sample and to understand better the difference between the various types there is a zoom on it (Figure 88 D). [20, 21, 40]

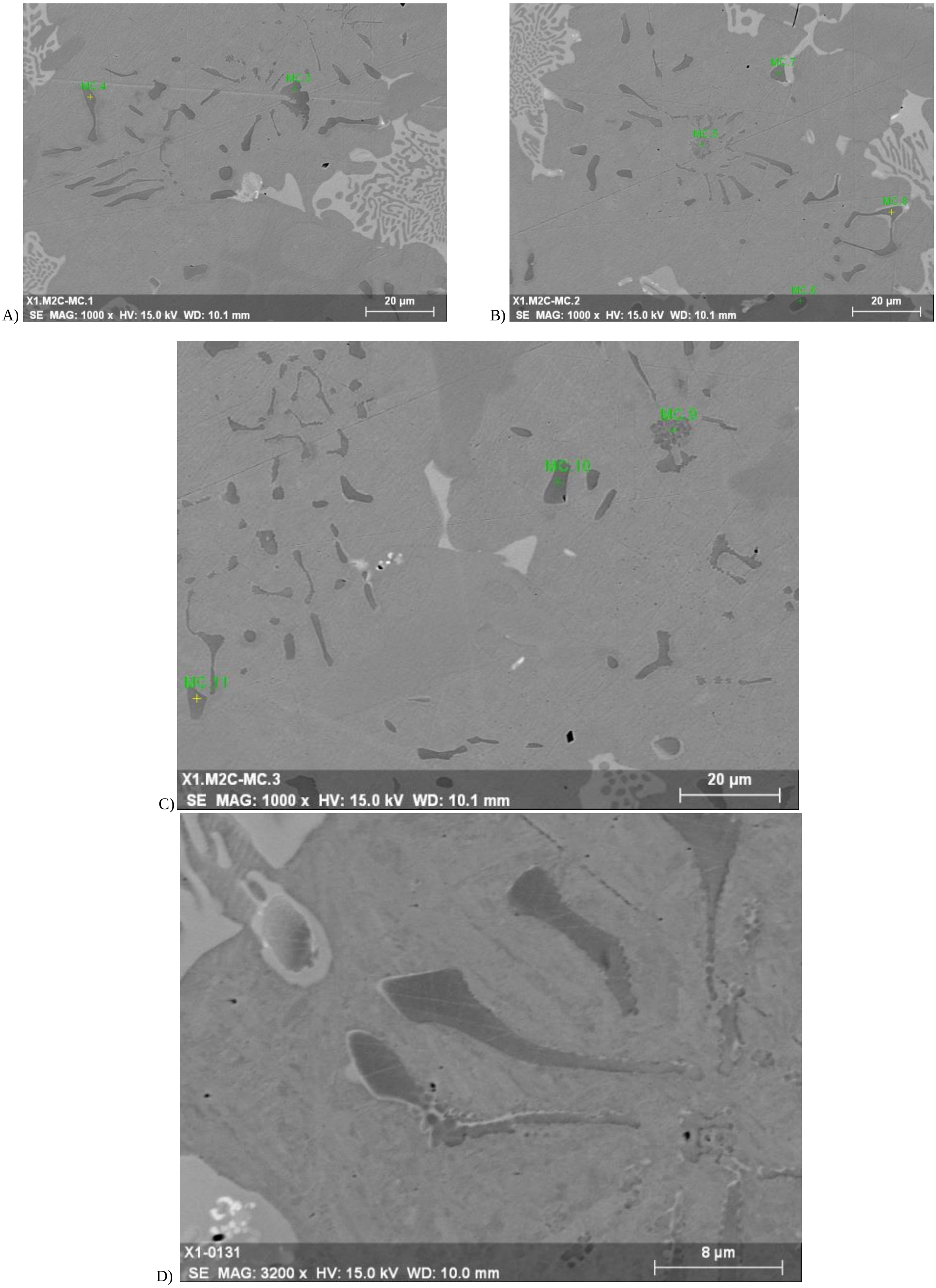

Figure 88 : A) SEM figure at 1000xwithtwo composition surveys on MC carbides, both considered branched petallike MC carbides; B) SEM figure at 1000x with four composition surveys on three different MC carbide types; C) SEM figure at 1000x with three composition surveys on two different MC carbide types; D) SEM figure at 3200x ; a zoom to show a primary carbide on the left and fibrous petallike MC carbides.

Morphology	Spectrum	C	Si	Ti	V	Cr	Mn	Fe	Ni	Nb	Mo
Branched petallike or Fibrous MC	**MC.2**	45,73	0,13		31,96	2,14	0,03	2,14		2,81	9,72
	MC.4	46,74	0,11		31,81	1,70	0,00	2,11	0,10	3,08	8,09
	MC.8	43,11	0,59		30,74	2,11	0,11	6,22	0,14	3,00	9,27
	Mean value	45,19	0,28		31,50	1,98	0,05	3,49	0,12	2,96	9,03
	Dev. St.	1,87	0,27		0,66	0,25	0,06	2,36	0,03	0,14	0,84
Idiomorphic MC	**MC.6**	46,45	0,08		32,54	1,67	0,00	1,79	0,00	3,46	8,37
	MC.7	46,00	0,13		32,61	1,64	0,00	1,83	0,06	3,68	8,43
	MC.10	45,42	0,10	0,00	33,31	1,41		1,76	0,10	3,95	7,11
	Mean value	45,96	0,10		32,82	1,57	0,00	1,79	0,05	3,70	7,97
	Dev. St.	0,51	0,03		0,42	0,14	0,00	0,03	0,05	0,24	0,75
"Raisin tige" MC	**MC.5**	43,93	0,21	0,96	30,61	0,69	0,02	1,69	0,09	11,16	4,06
	MC.9	44,78	0,22	0,34	32,75	0,77	0,02	1,86	0,03	9,08	4,33
	Mean value	44,35	0,22	0,65	31,68	0,73	0,02	1,78	0,06	10,12	4,20
	Dev. St.	0,60	0,01	0,44	1,51	0,06	0,00	0,12	0,05	1,47	0,19

Table 24: Compositions of the MC carbides in Figure 88 with the relative mean value and stardard deviation.

All the MC carbides show similar percentages for all the elements except for chromium, iron, niobium and molybdenum; those little changes mean that probably all those carbides are formed in different moments in the solidification. The different compositions can be correlated with the color of the carbides in the pictures in fact the carbides with a low percentage of molybdenum and niobium tend to be darker and the contrary. The second group of MC carbides in the previous table is about the primary carbides considered as VC carbides for the high value of the vanadium, but as shown in the Figure 89 there is the presence of little primary NbC carbide. Its composition is shown together; it is important to underline the high value of niobium and the lower vanadium amount in comparison with other MC carbides.

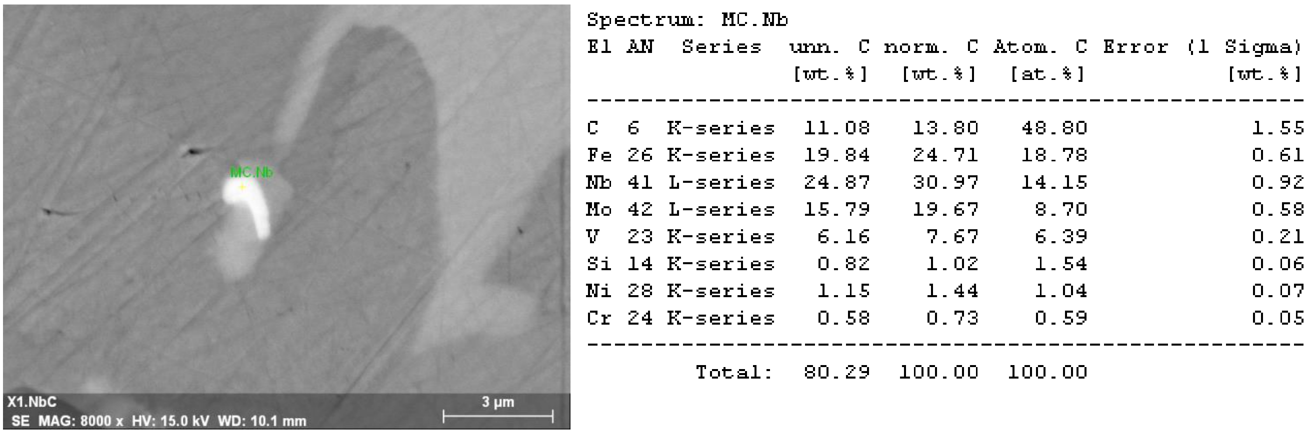

```
Spectrum: MC.Nb
El AN  Series   unn. C norm. C Atom. C Error (1 Sigma)
                [wt.%]  [wt.%]  [at.%]          [wt.%]
-----------------------------------------------------
C   6  K-series  11.08   13.80   48.80            1.55
Fe 26  K-series  19.84   24.71   18.78            0.61
Nb 41  L-series  24.87   30.97   14.15            0.92
Mo 42  L-series  15.79   19.67    8.70            0.58
V  23  K-series   6.16    7.67    6.39            0.21
Si 14  K-series   0.82    1.02    1.54            0.06
Ni 28  K-series   1.15    1.44    1.04            0.07
Cr 24  K-series   0.58    0.73    0.59            0.05
-----------------------------------------------------
         Total:  80.29  100.00  100.00
```

Figure 89 : SEM figure at 8000x with one composition surveys on a NbC carbide and relative composition in a table.

6.5.1.1.3. Carbides observation: M_2C

The M_2C carbides were characterized in the same way studying the variation of the composition in different positions of the microstructure and morphology.

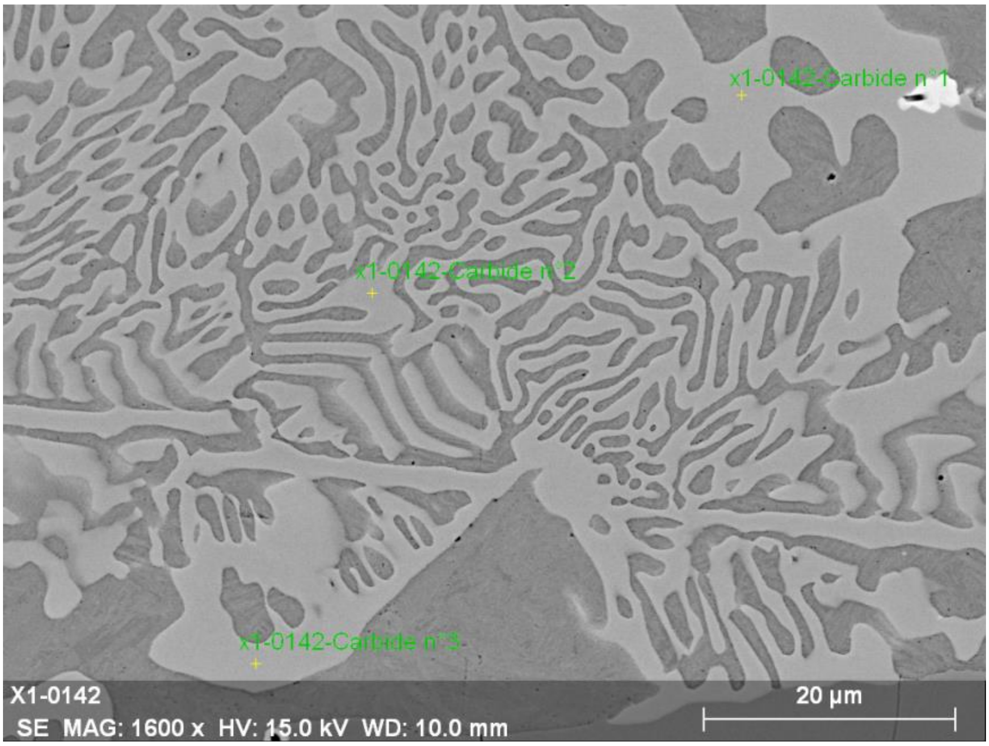

Figure 90 : SEM figure at 1600x with three composition surveys on a M_2C carbide.

As shown in the Figure 90 and the Figure 88 the M_2C carbides present a unique morphology in the microstructure called complex irregular as shown also in the Figure 11. In the Figure 90 some compositions surveys are shown and it is possible to see that the deviation standard is very low, thus means homogeneity of the various M_2C composition presences. Those carbides can be considered Mo_2C carbides due to the high amount of molybdenum and it is important to underline the high amount of silicon, higher than the amount of the matrix. The surveys are taken in the X1 sample; one example of the M_2C surveys is in the Figure 91 (A). [20]

Spectrum	C	Si	V	Cr	Mn	Fe	Ni	Nb	Mo
M_2C	28,00	4,19	2,28	2,57	1,29	52,19	1,47	0,02	8,00
M_2C.1	27,52	4,23	1,74	2,76	1,35	52,64	1,39	0,02	8,35
M_2C.2	28,07	4,12	1,72	3,10	1,33	52,58	1,47		7,62
M_2C.3	27,87	4,29	2,34	2,87	1,30	51,97	1,53		7,83
M_2C.4	28,11	4,01	1,39	2,58	1,49	52,37	1,42	0,00	8,62
M_2C.5	27,27	4,27	1,79	3,09	1,26	52,79	1,49		8,05
M_2C.6	27,86	4,18	2,06	2,81	1,27	52,39	1,45		7,99
M_2C.7	28,11	4,20	1,94	2,83	1,36	52,19	1,42	0,03	7,93
M_2C.8	28,62	4,05	2,37	2,63	1,33	51,84	1,66		7,50
M_2C.9	28,36	4,10	2,42	2,65	1,26	51,88	1,50		7,83
Mean value	27,98	4,16	2,00	2,79	1,32	52,28	1,48	0,02	7,97
Dev. St.	0,39	0,09	0,34	0,19	0,07	0,33	0,07	0,01	0,33

Table 25: Compositions of the M_2C carbides with the relative mean value and stardard deviation.

6.5.1.1.4. Carbides observation: M_7C_3

The last carbide type that was analyzed is the M_7C_3 carbide. All the surveys about it were taken on the X2 sample because here are present two or more different morphologies; in the Figure 92 the M_7C_3 lanceolate or dendritic like carbide and M_7C_3 massive globular carbide are shown.

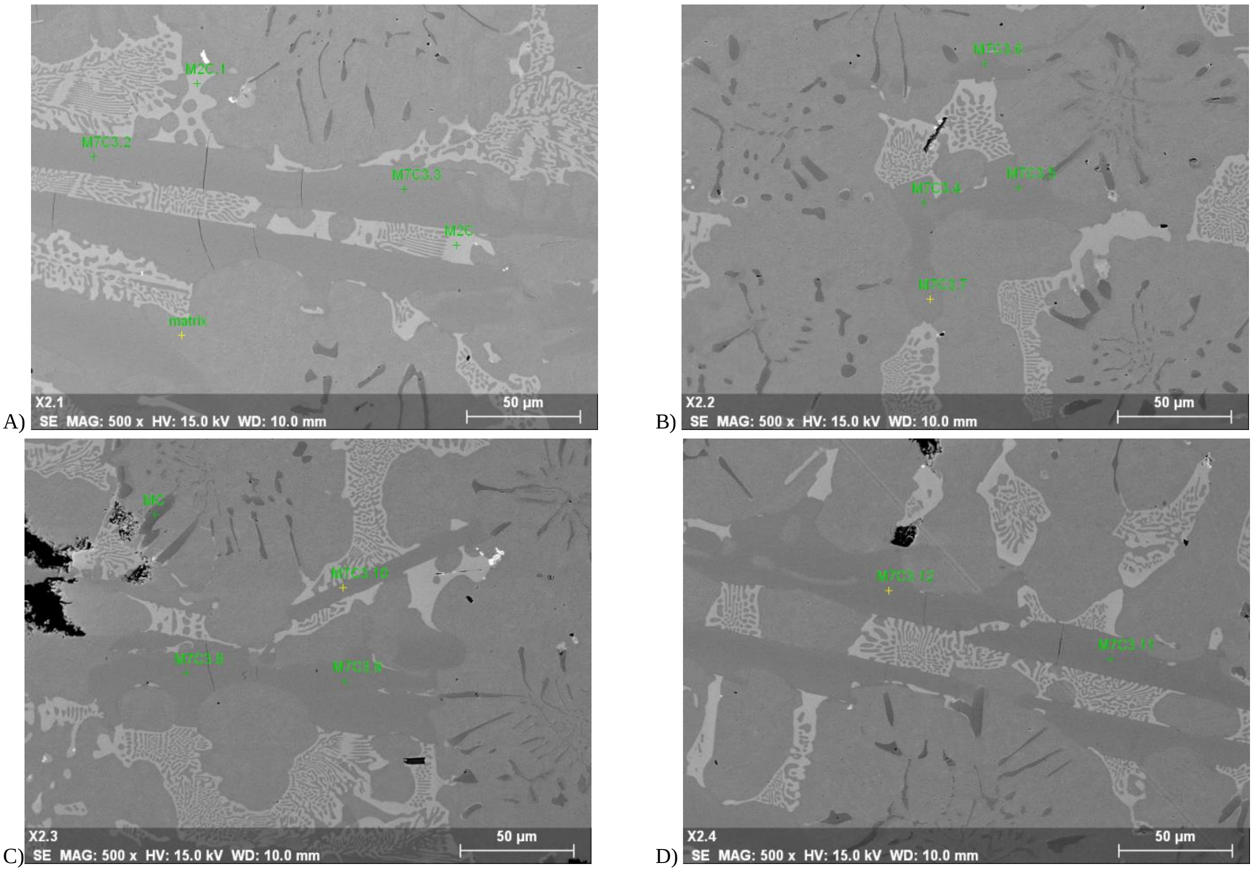

Figure 91 : A) SEM figure at 500x with two composition surveys on M_7C_3 carbides; B) SEM figure at 500x with four composition surveys on M_7C_3 carbides; C) SEM figure at 500x with four composition surveys on M_7C_3 carbides; D) SEM figure at 500x with two composition surveys on M_7C_3 carbides.

In the Figure 91 some surveys are shown and in the results are reported. It is possible to see that the compositions do not change even whether the shape or the color is different; probably the different morphologies are due to the position of it in the solidification and those carbides follow the matrix morphology that can change in the depth.

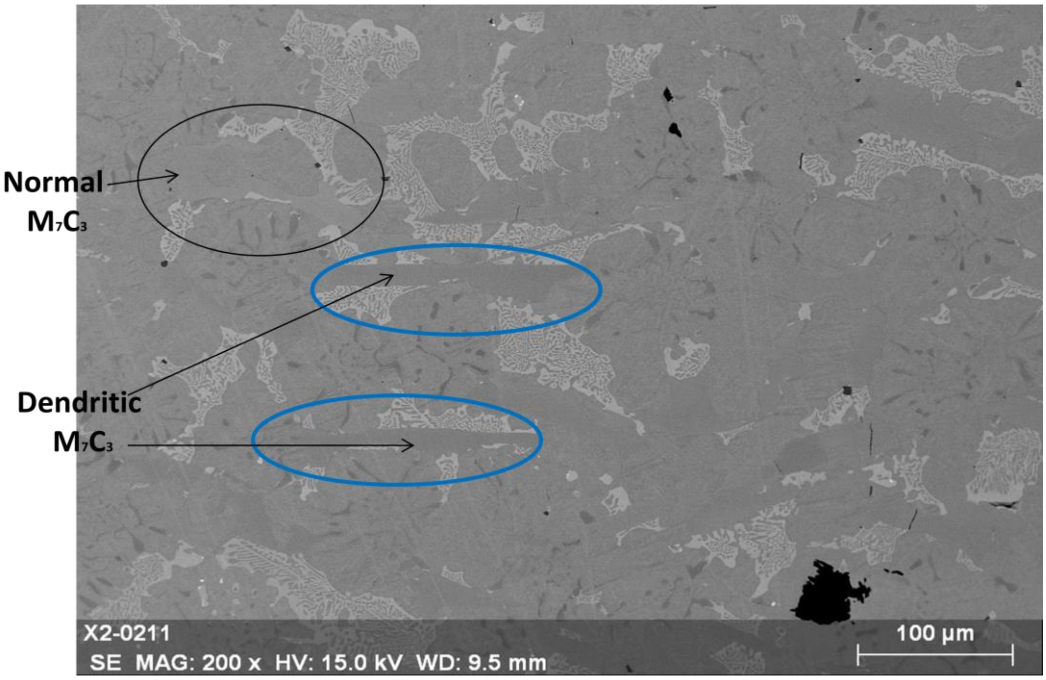

Figure 92 : Zoom at 200x about the X2 sample at 16mm to the left board

Spectrum	C	Si	V	Cr	Mn	Fe	Ni	Mo
M_7C_3.2	29,16		1,90	5,27	1,35	60,02	0,75	1,55
M_7C_3.3	28,63	0,00	1,72	5,15	1,38	60,76	0,69	1,68
M_7C_3.4	28,62		1,84	5,39	1,39	61,15		1,62
M_7C_3.5	28,88	0,00	1,92	5,46	1,35	60,21	0,72	1,46
M_7C_3.7	28,67		1,56	4,86	1,31	60,93	0,74	1,94
M_7C_3.8	28,24		2,02	5,62	1,33	60,68	0,68	1,42
M_7C_3.9	27,90		2,10	5,74	1,29	60,86	0,66	1,44
M_7C_3.10.1	27,94		1,86	5,28	1,34	61,33	0,78	1,47
M_7C_3.11	28,76		2,05	5,65	1,23	60,23	0,73	1,35
M_7C_3.12	28,47		2,07	5,63	1,35	60,31	0,72	1,45
Mean value	28,53	0,00	1,90	5,41	1,33	60,65	0,72	1,54
St. Dev.	0,40	0,00	0,17	0,27	0,05	0,44	0,04	0,17

Table 26 : Compositions of the M_7C_3 carbides in Figure 91 with the relative mean value and standard deviation.

In the Figure 91 (B) it is well enhanced it because it is possible to distinguish the matrix dendrites in the z axis, with some fibrous MC carbides, and the M_7C_3 carbide follows the direction of their growing; thus the M_7C_3 carbides can appear in different morphology and this depends only on the matrix structure and on the observing axis. The presence of Manganese sulfide MnS was found in the X1 sample as shown in the following picture with the composition analysis:

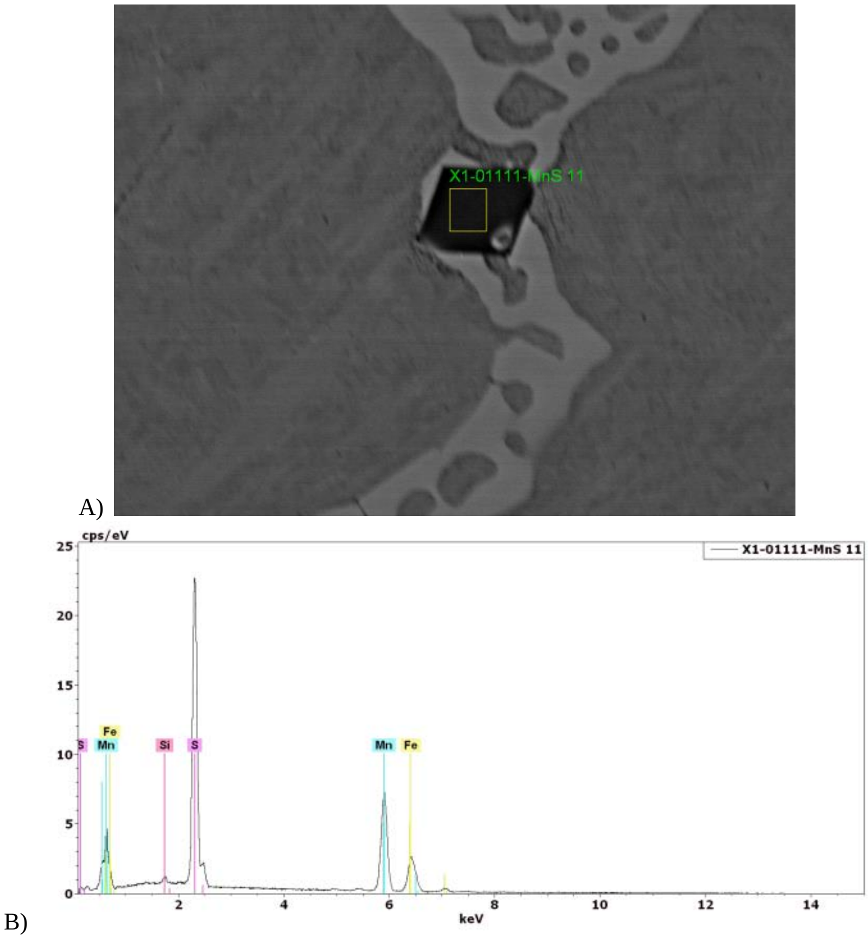

Figure 93 : A) SEM figure a MnS particle with the composition survey on it; B) the results of the composition survey of (A)

6.5.1.2. DTA samples

Scanning electron spectroscopies were done also to the DTA samples to analyze the structure after the test and to verify the phase presences. The most interesting part was to check the graphite presence, the carbide presences and morphologies with also some surveys on the phenomena observed in the optical microscope. First there were verified that the black forms in the optical microscope:

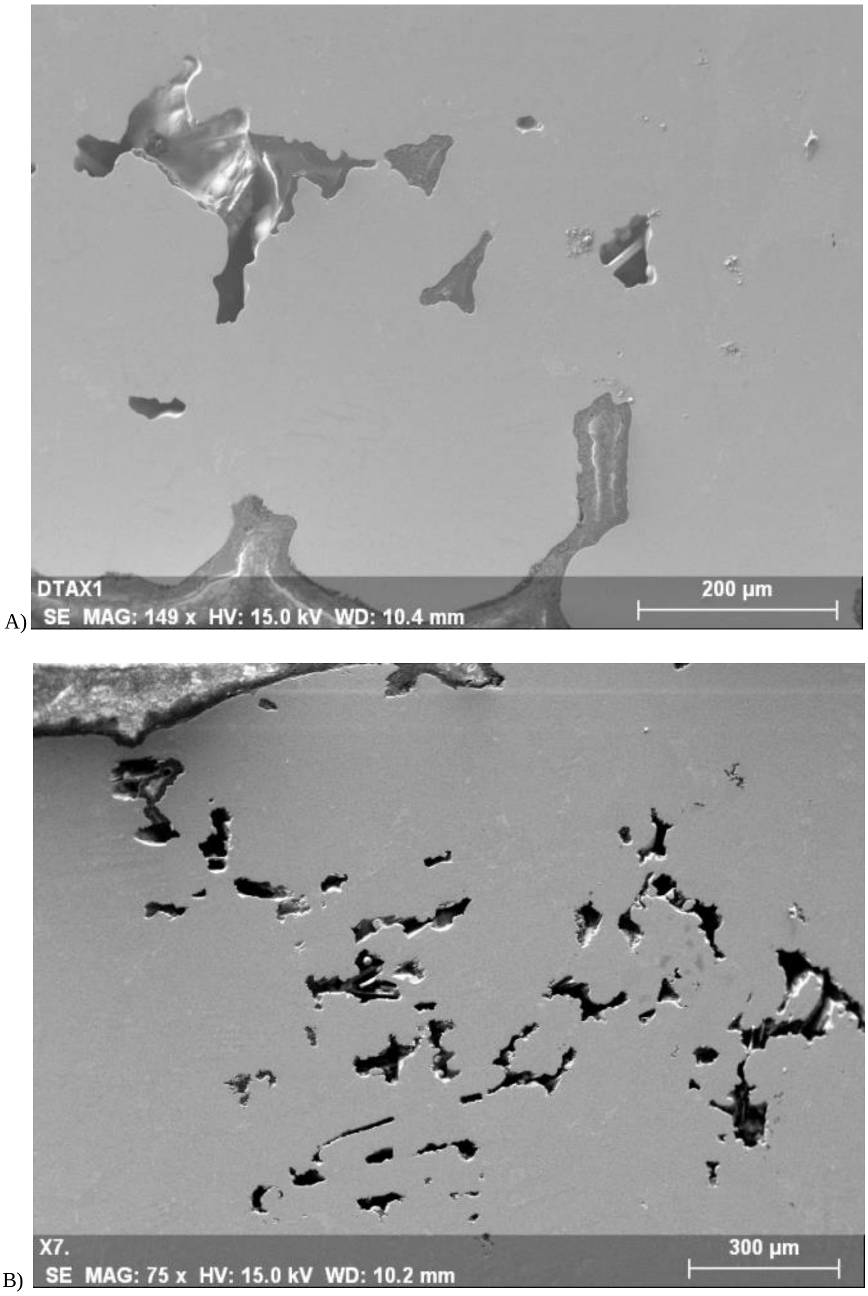

Figure 94 : A) SEM Figure at 149x about holes due to the presence of gas in the DTX1 sample.
B) SEM Figure at 75x about holes due to the presence of gas in the DTX7 sample.

It was discovered that they were holes due to the presence of some gases like oxygen under the sample and during the test they came up and remained inside the material. All the carbides present in the normal samples are found also here but with some differences especially for the M_7C_3 carbides that change the morphology. In the Figure 95 there are reported some examples of carbides; MnS particles are present still in the microstructure after the DTA test as it is possible to observe in the pictures.

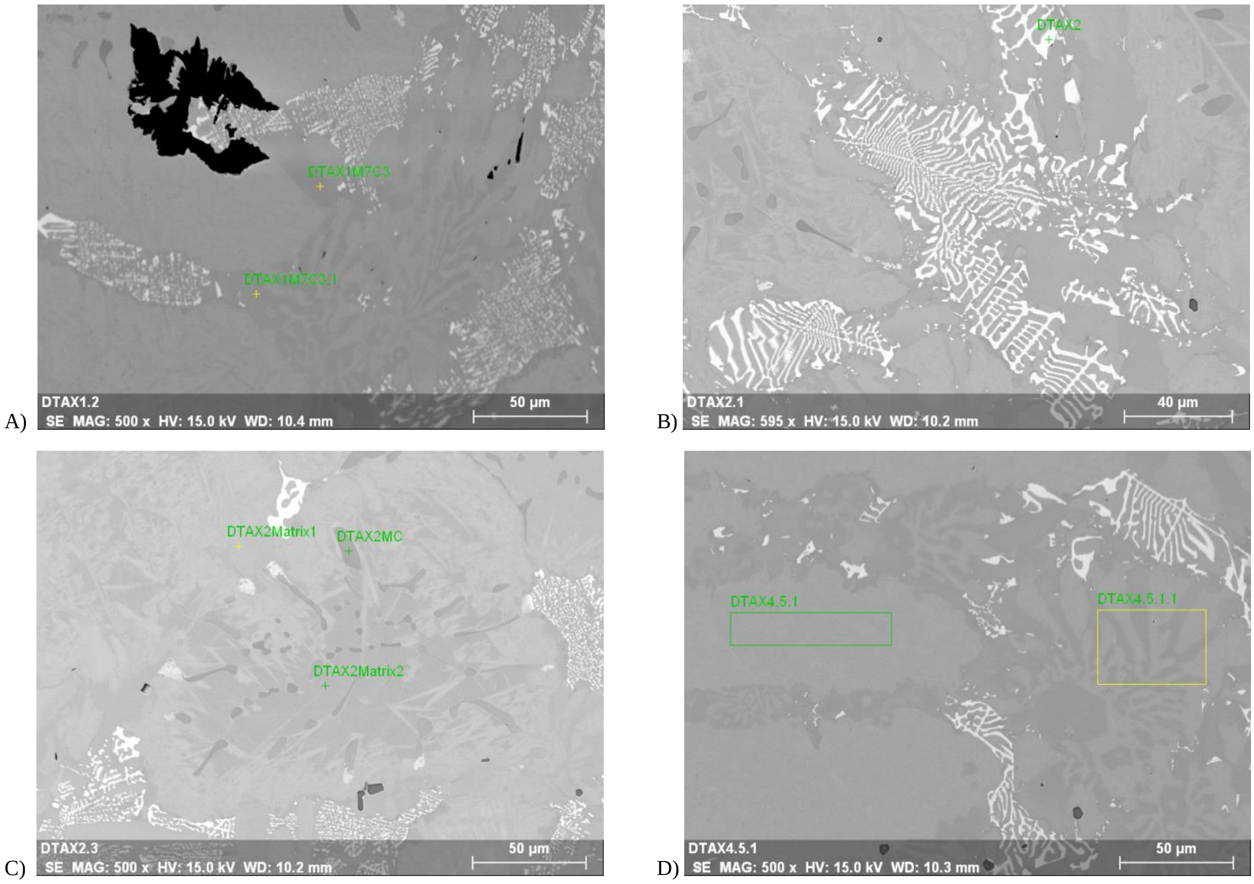

Figure 95 : A) SEM figure at 500x with two composition surveys on M_7C_3 carbides in the DTX1 sample; B) SEM figure at 595x with the microstructure and a composition survey on the M_2C carbide in the DTX2 sample; C) SEM figure at 500x with the microstructure and some MC carbides in the DTX2 sample; D) SEM figure at 500x with two composition surveys in the DTX4 sample.

It can be observed that the MC carbides morphologies are not modified, whereas M_2C carbides shows a fish-bone morphology and the M_7C_3 carbides that is in dark grey tend to grow together with the M_2C or to have a lanceolate morphology (as in Figure 14) in all the samples; one survey result about the figure (A) is reported to show that it is a M_7C_3 carbide:

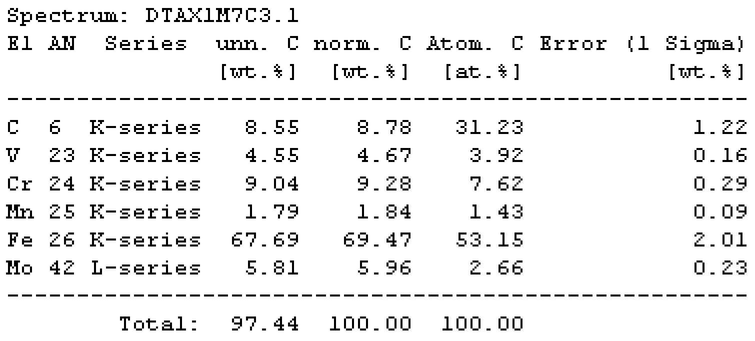
```
Spectrum: DTAX1M7C3.1
El AN  Series   unn. C norm. C Atom. C Error (1 Sigma)
                [wt.%]  [wt.%]  [at.%]          [wt.%]
-----------------------------------------------------
C   6  K-series   8.55    8.78   31.23            1.22
V  23  K-series   4.55    4.67    3.92            0.16
Cr 24  K-series   9.04    9.28    7.62            0.29
Mn 25  K-series   1.79    1.84    1.43            0.09
Fe 26  K-series  67.69   69.47   53.15            2.01
Mo 42  L-series   5.81    5.96    2.66            0.23
-----------------------------------------------------
        Total:   97.44  100.00  100.00
```
Figure 96 : Composition survey results about the Figure 95 (A).

The M_7C_3 carbide composition is different in comparison with the normal samples with lower iron content and all the rest higher; for the MC carbides a comparison with the normal samples is not useful for the variety of it, but for the M_2C carbide it has a sense due to the low standard deviation.

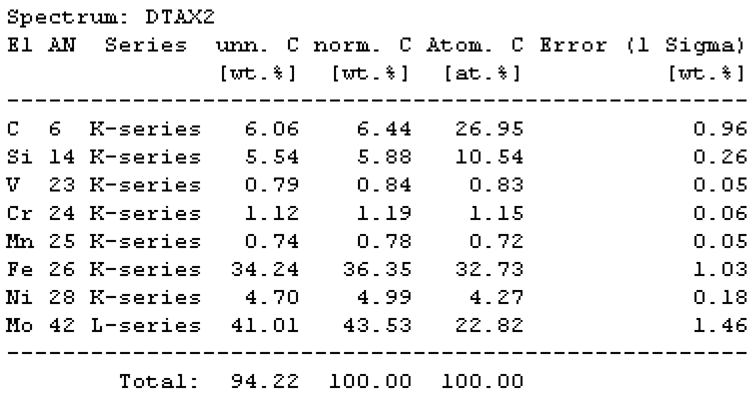

```
Spectrum: DTAX2
El AN  Series   unn. C norm. C Atom. C Error (1 Sigma)
                [wt.%]  [wt.%]  [at.%]          [wt.%]
-----------------------------------------------------
C   6  K-series   6.06    6.44   26.95            0.96
Si 14  K-series   5.54    5.88   10.54            0.26
V  23  K-series   0.79    0.84    0.83            0.05
Cr 24  K-series   1.12    1.19    1.15            0.06
Mn 25  K-series   0.74    0.78    0.72            0.05
Fe 26  K-series  34.24   36.35   32.73            1.03
Ni 28  K-series   4.70    4.99    4.27            0.18
Mo 42  L-series  41.01   43.53   22.82            1.46
-----------------------------------------------------
        Total:   94.22  100.00  100.00
```

Figure 97 : Composition survey results about the Figure 95 (B).

In comparison with the normal sample the M_2C carbides in the DTA samples are richer in silicon and molybdenum, with the same carbon amount and with fewer amounts of the other elements. NbC carbides or “raisin tige” MC carbides were not observed.

The graphite presence was observed but not everywhere and with qualitatively different amount in the different samples:

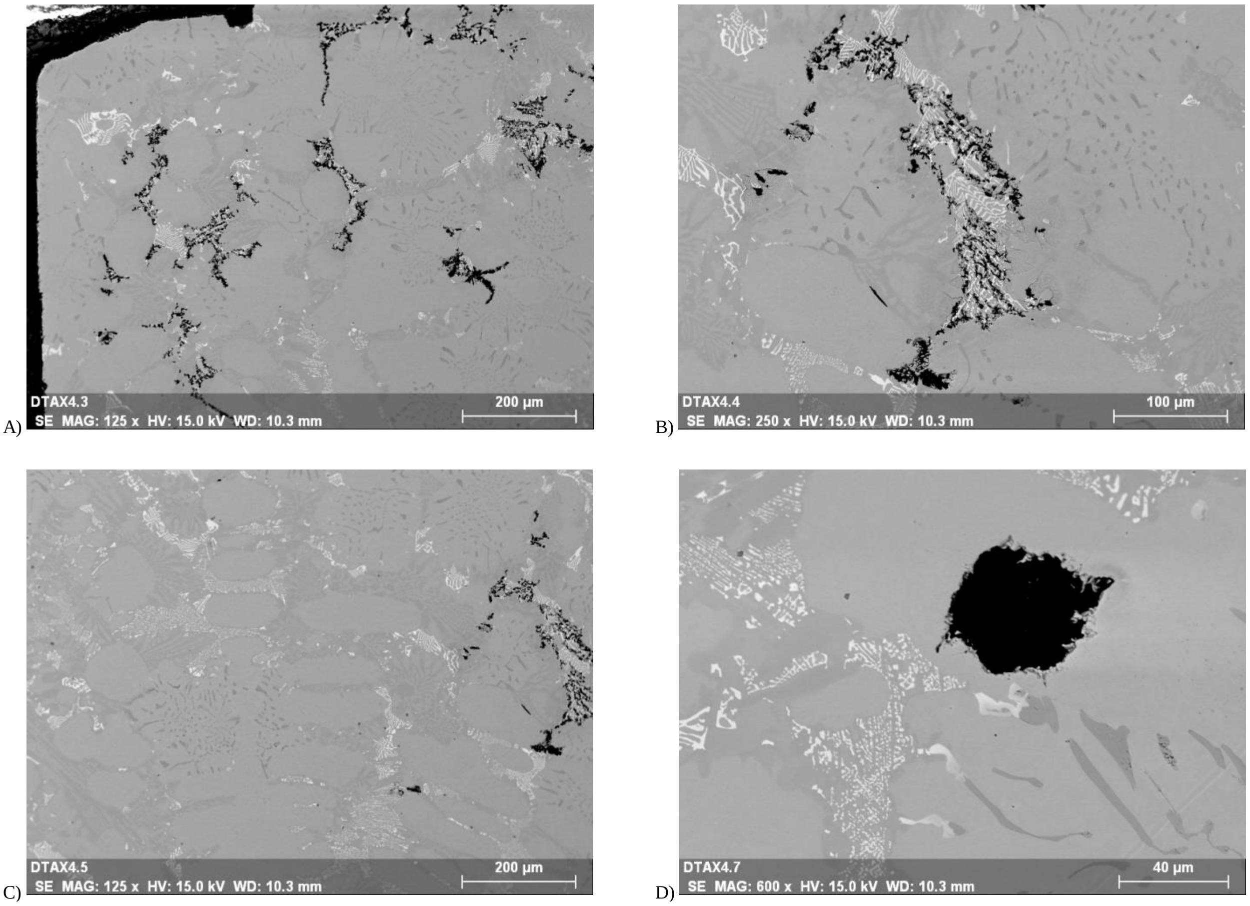
A) B) C) D)

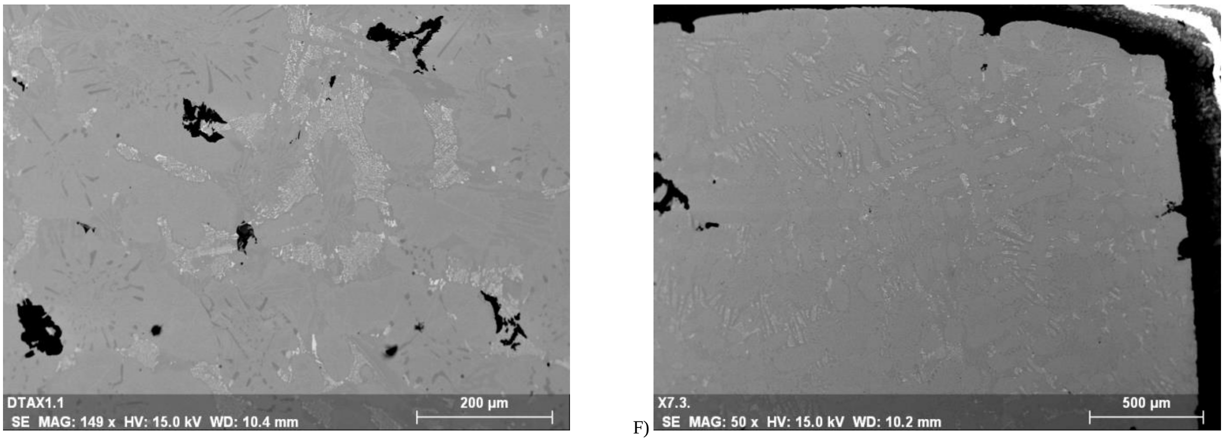

E) F)

Figure 98 : A) SEM figure at 125x about the upper part of the DTX4 sample; B) SEM figure at 250x ; zoom about the figure (A) about the graphite growing; C) SEM figure at 125x about the middle zone of the DTX4 sample; D) SEM figure at 500x about a graphite particle in the lower part of the DTX4 sample; E) SEM figure at 149x about microstructure and graphite particles in the DTX1 sample; F) SEM figure at 50x about the upper part of the DTX7 sample without graphite.

The first four figures can explain the situation of total not homogeneity in the samples after DTA test; the presence or not of the graphite can be due to the position of the observation but it is possible say that near the sample boards, where the cooling rate is faster, the graphite tends to grow together with the M_2C carbide and in the lower or centre part of the sample graphite tends to be divided from it as in the picture (D). In the picture (F) there is not any graphite presence in the DTX7; but composition differences were not founded between the samples to explain the presence of graphite in the various zones of the DTA samples. The DTX4 sample is the one that showed more graphite presence in the upper part and in general, whereas the DTX7 sample is the contrary. Two composition surveys about that sample are showed in the Figure 99, and the results are reported in the Figure 100.

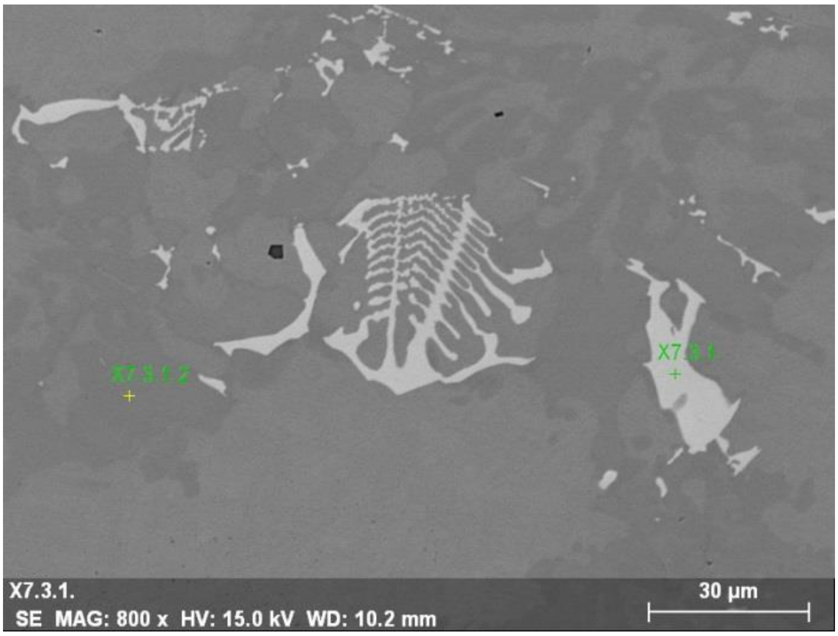

Figure 99 : SEM figure at 800x ; zoom of the Figure 95 (F) about the microstructure and two composition surveys on different carbides of the DTX7 sample.

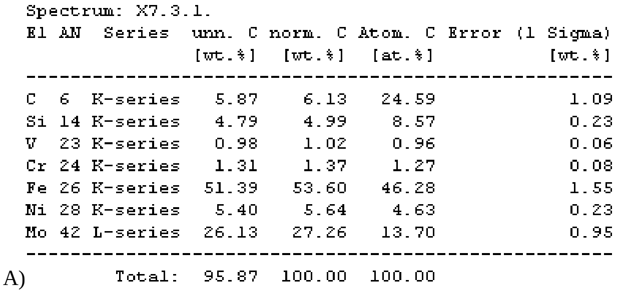

```
Spectrum: X7.3.1.
El AN  Series   unn. C norm. C Atom. C Error (1 Sigma)
                [wt.%]  [wt.%]  [at.%]           [wt.%]
-----------------------------------------------------
C   6  K-series   5.87    6.13   24.59            1.09
Si 14  K-series   4.79    4.99    8.57            0.23
V  23  K-series   0.98    1.02    0.96            0.06
Cr 24  K-series   1.31    1.37    1.27            0.08
Fe 26  K-series  51.39   53.60   46.28            1.55
Ni 28  K-series   5.40    5.64    4.63            0.23
Mo 42  L-series  26.13   27.26   13.70            0.95
-----------------------------------------------------
        Total:   95.87  100.00  100.00
```

A)

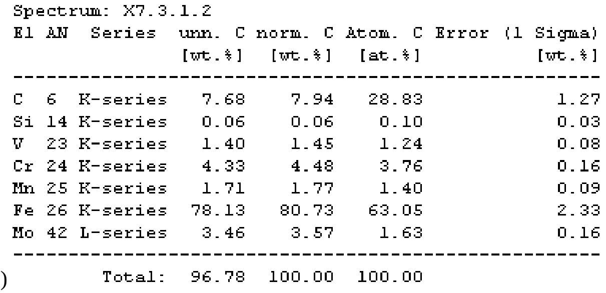

```
Spectrum: X7.3.1.2
El AN  Series   unn. C norm. C Atom. C Error (1 Sigma)
                [wt.%]  [wt.%]  [at.%]           [wt.%]
-----------------------------------------------------
C   6  K-series   7.68    7.94   28.83            1.27
Si 14  K-series   0.06    0.06    0.10            0.03
V  23  K-series   1.40    1.45    1.24            0.08
Cr 24  K-series   4.33    4.48    3.76            0.16
Mn 25  K-series   1.71    1.77    1.40            0.09
Fe 26  K-series  78.13   80.73   63.05            2.33
Mo 42  L-series   3.46    3.57    1.63            0.16
-----------------------------------------------------
        Total:   96.78  100.00  100.00
```

B)

Figure 100 : Results about Figure 99 A) Composition survey results about the M_2C carbide; B) Composition survey results about the M_7C_3 carbide.

The results say that the DTX7 has M_7C_3 carbides more similar to the normal samples as composition, in comparison with the DTX4; the M_2C carbides in both the DTA samples are different in comparison with the normal M_2C carbide with higher silicon and molybdenum amount. The graphite presence can be bonded with the carbide compositions; in particular the silicon amount has to be taken in strong consideration.

6.5.1.3. Dilatometer samples

SEM analyses were done also to the Dilatometer samples to analyze the structure after the test and to verify the phase presences and modification. The thermal treatment up to 1025°C during 1h done on the sample in theory is below the Solidus temperature and it is not possible observe remelting phenomena but only phase modifications. The main part of this observation is to verify the phase presences and any modifications of the composition or morphology. All the carbides present in the normal samples are observed in the Dilatometer samples except for the dark small secondary carbides inside the grains. In the Figure 101 it is possible to see the microstructure of the XD2 sample with two composition surveys on a M_7C_3 carbide and a M_2C carbide; MC carbides are present inside grains in various morphologies.

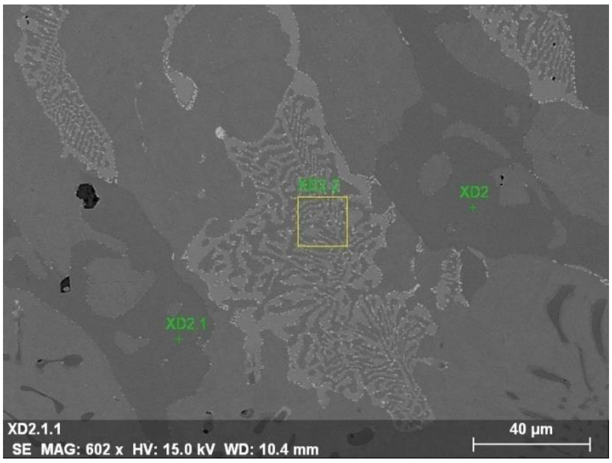

A)

B)

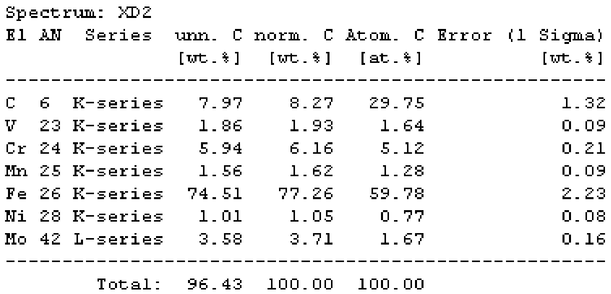

```
Spectrum: XD2
El AN  Series   unn. C norm. C Atom. C Error (1 Sigma)
                [wt.%]  [wt.%]  [at.%]           [wt.%]
-----------------------------------------------------
C   6  K-series   7.97    8.27   29.75            1.32
V  23  K-series   1.86    1.93    1.64            0.09
Cr 24  K-series   5.94    6.16    5.12            0.21
Mn 25  K-series   1.56    1.62    1.28            0.09
Fe 26  K-series  74.51   77.26   59.78            2.23
Ni 28  K-series   1.01    1.05    0.77            0.08
Mo 42  L-series   3.58    3.71    1.67            0.16
-----------------------------------------------------
        Total:   96.43  100.00  100.00
```

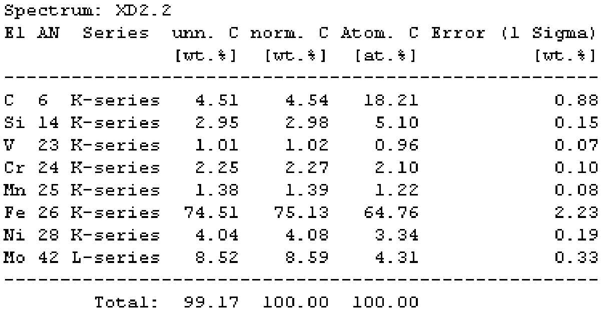

```
Spectrum: XD2.2
El AN  Series   unn. C norm. C Atom. C Error (1 Sigma)
                [wt.%]  [wt.%]  [at.%]           [wt.%]
-----------------------------------------------------
C   6  K-series   4.51    4.54   18.21            0.88
Si 14  K-series   2.95    2.98    5.10            0.15
V  23  K-series   1.01    1.02    0.96            0.07
Cr 24  K-series   2.25    2.27    2.10            0.10
Mn 25  K-series   1.38    1.39    1.22            0.08
Fe 26  K-series  74.51   75.13   64.76            2.23
Ni 28  K-series   4.04    4.08    3.34            0.19
Mo 42  L-series   8.52    8.59    4.31            0.33
-----------------------------------------------------
        Total:   99.17  100.00  100.00
```

C)

Figure 101 : A) SEM figure at 602x about the XD2 sample; B) Composition survey results about the M_7C_3 carbide; C) Composition survey results about the M_2C carbide.

In both samples the Budding Phenomenon was found and it represents the main change in the microstructure. The M_2C carbides are involved in a destabilization of it and there are some migrations of atoms that escape from the parent or original M_2C carbide to diffuse further away from their initial site with increasing time and temperature. The result of it is the formation during cooling of Mo-rich secondary carbides M_6C and “secondary” graphite formation in the M_2C/γ interface as shown in the Figure 102. [2]

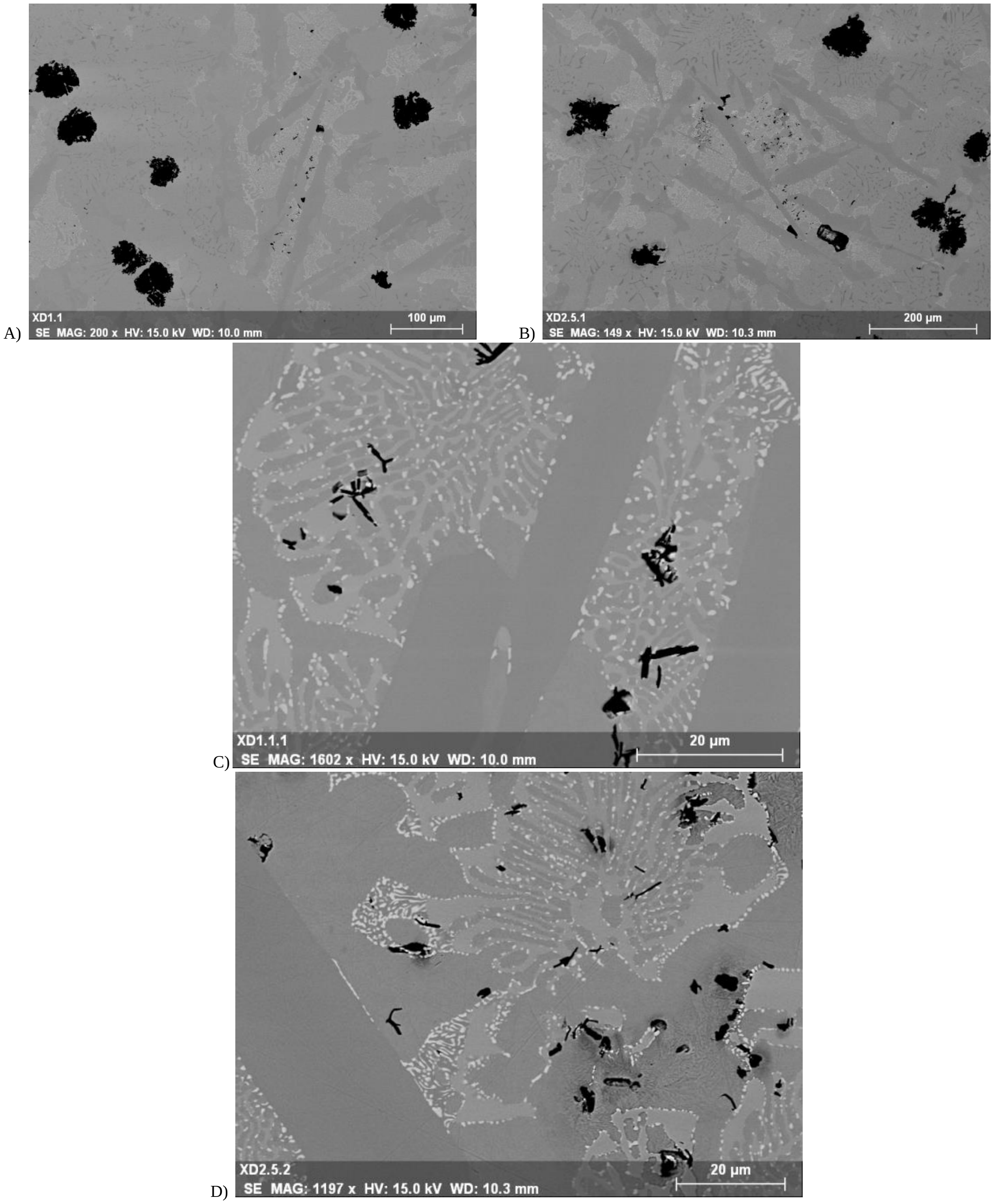

Figure 102 : A) SEM figure at 200x about microstructure of the XD1 sample; B) SEM figure at 149x about microstructure of the XD2 sample; C) SEM figure at 1602x about a zoom of the Figure (A) on the M_2C carbide destabilization; D) SEM figure at 1197x about a zoom of the figure (B) on the M_2C carbide destabilization.

This phenomenon occurs with the presence near to the carbide of a chromium-rich phase that in this case can be the matrix or a M_7C_3 carbide; the remaining carbide change to a Cr-rich carbide while keeping the shape similar to that of previous M_2C carbide. The latter fact can be proved by two composition surveys done on the remaining carbide and on the M_6C secondary carbide as shown in the Figure 103.

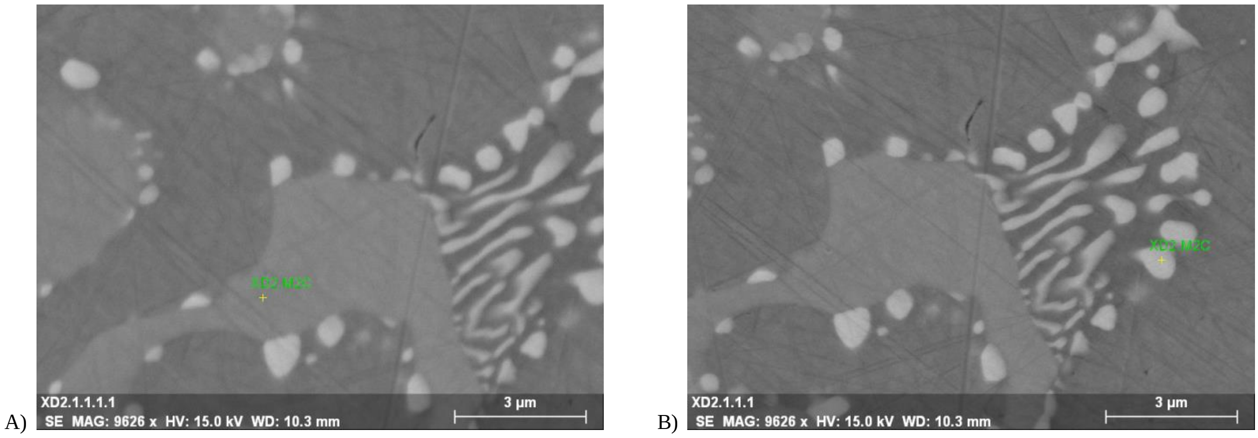

Figure 103 : A) SEM figure at 9626x with a composition survey on a M_2C carbide in the XD2 sample; B) the same picture with a composition survey on a M_6C carbide in the XD2 sample

The composition surveys were done on a zoom of the Figure 101 in the same area; the results are reported in Figure 104.

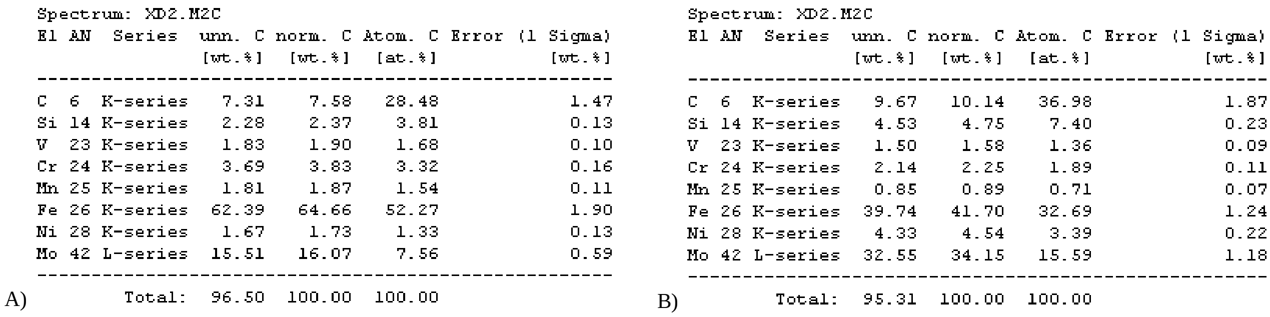

A)

```
Spectrum: XD2.M2C
El AN  Series   unn. C norm. C Atom. C Error (1 Sigma)
                [wt.%]  [wt.%]  [at.%]          [wt.%]
-----------------------------------------------------
C   6  K-series   7.31    7.58   28.48            1.47
Si 14  K-series   2.28    2.37    3.81            0.13
V  23  K-series   1.83    1.90    1.68            0.10
Cr 24  K-series   3.69    3.83    3.32            0.16
Mn 25  K-series   1.81    1.87    1.54            0.11
Fe 26  K-series  62.39   64.66   52.27            1.90
Ni 28  K-series   1.67    1.73    1.33            0.13
Mo 42  L-series  15.51   16.07    7.56            0.59
-----------------------------------------------------
        Total:   96.50  100.00  100.00
```

B)

```
Spectrum: XD2.M2C
El AN  Series   unn. C norm. C Atom. C Error (1 Sigma)
                [wt.%]  [wt.%]  [at.%]          [wt.%]
-----------------------------------------------------
C   6  K-series   9.67   10.14   36.98            1.87
Si 14  K-series   4.53    4.75    7.40            0.23
V  23  K-series   1.50    1.58    1.36            0.09
Cr 24  K-series   2.14    2.25    1.89            0.11
Mn 25  K-series   0.85    0.89    0.71            0.07
Fe 26  K-series  39.74   41.70   32.69            1.24
Ni 28  K-series   4.33    4.54    3.39            0.22
Mo 42  L-series  32.55   34.15   15.59            1.18
-----------------------------------------------------
        Total:   95.31  100.00  100.00
```

Figure 104 : Results about the composition surveys in the Figure 103: (A) the M_2C carbide and (B) the M_6C carbide.

The results show that the M_2C carbide is chromium richer and the M_6C secondary carbide is a Mo-rich carbide; those carbides are present also near to M_7C_3 carbides and inside the grains for a precipitation that occurs in the increasing of the time as shown in the Figure 105.

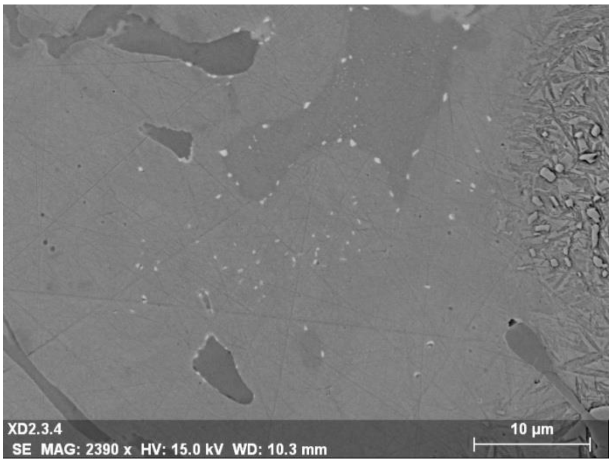

Figure 105 : A) SEM figure at 2390x about the M_6C carbides precipitation inside the grain in the XD2 sample.

In the Figure 102 (A) and (B) it can be noted that in the zones without bigger graphite particles, the destabilization products also the “secondary” graphite. In the following picture there is a zoom about a “secondary” graphite particle inside a M_2C carbide with the composition; it is graphite due to its high carbon amount.

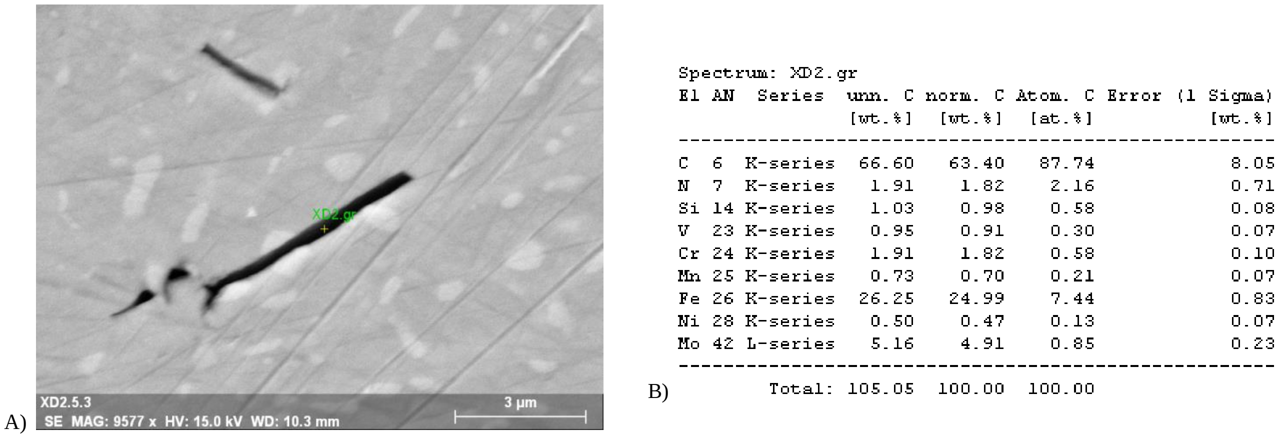

```
Spectrum: XD2.gr
El AN  Series   unn. C norm. C Atom. C Error (1 Sigma)
                [wt.%]  [wt.%]  [at.%]          [wt.%]
------------------------------------------------------
C  6  K-series  66.60   63.40   87.74            8.05
N  7  K-series   1.91    1.82    2.16            0.71
Si 14 K-series   1.03    0.98    0.58            0.08
V  23 K-series   0.95    0.91    0.30            0.07
Cr 24 K-series   1.91    1.82    0.58            0.10
Mn 25 K-series   0.73    0.70    0.21            0.07
Fe 26 K-series  26.25   24.99    7.44            0.83
Ni 28 K-series   0.50    0.47    0.13            0.07
Mo 42 L-series   5.16    4.91    0.85            0.23
------------------------------------------------------
        Total: 105.05  100.00  100.00
```

Figure 106 : A) SEM figure at 9577x about a graphite particle inside a M_2C carbide due to the destabilization of the latter with the composition survey; B) Results of the composition survey in the figure (A).

6.5.2. Composition 2: Industrial as-cast conditions sample

SEM analyses were done on Industrial as-cast conditions or N0 sample to check phase composition, morphology, solidification steps and the phase’s amount. The Industrial as-cast conditions analyses can be the base to understand especially the graphite changes during the double tempering treatment. It has to be noted that the figures were taken on the N0 bar sample shown in the Figure 37 (A) and the use of a big conductive sample disturb the microscope; the consequence can be a continuous movement of the figure in some zones, this means not perfect figures and can give no-precise composition surveys. In the Figure 107 the microstructure of the Industrial as-cast conditions sample is showed and it is possible to observe all the different carbides except for the small secondary carbides; the M_7C_3 carbides look slightly different, they tend to appear with the complex regular morphology that is more near to the M_2C carbide morphology. Some composition surveys were taken to check whether differences are present between the carbides of the two compositions.

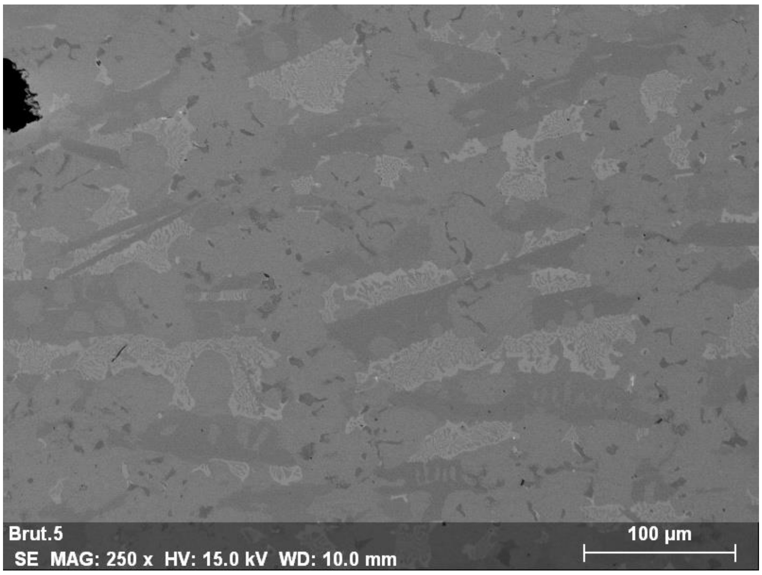

Figure 107 : A) SEM figure at 250x about the microstructure of the Industrial as-cast conditions sample at 5mm from the surface.

In the Figure 108 it is possible to see the composition surveys, the different graphite shape in the depths and the carbides morphologies. The figure (A) is taken at 5mm from the surface and it is a zoom of the Figure 107, the figure (B) is taken at 30mm, the figure (C) at 35mm and the figure (D) at 40mm.

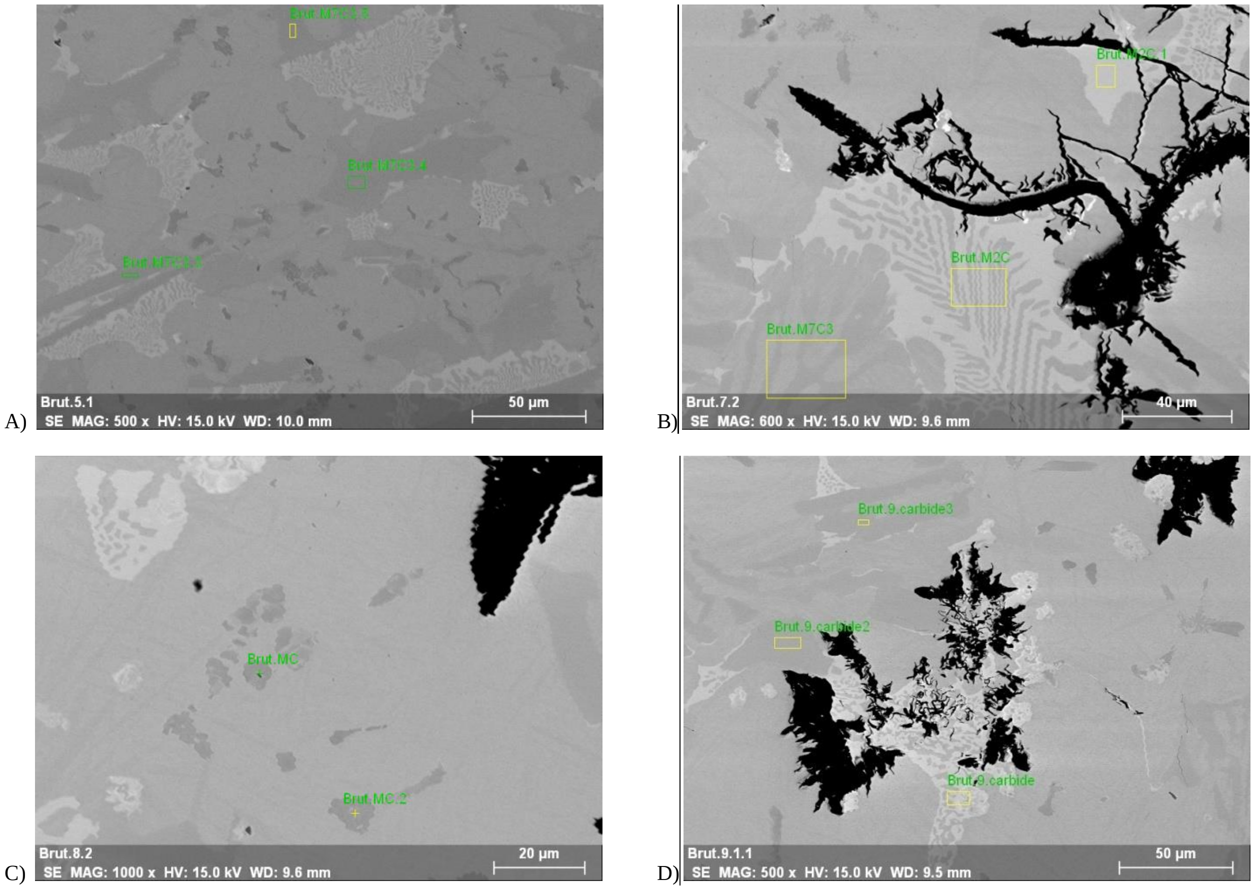

Figure 108 : A) zoom at 500x of the Figure 107 with three composition surveys; B) SEM figure at 600x about a graphite particle at 30mm from the surface with three composition surveys; C) SEM figure at 1000x about some MC carbides at 35mm from the surface; D) SEM figure at 500x about microstructure and a graphite particle bonded with a M_2C carbide at 40mm from the surface; there are three composition surveys about carbides.

Spectrum	C	Si	V	Cr	Mn	Fe	Ni	Nb	Mo
Brut.M$_7$C$_3$.2	27,32		1,97	5,27	1,18	62,17	0,76		1,32
Brut.M$_7$C$_3$.3	27,66	0,18	1,67	4,65	1,11	62,03	0,81		1,87
Brut.M$_7$C$_3$.4	27,24	0,27	1,79	4,96	1,18	62,21	0,97		1,39
Brut.M$_7$C$_3$.carbide2	30,39	0,00	4,01	6,48	1,29	55,21			2,63
Brut.M$_7$C3. carbide3	30,65	0,13	4,04	7,34	1,34	53,99			2,50
Mean value	28,65	0,15	2,70	5,74	1,22	59,12	0,85		1,94
St. Dev.	1,71	0,11	1,22	1,13	0,09	4,15	0,11		0,61
Brut.M$_2$C.1	24,04	4,08	1,74	2,67	1,14	56,72	1,57		8,04
Brut.MC	42,34	0,17	30,03	1,67	7,77	1,56		3,63	12,82
Brut.MC.2	48,37	0,41	33,14	1,13	0,00	3,92		6,78	6,25
Mean value	45,36	0,29	31,58	1,40	3,89	2,74		5,21	9,54
St. Dev.	4,26	0,17	2,20	0,38	5,50	1,66		2,22	4,65

Table 27 : Results about the composition surveys of Figure 108.

The results of the composition surveys about the carbides are reported in the previous table. The M_7C_3 carbides have slightly differences in comparison with the carbides of the X sample and there is an evident composition difference in the depth; the MC and M_2C carbides do not show any difference. The M_7C_3 carbide probably is the carbide that sense more the little changing of composition, both for the total composition change and for the local composition changing during the increasing of the depth to the surface. The fourth and fifth composition surveys are taken on the Figure 108 (D) and it is possible to see that probably in this position the solidification conditions are particular since the graphite is growing together with a M_2C carbide.

6.5.2.1. Connection zone of the as-casted condition sample (N0)

The N0 at 50-52mm unlike the other samples shows a sudden change of the graphite shape that underlines the point of connection between the shell material and the core material as showed in the two following figures together.

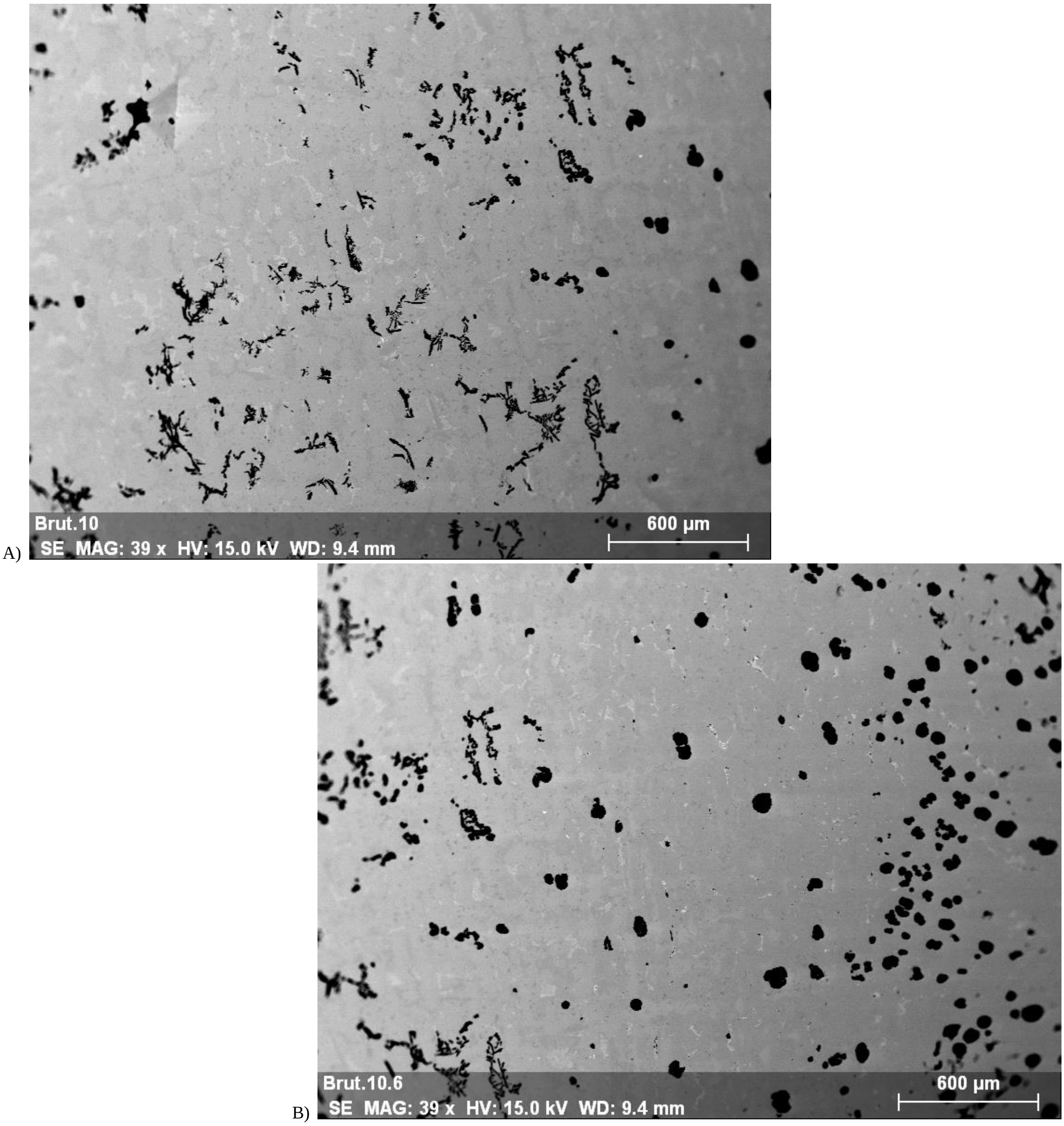

Figure 109 : A) and B) SEM figures about the microstructure at 50mm from the surface.

That connection zone shows in almost 1 mm a lot of graphite shape types as shown in Figure 110. Some composition surveys were also taken on the matrix in different points near different graphite shapes. The graphite shapes can vary from the branched graphite to chinese script graphite, from almost nodular to a elongated shape.

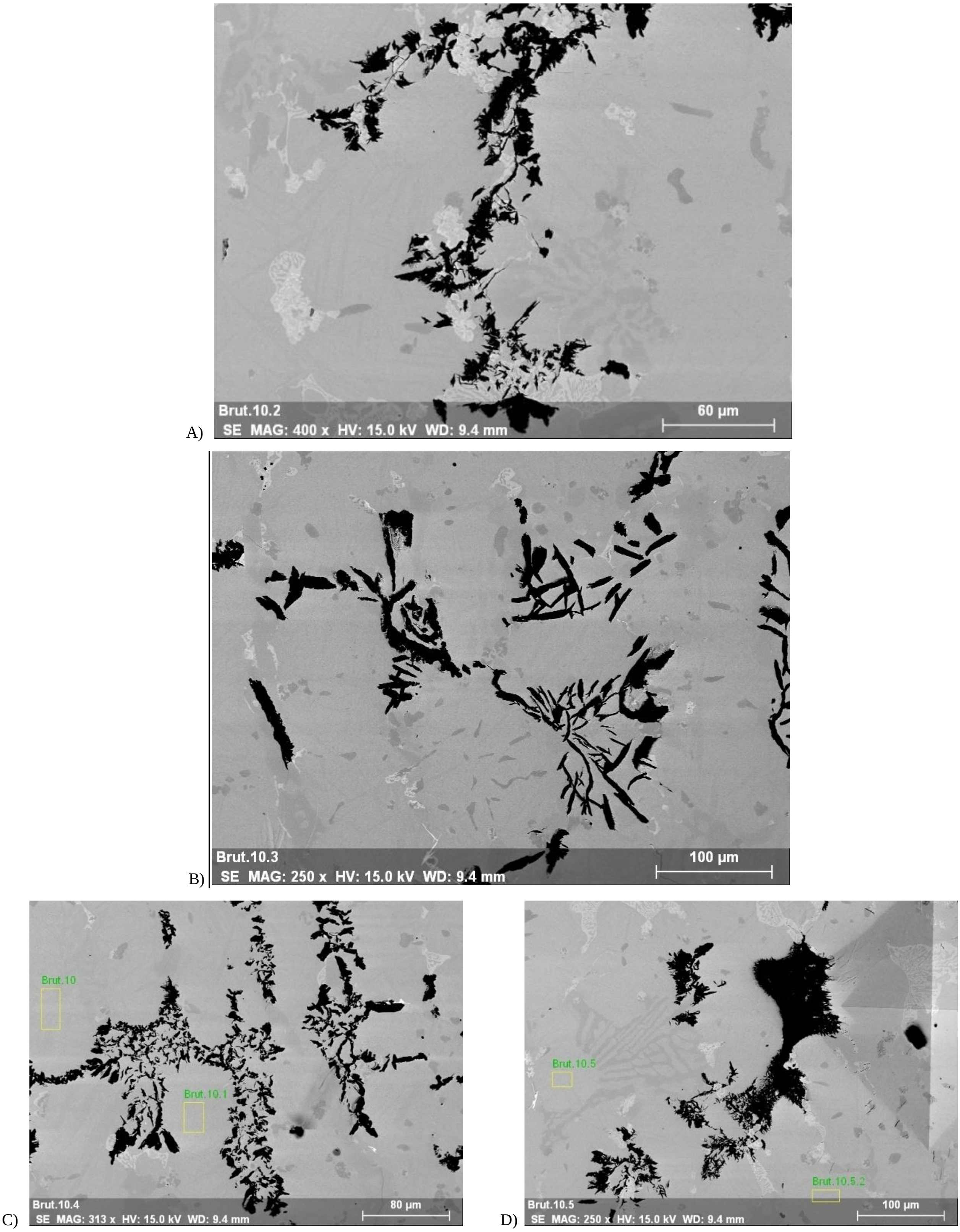

Figure 110 : SEM figures about zooms of the Figure 109 with different graphite shapes in the connection point; in the figure (A) there is branched graphite, in the (B) elongated shape graphite, in the (C) Chinese script and in (D) almost nodular with also the hardness indentation.

In the Figure 109 (B) it can be observed a zone with a low presence of graphite and more on the right the core material starts; a zoom of this division is taken in the Figure 111 and also here the matrix was examined to check the composition differences. All the compositions results were taken in the Table 28 with an explication about from which figure the survey was taken.

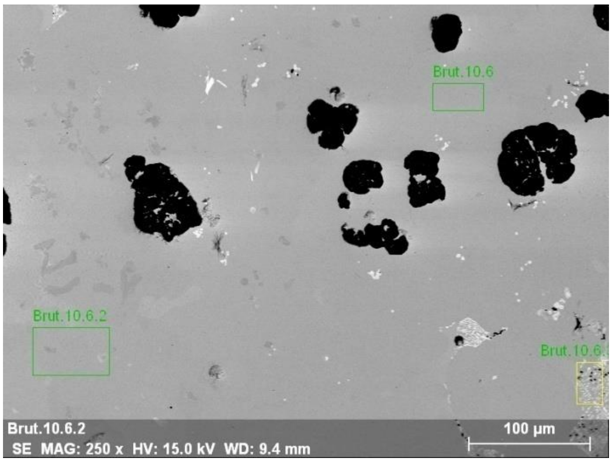

Figure 111 : SEM figure at 250x of the starting point of the core with three composition surveys.

	Spectrum	C	Si	V	Cr	Mn	Fe	Ni	Nb	Mo
From Figure 110 (C)	**Brut.10**	7,98	4,96	0,40	1,10	0,87	79,45	4,79	0,00	0,44
	Brut.10.1	9,03	4,95	0,40	1,21		79,38	4,56		0,48
From Figure 110 (D)	**Brut.10.5**	8,03	5,11	0,26	1,05		79,96	5,09		0,49
	Brut.10.5.2	8,77	4,93	0,30	1,22		79,39	4,94		0,44
From Figure 111	**Brut.10.6**	8,26	4,91	0,32	0,63		83,39	2,28		0,21
	Brut.10.6.2	11,03	5,03	1,27	0,66	0,68	77,48	3,13		0,71
	Brut.10.6.3carbide M_2C	17,93	3,90	0,55	1,16		72,21	1,31		2,94

Table 28 : Results of the compositions surveys of the previous figures.

Those surveys show that in the middle of the graphite network in figure (C) the carbon amount increases in a comparison with a point far from it; whilst there are no differences between two points near different carbides as a M_7C_3 and MC carbides as shown in figure (D). In the Figure 111 there is a huge difference of composition especially for the vanadium and carbon.

6.6. Dilatometer tests

The dilatometer tests were done to analyze and investigate about the behavior of the phases and their transformations under the Solidus temperature; the available samples were: XD1, XD2 and XD3 as explained in the chapter 5.1. The XD1 and XD2 samples were thermal treated with a double tempering at 530°C and XD3 sample after it was again treated with a reaustenitization at 1025°C during 1 h.

6.6.1. Heating curves

Dilatometer heating curves obtained on the samples during the heating stage up to 1050°C with a heating rate of 5°/min are given in the Figure 112. In a curve a high slope means a more saturated lattice with the interstitial atoms (ex. Martensite) and a low slope means a less saturated lattice (ex. Ferrite).

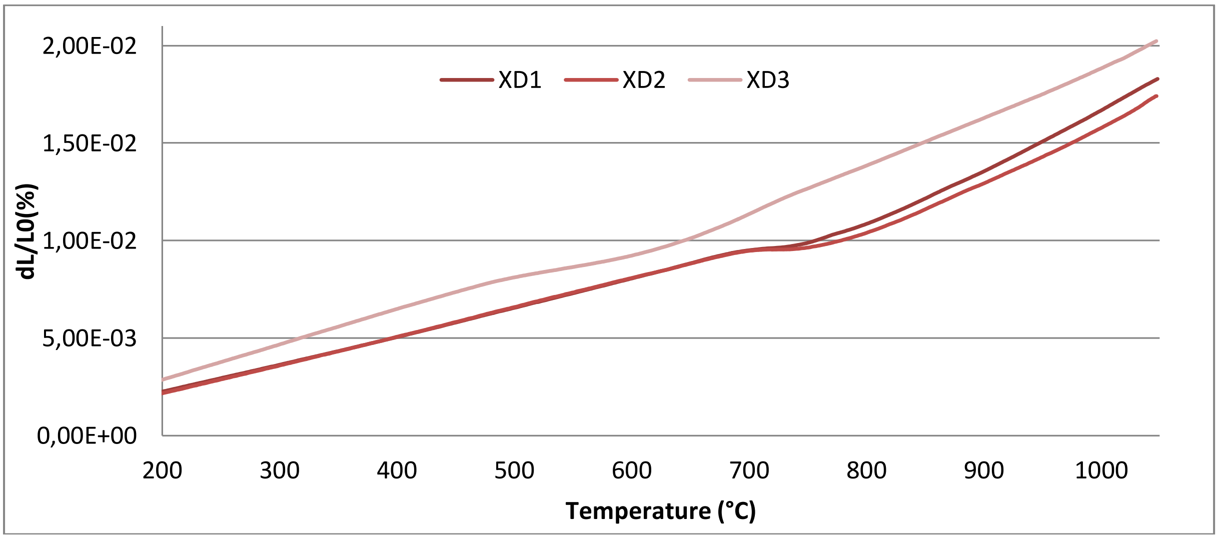

Figure 112 : Dilatometer heating curves obtained about the XD1, XD2 and XD3 sample

6.6.2. Cooling curves

Dilatometer cooling curves obtained on the samples during the cooling stage after the heating up to 1050°C with a heating rate of 5°/min are given in Figure 113.

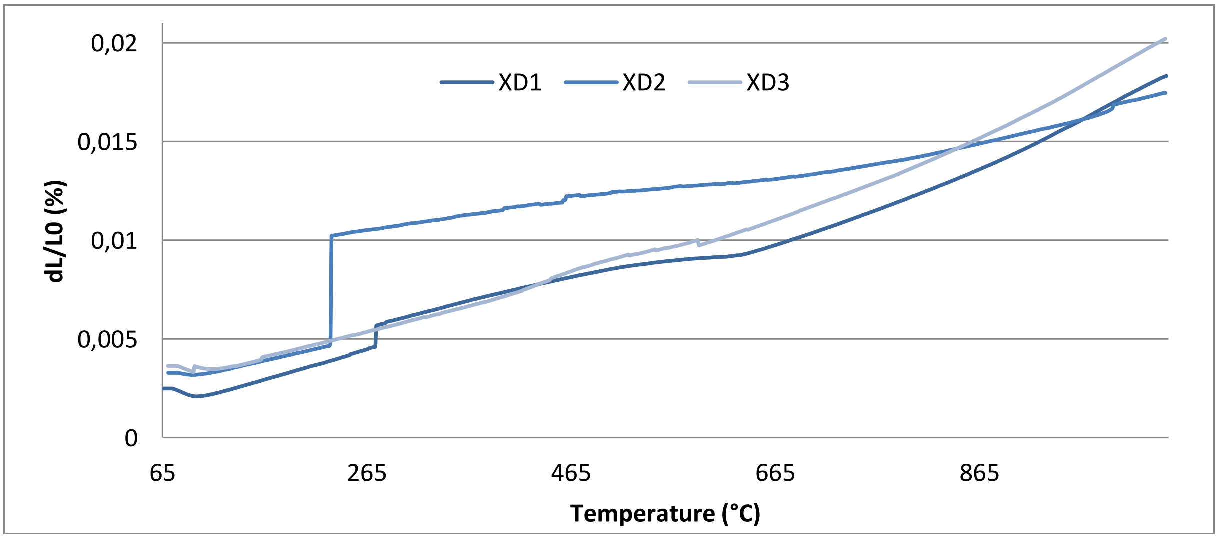

Figure 113 : Dilatometer cooling curves obtained about the XD1, XD2 and XD3 sample.

The results are discussed in the chapter 7.2.

6.7. Magnegage analyses

Magnegage tests were taken on the Composition 2 samples, on the Composition 1 (X1 and X3 for two different depth) and on the R1 sample to investigate the retained austenite amount and evolution after different thermal treatment; the surveys were done at 20 mm and 50 mm from the surface for every sample and the results are reported in the Table 29:

Sample	Position		Value 1	Value 2	Final Value	Position		Value 1	Value 2	Final Value
X1/X3	20	1	59,81	27,85	87,66	50	1	59,81	80	139,81
		2	59,81	38,3	98,11		2	59,81	76	135,81
		3	59,81	45	104,81		3	59,81	85	144,81
R1	20	1	59,81	59,8	0,01	50	1	59,81	47,6	107,41
		2	59,81	59,8	0,01		2	59,81	11,2	48,61
		3	59,81	59,8	0,01		3	59,81	18,8	41,01
N0	20	1	59,81	40,75	19,06	50	1	59,81	6,48	53,33
		2	59,81	42,68	17,13		2	59,81	27,41	32,4
		3	59,81	33,1	26,71		3	59,81	27,41	32,4
N1	20	1	59,81	13,54	73,35	50	1	59,81	22,1	81,91
		2	59,81	8,76	68,57		2	59,81	28,8	88,61
		3	59,81	7,85	67,66		3	59,81	21,15	80,96
N2	20	1	59,81	33,53	93,34	50	1	59,81	41,17	100,98
		2	59,81	46,86	106,67		2	59,81	37,35	97,16
		3	59,81	44,99	104,8		3	59,81	37,28	97,09
N3	20	1	59,81	32,56	92,37	50	1	59,81	43,02	102,83
		2	59,81	37,32	97,13		2	59,81	31,66	91,47
		3	59,81	41,15	100,96		3	59,81	32,6	92,41
N4	20	1	59,81	30,7	90,51	50	1	59,81	49,74	109,55
		2	59,81	38,3	98,11		2	59,81	38,3	98,11
		3	59,81	40,2	100,01		3	59,81	39,27	99,08
N5	20	1	59,81	41,16	100,97	50	1	59,81	62,07	121,88
		2	59,81	44,97	104,78		2	59,81	62,1	121,91
		3	59,81	50,66	110,47		3	59,81	72,56	132,37
N6	20	1	59,81	4,9	64,71	50	1	59,81	41,15	100,96
		2	59,81	30,73	90,54		2	59,81	55,44	115,25
		3	59,81	38,22	98,03		3	59,81	51,66	111,47

Table 29 : Results of the Magnegage tests on the samples in two different depths.

In the table for every sample the position, the values of the first part, second part of the test and the union of those two that is the final results are reported; for every position three surveys were taken. The residual austenite amount increases at the decreasing of the final value and the contrary means a low amount. It is important to know that this value depends to how much the matrix is magnetic but it is necessary remember that all the other possible phases present are not magnetic; thus a low value of the Magne-gage can means a high amount of retained austenite plus also a relevant amount of phases like carbides. In a material rich of phases as graphite and carbides probably the Magne-gage value is considerable higher than the one measured.

The results are discussed in the chapter 7.3.

6.8. Hardness tests

Macrohardness tests (Vickers HV 30) were taken on the Composition 2 samples, on the Composition 1 (X1 and X3 for the two different depth) and on the R1 sample to calculate the surface hardness evolution and the effect of different thermal treatments on it. The surveys were taken in every sample at 20 mm and 50 mm to the surface, for the sample X3 and N0 surveys were taken also at 60 mm to the surface to evaluate better the evolution of the hardness in the sample thermal treated and the Industrial as-cast conditions sample. For every position five indentations were done, in the Table 30 all the hardness values are reported in their corresponding position and the diameter of the indentation.

Sample	Position		Value	Diameter (µm)	Sample	Position		Value	Diameter (µm)
X1	20	1	619	299,74	N2	20	1	749	272,49
		2	644	294			2	730	276,07
		3	628	297,58			3	701	281,81
		4	628	297,58			4	741	273,92
		5	605	303,32			5	730	276,07
X3	50	1	530	324,12		50	1	693	283,24
		2	541	320,53			2	561	314,79
		3	472	343,48			3	708	280,37
		4	484	339,17			4	722	277,51
		5	486	338,46			5	676	286,83
	60	1	193	537,09	N3	20	1	757	271,05
		2	200	527,76			2	693	283,24
		3	198	530,63			3	680	286,11
		4	198	530,63			4	708	280,37
		5	201	525,61			5	726	276,37
R1	20	1	537	321,96		50	1	680	286,11
		2	556	316,23			2	690	283,96
		3	549	318,38			3	697	282,53
		4	554	316,94			4	569	312,64
		5	534	322,69			5	669	288,26
	50	1	440	355,67	N4	20	1	680	286,11
		2	442	354,95			2	656	291,13
		3	460	347,78			3	711	279,66
		4	440	355,67			4	676	286,83
		5	505	332			5	693	283,24
N0	20	1	704	281,09		50	1	650	292,56
		2	683	285,39			2	634	296,15
		3	690	283,96			3	635	291,85
		4	686	284,68			4	660	290,41
		5	673	287,68			5	637	295,43
	50	1	596	305,47	N5	20	1	656	291,13
		2	530	324,12			2	656	291,15
		3	591	306,91			3	628	297,58
		4	572	311,93			4	708	280,37
		5	608	302,6			5	665	288,98
	60	1	218	505,53		50	1	640	294,72
		2	234	487,61			2	561	314,79
		3	236	485,46			3	580	309,77
		4	241	480,44			4	622	299,02
		5	257	465,38			5	530	324,12
N1	20	1	690	283,96	N6	20	1	582	309,06
		2	669	288,26			2	605	303,32
		3	734	275,35			3	572	311,93
		4	656	291,13			4	619	299,74
		5	676	286,83			5	608	302,6
	50	1	511	329,85		50	1	559	315,51
		2	585	308,34			2	511	329,85
		3	588	307,62			3	505	332
		4	613	301,17			4	503	332,72
		5	580	309,77			5	462	347,06

Table 30 : Results of the Macrohardness tests on the samples in two different depths.

The results are discussed in the Chapter 7.4.

7. Discussion

7.1. DTA test discussion

DTA tests were taken on several Composition 1 samples in different depth; the results will be discussed analyzing the heating curves of the normal DTA tests, the heating curves of the DTA three steps, all the cooling curves and finally the temperature effect on the samples.

7.1.1. Heating curves

All the heating curves are reported together in the following graphs since the test conditions are the same. The results are divided in three different graphs; the Figure 76 and Figure 80 are united and all the peaks are shown with zooms at 1140-1260°C, 1100-1140°C and 400-1100°C. It is possible to have as a reference the Table 18 and Table 22 for the peak explanations because the peak numbers are the same; in the following figures the number corresponds to the theoretical solidification steps of the real material whether they are follow backwards. In the Figure 114 four principal phases are formed at high temperature and showed with arrows; in this part of the spectra not all the curves are simple to interpret like the X4 and X5 that not show clear MC peaks, but primary MC carbides and austenite are evident almost in all the curves. All the MC carbides showed in the Figure 88 with SEM figures can be formed between the peak (12) and (9); they can be primary MC carbides with different amount of vanadium and niobium or intragrain and intergrain eutectic MC carbides. The morphology of the eutectic MC carbides and the primary MC carbides depends on the position of the sample.

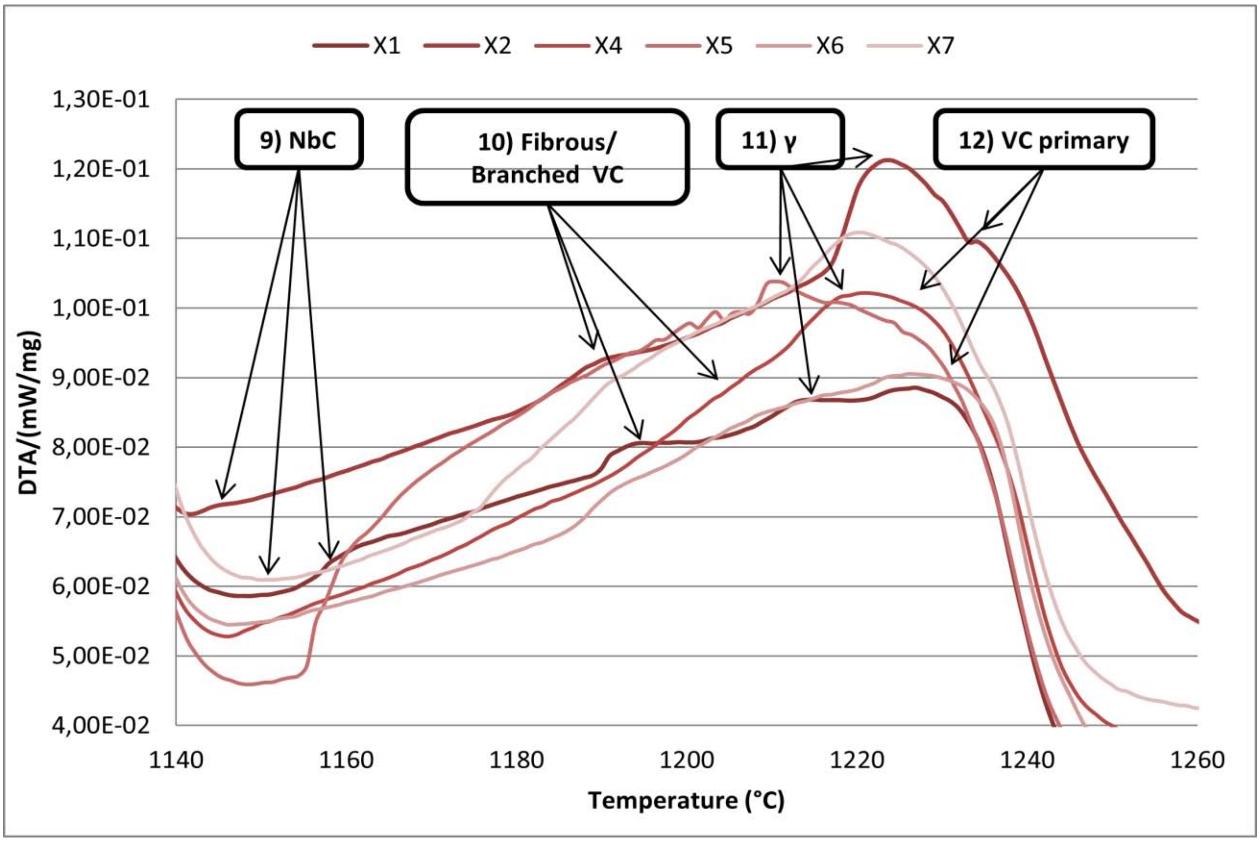

Figure 114: Zoom about the “X” DTA in the temperature range 1140-1260°C with the possible explanations of all the peaks.

At lower temperature before the Solidus temperature there is the formation of two eutectic carbides of different types. In the Figure 115 there is in the peak (8) the formation of M_7C_3 carbides in two possible different morphologies: lanceolate and normal M_7C_3 (massive globular) carbides as it is shown in the Figure

11 and Figure 14, the morphology depends on the position and to the cooling rate since the composition does not change in this range of depths. In fact it is reported in Figure 96 and Figure 108 (D) that there is the presence of a M_7C_3 carbide with a different composition (richer in vanadium) but only in the range of depths 40-55mm. The peak (6) can be only the M_2C carbide since the SEM figures about the Dilatometer tests at 1025°C show its destabilization and the M_7C_3 carbides do not show any changes, thus M_2C carbide is the first eutectic that is dissoluted because the sequence of destabilization is the same of the dissolution sequence. The M_2C carbide dissolution can be observed in the Figure 102.

It was observed that the graphite is present in all the samples in the interdendritic zone and near or a M_7C_3 carbide or a M_2C carbide; it is also observed that the graphite can grow directly together with the M_2C carbide as showed in the Figure 110 about the Industrial as-cast conditions sample. The peak (7) as a consequence is the graphite since the link between the M_2C carbide and graphite is evident in all the samples as shown also in the Figure 84 for the X sample and in the Figure 98 in the DTA samples. The various position of the peak can lead to the different amount in the depth of the graphite as shown in the Stream analyses; the consequence of the amount is the different evidence of the peak. The composition surveys about the carbides confirm this hypothesis since the two carbide peaks are sharp; instead of it, the graphite exhibits a large peak due to the nearness at other two. It is correct to say also that after the primary carbides and the austenite, those are the only possible eutectic phases. In the Figure 116 shows that qualitatively there is less presence of M_2C carbides near to the graphite big particles in some zones of the X2 sample. Those considerations and the SEM delays can say that probably the slope changes or non-evident peaks are the graphite. Those solidification steps can be justified with SEM figures and the observation of the carbides shape in different positions.

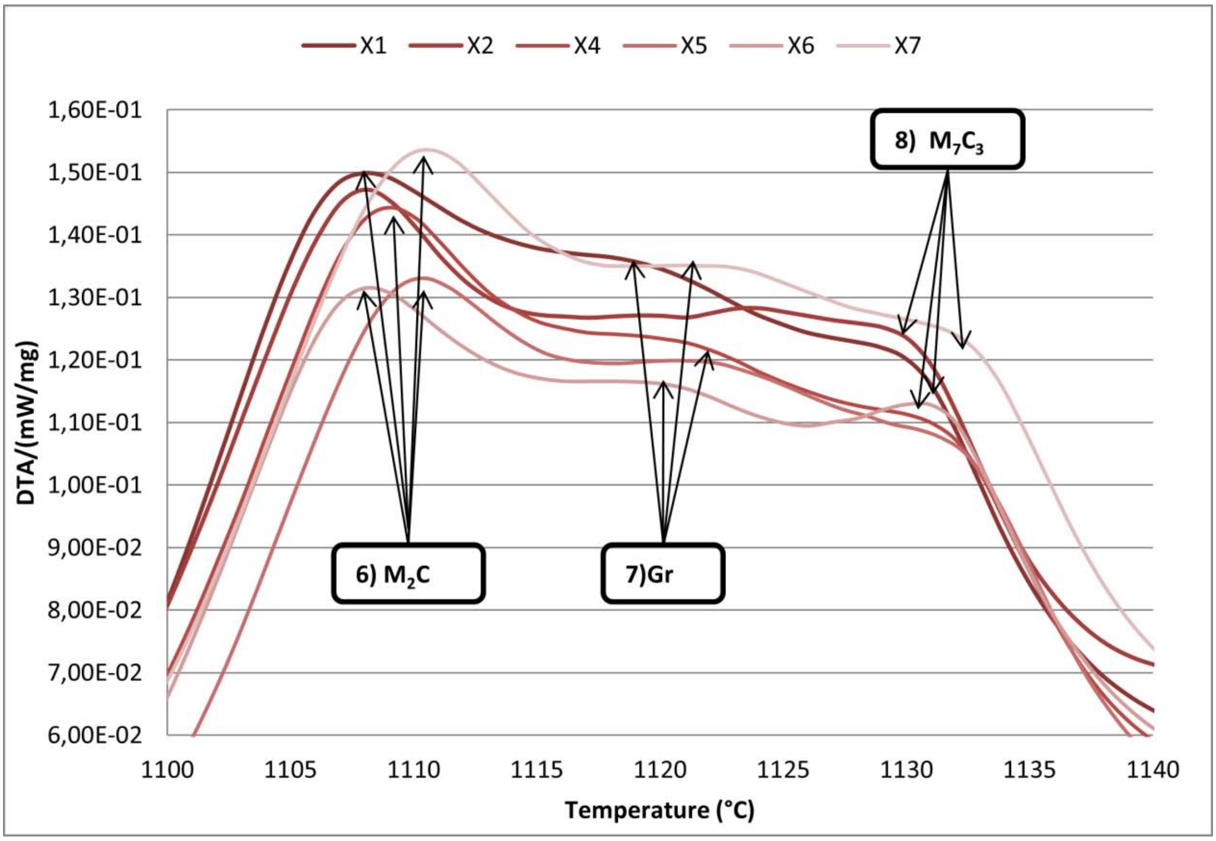

Figure 115 : Zoom about the "X" DTA in the temperature range 1100-1140°C with the possible explanations of all the peaks.

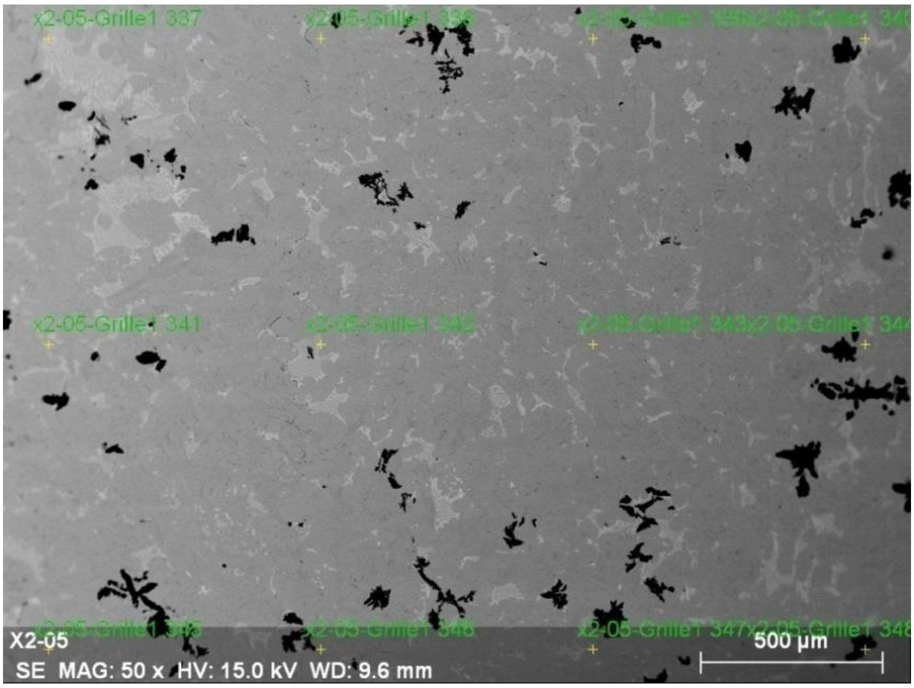

Figure 116 : SEM figure at 50x about the X2 sample at 5mm to the left board with a grille point delays.

The SEM analyses show clearly the MC carbide, M_2C carbide and M_7C_3 carbide in various morphology and compositions. It is also possible to see inside the grain the secondary carbides but is not possible to have a precise analysis of it. In the following Figure 92 there are shown three types of carbides:

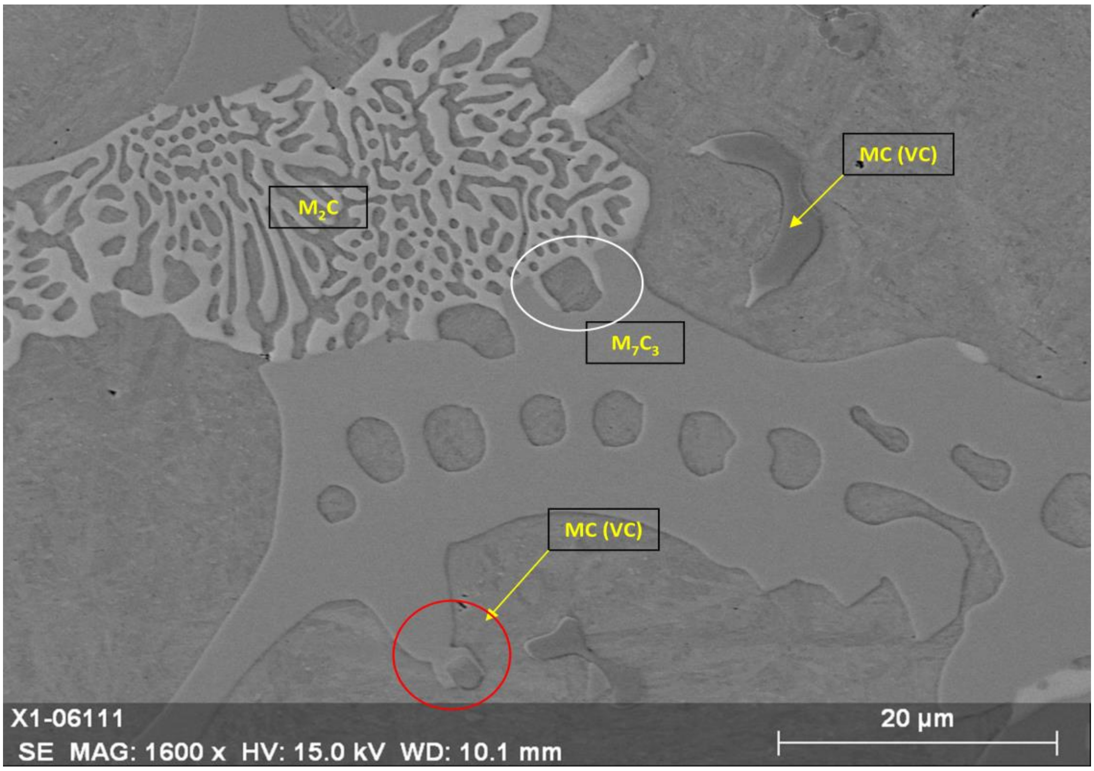

Figure 117 :Zoom at 1600x about the X1 sample near the surface

The figure can be a good explanation of the solidification steps in fact in the red circle a M_7C_3 carbide is covering a MC carbide explaining that the latter was the first formed; the same argument can be used in the white circle where the M_2C carbide is covering the M_7C_3 carbide. Another example of this covering can be seen in the Figure 92 (B) where in the blue circles there are a few M_2C carbide that are covering a lanceolate or dendritic like M_7C_3 carbide.

The last part of the solidification can be explained by the Figure 118:

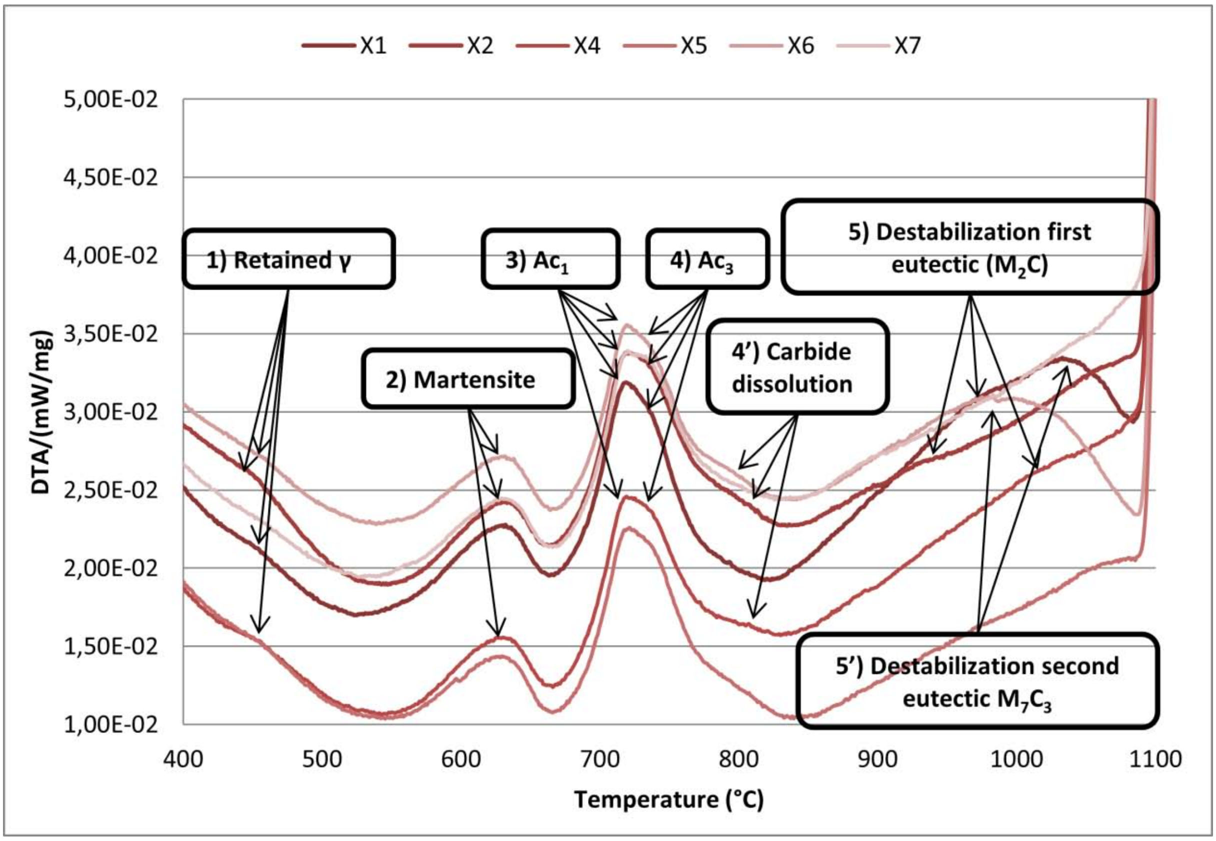

Figure 118 : Zoom about the "X" DTA in the temperature range 400-1100°C with the possible explanations of all the peaks.

As it is possible see the steps (5) and (5') about the destabilization of the eutectic carbides are more evident for the samples nearer to the surface with one type or two. This can be explained by the phenomenon reported in the Paragraph 4.2.5 about the effect of vanadium and niobium; in a centrifugal casting the niobium present tends to move near to the core for its density. Here as it is possible to see in the Figure 88 and Figure 89 it tends to form NbC carbides or "Raisin tige" carbides with a high niobium amount and it is enough to have an amount of vanadium that gives precipitation. The temperature range 400-850°C was analyzed with three steps reheating cycle more into the depth.

7.1.2. Heating curves of the three steps reheating cycle

The main aspect of this test was checking the effect of the secondary carbides dissolution present in the original material on the M_s and in general on the other main temperatures (Ac_1 or Ac_3). In the X1 heating curve the peak of the secondary carbides dissolution and the peaks of the two eutectic carbide destabilizations are evident in the temperature range 750-1100°C as shown in the Figure 119 and it was taken as an ideal sample for the test to check the consequence of the carbides dissolution. There is also a third peak at 1060°C about another carbide but it is not possible to investigate about that because to check the effect of the dissolution it is necessary to stay below the melting point as explained previously (to have the dissolution of that carbide there is risk of arrive to it). The peaks numeration is present also in the Figure 120.

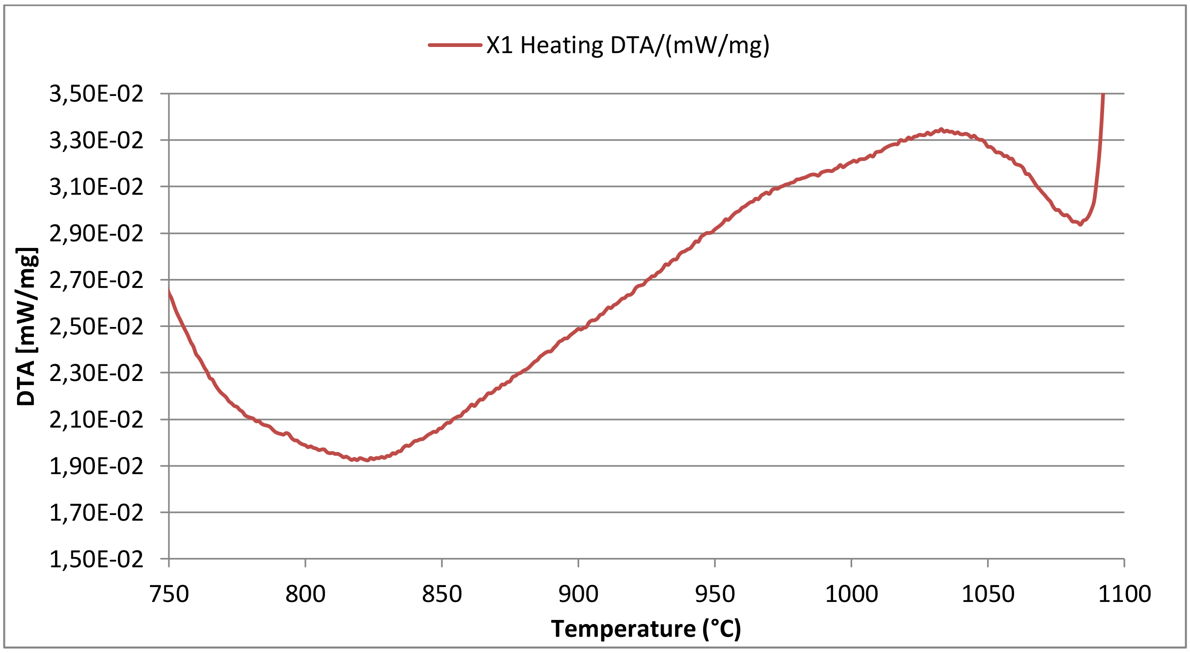

Figure 119: Zoom from 900°C to 1100°C in the X1 heating spectra

The results of the dissolution can be seen in the Figure 120 on Ac_1 and Ac_3:

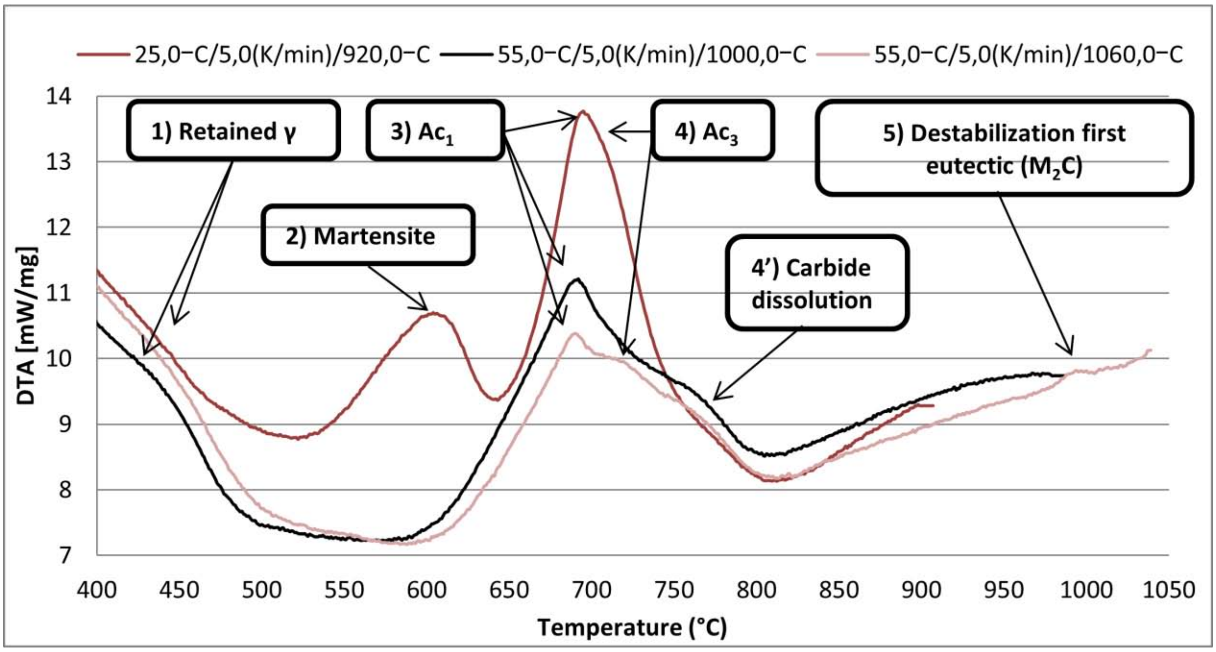

Figure 120: Zoom from 400 to 1050°C about the heating curves

The results for every temperature are:

- 920°C: The destabilization of the austenite is not evident and the spectrum is very similar from the normal DTA (Figure 119).
- 1000°C: The residual austenite is more evident here than the others. The martensite decomposition that was at almost 550°C is disappeared or is present as a complex peak with the Ac_1. The increased elbow on the right of the Ac_1 peak probably is due to the carbide dissolutions of the martensite decomposition; it was present also in the normal DTA curve and probably it is due to the double tempering treatment that started the martensite decomposition. The effect of the decomposition probably is enhanced to the supersaturation of the matrix. It is not excluded that in general the peak

(4’) has both secondary carbides from the martensite decomposition and secondary carbides from the precipitation due to supersaturation. There is a large complex peak because the Ac_1 range of temperature is larger and so it can contain the martensite decomposition shifted of 50°C and the Ac_3 (more evident after). The higher amount of carbon brings the martensite decomposition near to the start of the austenitization.

- 1060°C: The residual austenite peak is present but not so evident; probably the first dissolution gave a little amount of it but with a reheating it was dispersed. The martensite peak also here is not present maybe for the same reason of the previous treatment; in this case it is more evident the carbide dissolution peak at 761°C and it is sure that it is not the Ac_3 because the latter is present at 721°C. The amount of carbon is not varied so but is decreased in the matrix because the Ac_3 is more evident, maybe this decrease of the carbon content comes from the disappearing of residual austenite in combination with the starting of the destabilization of the first eutectic carbide. It is possible to see the destabilization of the first carbide type in the same point of the normal X1 but with a different shape.

The carbides presented after a double tempering usually are more stable and probably the delay of the carbides dissolution is due to this fact (the carbides that come from the martensite decomposition). The same argument can be done for the martensite peak, in fact in the first curve the peak starts at almost 540°C according to the precedent heat treatment (2*530°C/24h). The martensite and thus the carbides with a “heat treatment” as the first step tends to be more stable and to have a delay at higher temperatures or with other phenomena. Probably the secondary carbides that were dissolved at lower temperature enhanced the effect of the supersaturation and thus the destabilization of the first eutectic carbide. The test shows the presences of different types of secondary carbides and the effects on the main temperatures also explain that the amount is relevant.

7.1.3. Cooling curves

DTA tests were taken on several Composition 1 samples in different depth; the second part of the results will be discussed analyzing the cooling curves of the DTA tests, they are showed all together for the high temperatures above the Solidus temperature and below it to underline the cooling phenomenon. The numbers on the DTA graphs are referred to the sequence of the formations from the liquid or of the transformations. For all the curves the measure scale on the left is for the three steps reheating cycle cooling curves, the right one is for the normal cooling curves.

7.1.3.1. High temperature

All the cooling curves, except the three-steps cooling curves, are showed in Figure 121. In the chapter 0 the results of these curves are shown in SEM figures, it is evident that the structure is similar to the normal samples but is not the same because the thermal history of them is very different. The different DTA tests consequence will be discussed more into the depth after, but it is possible to say that almost all the formed phases present also in the normal samples are formed after a DTA test. The first phase formation is about primary VC carbide, its formation depends on the maximum temperature of the DTA test and at the same conditions the peak is in the same location. The second formation is about the austenite in a range of 30°C in every condition; the closest formation peak is the branched like or fibrous VC eutectic carbides that grow together with the austenite intergrain or intragrain. The latter peak can be near enough to the austenite peak to form a complex peak with the austenite as in the X1 sample at almost 1210°C. In the range of temperature 1160-1210°C so there are formations of the various MC carbide types observed in the different depths, reported in the Figure 88 and explained in the Table 24.

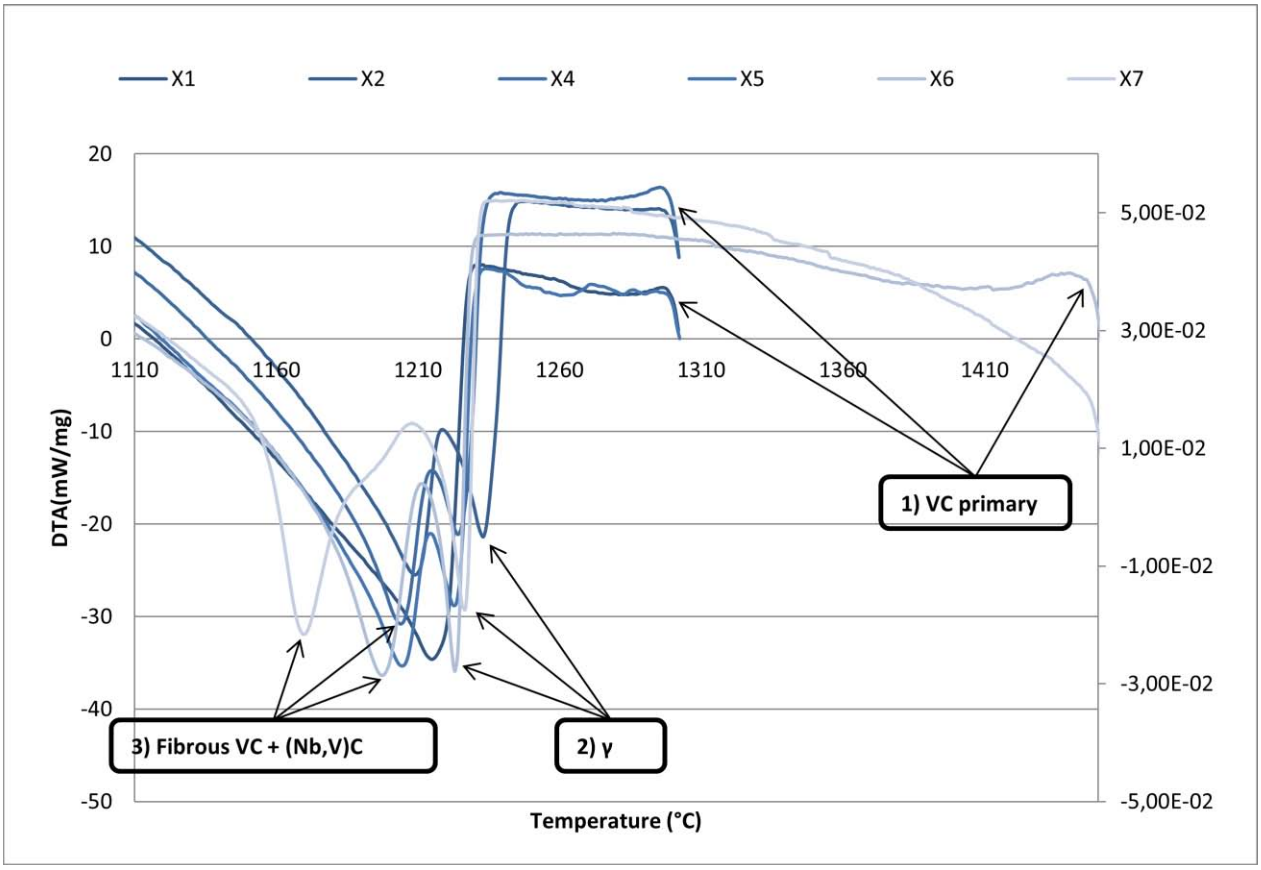

Figure 121 : Zoom about the "X" DTA cooling curves in the temperature range 1100-1450°C with the possible explanations of all the peaks.

In this range two peaks are evident, one at almost 1200-1210°C and the second at 1170-1180°C; the first probably can be related to the fibrous petallike MC morphology that is more evident in the X1 and X4 samples in the Figure 98 (A) and (E), and the second can be related to the branched like MC carbide that is more evident in the X7 as shown in the following figure. Either the carbide presences are evident with a peak or a slope change and they are also very similar as morphology but situated in different positions. In the Figure 122 it is possible to note matrix zones without MC intragrain carbides and on the right a branched like MC carbide in the intergrain zone. The NbC formation is not evident but the peak can be collocated in this range.

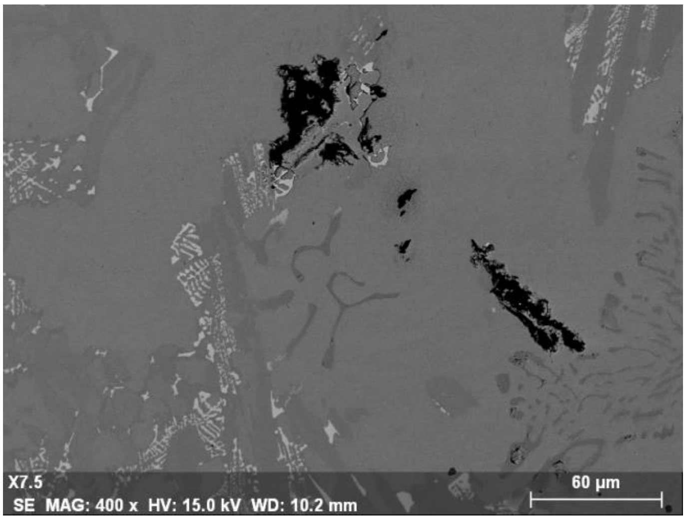

Figure 122 : SEM figure about a branched like VC carbide in the DTX7 sample.

It is important to make an observation on the figures mentioned before about the X1 and X4 samples because in the first one the fibrous MC carbides are extended in all the diameter of the austenite dendrites, instead in the second sample the carbide is smaller; probably this fact confirm the peak definition since in the X1 austenite and the carbide form a unique complex peak.

The second temperature range examined above the Solidus temperature is the 1000-1150°C; in this range there is a formation of two eutectic carbides M_7C_3 and M_2C carbides. The two peaks are evident and see in the chapter 0 the composition differences between the M_2C of the different DTA samples is less relevant than the M_7C_3 differences, and this is confirmed with the distances between the peaks that are higher for the latter carbide. Probably in the normal material the distance between the M_2C and the M_7C_3 peaks is higher because in the DTA samples two carbides seem to grow together in the same liquid as opposed to the normal sample structures. In the Figure 98 (A) the division between the two carbides is more evident and the M_2C grows together with graphite, thus the graphite peak probably is present near to the M_2C peak. The graphite amount is very low as it is possible to see also in the various pictures, thus its formation is not so evident especially whether there is a strong correlation with another phase in the same position. Probably based on the solidification steps, especially based on the M_7C_3 formation, the M_2C and graphite formations are bonded; in the X7 sample for example the M_7C_3 and M_2C formations are very close one to the other and the graphite is not present as shown in the Figure 98 (F). The graphite peak is theoretically collocated between the M_7C_3 and the M_2C peaks, nearer the latter one.

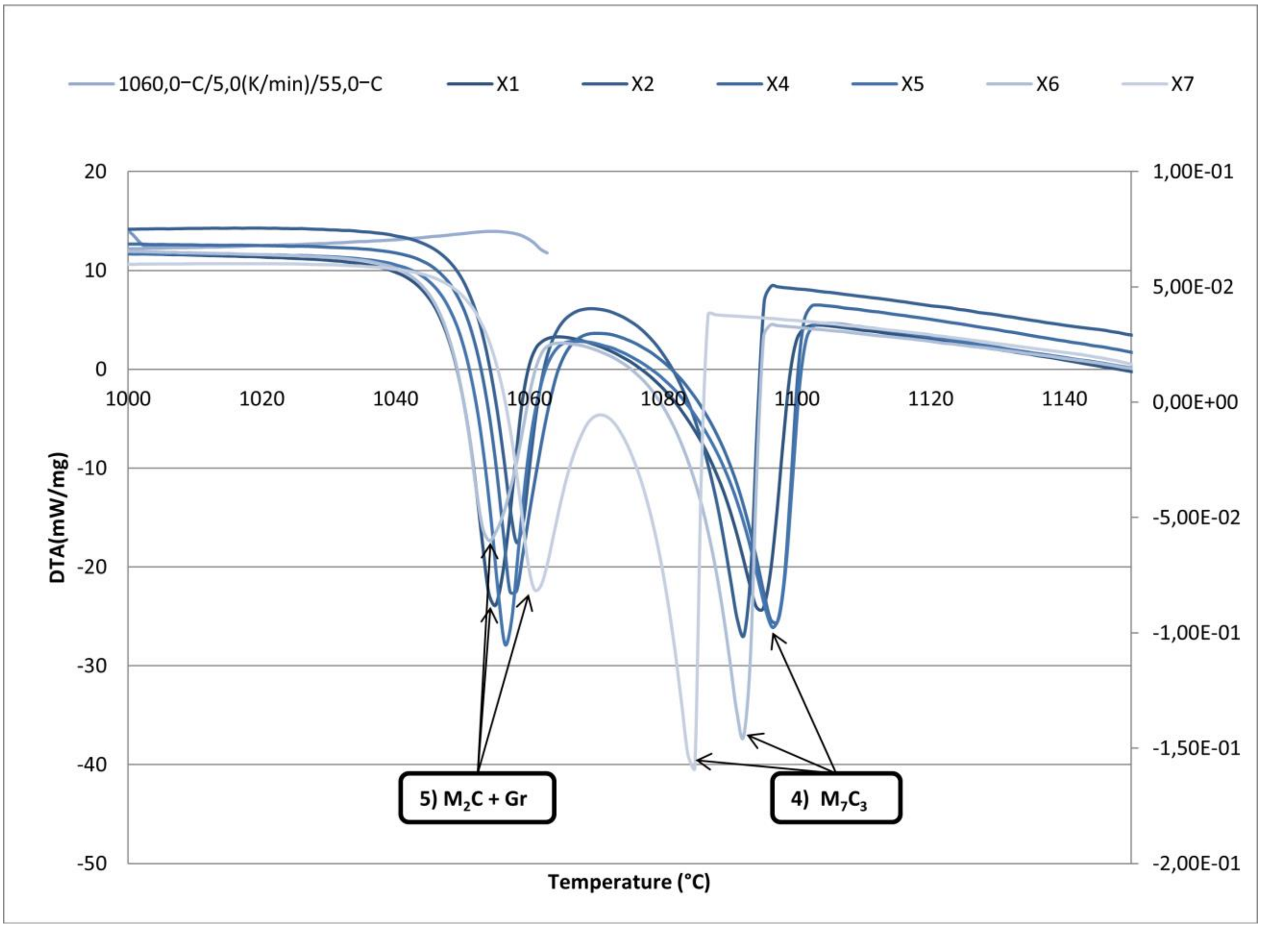

Figure 123 : Zoom about the "X" DTA cooling curves in the temperature range 1000-1150°C with the possible explanations of all the peaks.

7.1.3.2. *Cooling phenomena at low temperature*

Below the Solidus temperature that is considered the M_2C formation, in the range of temperature 830-1030°C it is possible to note in three curves a phenomenon of continuous precipitation of secondary carbides due to the supersaturation of the matrix. This effect is more evident near to the surface for the effect of the centrifugal casting explained in the subchapter 4.2.5 on the composition, especially on the composition of vanadium and niobium. The local high vanadium content gives as an effect a precipitation of small secondary carbides after their formation; as a proof, the phenomenon is evident in the nearest two samples to the surface and on the X5, probably for a local high vanadium amount. The presence of supersaturation means also that the niobium is not present in the matrix to relieve the vanadium effect; probably the niobium tendency is to form only carbides.

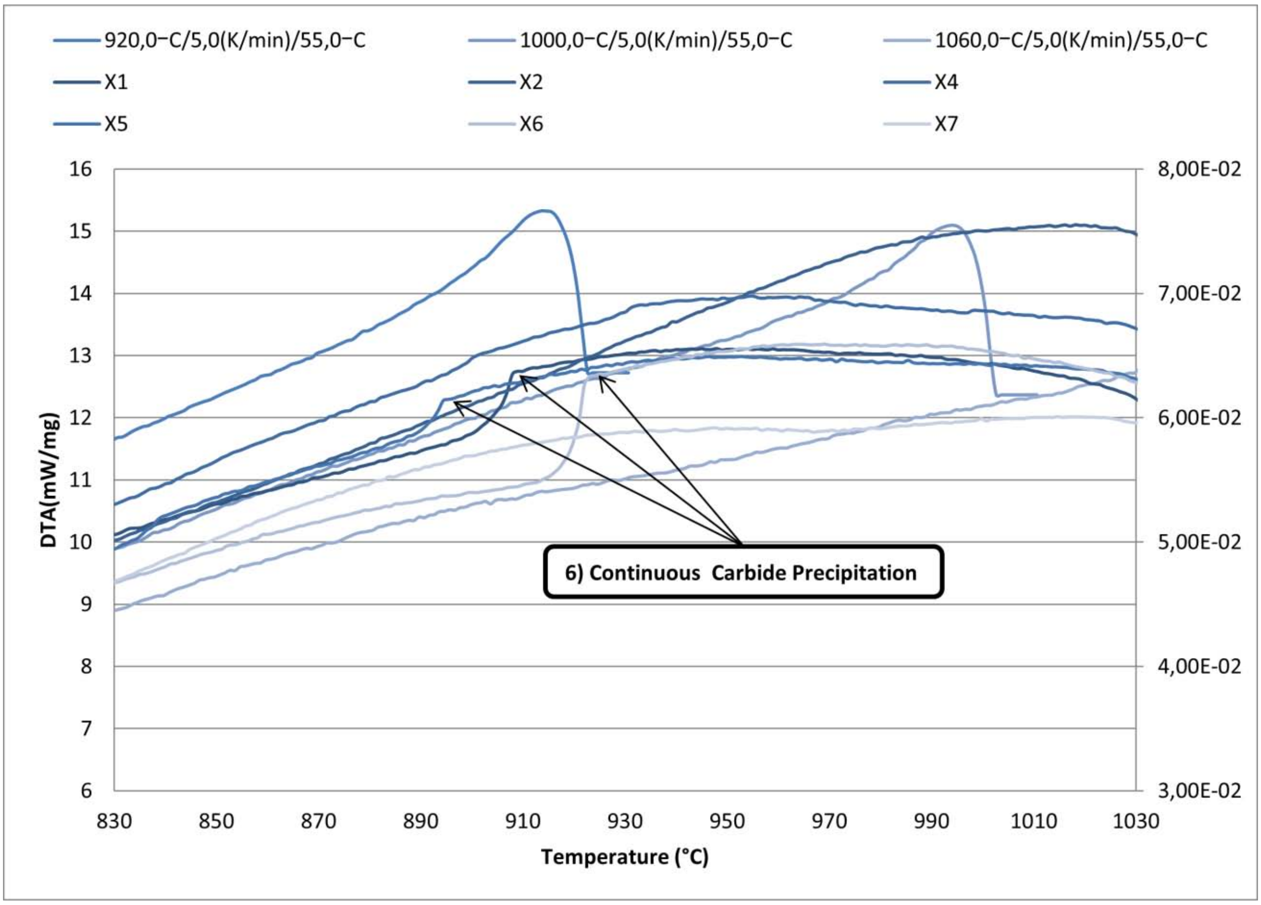

Figure 124 : Zoom about the “X” DTA cooling curves in the temperature range 830-1030°C with the possible explanations of all the peaks.

The second particular phenomenon below Solidus temperature is present in the range of temperature 500-750°C; it is not related to the material but it is due to gas presence that is diffused at high temperature inside the material from the bottom part of the sample. The test has a protective atmosphere but the bottom shape of the sample and the melting pot cavity are not the same and some gas as oxygen can stay present under the sample. In the Figure 125 all the curves are showed including the DTA three-steps curves because the first step of the latter test is the only one that does not present this disturbation; this can be explained because the temperature of 920°C was not high enough to allow the gas diffusion through the metal from the bottom part. At the melting temperature the gravity pushed the metal to the bottom of the melting pot and the gas to the up due to the temperature but not enough to escape probably due to the applied pressure. As proof it is possible to observe the Figure 94 where the holes left from the gas are evident, and can be noted that for the X1 the holes are in the bottom part instead of the X7 they are in the upper part of the sample. High temperatures and a longer time with it allow the gas to diffuse upper and this effect can be observed also on the curves since the X7 has the longest phenomenon from 700°C to 500°C. These gas movements and probably volume changing can disturb the thermocouple and give these artifacts.

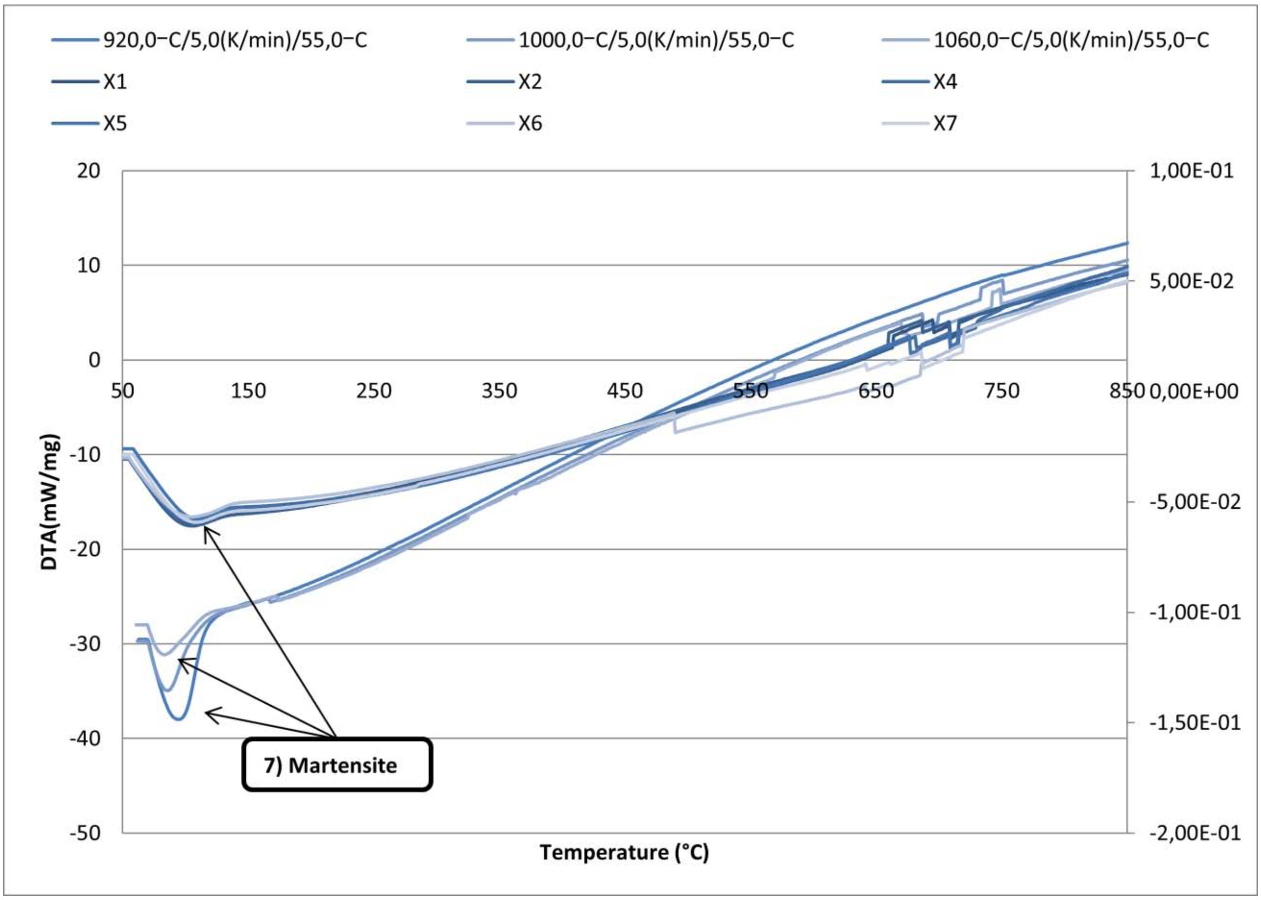

Figure 125 : Zoom about the “X” DTA cooling curves in the temperature range 50-850°C with the possible explanations of all the peaks.

At lower temperature is present the start of the martensite transformation (Ms) in the same position in all the conditions and it can be noted its tendency to shift at lower temperature for the DTA three-steps due to the increasing of the carbon content inside the matrix.

7.1.4. Temperature effect

As it is shown in the previous subchapter below the Solidus temperature there are not differences between two different DTA test temperatures; whereas above the Solidus temperature a longer period at high temperature can modify the morphology and the solidification steps of the material. In the Figure 126 and Figure 127 there are reported two situations with two close samples at different test conditions. The effects of the different temperature are not the same because between the samples with the same conditions there is a different local composition as the peak positions can show and between close samples the peak positions can also show some similitude. The Figure 126 shows that in both samples the MC primary carbide peak is evident unlike the other graph but in both graphs there is an effect due to the longer period at high temperatures to increase the distance between austenite and eutectic MC formations. This effect probably is due to higher growing of the primary MC carbides that consume more carbides-forming elements changing the local composition and as consequence it gives a delay of all the formations or a change of morphology or preferential carbide type formation as in the case of X2 and X7.

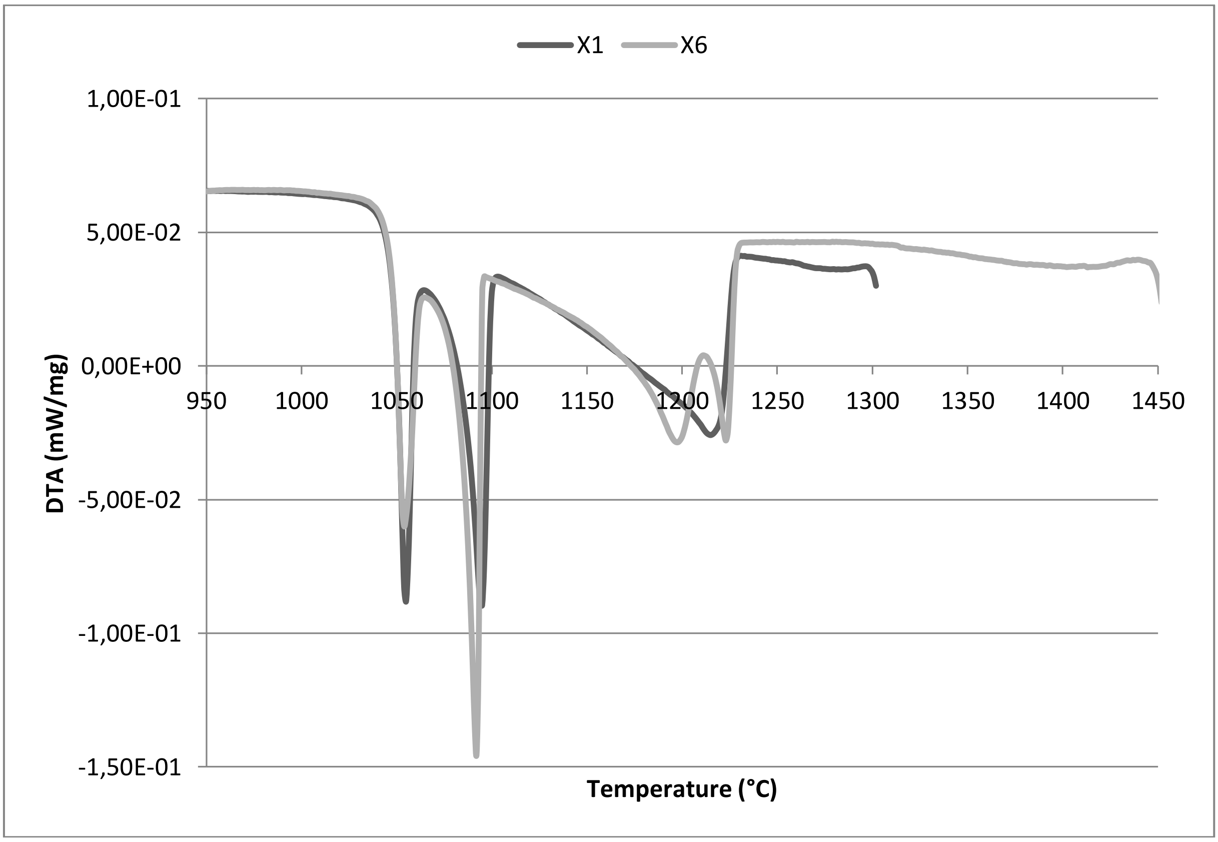

Figure 126 : Zoom about the X1 and X6 samples cooling curves in the temperature range 950-1450°C.

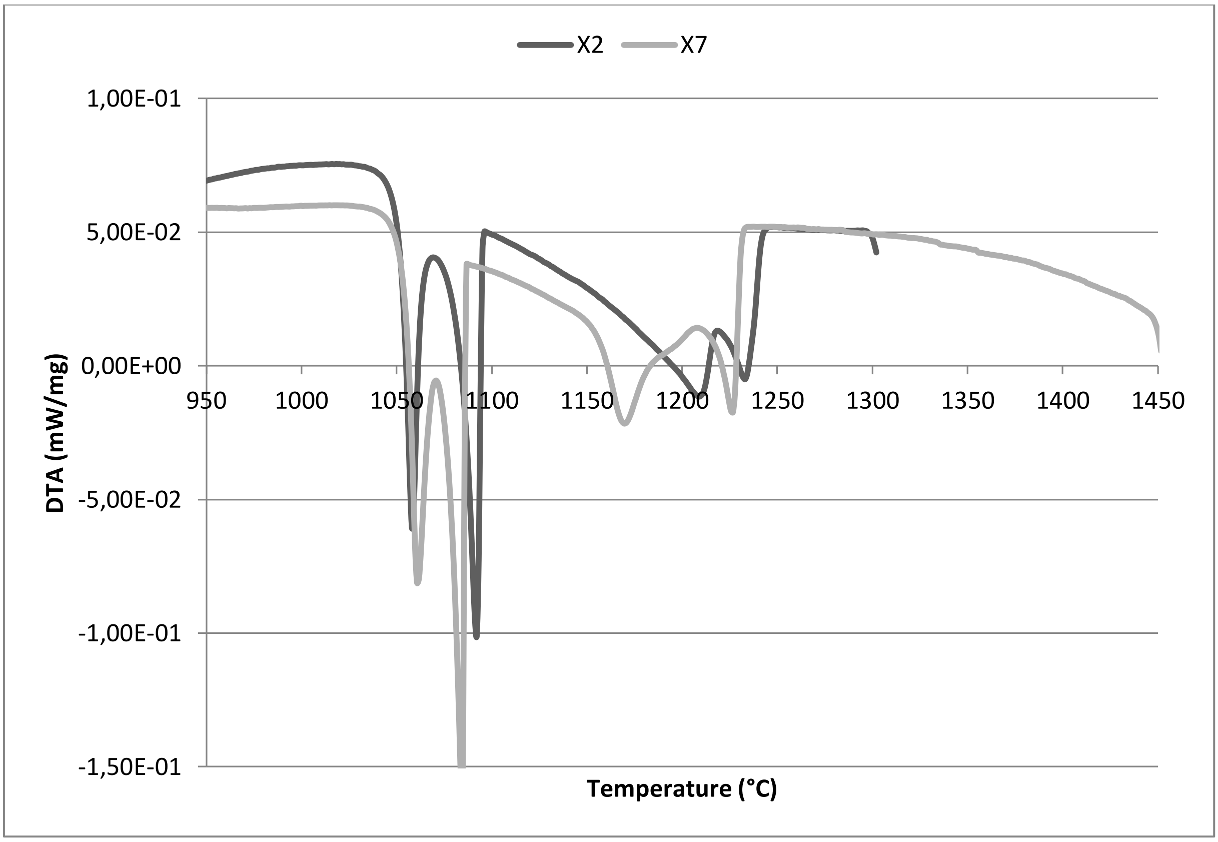

Figure 127 : Zoom about the X2 and X7 samples cooling curves in the temperature range 950-1450°C.

The formation of the MC primary carbides above 1400°C is not usual (Figure 126) and it is due to the presence of little inclusions that act as nucleus particles; in the case of the MC carbides can be especially the TiN (titanium nitrite). In the normal Industrial conditions this fact does not happen because all those particles are removed with the adding of some substances as foam, but some of it can be present in the final material as shown in the Figure 93. The consequence of this formation advance is a possible delay of the formation of the other phases that can be correlated.

In fact the consequence of longer time at high temperature can be extended on the eutectic M_2C and M_7C_3 because of higher growth of the MC primary carbides and more liberty for the austenite to grow without other phases that use the carbide-forming elements can lead to a higher growth of the matrix. Bigger dendrites mean as a consequence less remaining liquid for the interdendritic carbides. Less liquid and probably less carbide-forming elements amount thus can give a delay of the M_7C_3 carbide formation that is more evident far to the roll surface due to less general elements amount. The formation of the latter carbide is fundamental for the M_2C carbide and graphite formations and those can be advanced at higher temperature for probably a composition change as in the situation of the Figure 127.

It is possible to underline some possible differences of the carbides and the structure in the Figure 114 and in the Figure 121; the austenite formation and direct fusion is approximately in the same range of temperatures (1220-1230°C) as the eutectic MC carbides in the range (1160-1180°C), meanwhile the MC primary carbides are moved at higher temperature in the cooling curves. As underline before the X7 curve in the cooling cannot be taken in consideration and all the other phase temperature formations are modified; but for all the other curves it is possible to affirm that the MC carbides present in the real material and in the DTA samples are not the same since the distance between primary and eutectic carbides are different. In the graphs all the names reported are the same but it is important to emphasize that probably all the phases present before and after the DTA tests are different and the common name is the system to classify it for type.

7.2. Dilatometer test comparisons

Dilatometer curves obtained on the Dilatometer samples during the heating stage up to 1050°C with a heating rate of 5°/min are given in the Figure 128. In a curve a high slope means a lattice more saturated of interstitial atoms (ex. Martensite) and a low slope means a lattice less saturated (ex. Ferrite). In the graph all the dilatometer curves are reported; in two reds the XD1 and XD2 samples and in blue the XD3 sample because before the test it was applied a reaustenitization treatment on it.

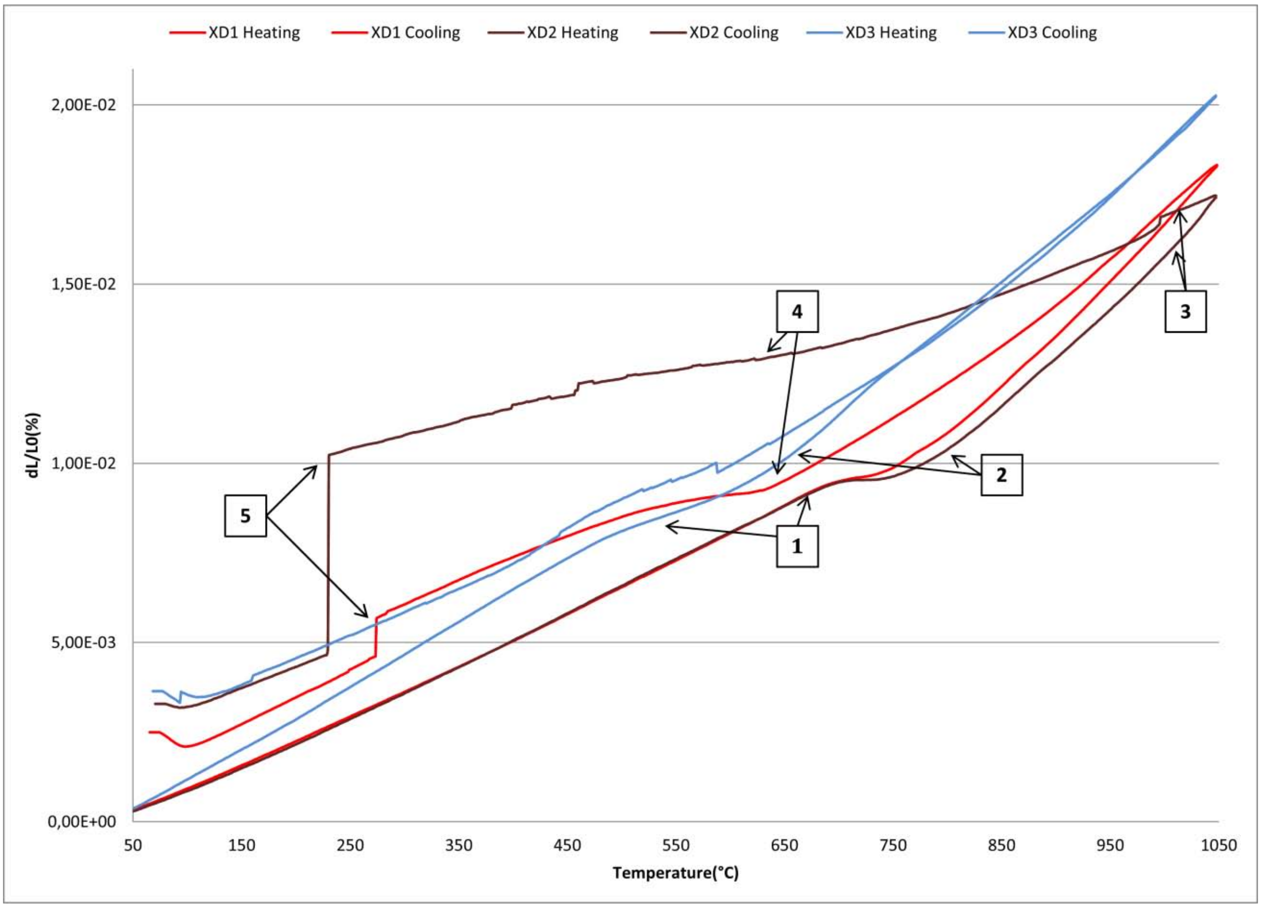

Figure 128 : Dilatometer curves obtained about the Dilatometer sample.

The XD3 sample shows a slightly different behavior in comparison with the other samples; the thermal treatment before the test activated two processes, the homogenization of the composition of carbon and the grain growth of the new austenite. The fist curve is probably accompanied with also the homogenization of the alloy elements due to the reastenitization at 1025°C in 1h, meanwhile the second cannot be considered due to the high alloyed element amounts. During the precedent thermal treatment all the possible transformations and formations have already happened; the results are less changing of the slope due to the homogenization, a lattice already supersaturated and probably a high retained austenite amount. In XD1 and XD2 samples curves the graphite contribution is evident and it gives phenomena that changes all the normal dilatometer curve behavior. In the heating curve on the temperature range 675-750°C there is a combination between the graphite expansion/growth and a contraction of the matrix due to the allotropic transformation; after that from the temperature 750°C there is a continuous dissolution of secondary carbides with a diffusion of the carbon. The martensite transformation is not evident as usual due to the supersaturation of the matrix and to the continuous dissolution of the small secondary carbides; in the XD3 sample the effect is enhanced. From the point (1) in the Figure 128 there is a continuous diffusion of carbon to the graphite, first from the cementite and after from the decomposition of the secondary carbides; during the dissolution of the latter the carbon diffuses to the graphite and to the austenite that becomes more saturated as shown in the Figure 129.

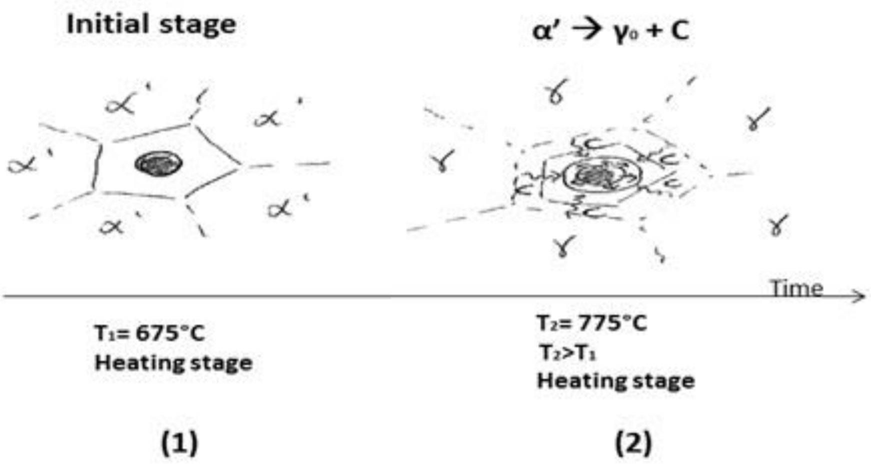

Figure 129 : Explanation of the phenomena occurring to the graphite during a heating dilatometer test; referred to the Figure 128.

In the last part of the heating curves in the range of temperatures 950-1050°C there are phenomena of the destabilization of the eutectic carbides as shown in the subchapter 6.5.1.3 and discussed in the 7.1.2. The “Budding phenomenon” transforms the metastable phases M_2C carbide and probably slightly the M_7C_3 carbide with the formation of secondary carbides and secondary graphite as shown in the Figure 102 and Figure 106. The free carbon presents after all the precedent phenomena gives a supersaturated lattice together with the chromium presents in the matrix and in the carbides create a the formation of M_6C carbides molybdenum-rich and “secondary graphite” formation. The composition analyses in the Figure 104 and Figure 106 confirm the thesis. In some zones due to the increasing of the temperature and time Mo_6C carbide precipitations are observed as shown in the Figure 105. It is possible that such a precipitation leads to the expansion of the material. [2]

The sequence of the Budding phenomenon observed is:

M_2C + C coming from the supersaturated neighbouring austenite	→	M_2C (same location as the parent M_2C but with different composition) + “secondary graphite” + Mo_6C (carbides are located within the matrix/carbide interface)

The “secondary graphite” formation means that a growth or a coarsening of the normal graphite is possible but probably not in a large scale; in the following pictures graphite nodules from the X2 sample and the XD2 sample are showed.

As explained in the chapter 5.1 the XD2 sample goes from a depth of 25 mm to 30 mm; the Figure 130 shows a comparison between two nodules, it is hard to declare that it is present a strong growth after dilatometer test due to the graphite particles dispersion shown in the chapter 6.3.

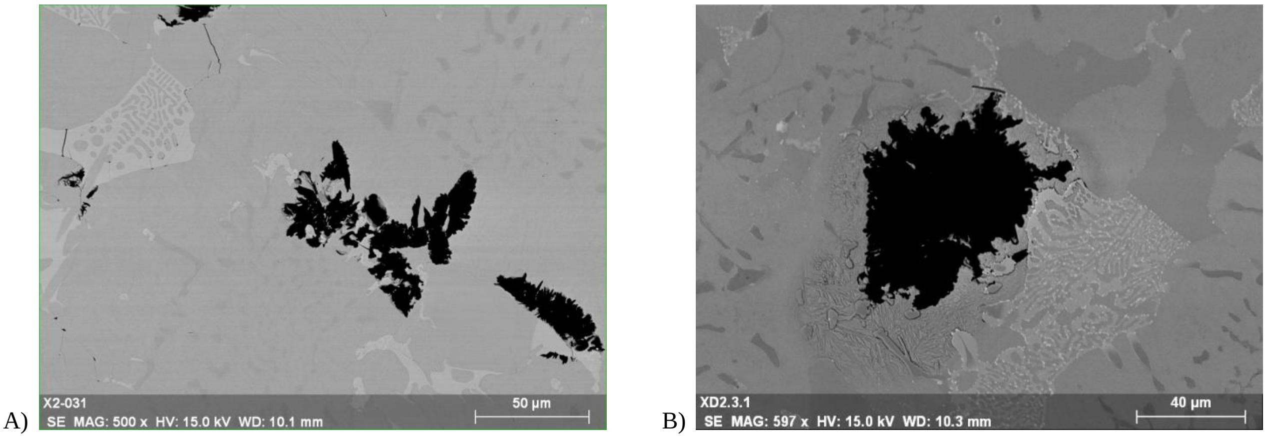

Figure 130 : A) SEM figure at 500x about a graphite nodule of the X2 sample, B) SEM figure at 597x about a graphite nodule of the XD2 sample.

In the picture (B) it is possible to observe a slightly etching near the graphite nodule due to the contact with water during the polishing that as consequence gives an oxidation of the zone; it is possible to observe a homogeneous matrix.

The first part of the cooling curve continues to have the growth of the graphite and the precipitation of the M_6C carbides until 850°C where it is present a zone without changing of the slope; in that range of temperature it is present the contraction of the matrix due to the cooling that decreases the slope continuously, with more evidence in the XD2 sample. From 650°C for the XD1 and 700°C for the XD2 it starts the formation of an oxide layer composed by hematite/magnetite on the surface as shown in the Figure 131 (point 4 in the Figure 128). The oxide layer growth increases the length of the sample and it has a different expansion coefficient in comparison with the material, thus the detector reports on the curve an expansion and a increase of the slope.

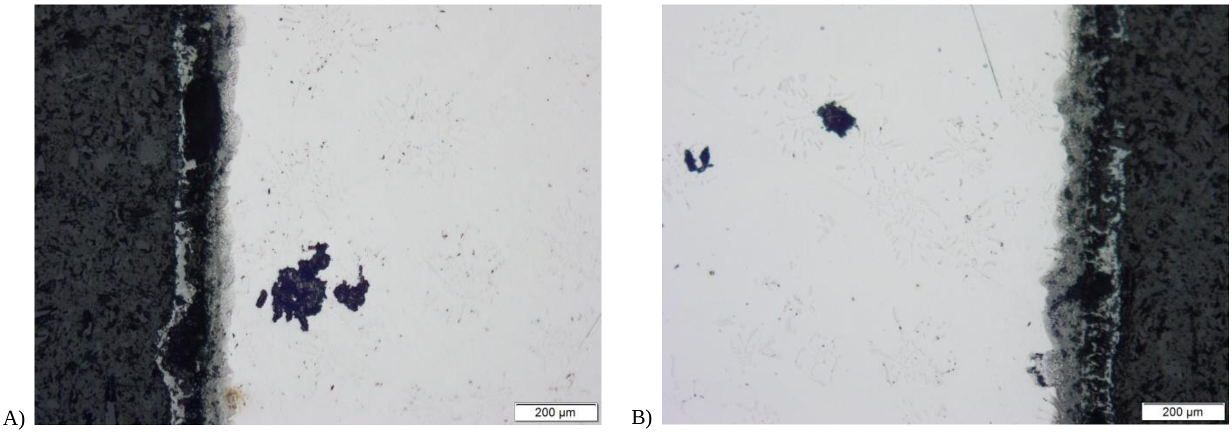

Figure 131 : Optical microscope figured of the XD2 sample at 10x of the left surface (A) and of the right surface (B).

The oxide growing goes on until the moment that the thermal stresses due to the cooling are enough high to crack the oxide layer and thus removing pressure on the detector. This happens almost at 250°C and it is reported as a strong contraction (point 5 in Figure 128), more evident in the XD2 sample because it is started at higher temperature and thus the oxide is grown more. In the XD1 curve the change from the baseline is clear in the 260-640°C, in fact after that disturb the curve has the same behavior (slope) than at higher temperature. The dilatometer pot after the XD2 test is reported in the Figure 132; it is possible to observe the flakes left from the sample. [23]

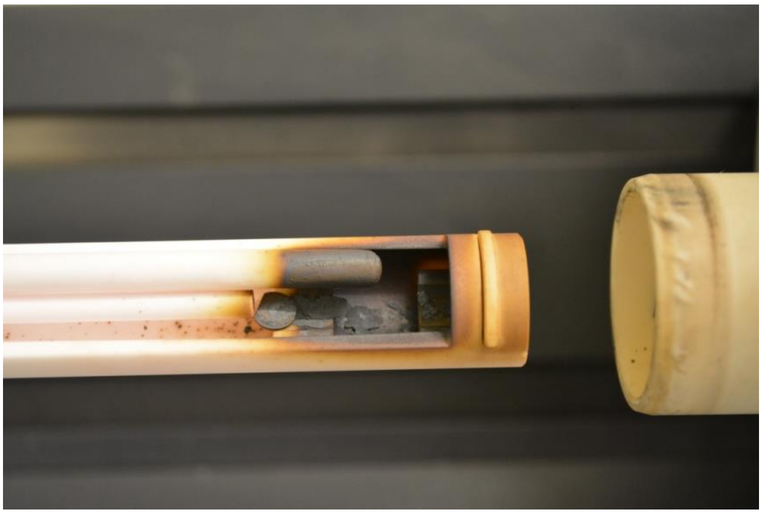

Figure 132 : Picture about the Dilatometer after the XD2 test.

In the XD3 sample probably the oxide layer is formed but is not so evident, there is an artifact from 600°C but probably the different treatment can give a different trend also to the formation of oxide on the surface or probably the surface was already oxide after the reaustenitization. As the magnegage test reports after the reaustenitization treatment the retained austenite amount is almost the 100% near to the surface and this can be another explanation of the behavior in the dilatometer test, in fact the transformation of the martensite is not simple to observe; probably after the test the percentage of retained austenite is lower due to the thermal treatment of the test.

7.3. Magnegage analyses

Magnagage analyses were taken on the Composition 2 samples and on two of the Composition 1 (R1 and X) to check the retained austenite amount. The austenite is not magnetic and a low value of this test means a high quantity of it; in the Table 31 all the results of the Table 29 are evaluated and analyzed with the mean value and the standard deviation to give an idea of the values dispersion. The magnegage values are difficult to correlate and they can give only an indication of the retained austenite amount, but it is possible to understand the evolution of it with the thermal treatments at two different depths: 20mm and 50mm.

	R1	**N0**	**N1**	**N2**	**N3**	**N4**	**N5**	**X1/X3**	**N6**
20	0,01	20,97	69,86	101,60	96,82	96,21	106,35	96,86	84,43
St. Dev.	0,00	5,07	3,06	7,22	4,30	5,03	6,04	8,64	17,48
50	65,68	39,38	83,83	98,41	95,57	102,25	129,22	140,14	109,23
St. Dev.	36,34	12,08	4,17	2,23	6,30	6,34	6,43	4,51	7,40

Table 31 : Mean of the Magnegage test results for the samples in the two depths with the standard deviation

In the Figure 133 all the samples are shown in order of double tempering temperature except for the R1 that has a reaustenitizated treatment. In the case of the latter it is normal that the residual austenite is almost the 100% especially near the surface and at 50mm there is a high dispersion of the value due to the fact that the microstructure probably is composed by austenite zones and martenisitic/ferritic zones. In all the samples there is the tendency to have the value at 50mm higher due to the fact that the core is nearer and thus it is another material with behavior.

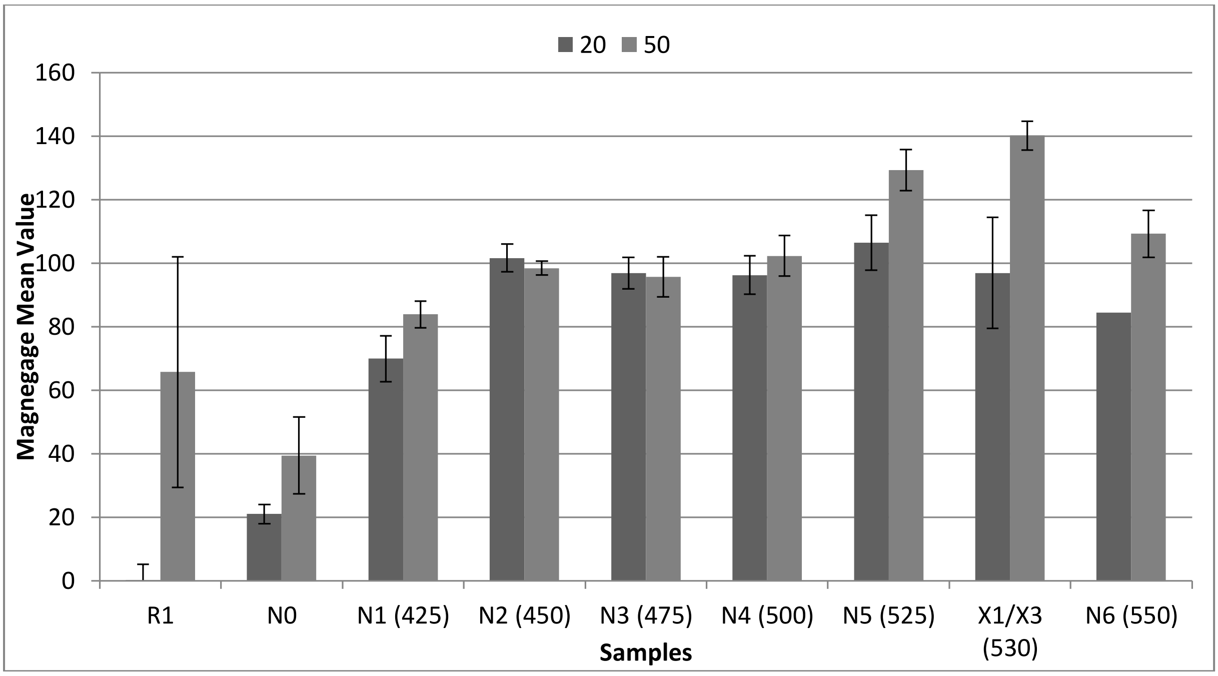

Figure 133 : Graph about Table 31 with all the samples in order of double tempering temperature with the deviation standard.

For all the other samples it is possible to see the double tempering effects in the two different depths; the X sample composed by X1 and X3 in theory is not the same composition but can explain the results for that treatment. One of the double tempering purposes is to eliminate as possible the retained austenite and with the comparison of the N0 sample value at 20 mm with all the other it is evident that the retained austenite amount decreases. In the depth 20mm the evolution say that the best double tempering temperature for this material is between the N5 sample (525°C) and the X sample (530°C) because at this temperature there is a maximum of the performance and for above there is a decreasing of it due to probably other transformations as saw in the DTA tests. Probably at 550°C there is the starting of the martensite decomposition and this can enhance the retained austenite amount as shown in the Figure 78; also the treatment can delay it in a subsequent heating at higher temperature. In the depth 50mm there is the same evolution and the maximum of the previous performance maximum is in the same position and more evident.

7.4. Hardness tests

Hardness tests were taken on the Composition 2 samples and on two of the Composition 1 (R1 and X) to check the hardness of the structure. In Table 32 all the results of the Table 30 are evaluated and analyzed with the mean value of it and the standard deviation to give an idea of the values dispersion; the indentation are taken in three different depths to check the differences where it was possible. The relative diameters are also reported.

	20	St. Dev.	D. 20	50	St. Dev.	D.50	60	St. Dev.	D.60
R1	546,00	9,97	319,24	457,40	27,91	349,21			
N0	687,20	11,30	284,56	579,40	30,51	310,21	237,20	14,02	484,88
N1 (425)	685,00	30,02	285,11	575,40	38,19	311,35			
N2 (450)	730,20	18,19	276,07	672,00	64,37	288,55			
N3 (475)	712,80	30,08	279,43	661,00	52,50	290,70			
N4 (500)	683,20	20,44	285,39	643,20	11,39	293,28			
N5(525)	662,60	28,94	289,84	586,60	44,74	308,48			
X1/X3 (530)	624,80	14,27	298,44	502,60	30,75	333,15	198,00	3,08	530,34
N6 (550)	597,20	19,49	305,33	508,00	34,50	331,43			

Table 32 : Mean of the Hardness test results for the samples in the three depths with the standard deviation.

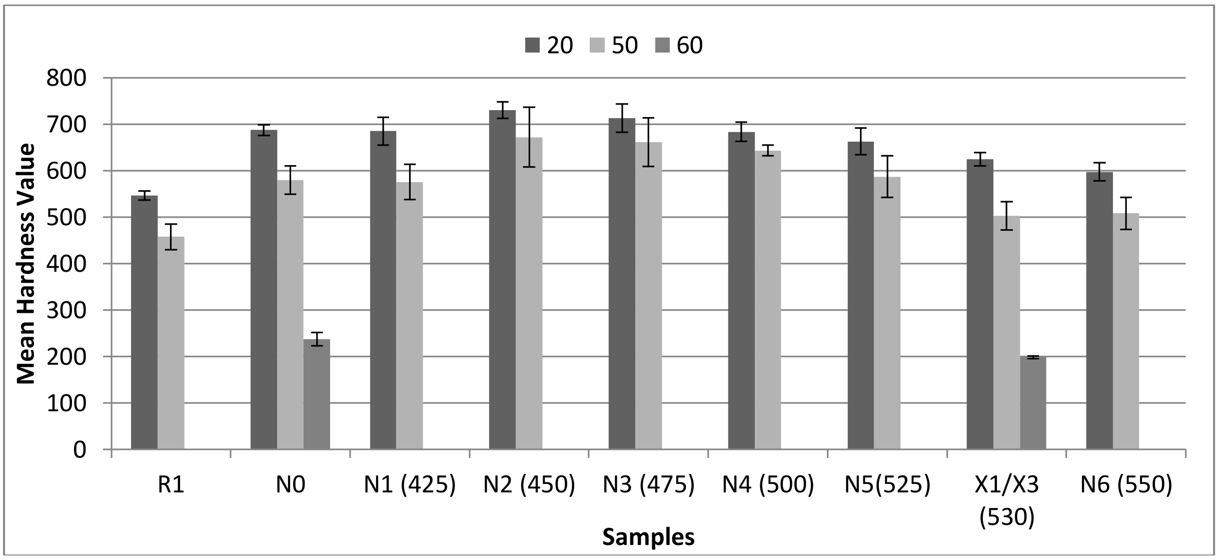

Figure 134 : Graph about Table 32 with all the samples in order of double tempering temperature with the deviation standard.

As it is possible to see in Figure 134, the graphic representation of the Table 32, the R1 has in all the depth a lower hardness value due to the thermal treatment of reastenitization; it probably does not change the amount of carbides because all the carbide dissolutions happen at higher temperature in comparison with the austenitization temperature (1025°C) but it changes the matrix. As shown in the Figure 133 the austenite amount is high in it and this can explain the small decreasing of the hardness holding the carbides. Only in the X sample and in the Industrial as-cast conditions sample were taken indentation at 60mm; in this depth there is the core and as shown in the following figure there is not a change of the hardness amount due to the core presence. The two depths have a similar behavior but the 50mm depth has more relevant differences in the samples. In comparison with the Industrial as-cast conditions (N0), the N2 and N3 samples show an improvement of the performance and after those there is a decreasing of the values due probably to the destabilization of the retained austenite at 450°C and after to the starting of martensite decomposition as described in the Table 18.

7.5. Solidification steps and liquid theory

To understand better the presence of the “strange shape graphite” and the different morphology of the M_7C_3 carbide an important aspect to consider is the remaining liquid in the solidification steps. In the X1 sample the graphite shape is almost spheroidal as shown in the Figure 51, whereas in the X2 and X3 samples in one zone is present this “strange graphite shape” as in the Figure 54 and in the Figure 57. In general the spheroidal graphite to grow in the isotropic way needs a lot of space (liquid space) and probably in the X1 sample the solidification microstructure has more spaces. It is known that in the rolls microstructure usually at almost 30 mm of depth there is an equiaxial zone that divides two columnar zones, for rolls with 1000-1300mm of diameter.

7.5.1. Complex thermal history consequence

The complex thermal history of the sample can be a problem to understand the real reason of the presence of the graphite shape and M_7C_3 carbide morphology changes; as shown in the chapters 6.2 and 6.3 the graphite shape changes in every depth and as shown in the Figure 61, Figure 63 and Figure 65 the thermal treatments can change it enhancing or adding the graphite branches. Those considerations can say that the graphite shape modifications are enhanced with the increasing of the thermal treatment temperature with the Solidus as the maximum possible temperature; as discussed in the chapter 7.2 the supersaturation of the matrix enhance every possible diffusion of the carbon and after the destabilization of the first eutectic carbide it is possible the “secondary graphite” formation, thus the graphite can be formed or modify in a large range of temperature.

7.5.2. The Reheating

To avoid the complex thermal history and understand the real solidification steps it is necessary to think about the solidification sequence in the Industrial as-cast conditions. In the Figure 135 is reported the graph only about the N0 sample of the Figure 74 placed up to a larger Figure 59 with the division in five zones and under the explanation of the zones. During the solidification in the centrifugal casting near the mould is formed first a layer of “small” Equiaxial microstructure that is of 8-9mm in this case (from point 1 to 10), the second instead is a “small” Columnar microstructure (from point 11 to 33 in this case). As said before almost at 30mm from the surface usually is present a “bigger” Equiaxial microstructure (from point 34 to 44 in the case) and finally there is the second Columnar microstructure that is the “bigger” one (from point 45 to 55). The presence of the second Equiaxial zone is more near the core due to the fact that this roll has diameter of 800mm. After those microstructures a point of connection between the shell material and the core material is present and underlined with wavy lines and as the sfericity can say there is the core. As it is possible to see in every microstructure the sfericity changes and the trend of the graphite shape is modified as shown also in Figure 61 and Figure 110. Those microstructures are formed in this way for the phenomena of the reheating; it involves an interior of the shell material (far from the surface) and it is due to the contact with the melted core material during the casting. This contact gives a reheating of the zone that is perturbed and the structure that was forming (“small” Columnar microstructure) is interrupted; from this position the microstructure will not continue as the latter but as “bigger” Equiaxial microstructure because the first two microstructure acts as a mould. The “bigger” Equiaxial microstructure is not similar actually to the small one because it is the result of the perturbation of the columnar structure, with in comparison less order.

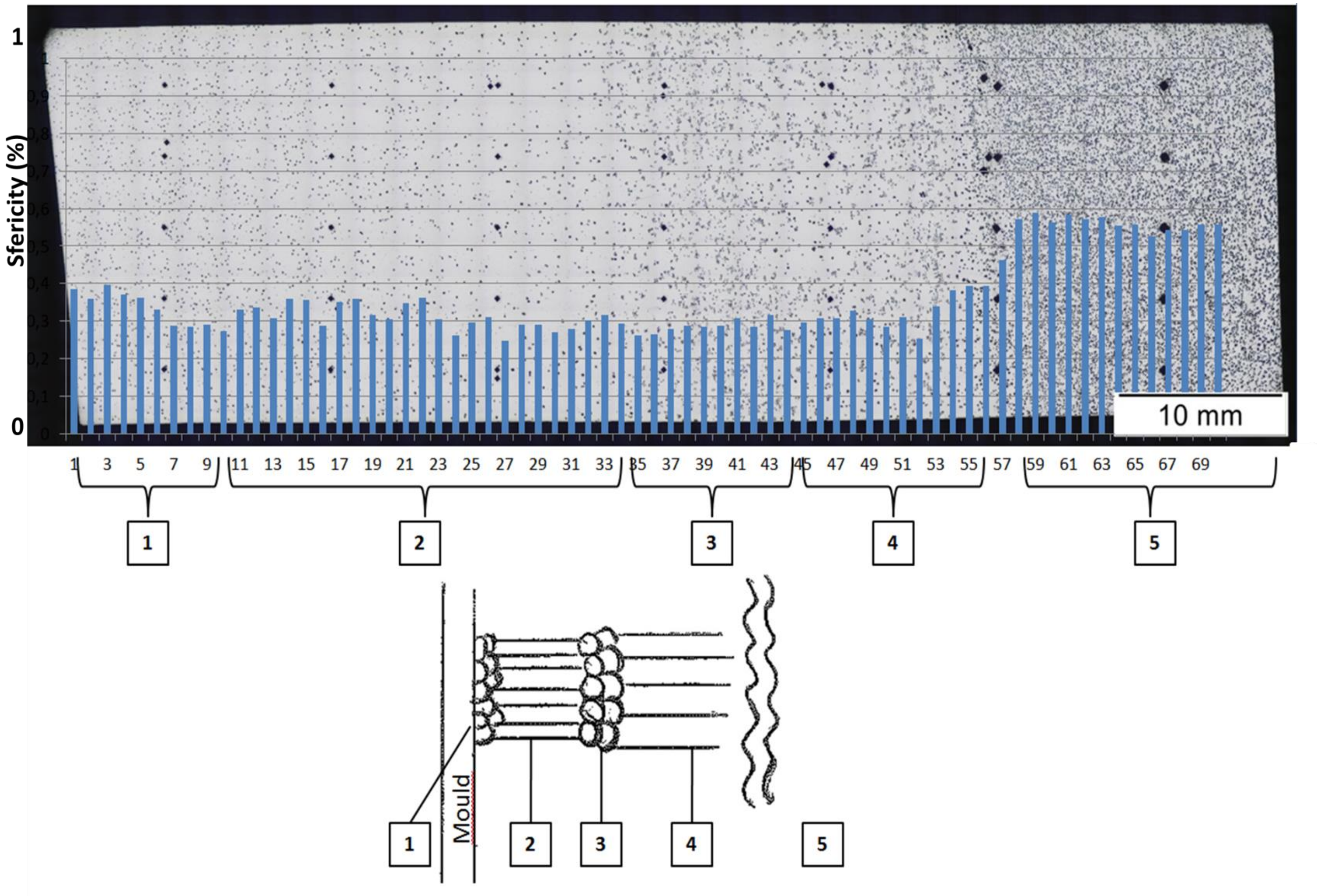

Figure 135 : The graph about graphite particles sfericity only about the N0 sample of the Figure 74 placed up to a larger Figure 59 with the division in five zones and under the explanation of the zones.

7.5.3. M_7C_3 carbide formation consequence

In these conditions it is possible to think about the solidification steps and the remaining liquid during solidification. The MC carbides do not have modification (of composition) from the different microstructures because the primary carbides precipitate in the liquid and the eutectic MC carbides grow together with the austenite. The composition surveys show that the silicon amount in the matrix is homogeneous, in the M_7C_3 carbides it is not present and in the M_2C it is present in a high amount. As it is shown in the DTA curves and in the DTA samples analyzed with the SEM the graphite is formed together with the M_2C or in a similar range of temperatures. Moreover, after the dilatometer results it is known that the Solidus temperature is about the M_2C carbide dissolution. As discussed in the chapter 7.1 the formation of M_7C_3 carbides is according to the structure of the matrix, thus tends to be lanceolate in the columnar zones where the austenite is with dendrite shape and massive globular in the equiaxial zones. Whether all those assumptions are correct the remaining liquid after the formation of the M_7C_3 carbide according to the matrix is rich of silicon and carbon, since in the latter carbide the silicon is not present and carbon comes from the austenite due to the decrease of the temperature. The Figure 136 shows the possible explanation in two possible microstructures referring to the X1 and X2 samples. In the columnar microstructure there is probably enough space for the nucleated graphite particles to grow in the isotropic way after the formation of the M_7C_3 lanceolate carbides that give a liquid zone rich in particular of silicon. In the equiaxial instead the spaces are not large enough to give the isotropic growing, thus the shape tends to be with branches because the carbon coming from the austenite during cooling grows the graphite but in the interdendritic spaces between matrix and M_7C_3 carbides that in this situation are like a blocking phase for the growing.

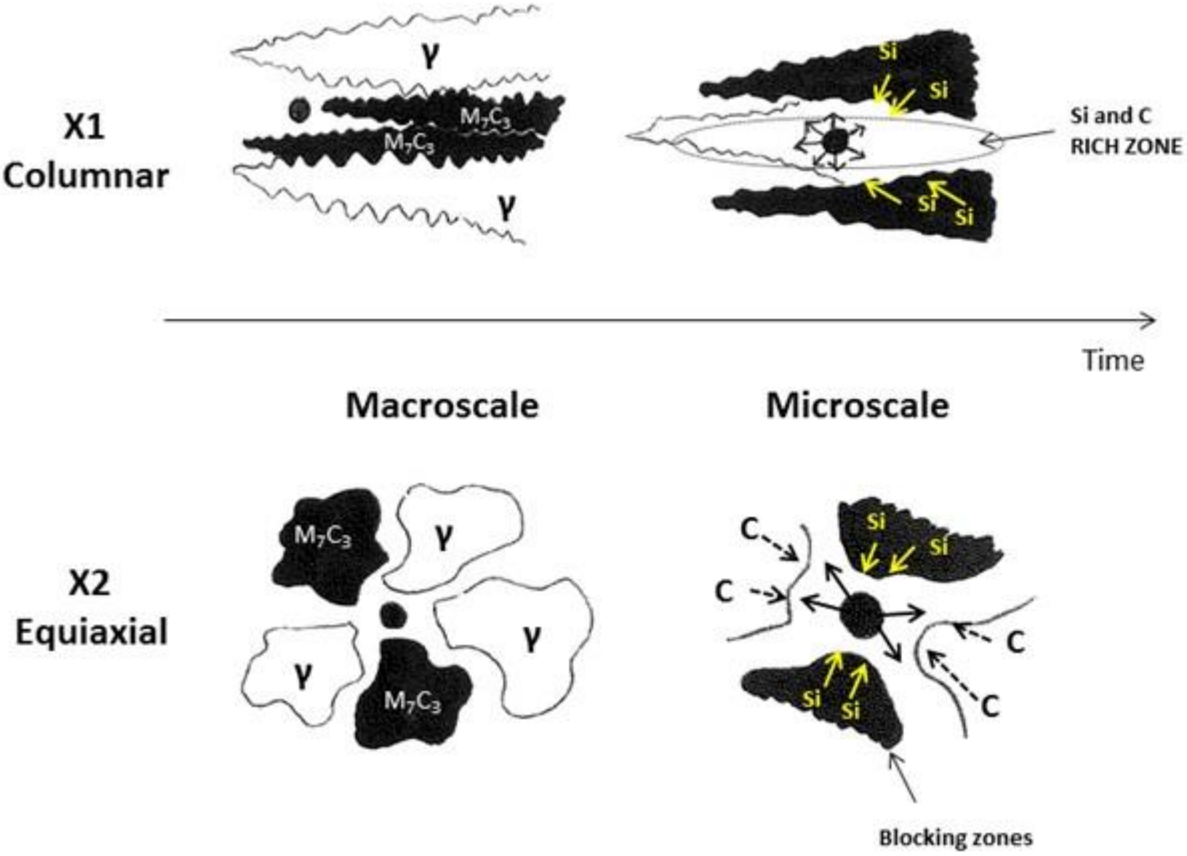

Figure 136 : Situation and possible graphite growth with two different solidification microstructures.

Probably the "small" Equiaxial microstructure presents a higher sfericity value in comparison with the others because the cooling rate near to the surface is higher and that condition it is not favorable for the graphite; as it is possible to see in the Figure 73 and Figure 75 the graphite amount in every sample near the surface is lower than in the majority of the zones.

7.5.4. *M_2C carbides and graphite connection*

The other important point is to understand the bond between M_2C carbides and graphite; the conditions for their formations as explained are optimal almost in the range of the temperature 1040-1080°C as shown in the Figure 123 and after the formation of a particular composition due to the formation of the M_7C_3 carbides. The cooling rate can give some explanation of the different amount of graphite or M_2C carbides in some zone but the possible real explanation after the consideration about the SEM analyses on the DTA samples is present in the Figure 137. After the nucleation of the graphite at T_0 during the cooling stage can be present three different situations and the only difference is the composition.

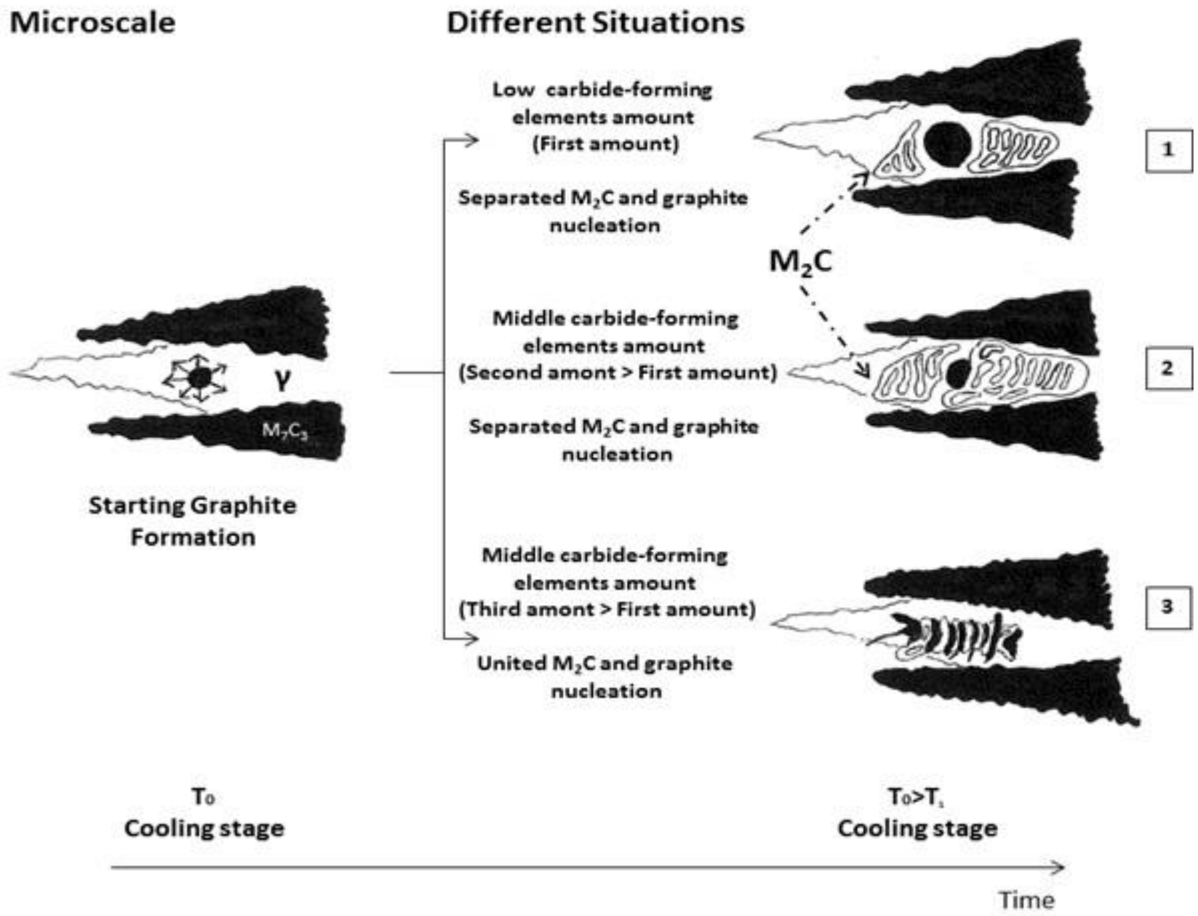

Figure 137 : Explanation in the microscale of the possible situations of the formation of the graphite and the M_2C carbides.

The first situation is for a low carbide-forming elements amount like molybdenum, vanadium or also silicon; the consequence is a high growing of the graphite because the elements for the formation of the M_2C carbides are not enough and the carbon is used all for the graphite growing.

The second is for a higher amount of elements and this means a more elevated growth of the carbides but the latter and the graphite remain divided because the nucleation points are different as in the case of the DTX1 as shown in the Figure 98 (E).

The last possible situation is still with elements amount higher than the first one but the nucleation points are enough near to have a growing together as in the Composition 1 (Figure 57 (C)) and in the Composition 2 (Figure 108 (D) and Figure 110 (A)) between the 40-55mm of depth to the surface, thus in the “big” columnar microstructure as explained. In the Table 27 about the N0 it was reported that in this zone there is the presence of different M_7C_3 carbide vanadium-richer and this composition changes can also give the unite-growing of the M_2C carbide and the graphite; this composition change probably is due to a different cooling rate that provide a lower growth or a nucleation delay of the MC eutectic carbides, that are the common users of the vanadium.

In the Figure 98 (A) about the DTX1 it is shown also the same M_7C_3 carbide composition but without the growing together of the graphite with the M_2C carbide; actually the latter appears to grows with the M_7C_3 carbide. DTX4 sample exhibits the growth of the graphite-M_2C carbide together near the surface of the sample where the cooling fluid cools it, thus with high cooling rate (Figure 98 (B)); meanwhile far from the surface (Figure 98 (D)) the graphite grows alone. Those observations mean that the situation especially for the DTA sample is complex and different in comparison with the material in the real rolls, thus it is better reason only on the real material.

Probably the MC carbides for the lower cooling rate are less formed in comparison with the zones near the surface and the elements can be used by other phases; at the distance of 34-44mm from the depth before the core pouring, the microstructure grows as “small” Columnar structure with probably the MC carbides that are not formed in high amount. When the reheating perturbs the microstructure and it makes restart the solidification from an Equiaxial microstructure that considers the first 30mm of shell as a mould; the temperature of the shell is above the Solidus and with reheating the interior part of it can arrive near the Liquidus temperature, with the melting of many phases. For the heat diffusion from the core probably this zone stay in a plateau of temperature and moreover it has a lower cooling rate; in this condition may the M_7C_3 carbide is more stable and can grow with elements that usually are used by other phases as vanadium according to the matrix. In fact in this zone M_7C_3 carbide vanadium-richer were founded. The consequence of a low cooling rate is the high formation of austenite and phases at high temperature, thus the remaining liquid between the grains is less than in the microstructure near the surface. As consequence the graphite and the M_2C carbide grows together with not enough space to form spheroidal graphite as shown in Figure 136. In the “big” Columnar microstructure as shown in the Figure 135 the sfericity increase until the point of connection with the core, that can means that the spaces in that structure are larger and the graphite can grow more like spheroidal. In the Columnar structure is simpler for the graphite to grow in the isotropic way as it is possible to see in the first two microstructures due probably to a higher order. The effects of the reheating are possible to see also in the 31-34mm with the presence of some strange graphite shape probably due to the heat coming from the “big” Columnar zone after the reheating phenomena. Finally the last possible situation in Figure 137 can occur with a low liquid amount and the two phases must have the formation temperature extremely near to grow together.

It is possible to say that in general the formations and morphologies of the phases can be modified by the cooling rate, composition, distance to the depth, microstructure of the matrix, casting steps and after by the thermal treatments. The graphite can be modify by the thermal treatment but not in a significant aspect, meanwhile the casting and in particular the reheating can change the graphite shape indirectly because it can change the structure, thus the M_7C_3 carbide, and as a chain reaction the graphite morphology.

7.6. EDL method and Performance function

The performance function is a selection method to analyze different materials and to discover which is the most proper for a particular utilization; the function can correlate many different material properties and based on the requirements it is possible assign an importance sequence with the EDL (Enhanced Digital Logic). In the study this methods were utilized to correlate the hardness values and the Magnegage values. The first is a complex value to understand because is due to the matrix and to the carbide present; instead the second is a value difficult to correlate due to the precise surveys and to the empiric bases of the analyses. In a HSS a property that is consider fundamental is the low percentage of retained austenite, thus the function is based on this assumption; as importance sign (α) the EDL method assigns 0.33 for the hardness and 0.67 for the retained austenite. The performance function is:

$$Z_p = \alpha_H \cdot \frac{\mathrm{H}}{\max(\mathrm{H})} + \alpha_M \cdot \frac{\mathrm{M}}{\max(\mathrm{H})} \tag{5}$$

Equation 5 : Performance function of the thermal treatments.

H and M are the sample values and they are divided for the maximum between them; with this important step the values are normalized, as consequence they can be correlated with other different properties and properties as Magnegage analysis can have a higher import. In the Table 33 all the performance function results (Z_p) are reported in the two relevant depths; to arrive at those values the data from Table 29 and Table 30 were used.

	R1	N0	N1	N2	N3	N4	N5	X1/X3	N6
20	0,25	0,44	0,75	0,97	0,93	0,91	0,97	0,89	0,80
50	0,54	0,47	0,68	0,80	0,78	0,80	0,91	0,92	0,77

Table 33 : Results of the performance function.

The samples are reported in order from the R1 (different thermal treatment) and N0 (as-cast conditions) to N6 that has the higher temperature of thermal treatment (double tempering). The results are putted in order from the higher value to the lower one in the two depths as shown in the Table 34.

A)

Sample	20
N2 (450)	0,97
N5(525)	0,97
N3 (475)	0,93
N4 (500)	0,91
X1/X3 (530)	0,89
N6 (550)	0,8
N1 (425)	0,75
N0	0,44
R1	0,25

B)

Sample	50
X1/X3 (530)	0,92
N5(525)	0,91
N2 (450)	0,8
N4 (500)	0,8
N3 (475)	0,78
N6 (550)	0,77
N1 (425)	0,68
R1	0,54
N0	0,47

C)

Sample	Mean value
N5(525)	0,94
X1/X3 (530)	0,905
N2 (450)	0,885
N3 (475)	0,855
N4 (500)	0,855
N6 (550)	0,785
N1 (425)	0,715
N0	0,455
R1	0,395

Table 34 : The results of Table 33 in order from the highest value to the lowest for the two depths (A and B). The different samples are written together with the thermal treatment temperature. The mean values of the two depths for every sample in (C).

The best material and in this case the best thermal treatment that can be applied on the material is the double tempering in the range of temperature 525-530°C as reported in the following table; to arrive at this conclusion it was done the mean value of the two depth values to try to consider the entire roll and not only a single part of it.

8. Conclusions

The main conclusions are reported afterwards following the purposes of the work proposed in the Abstract, all those can be considered the progress of the aim to combine the hard martensite matrix and spheroidal graphite particles in the shell of a duplex material roll.

- ✓ The carbides presence has been evaluated; several carbides were cataloged with different compositions and morphology: MC carbide, M_7C_3 carbide, M_2C carbide, M_XC_Y secondary carbides and M_6C carbides from the destabilization of the M_2C carbides. The niobium and the vanadium were founded in particular in the MC carbides that are considered hard carbides (2000-3000HV). Two different morphology of M_7C_3 carbide were noted with the same composition, they were in different positions and according to the structure of the matrix. The M_2C carbide is present with only a complex regular morphology but it is important to underline the high amount of silicon and molybdenum in its composition; the silicon is present in a constant amount in the matrix and this carbide is the only one that is composed by this element, moreover in high quantity. This fact probably correlate the M_2C carbide with the graphite, they can be formed from the same liquid and in the same range of temperatures.
- ✓ The graphite amount and shape evolution have been evaluated; in comparison with the precedent study the graphite amount has remarkable increase in the material for shell in the duplex roll. It is passed from 0.7 % to the 2-3 %. The graphite shape tends to be roughly spheroidal in the first 35-40mm from the roll surface with the tendency to form some branches according to the increase of the depth due to the different cooling rate and the different microstructure; from the 40mm to the core material it is present a “strange shape” zone where the graphite shows a vermicular or a flakes morphology due to the reheating phenomenon during the casting of the roll after the pouring of the core material.
- ✓ The behavior of the HSS during a heating below the Solidus temperature has been investigate with DTA tests and Dilatometer tests; the destabilization of the M_2C carbides and the formation of an oxide layer were observed. The supersaturated matrix was confirmed with a continuous change of the saturation of the lattice, moreover this quantity of carbon creates several phenomena on the material.
- ✓ The effects of several thermal treatments on the graphite have been evaluated; after the observation of the as-cast conditions, double tempering conditions and reaustenitization conditions with the microscopes plus the observation of the Dilatometer phenomena, in particular the destabilization of the M_2C carbides that give the formation of “secondary graphite”, it is possible to affirm that below the Solidus temperature the graphite is active and the shape can be modify with the different thermal treatments. Those changes are not large and they can only create some small new branches or level the surface of the parent graphite particle probably with the carbon coming from the supersaturated matrix. The process that determines the shape of the graphite in the different depth probably is only the manufacturing of the roll.
- ✓ The solidification steps have been investigated and all the phases were identified; the connection between the eutectic carbides and the graphite formation was discovered, the M_7C_3 carbide in particular has a key role in the formation of it. The formation of this carbide creates the adapt liquid composition during the cooling that achieve the creation of the graphite nodules; the perturbation of it and of the matrix by the reheating phenomenon probably causes the change of the graphite shape and the growth of it together with the eutectic M_2C carbides from the same liquid. The main difference that changes the graphite shape is the amount of liquid during solidification and thus the space to have an isotropic growth.
- ✓ The consequences of the thermal treatments have been evaluated on the phases and on the structure; the different thermal treatments can give a delay of the transformations, for evidence the martensitic

decomposition, and can induce the precipitation and formation of more stable secondary M_XC_Y carbides after the casting. The evolutions of the hardness and the retained austenite amount were analyzed first separately and after together. The hardness was analyzed with several indentations in two different depths and the performance maximum is for the double tempering at 450-475°C; meanwhile the retained austenite amount was analyzed with a Magne-gage in the same two depths of the hardness tests. The maximum performance was for the double tempering at 525-530°C and after a performance function it was underline that that treatment is the most adapt, since the low retained austenite amount is the basic requirement.

9. Prospective

The prospective of the study have the purpose to know more into the deep the properties of the new material, to understand better the phenomena occurring during all the tests and to investigate optional properties that are not taken in consideration. The future work can be divided in:

- Check the real anti-sticking properties of the graphite into the material with specific test or an actual test with real manufacturing conditions.
- Separate the study on the different microstructures present in the roll depth to investigate eventual significant differences. Check the carbides amount in the different microstructure to investigate the possible consequence of the reheating on it; if the MC carbide amount decrease and the M_7C_3 carbide amount increase (with also an increase of vanadium amount on it) in the “Bigger” Columnar microstructure this means that the assumptions about the reheating zone are correct and the graphite shows a shape change only due to the reheating. DTA tests on the different microstructures can underline the different compositions, thus a DTA test at 40-45mm to the surface can confirm the presence of the second carbide composition with a comparison with a previous tests at the same conditions.
- The Stream Motion Analyses showed good indications of the graphite shape evolution and underline the differences of the four different microstructures with the changes of the sfericity, but the comparison between the samples to investigate the real effects of the different thermal treatments was not possible since the material is very heterogeneous and every sample is different. To investigate the real consequence of a thermal treatment it possible to analyze a future sample with the software, submit it on a thermal treatment and after analyze again with the Stream Motion analysis; this sequence probably need time, but can give real results since the comparison between the initial and post-treatment conditions is on the same sample. That investigation can exploit the graphite as an indicator of the reheated zone. In general with this material it is important do not use many different samples for the graphite amount or graphite sfericity comparison since the material is heterogeneous.
- Investigate the tendency of the oxide formation during the dilatometer tests, and if it is possible to avoid it to investigate the real metal behavior. Bonded with this problem, it was possible to observe the different behavior of the reaustenitizated sample on the dilatometer test; investigate the microstructure after the thermal treatment and then after the test can explain the differences. For the next tests it is important to cut a sample that is parallel to the surface in order to analyze only the situation of a single depth to the surface; analyze the sfericity and the amount pre and posttest can confirm the activity of the graphite during thermal treatments. It is possible also analyze the composition of the oxide layer to understand the exact oxide that it is formed, and in particular the elements involved.
- The heat treatment selection with the performance function can be more depth and precise with the adding of other properties as the graphite amount, graphite sfericity or carbide amounts. It can show with an interpolation the possible ideal thermal treatment and it can underline the real effect of the carbide presences on the total hardness value.
- Since the material is new, the real behavior is not known; the material can be considered a composite because it is composed to a metallic matrix and non-metallic particles inside it. In the composite world there are many examples of materials with saving properties due to the particles presence that extend the life of the entire composite. The graphite particles may are able to have additional properties on the entire material in addition to the anti-sticking and lubricant properties (this has to be checked). The purpose can be to correlate the graphite presence with the load of the compression test (the nearest test to the real manufacturing conditions) to investigate the possible increasing of the

elastic zone of the deformation. The micro-deformation of well distribute spheroidal graphite particles can consumes energy coming from the applied forces and extend the elastic zone of the material, that actually is the metal elastic zone. The way to study it could be as follows; that hypothesis can be verified correlating the compression tests of normal HSS (without graphite), the Composition 0 material and the Composition 1 or 2 (higher graphite amount in comparison with the Composition 0). The sample can be the standard one or a small metal sheet to consider more surfaces on contact. To observe the direct graphite deformation it is possible to make SEM observation on the graphite particles after different loading of the compression test that should give different deformation of it: test up to the yield stress(Y), up to the 0.7*Y, 0.5*Y and 0.3*Y.

10. References

[1] J. Lecomte-Beckers, M. Sinnaeve, J. Tchoufang Tchuindjang, O. Dedry; Etude de l’endommagement des cylindres de travail des dernières cages finisseuses d’un train à bandes à chaud pour mise au point d’une nouvelle nuance; Convention RW 6929 Project ENDEFINU; (December 2014).

[2] J. Lecomte-Beckers, M. Sinnaeve, J. Tchoufang Tchuindjang ; Influence of High Temperature Heat Treatment on in situ Transformation of Mo-rich Eutectic Carbides in HSS and Semi-HSS Grades; Conference Proceedings, Abrasion Wear Resistant Alloyed White Cast Irons for Rolling and Pulverizing Mills, Abrasion (August, 2011) ; p. 61-75; ISBN 978-2-8052-0124-0.

[3] M. Durand-Charre; Microstructure of Steels and Cast Irons; Springer; (Paris, 2003); ISBN 3-540-20963-8 Springer-Verlag Berlin Heidelberg New York; Chapter 5, 6 and 21.

[4] N. Oda, P. Fleiner, T. Hattori; Latest Developments of a new technology HSS Work Roll for Later Stands (F4-F7) in Hot Strip Mill Finishing Trains; AISTech 2013 Proceedings; (2013); p. 1977-1984.

[5] M. Brandner, T. Nylén, A. Paar ; Indefinite Chill Cast Iron rolls and future possibilities; 50th Rolling seminar- Processes, Rolled and Coated products- International, Brazil; (2013); p. 495-500.

[6] J. Lecomte-Beckers, J. Tchoufang Tchuindjang, F. Delaunois, J.P. Breyer ; Metallurgical assessment of two HSS rolls grades for Hot Strip Mill; AIStech 2007 Proceedings.

[7] J. Lecomte-Beckers, J. Tchoufang Tchuindjang, M. Sinnaeve ; Recent trends in Hot Strip Mill roughing mills: High Chromium steel versus Semi-HSS; Proceedings of the 47th Rolling Seminar p. 689-702 (October 2010).

[8] S.V. Bravo, K. Yamamoto, H. Miyahara, K. Ogi; Control of carbides and graphite in Cast Irons Type Alloy’s Microstructure for Hot Strip Mills, Research article; Hindawi Publishing Corporation, Journal of Metallurgy, Volume 2012, Article ID 438659, 6 pages; (2012).

[9] M. Boccalini, H. Goldenstein; Solidification of high speed steels; International Materials Reviews, Vol. 46, No. 2; (2001); p. 92-114.

[10] T. Tanaka, T. Koie, M. Ayagaki, M. Yamashita, M. Hashimoto, S. Otomo, T. Inoue; High Speed Steel Type Cold Rolling Mill Roll by Conitnuous Process for Cladding; Nippon steel technical report No. 86 July 2002; p. 80-85.

[11] M. Hashimoto, T. Tanaka, T. Inoue, M. Yamashita, R. Kurahashi, R. Terakado ; Development of Cold Rolling Mill Rolls of High Speed Steel Type by Using Continuous Pouring Process for Cladding; ISIJ International, Vol. 42 (2002), No. 9, p.982-989.

[12] J. Yu, J. McMahon; The effects of the composition and carbide precipitation on the temper embrittlement of 2.25 Cr-1 Mo Steel: Part I. Effects of P and Sn; 1980 American society for metals and the metallurgical society of AIME, volume 11A, February 1980; p. 277-280.

[13] A. Inque, T. Masumoto; Carbide Reactions ($M_3C \rightarrow M_7C_3 \rightarrow M_{23}C_6 \rightarrow M_6C$) during tempering of rapidly solidified high carbon Cr-W and Cr-Mo Steels; 1980 American society for metals and the metallurgical society of AIME, volume 11A; (1980); p. 745-747.

[14] Properties and characteristics of graphite; ENTEGRIS Inc. For semiconductor industry May 2013; (2013); p. 1-37.

[15] V. Kumar; Formation and morphology of M_7C_3 in low Cr White Iron Alloyed with Mn and Cu; Journal of materials engineering and performance, Volume 12(1) February 2003; (2003); p. 14-18.

[16] J. Lecomte-Beckers, O. Dedry, B. Diawara, S. Reginster, J. Tchoufang Tchuindjang ; Fabrication de cylindres bimétalliques par rechargement laser (laser cladding) d’aciers à outils optimisés sur axes réutilisables ; Convention RW 11-1-7335 Project RECYLCLAD ; (2012) ; p. 23-47.

[17] J. Lecomte-Beckers, J. Tchoufang Tchuindjang ; Structural Investigations of Solidification and Heat Treatments Influence on High Alloyed Cast Irons Grades with Nb-V-Ti additions; Defect and Diffusion Forum Vols. 289-292 (2009) Trans Tech Pubblications Switzerland; p. 77-86; online at http://www.scientific.net.

[18] J. Lecomte-Beckers, J. Tchoufang Tchuindjang; Study of the origin of the unexpected pearlite during the cooling stage of two cast HSS; Solid state phenomena vols. 172-174 (2011)Trans Tech Pubblications Switzerland; p. 803-808; online at http://www.scientific.net.

[19] G.S. Cho, L.H. Choe, K.W. Lee, A. Ikenaga; Effects of allying elements on the microstructures and mechanical properties of heavy section ductile cast iron; J. Mater. Sci. Technol., Vol. 23 No. 1; (2007); p. 97-101.

[20] J.M. Artimez, J. Garcia, J.M. Llano Abaitua, M. Alvare, J. Belzunce ; Characterization of M_XC_Y carbides present in high speed steel (HSS) rolls manufacturing by centrifugal casting method; 17th rolling conference, Rosario, Argentina; (2008); p. 1-10.

[21] Q. Wang, X. Li; Effects of Nb, V, and W on Microstructure and Abrasion Resistance of Fe-Cr-C Hardfacing Alloys; Supplement to the welding journal, July (2010); p. 133-139.

[22] S. Bruschi; Lesson notes of Mechanical Technology; (2013).

[23] R.Y. Chen, W.Y.D. Yuen; Oxide-scale Structures Formed on Commercial Hot-Rolle Steel Strip and Their Formation Mechanisms; Oxidation of Metals, Vol. 56, Nos. 1/2; (January, 2001); p. 89-117.

[24] L. Studer; Modelling the Vertical Spincasting of Large Bimetallic Rolling Mills; (2007); p. 1-6.

[25] S.E.M. Industry website; http://www.h-bastiaens.be/page19022.htm; date 04/07/15.

[26] Marichal Ketin Industries (MK) website; http://www.mkb.be/index2.html; date 04/05/15.

[27] Union Electric Steel, Forged and Cast Rolls website; http://www.uniones.com/the-ues-difference/cast-roll-technology/static-casting; date 04/05/15.

[28] Union Electric Steel, Forged and Cast Rolls website; http://www.uniones.com/the-ues-difference/cast-roll-technology/centrifugal-casting; 04/05/15.

[29] GIBSONCENTRITECH website channel, Roll Manufacture Horizontal Static Fill; https://www.youtube.com/channel/UC6BuSL0byvp1sL0P-Dg3m6w; date 03/05/15.

[30] AZO materials website; http://www.azom.com/article.aspx?ArticleID=1630; date 15/07/15.

[31] M. Pellizzari, A. Tremea, S. Ricco; Abrasive wear behaviour of hot roll materials; 5th conference on abrasion wear resistant cast iron and forged steel for rolling and pulverizing mills.

[32] Thermo-calc Software website; http://www.thermocalc.com/products-services/databases/the-calphad-methodology/; date 11/08/15.

[33] NETZSCHwebsite;https://www.netzsch-thermal-analysis.com/us/products-solutions/simultaneous-thermogravimetry-differential-scanning-calorimetry/sta-449-f1-jupiter/; date 11/08/15.

[34] Olympus technical brochure; http://www.olympusmicro.com/brochures/pdfs/bx51.pdf; date 11/08/15.

[35] Technical manual of DIL 402C; http://www4.dcu.ie/sites/default/files/mechanical_engineering/images/Manual_DIL402PC_e.pdf; date 11/08/15.

[36] KU Leuven website; https://www.mtm.kuleuven.be/equipment/ESEM-XL30-FEG/ESEM-XL30-FEG; date 11/08/15.

[37] Magne-gage website; http://www.magne-gage.com/gauges.htm; date 11/08/15.

[38] Technical manual of EMCO M1C 010; http://www.decca.si/modules/store/uploads/pdf/emco-test-m1c-1.pdf; date 12/08/15.

[39] STRUERSwebiste ;http://www.struers.com/default.asp?top_id=3&main_id=10&sub_id=300 &doc_id=1197 and http://www.struers.com/default.asp?top_id=3&main_id=9&doc_id=817; date 12/08/15.

[40] J. Lecomte-Beckers, J. Tchoufang Tchuindjang; Cartographies SEM/EDX et Caractérisation Microstructurale des Carbures d'un barreau de Contrôle ICDP, présentant une ségrégation en Nb et Ti ; Convention RW114877 Project INCA; (August 2003) ; p. 14-21.

Figure list

Table list

Equation list